FERMILAB-THESIS-2005-14

Angular correlations in beauty production at the Tevatron at $\sqrt{s} = 1.96$ TeV

Angular correlations in beauty production at the Tevatron at $\sqrt{s}$ = 1.96 TeV

EEN WETENSCHAPPELIJKE PROEVE OP HET GEBIED DER
NATUURWETENSCHAPPEN, WISKUNDE EN INFORMATICA

PROEFSCHRIFT

TER VERKRIJGING VAN DE GRAAD VAN DOCTOR
AAN DE RADBOUD UNIVERSITEIT NIJMEGEN
OP GEZAG VAN DE RECTOR MAGNIFICUS PROF. DR. C.W.P.M. BLOM,
VOLGENS BESLUIT VAN HET COLLEGE VAN DECANEN
IN HET OPENBAAR TE VERDEDIGEN OP WOENSDAG 22 JUNI 2005
DES MORGENS OM 10.30 UUR PRECIES

DOOR

Daniel Abraham Wijngaarden

GEBOREN OP 1 SEPTEMBER 1975
TE AMSTERDAM

Promotor:	Prof. dr. S. J. de Jong	
Co-promotor:	Dr. F. Filthaut	
Manuscriptcommissie:	Dr. W.J.P. Beenakker	
	Prof. dr. M.W.J.M. Demarteau	Universiteit van Amsterdam
	Prof. dr. ing. B. van Eijk	Universiteit Twente
	Prof. dr. P. Mättig	Bergische Universität Wuppertal
	Dr. M. Vreeswijk	Universiteit van Amsterdam

ISBN 90-9019503-3

Contents

Chapter 1

Introduction

After centuries of fundamental physics research we know next to nothing about the fundamental structure of the universe. Despite hundreds of years of extremely successful theories - from Newton's theory of gravity right down to modern quantum field theories - the remaining questions are stunning. Why are there so many different particles? Why do they have such a wide range of masses? Why is there so much more matter than antimatter? What is mass?

A lot of progress has been made in the 20^{th} century, culminating in the Standard Model of elementary particle physics. The Standard Model describes twelve elementary matter particles and their antimatter counterparts, twelve force particles and a hypothetical Higgs boson. The particle theory of the electromagnetic force, known as Quantum Electro Dynamics (QED), has been tested to an accuracy better than fifty parts per billion[1]. The theory of the weak force, responsible for radioactive decays and for the power of the sun, will be complete within the framework of the Standard Model when the existence of the Higgs boson is experimentally confirmed. And despite insistence by the man who first used the word "quark" to describe an elementary particle that "A search for stable quarks [...] at the highest energy accelerators would help to reassure us of the non-existence of real quarks" [3], experiments at those accelerators have instead shown how successful the quark theory is in describing the strong force keeping protons and neutrons together. Gravity, the most obvious force in every day life, is the only force that particle physicists seem unable to incorporate in the Standard Model.

Beyond the Standard Model, supersymmetric theories ("SUSY") predict a host of mirror particles accompanying the known particles. String theorists try to address more fundamental questions left open by the Standard Model, including the incorporation of gravity. Unfortunately, while tests of SUSY are already underway and experiments at the Large Hadron Collider at CERN in Geneva, Switzerland (expected to start in 2007) should give a final answer on whether supersymmetric particles do or do not exist, string theories have not yet yielded any unique predictions that can be experimentally tested.

In high energy collider experiments, the predictions made by the Standard Model and its possible extensions are tested by colliding beams of very energetic particles. The energy released in the collisions is converted into new particles whose trajectories and energies are measured by large

---

[1] The world average measurement of the anomalous magnetic moment of the electron is $(g^{\text{exp}} - 2)/2 = (1159652185.9 \pm 3.8) \times 10^{-12}$ [1]. The Standard Model prediction is $(g^{\text{th}} - 2)/2 = (1159652140 \pm 28) \times 10^{-12}$ [2], which means that the value of the magnetic moment g agrees with the theoretical value to within 45 parts in 10^{12}.

detectors constructed around the collision point. The measured properties and production rates of the different types of particles are compared to the theory predictions.

Despite the success of the Standard Model, experiments have revealed several discrepancies and unanswered questions. One problem that has surfaced in experiments performed at the Tevatron collider at the Fermi National Accelerator Laboratory near Chicago in the 1990s is the rate of production — the cross section — of the production of beauty quarks in proton-antiproton collisions. Beauty — more commonly referred to as bottom or just b — is one of the six quarks described by the Standard Model. The bottom quark was first experimentally observed in 1977 [4, 5]. Early measurements of the b production cross section at the UA1 experiment at CERN [6, 7] showed good agreement with theory predictions [8–10]. However, measurements at higher energies by the DØ and CDF experiments at the Tevatron have consistently yielded cross sections in excess of the central value of theory predictions. While a lot of progress has been made by theorists to debunk the significance of this excess [11], additional measurements are necessary to confirm that the b quark production mechanisms are now well understood.

This thesis concerns a measurement of the angular correlation between pairs of b quarks produced in the same collision. The angular correlation is directly sensitive to the difference between the first- and second order approximations of the theory of the strong force, known as Quantum Chromodynamics (QCD), which is the dominant source of b quark production at the Tevatron.

Beauty production through the strong force is an important background for many other physics studies, including tests of SUSY and the search for the Higgs boson. If the Higgs boson is light enough to be detected at the Tevatron, it will decay to a b-anti-b quark pair most of the time. In these decays the b quark and the anti-b quark emerge nearly back-to-back. A good understanding of the angular distribution of b quarks produced in other processes is very important for measurements of new physics.

This thesis begins with a summary of the relevant parts of the Standard Model of elementary particle physics in Chapter 2. Special attention is given to the production and decay of bottom quarks. Chapter 3 describes the Tevatron accelerator and the DØ detector used to detect the particles produced in the proton-antiproton collisions. Because the collisions happen at a rate faster than can be permanently stored, interesting events are selected by an online filter system described in Chapter 4. The algorithms used to reconstruct the signals provided by the detector into physically meaningful objects are discussed in Chapter 5. In Chapter 6, the method to select events in which bottom quarks were produced is developed. Finally, the measurement of the angular correlations between b quarks is presented in Chapter 7.

1.1 Units and coordinates

In the title of this thesis, $\sqrt{s}$ represents the centre of mass energy in collisions. The s is one of the three Mandelstam variables defined as a function of the momenta of incoming and outgoing particles in a scattering process AB → CD:

$$s = (p_{\mathrm{A}} + p_{\mathrm{B}})^2, \tag{1.1}$$
$$t = (p_{\mathrm{A}} - p_{\mathrm{C}})^2, \tag{1.2}$$
$$u = (p_{\mathrm{A}} - p_{\mathrm{D}})^2, \tag{1.3}$$

where p_{A} and p_{B} are the momenta of the incoming particles and p_{C} and p_{D} are the momenta of the outgoing particles.

A right handed coordinate system is used in the DØ detector, with the positive z axis aligned with the beam in the direction of the proton beam and $z = 0$ at the centre of the detector. Protons enter the detector from the north, travelling clockwise around the Tevatron. Spherical (r, ϕ, θ), cylindrical (r, ϕ, z) and Cartesian coordinates are used. The azimuthal angle ϕ is defined as a counterclockwise rotation when looking toward $z = 0$ (i.e. into the detector) with $\phi = 0$ at the 3 O'clock position. The polar angle θ is defined with respect to the z axis. The Cartesian coordinates (x,y) are defined such that $x = r\cos\phi$ is the horizontal coordinate, and $y = r\sin\phi$ the vertical coordinate.

Instead of the polar angle θ, the pseudorapidity η is usually used:

$$\eta = -\ln(\tan(\theta/2)). \tag{1.4}$$

The pseudorapidity is normally defined with respect to the event primary vertex (the interaction point). Pseudorapidity can also be defined with respect to the centre of the detector, $z = 0$, in which case we speak of *detector* η. In the limit that $m << E$, where m is the invariant mass defined by $m^2 = E^2 - \vec{p}^2$, the pseudorapidity approximates the true rapidity

$$y = \frac{1}{2}\log\left(\frac{E + p_z}{E - p_z}\right). \tag{1.5}$$

Differences in rapidity are invariant under Lorentz boosts in the z direction, making (pseudo) rapidity a very useful coordinate in hadron collider physics.

In addition to the pseudorapidity η and the azimuthal angle ϕ, the space angle ΔR between particles is also used. This angle is defined as

$$\Delta R = \sqrt{\Delta\eta^2 + \Delta\phi^2}. \tag{1.6}$$

The space or opening angle ΔR is especially useful for clustering particles.

Chapter 2

Heavy quark production in $p\bar{p}$ collisions

At hadron colliders, b quarks are predominantly produced through the strong force[1], described by Quantum Chromodynamics (QCD). QCD is one of the elementary field theories making up the Standard Model of particle physics. In this chapter, an overview of bottom production and correlations between $b\bar{b}$ pairs in QCD is presented. The weak decay of the produced B hadrons and the simulation of heavy flavour events in PYTHIA are also discussed. Many overviews of QCD are available; some good sources are [13, 14].

2.1 The Standard Model

The Standard Model is a quantum field theory of fundamental particles and interactions. The fundamental principle of the Standard Model is the invariance of physics under local gauge transformations. The gauge symmetry group is $SU(3)\otimes SU(2)\otimes U(1)$, where the SU(3) group corresponds to the strong interaction and the $SU(2) \otimes U(1)$ group corresponds to the electroweak interactions.

Matter particles in the Standard Model are described as spin $\frac{1}{2}$ fermion fields. The forces are carried by spin 1 boson fields — the photon (γ) and three massive bosons (W^+, W^-, Z^0) for the electroweak force, and eight gluons (g_a, $a = 1 \ldots 8$, or generally just g) for the strong interaction. The force carriers are shown in Table 2.1.

Force	Group	Mediator	Spin	Mass (GeV/c^2)
Strong	SU(3)	8 gluons (g_a)	1	0
Weak	$SU(2) \otimes SU(1)$	W^-, W^+	1	80.425 ± 0.038
		Z^0	1	91.1876 ± 0.0021
Electromagnetic		photon (γ)	1	0

Table 2.1: The three forces in the Standard Model and the intermediating bosons. The particle properties are taken from [1].

---

[1] The cross section for electroweak production of $b\bar{b}$ pairs $\sigma(p\bar{p} \to \gamma^*/Z^0 \to b\bar{b})$ is more than an order of magnitude lower than the strong production cross section even for relatively large quark p_T [12].

generation	1	2	3	Q
quarks	$\begin{pmatrix} \mathrm{u} \\ \mathrm{d} \end{pmatrix}$	$\begin{pmatrix} \mathrm{c} \\ \mathrm{s} \end{pmatrix}$	$\begin{pmatrix} \mathrm{t} \\ \mathrm{b} \end{pmatrix}$	$+2/3$ $-1/3$
leptons	$\begin{pmatrix} \nu_\mathrm{e} \\ \mathrm{e} \end{pmatrix}$	$\begin{pmatrix} \nu_\mu \\ \mu \end{pmatrix}$	$\begin{pmatrix} \nu_\tau \\ \tau \end{pmatrix}$	0 -1

Table 2.2: The three generations of quarks and leptons. Q is the electric charge in units of proton charge.

There are three generations each of quarks and leptons, beginning with the up and down quarks and the electron and electron neutrino and increasing in mass with each generation. The fermions of the three generations and their charge are listed in Table 2.2.

The quark masses are not well defined as quarks are not observed as free particles in experiments. However, their constituent mass can be estimated (introducing some model dependence) from the hadrons they compose. The top quark is the one exception, since it decays too quickly to form hadrons. As a result, its mass is relatively the most precisely known of all quarks, at $m_\mathrm{t} = 178.0 \pm 4.3\ \mathrm{GeV}/c^2$ [15].

The SU(3) theory of the strong interaction is known as Quantum Chromodynamics or simply QCD. The QCD coupling strength α_s depends on the energy scale of the interaction and decreases as the energy scale increases. For energy scales larger than the QCD scale Λ_QCD, perturbative calculations can be used to calculate scattering amplitudes. The QCD scale Λ_QCD can be determined from measurements of α_s and is of the order of a few hundred MeV.

The charm ($m_\mathrm{c} = 1.47 - 1.83\ \mathrm{GeV}/c^2$) and bottom ($m_\mathrm{b} = 4.7 - 5.0\ \mathrm{GeV}/c^2$) quarks both have pole masses significantly larger than the QCD scale. The heavy quarks play a special role in perturbative QCD as their large masses set the scale for perturbative calculations. The bottom quark is of special interest because it is heavy enough to allow perturbative calculations but light enough to be produced copiously at current accelerators.

The strong interaction is the dominant source of bottom quark production at the Tevatron. The produced B hadrons decay through the weak force. Production and decay of b flavoured particles are described in more detail in the following sections.

2.2 Quantum Chromodynamics

The fundamental particle fields in QCD are quark colour fields. The colour quantum number is the charge of the strong force — red, green or blue for the quarks, anti-red, anti-green or anti-blue for the antiquarks. The QCD SU(3) group of phase transformations on the quark colour fields is non-abelian, that is, the generators T_a do not commute. The free Lagrangian in QCD is

$$\mathcal{L}_0 = \bar{q}(i\gamma^\mu \partial_\mu - m)q \tag{2.1}$$

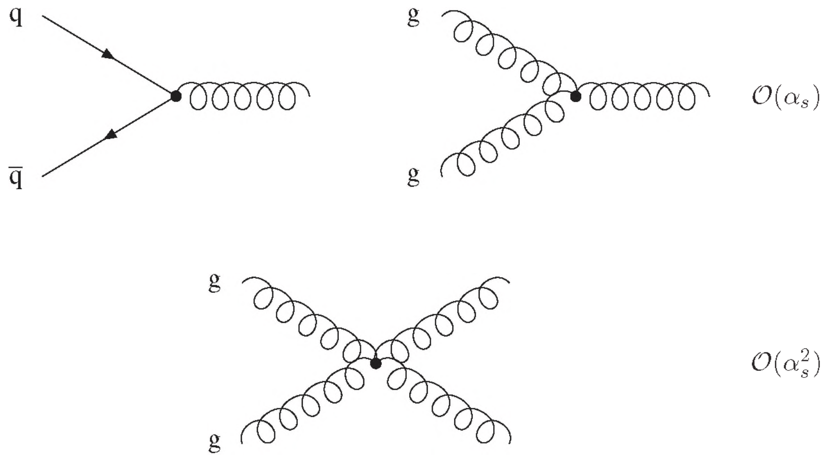

Figure 2.1: The three vertices in QCD.

where q is the quark field vector in colour space. (For simplicity, only one quark flavour is shown.)

To make the Lagrangian invariant under infinitesimal local gauge transformations, $q(x) \rightarrow [1 + i\alpha_a(x)T_a]q(x)$, eight gauge fields (index $a = 1 \ldots 8$) must be introduced, which are associated with the gluons. Because the group is non-abelian, gauge invariance requires the gluon fields to transform as

$$G^a_\mu \rightarrow G^a_\mu - \frac{1}{g}\partial_\mu \alpha_a(x) - f_{abc}\alpha_b(x)G^c_\mu, \tag{2.2}$$

where f_{abc} are the structure constants for QCD.

Adding a gauge invariant kinetic energy term for each of the G^a_μ fields, the final gauge invariant QCD Lagrangian is

$$\mathcal{L} = \bar{q}(i\gamma^\mu \partial_\mu - m)q - g_s(\bar{q}\gamma^\mu T_a q)G^a_\mu - \frac{1}{4}G^a_{\mu\nu}G^{\mu\nu}_a, \tag{2.3}$$

where the field strength tensor $G^a_{\mu\nu}$ is given by

$$G^a_{\mu\nu} = \partial_\mu G^a_\nu - \partial_\nu G^a_\mu - g_s f_{abc} G^b_\mu G^c_\nu, \tag{2.4}$$

and g_s specifies the coupling strength.

The kinetic energy term in Eq. 2.3 is not purely kinetic but includes an induced self-interaction between the gluons. This also reflects the fact that, unlike the photon in the electromagnetic interaction, the gluons themselves carry colour charge. (In fact, the gluons carry a combination of colour and anti-colour charge.) The Lagrangian describes free particles and interactions; the interactions are generated by the terms containing the coupling constant $g_s = \sqrt{4\pi\alpha_s}$.

Calculations in QCD can be performed using a perturbative expansion in the coupling constant, leading to the Feynman rules for free particles and interactions. The resulting terms can be related one-to-one to a set of Feynman diagrams. The calculation of the amplitude for the transition from an initial state to a final state then involves all Feynman diagrams that have the same initial and final state. Examination of the Lagrangian leads to the elementary interaction vertices of QCD, shown in Fig. 2.1.

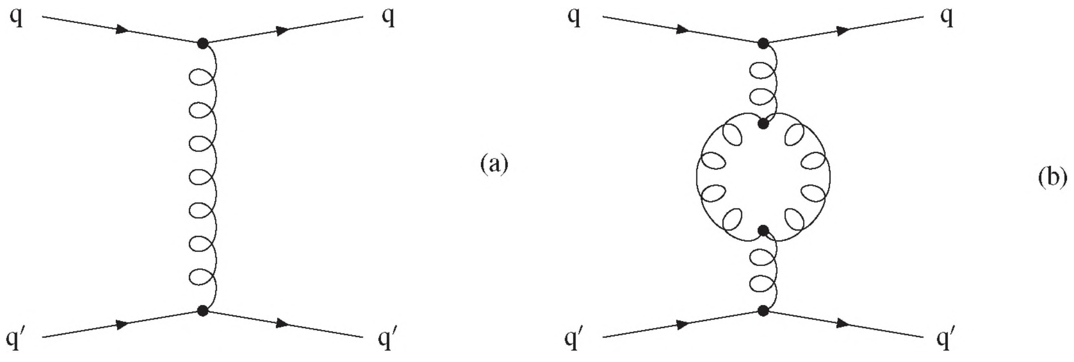

Figure 2.2: Quark scattering in QCD. Figure (a) shows a leading order diagram. Figure (b) shows a higher order correction involving a gluon loop.

2.2.1 Renormalisation

The strength of the strong coupling depends on the coupling constant. Figure 2.2(a) shows a Leading Order (LO, i.e. lowest order in α_s) diagram for quark-quark scattering. Vacuum polarisation through higher order diagrams involving gluon loops, as shown in Fig. 2.2(b), has a net anti-screening effect on the visible coupling charge. The effective or running coupling constant therefore depends on the range of the interaction, or equivalently on the squared momentum transfer $|Q^2|$.

Loops with infinite (ultraviolet) loop momenta lead to divergences in amplitude computations. These ultraviolet divergences must be regulated in a consistent way. The divergences can be consistently absorbed by the parameters in the QCD Lagrangian: the coupling constants, masses and field strengths. This is the process of renormalisation. A particular renormalisation scheme must be chosen. In the renormalisation process, the renormalisation scale μ is introduced. A consistent choice must be made for the renormalisation scale, typically characteristic of the energy scale of the physics process. For heavy quark production, a common choice is $\mu^2 = m_Q^2 + p_T^2$, where m_Q and p_T are the mass and transverse momentum of the heavy quark. It should be noted that although μ has the dimension of mass it is only introduced as an intermediate parameter to make the calculation possible. It is neither a cutoff, nor a physical parameter.

The coupling constant depends on the renormalisation scale μ. (At higher orders, α_s also depends on the renormalisation scheme.) To first order, the dependence of the coupling constant on μ is

$$\alpha_s(\mu^2) = \frac{\alpha_s(\mu_0^2)}{1 + (\alpha_s(\mu_0^2)/12\pi)(11n - 2f)\ln(\mu^2/\mu_0^2)}, \tag{2.5}$$

where n is the number of colours and f is the number of active[2] flavours. The value of $\alpha_s(\mu^2)$ at any value of μ can now be related to the value at a fixed reference scale μ_0. The current standard choice is $\mu_0 = m_{Z^0}$.

---

[2] Only quark flavours with masses lower than the scale $\mu/2$ at which α_s is required contribute significantly to the physics process.

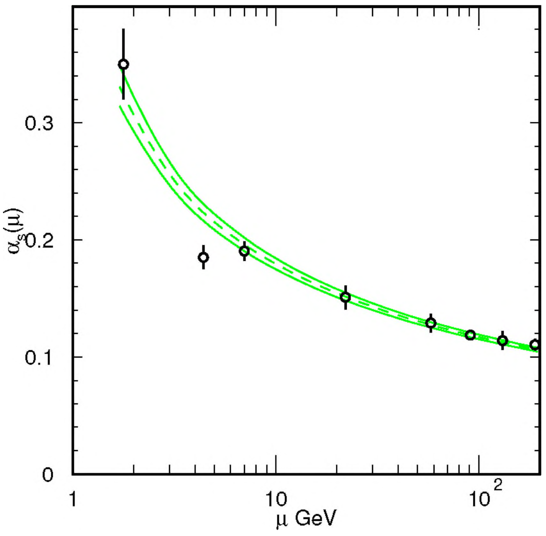

Figure 2.3: Summary of the values of $\alpha_s(\mu)$ at the values of μ at which they were measured. The lines indicate the central value and $\pm 1\sigma$ limits of the average [1].

The scale dependence of the coupling constant can also be expressed in terms of a single parameter,

$$\alpha_s(\mu^2) = \frac{12\pi}{(11n - 2f)\ln(\mu^2/\Lambda^2_{\text{QCD}})}, \tag{2.6}$$

where Eq. 2.5 and 2.6 define the QCD scale parameter Λ_{QCD}. This is a fundamental parameter of QCD and can be determined from measurements of α_s. The (renormalisation scheme dependent) world average value for five active flavours, based on a next-to-next-to-leading order approximation of α_s rather than the first order approximation given in Eq. 2.6, is $\Lambda^{(5)}_{\text{QCD}} = 217^{+25}_{-23}$ MeV [1].

From Eq. 2.5 it can be seen that α_s approaches zero as the scale of the interaction goes to infinity. This effect is known as asymptotic freedom [16, 17]. At high momentum transfer, the coupling constant is small and quarks and gluons can be treated as unbound particles. Amplitudes can then be calculated using perturbative techniques, based on expansion in α_s. Currently, Next-to-Leading Order (NLO) calculations are available for most processes.

Around the QCD scale, the strong force indeed becomes strong. As a result, quarks and gluons are never observed as free particles but confined inside the low-$|Q^2|$ bound states of the observed hadrons. How precisely this happens is not known; however, this is not fatal for the predictive power of QCD, thanks to the factorisation theorem (see Section 2.2.2). The running of the coupling constant has been experimentally confirmed (see Fig. 2.3.)

Physical quantities — which can be measured in experiment — should not depend on the choice of μ if an exact calculation is made. However, the use of finite order calculations introduces uncertainties of the order of the first uncomputed term, i.e. one order higher. Uncertainties arising from the choice of the renormalisation scale are usually estimated by varying the scale between $\mu/2$ and 2μ.

Aside from the ultraviolet divergences, infrared divergences occur in loop contributions as well as through emission of soft (low momentum) or very collinear particles in the initial or final state. Most of these divergences cancel when adding real and virtual contributions. Initial state collinear divergences do not cancel, but can be removed through factorisation (see Section 2.2.2).

After the divergences are removed, powers of logarithms remain at every order in α_s. When these logarithms are numerically large they may threaten the convergence of the perturbative expansion, even if α_s is small. Resummation of the logarithm terms makes the series better behaved. The calculation can then be approximated by summing the leading logarithm (LL) terms to all orders. Higher order (NLL and beyond) terms of the logarithm can also be included.

2.2.2 Factorisation

The collision of two hadrons can be roughly described as a sequence of distinct steps. The exact separation between the parts is not unambiguous. However, a distinction between perturbative and nonperturbative parts of the calculation can be made. The factorisation theorem allows the separation of short-distance effects, which can be calculated perturbatively, and long-distance effects which need to be modelled in other ways.

At the centre of the collision is the hard scattering of partons from the incoming hadrons. The partons are treated as unbound particles, and the process can be calculated at a fixed order in perturbation theory.

The structure of the incoming hadrons is described by parton distribution functions (PDFs). The parton distribution $f_i^A(x, Q^2)$ gives the probability to find a parton i with a fraction x of the beam energy in beam particle A. Q is the scale of the interaction. The primary partons may undergo initial state radiation or splitting, and from this initial state shower two partons (each connected to one of the incoming hadrons) are selected to participate in the hard scatter interaction. In the case of QCD, the remnants of the incoming hadrons are not completely disconnected from the rest of the event. However, the nonperturbative effects on the calculable cross section — sometimes called *higher twist corrections* — are negligible if the relevant kinematic scale is large enough.

The cross section for the production of a b quark can be written as

$$\sigma^{\mathrm{b}} = \sum_{i,j} \int \mathrm{d}x_i \mathrm{d}x_j f_i^A(x_i, \mu_F^2) f_j^B(x_j, \mu_F^2) \hat{\sigma}_{ij}^{\mathrm{b}}(p_i, p_j, \mu^2, \mu_F^2). \tag{2.7}$$

Here, $\hat{\sigma}_{ij}^{\mathrm{b}}$ is the — perturbatively calculated — cross section for the interaction of two partons i, j resulting in the production of a b quark, μ and μ_F are the renormalisation and factorisation scales and f_i^A and f_j^B are the parton distribution functions.

The factorisation theorem allows divergences occurring through particle branchings in the initial state to be absorbed in the parton distribution functions. As for renormalisation, a specific factorisation scheme must be chosen to consistently separate the low momentum processes from the parton cross section $\hat{\sigma}_{ij}^{\mathrm{b}}$. In separating the perturbative and nonperturbative parts, the fragmentation scale μ_F is introduced. Very roughly speaking, any propagator that is off-shell by μ_F^2 or more will contribute to the hard scatter part of the calculation. Below this scale, it will be included in the nonperturbative parton distribution functions. For heavy quark production, the factorisation and renormalisation scales are usually chosen to be equal, $\mu_F = \mu$.

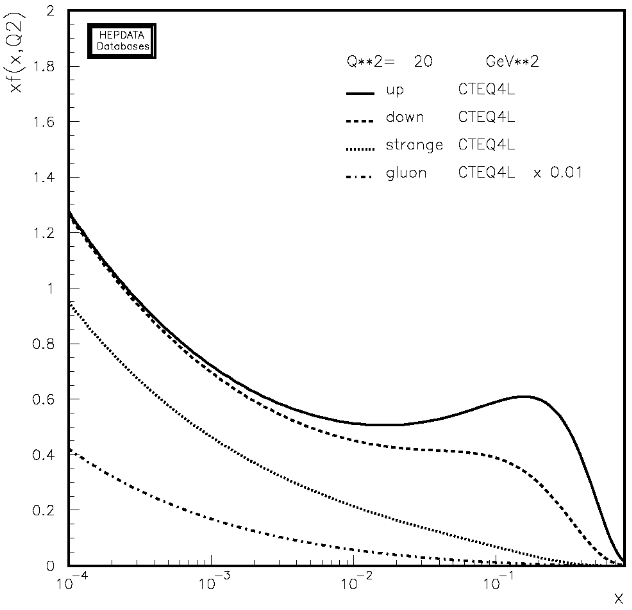

Figure 2.4: CTEQ4L parton distributions $xf(x, Q^2)$ in the proton for $Q^2 = 20$ GeV^2. Only u, d, and s quarks and gluons ($\times 0.01$) are shown. The figure was generated using [19].

2.2.3 Parton Distribution Functions

The parton distribution functions contain all the infrared sensitivity of the initial phase of the interaction. They are specific to the incoming hadron, and could be described as the momentum distributions of partons inside the hadron. Since the interactions inside the proton or antiproton are dominated by low momentum transfer processes, the PDFs cannot be calculated perturbatively. Instead, they are determined by global fits to selected sets of data, e.g. from deep inelastic scattering experiments. The factorisation theorem ensures that the PDFs are universal and can be applied to any process. The CTEQ [18] group, among others, provides PDFs updated for recent data and theoretical developments.

The PDF analyses are typically carried out at NLO in a specific renormalisation and factorisation scheme. To correctly match the PDFs with the matrix element calculations the same scheme must be used. LO PDFs are also available, and are the natural choice when using LO matrix elements (as in PYTHIA)[3]. At LO the PDFs are not scheme dependent. In this thesis, the CTEQ4L PDF set is used, which is based on a lowest order approximation matched to data. The u, d, s and gluon distributions for $Q^2 = 20$ GeV^2 are shown in Fig. 2.4.

2.2.4 Fragmentation

The final state partons from the hard scatter process may radiate gluons or split in $q\bar{q}$ pairs, creating a final state shower of secondary partons. Since only colourless hadrons are observed in nature, a transition must be made from coloured partons to colourless hadrons. The transition from the

---

[3] The differences between LO and NLO PDFs are formally NLO, though, so the error introduced by using a NLO PDF with LO matrix elements should not be significant.

final state particles in the hard interaction of Eq. 2.7 into colourless hadrons cannot be calculated perturbatively. Instead, fragmentation functions are used. Formally, the fragmentation function is related to the probability of finding a hadron H with a certain momentum fraction z of the parton, defined as

$$z = \frac{(E + p_{||})_{\text{hadron}}}{(E + p)_{\text{quark}}}, \tag{2.8}$$

where $p_{||}$ is the momentum component parallel to the quark direction. The higher the value of z, the *harder* the fragmentation.

The fragmentation of a heavy quark can be interpreted as a process $\mathrm{Q\overline{Q}} \rightarrow \mathrm{Q\overline{q}} + \mathrm{q\overline{Q}}$, where each heavy quark picks up a light quark to form a meson. Baryons are formed in a similar way. The hadron will lose some fraction of its momentum with respect to the momentum of the open quark. For b quarks, the fraction of momentum lost to fragmentation is small and z will be close to one.

While the momentum loss is small (roughly 10%), it has a large impact on the value of the cross section, because of the steeply falling momentum spectrum of the b quark. A good understanding of the fragmentation function is therefore very important when comparing to experimental data.

Several models are available for the fragmentation process in event simulations. In the coloured string fragmentation model [20], fragmentation proceeds along colour-flux lines between the quarks and gluons. As the distance between quark and antiquark increases, the string is stretched and will eventually break, producing a new quark-antiquark pair at the endpoints. The new systems may split again, until only on-mass shell hadrons remain. Energy and momentum are conserved at each step in the process.

Hadronisation

Radiation of gluons from a final state parton, splitting of gluons and the subsequent formation of hadrons from the coloured partons leads to a shower of colourless particles, known as a jet. (The precise definition of a "jet" depends on the way the particles are clustered. See also Section 5.1.) The heavy quark and other coloured partons combine with other quarks to form colourless hadrons. The complete hadron formation process is also known as hadronisation.[4]

2.3 Heavy flavour production at the Tevatron

2.3.1 Previous measurements of b production

The existence of the b quark was first directly confirmed at the E288 experiment at Fermilab in 1977 [4,5]. Early measurements of the b quark production cross section at $\sqrt{s} = 630$ GeV by the UA1 collaboration at CERN [7,22,23] were in good agreement with (NLO) theoretical predictions [8–10].

Measurements of the b quark cross section performed at the Tevatron at $\sqrt{s} = 1.8$ TeV by the CDF [24–32] and DØ [33–36] collaborations showed a consistent excess over the predicted cross section and cast some doubt on the accuracy of the NLO calculations. A short run at the Tevatron

---

[4] In some references (e.g. [21]), the term hadronisation also includes the decay of unstable hadrons.

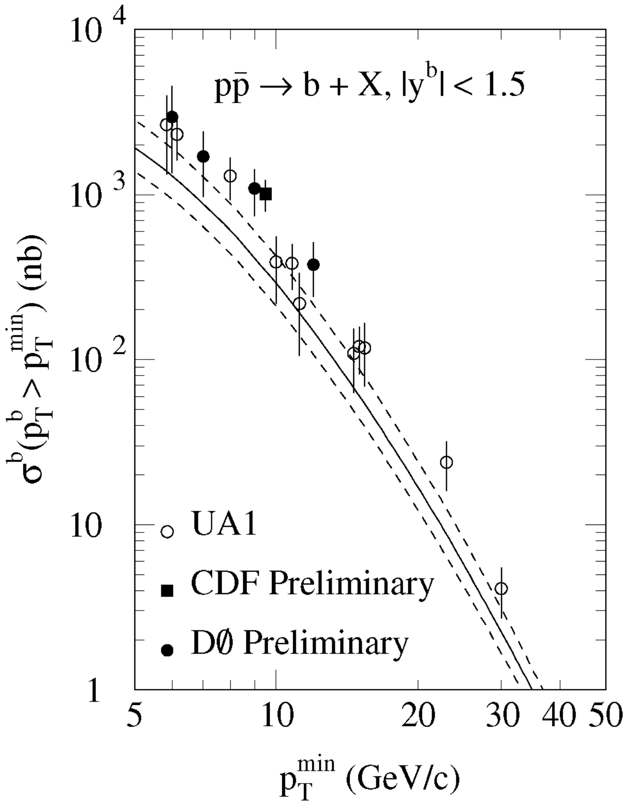

Figure 2.5: Measurements of the b quark production differential cross section at $\sqrt{s} = 630$ GeV. p_T^{min} is defined such that after kinematic cuts, 90% of all b quarks have $p_T^b > p_T^{min}$.

at $\sqrt{s} = 630$ GeV also yielded higher cross section measurements [37, 38] than those reported by UA1 (see Fig. 2.5). Likewise, measurements of exclusive B meson cross sections [39, 40] were also higher than the theoretical predictions. Some of the measurements performed by the DØ and CDF collaborations at $\sqrt{s} = 1.8$ TeV are shown in Fig. 2.6.

Recent work [41, 42] on a consistent comparison between theory and experiment has indicated that the difference in the reported cross sections is far from alarming. (And was perhaps never that large to begin with.) Two important factors in the reported discrepancies are the deconvolution of experimentally measured observables (such as the p_T spectra of B mesons or their decay products) to yield b quark cross sections, and the matching of perturbative and nonperturbative aspects of the calculation. The treatment of the fragmentation of the b quarks is especially important. These considerations are discussed in the following sections.

Many of the experimental papers report an excess over the central value of the theoretically predicted cross sections without taking into account the uncertainty on those predictions. While the discrepancy between data and theory is perhaps overstressed, the magnitude of the uncertainties in the predictions themselves is disturbing. One would have hoped that the NLO calculations would be less sensitive to variation of the scale parameters [18]. Measurements of correlations between produced $b\bar{b}$ quark pairs can give additional insight into the QCD production process [43, 44] and are the main focus of this thesis. Correlations in $b\bar{b}$ hadroproduction are discussed in Section 2.4.

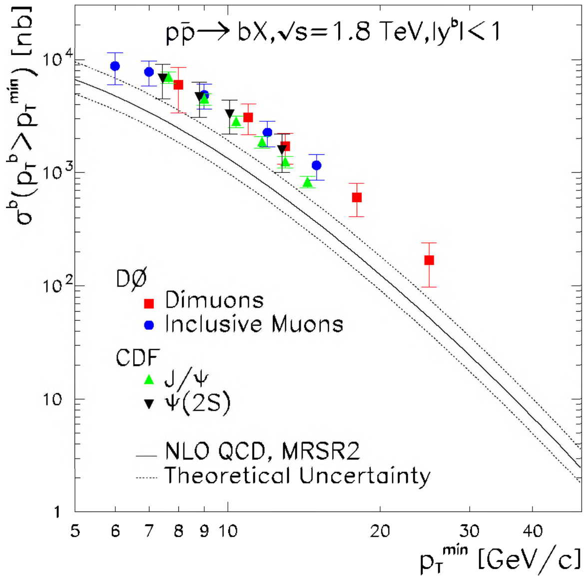

Figure 2.6: Measurements of the b quark production differential cross section at $\sqrt{s} = 1.8$ TeV.

2.3.2 Fragmentation functions

One source of the discrepancy between the predicted value of the cross section and the experimental results is the uncertainty associated with the fragmentation functions that are used. As mentioned in Section 2.2.4, the differential cross section $\mathrm{d}\sigma/\mathrm{d}p_T$ depends strongly on the fragmentation function because of the steeply falling momentum distribution.

The nonperturbative hadron formation effect can be introduced by writing the hadron-level cross section for B mesons as

$$\frac{\mathrm{d}\sigma^{\mathrm{B}}}{\mathrm{d}p_T} = \int \mathrm{d}\hat{p}_T \mathrm{d}z \frac{\mathrm{d}\sigma^{\mathrm{b}}}{\mathrm{d}\hat{p}_T} D(z)\delta(p_T - z\hat{p}_T). \tag{2.9}$$

The function $D(z)$ is a phenomenological parametrisation of hadronisation effects. One parametrisation is the symmetric Lund model [20],

$$D(z) \propto \frac{1}{z}(1-z)^a \exp(-\frac{bM_T^2}{z}), \tag{2.10}$$

where M_T is the transverse mass, defined as $M_T^2 = m^2 + p_T^2$.

Data indicate the need for a harder fragmentation function for bottom (and charm) fragmentation. A widely used model is the Peterson model [45],

$$D(z;\epsilon) \propto \frac{1}{z(1-\frac{1}{z}-\frac{\epsilon_{\mathrm{Q}}}{1-z})^2}. \tag{2.11}$$

The parameter ϵ_{Q} is determined from fits to $\mathrm{e^+e^-}$ data [46].

An alternative approach is to consider only the moments of the fragmentation function. Assuming $\mathrm{d}\hat{\sigma}/\mathrm{d}\hat{p}_T = A\hat{p}_T^{-n}$, the differential hadronic cross section can be written as

$$\frac{\mathrm{d}\sigma}{\mathrm{d}p_T} = \int \mathrm{d}z\mathrm{d}\hat{p}_T D(z)\frac{A}{\hat{p}_T^n}\delta(p_T - z\hat{p}_T) = \frac{A}{p_T^n}D_n. \tag{2.12}$$

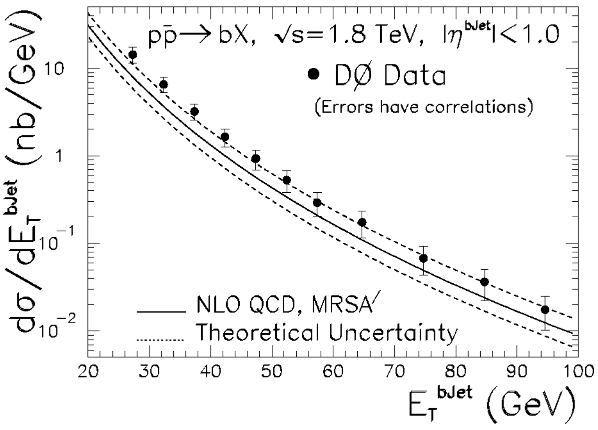

Figure 2.7: The differential cross section for b jet production at $\sqrt{s} = 1.8$ TeV [47].

Only the n^{th} moment of the fragmentation function, $D_n \equiv \int D(z)z^{n-1}\mathrm{d}z$, needs to be considered. The moments can be calculated from the distribution of the B meson energy fraction with respect to the beam energy (x_E). The free parameter of a nonperturbative fragmentation function can then be fixed from the n^{th} moment. The value of n depends somewhat on the p_T range considered. Using this method, a smaller discrepancy between b quark production data and theoretical predictions was found [11].

2.3.3 Study of b jets

The uncertainty introduced by the treatment of soft and collinear emissions can also be reduced by looking at b jet instead of open b quark production. In this case, the observable under study is the jet in which a b quark is found, irrespective of the fraction of momentum carried by the b quark. Because jets — as opposed to quarks — are directly observable, they provide a much more robust comparison with QCD predictions.

By explicitly including the collinear emissions in the jet, large logarithms in the cross section calculation are avoided. Since the fraction of the available momentum carried by the b quark itself is no longer relevant, the choice of fragmentation model also becomes less important.

A measurement of the differential b jet cross section $\mathrm{d}\sigma^{\mathrm{b\,jet}}/\mathrm{d}p_T$ is presented in [47] and compared to a NLO QCD calculation [48]. The cross section is shown in Fig. 2.7. The measured cross section is now found to be compatible with the NLO prediction, although the experimental result is still above the predicted central value.

Although in the current analysis the production of b jets is not studied as a function of p_T, cuts on transverse energy are applied. Studying b jets rather than quarks should reduce the uncertainty introduced by these cuts and the fragmentation model.

A complication in studying b jets is the possibility that the b and $\bar{\mathrm{b}}$ quarks both end up in the same jet. This effect is discussed in more detail in Chapter 7.

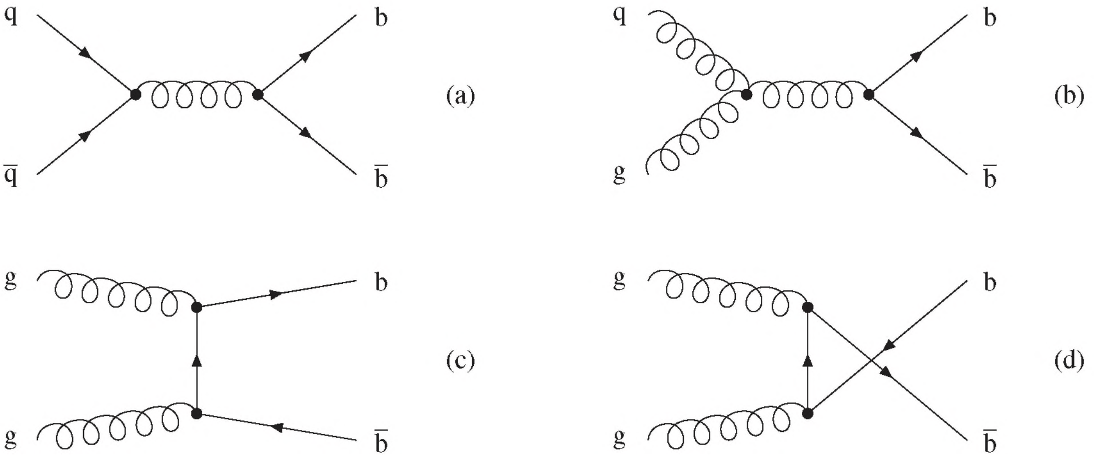

Figure 2.8: Leading order ($\mathcal{O}(\alpha_s^2)$) $\mathrm{b\bar{b}}$ production mechanisms in QCD: (a) quark-antiquark annihilation, (b,c) gluon fusion.

2.4 Correlations in $\mathrm{b\bar{b}}$ production

Although in the current view there is no difference between the data and the predicted cross sections, the theoretical uncertainties remain large. Another means to study $\mathrm{b\bar{b}}$ production in more detail is to look at the correlations between the b and $\bar{\mathrm{b}}$ quarks.

At NLO, $\mathrm{b\bar{b}}$ production processes can be classified in dynamically distinct processes. The correlations between the quarks can be used to determine the relative normalisation of these processes.

Measurements of the correlations between $\mathrm{b\bar{b}}$ quarks [23, 49] and an exclusive measurement of the leading order production mechanism [6] have shown the importance of higher order diagrams at $\sqrt{s} = 630$ GeV. More recently, measurements of rapidity correlations [50], azimuthal correlations [30, 31, 36, 51] and double tag rates [32] at $\sqrt{s} = 1.8$ TeV have reinforced this awareness.

The distinction between the processes is formally ambiguous[5] but can be made more easily when considering event generation in Monte Carlo simulations. Because a comparison with Monte Carlo samples will be made in this thesis (see Chapter 7), the processes are discussed in this section in a way more appropriate to such simulations rather than a formal discussion in terms of QCD.

NLO processes in QCD $\mathrm{b\bar{b}}$ production

At LO ($\mathcal{O}(\alpha_s^2)$), contributing processes to the $\mathrm{b\bar{b}}$ cross section are the $2 \rightarrow 2$ "flavour creation" (FCR) process shown in Fig. 2.8:

$$\mathrm{q\bar{q}} \rightarrow \mathrm{Q\bar{Q}}, \qquad \mathrm{gg} \rightarrow \mathrm{Q\bar{Q}}, \tag{2.13}$$

where Q denotes a heavy quark, and the "flavour excitation" (FEX) process:

$$\mathrm{qQ} \rightarrow \mathrm{qQ}, \qquad \mathrm{q\bar{Q}} \rightarrow \mathrm{q\bar{Q}}, \qquad \mathrm{gQ} \rightarrow \mathrm{gQ}. \tag{2.14}$$

---

[5] In fact, when the distinction is based purely on the diagrams the separate processes are not each gauge invariant and the cross sections cannot be calculated. In the Monte Carlo simulation used in this thesis, a leading order calculation is used along with a shower model simulating the higher order contributions. The processes can then be separated based on the way they are generated.

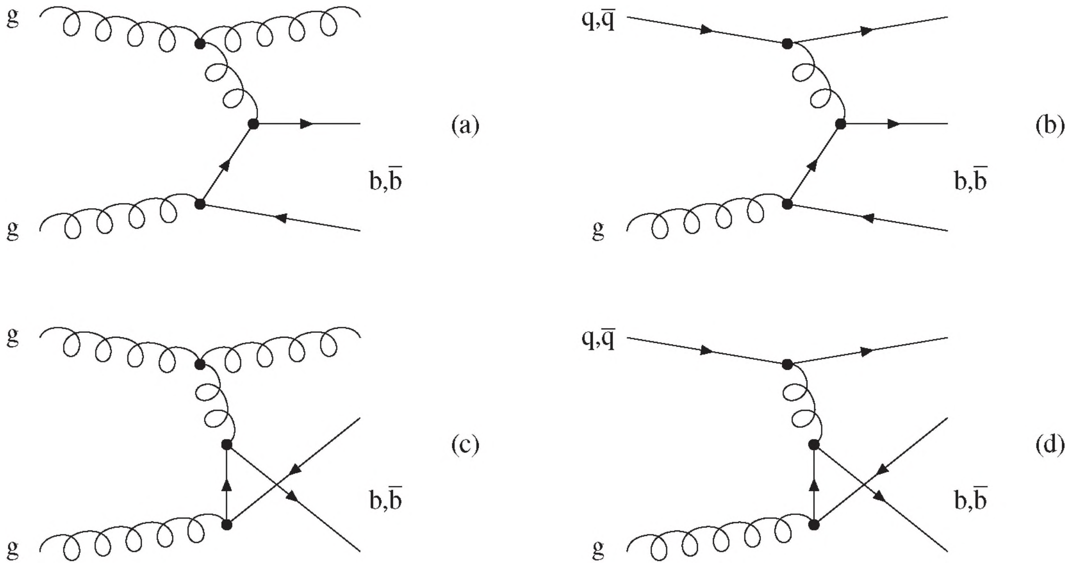

Figure 2.9: The *flavour excitation* process at next-to-leading-order.

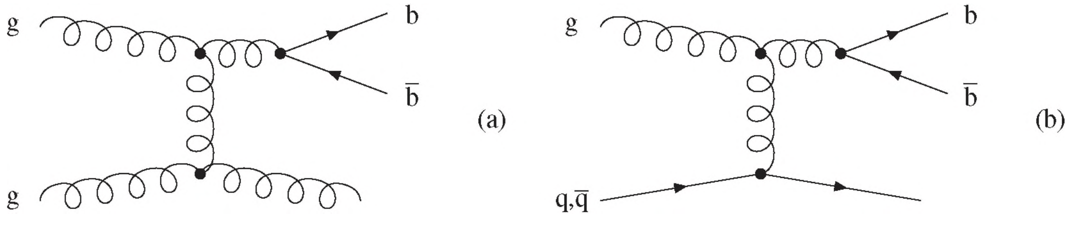

Figure 2.10: The next-to-leading-order *gluon splitting* process.

The charge conjugate processes are implicitly included. In LO calculations, the flavour excitation process only comes into effect if heavy quarks are present in the PDFs ("intrinsic production").

At NLO ($\mathcal{O}(\alpha_s^3)$), along with the $2 \rightarrow 2$ processes also $2 \rightarrow 3$ processes have to be considered

$$\mathrm{q\bar{q}} \rightarrow \mathrm{Q\overline{Q}g}, \qquad \mathrm{gg} \rightarrow \mathrm{Q\overline{Q}g}, \qquad \mathrm{gq} \rightarrow \mathrm{Q\overline{Q}q}, \qquad \mathrm{g\bar{q}} \rightarrow \mathrm{Q\overline{Q}\bar{q}}. \tag{2.15}$$

At NLO, flavour excitation is a true $2 \rightarrow 3$ process as shown in Fig. 2.9. The $2 \rightarrow 3$ processes also include final-state gluon radiation off one of the b quarks produced in the $2 \rightarrow 2$ leading order FCR process, and the "gluon splitting" (GSP) process shown in Fig. 2.10, where a final-state gluon splits into a $\mathrm{b\bar{b}}$ pair. In event simulations using LO matrix elements for the hard scatter interaction, the FEX and GSP processes can be produced through initial and final state gluon splitting simulated by a shower model.

Because of the large gg → gg cross section at the Tevatron ($\sigma(\mathrm{gg} \rightarrow \mathrm{gg})/\sigma(\mathrm{gg} \rightarrow \mathrm{Q\overline{Q}}) \approx 100$ at $\sqrt{s} = 1.8$ TeV) and the relatively large probability for a gluon to split into a heavy quark pair ($P(\mathrm{g} \rightarrow \mathrm{Q\overline{Q}} \approx 0.01)$) [52], the FEX and GSP processes are especially important in $\mathrm{b\bar{b}}$ production at the Tevatron. In Fig. 2.11, the PYTHIA [21] cross sections for flavour creation, flavour excitation and gluon splitting processes at $\sqrt{s} = 1.8$ TeV are compared to the total cross section.

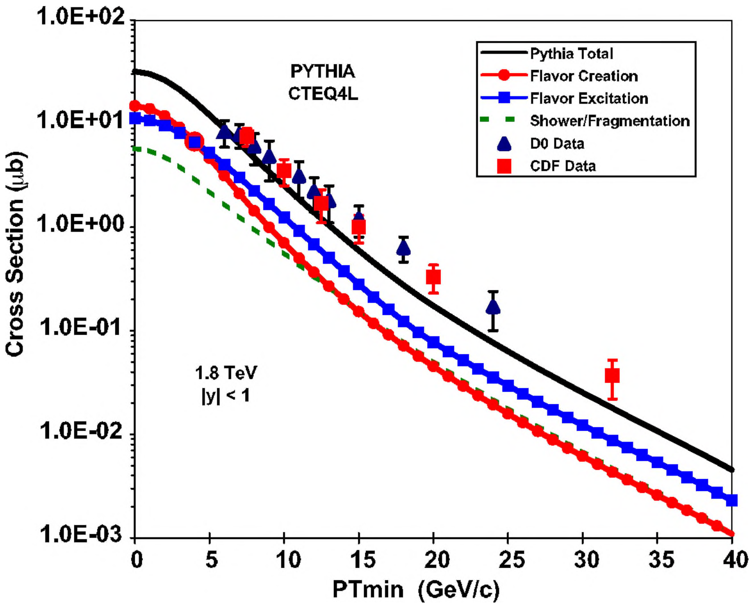

Figure 2.11: Integrated inclusive b quark production cross section ($p_T > p_T^{min}$, $|y| < 1$) in PYTHIA 6.158 and contributions from direct, gluon splitting and flavour excitation subprocesses [43].

The FCR, FEX and GSP processes lead to distinctly different kinematic distributions. It is therefore possible to measure their relative contributions to the total cross section in data. This measurement is the main goal in this thesis. In the next section, the three processes and their kinematic distributions will be discussed in more detail.

Formally, the flavour excitation and gluon splitting processes are NLO $2 \rightarrow 3$ processes. However, initial and final state showering in the $2 \rightarrow 2$ processes of Eq. 2.13 can lead to configurations identical to some of the $2 \rightarrow 3$ processes of Eq. 2.15. Special care must therefore be taken when combining NLO calculations with shower models to avoid overlap. This is discussed in Section 2.8.

Kinematic distributions

As can be deduced from the Feynman diagrams for the flavour creation, flavour excitation and gluon splitting processes (see Figs. 2.8, 2.9 and 2.10), the kinematic distributions of the $b\bar{b}$ pair will differ for the various processes. In particular, the azimuthal opening angle between the $b\bar{b}$ quark pair will depend strongly on the production process. In addition, the polar angle and p_T spectrum show a dependence on the production process.

- In FCR events, the b and $\bar{b}$ quark both participate in the hard scatter interaction and will emerge nearly back-to-back in azimuth. The quarks are well balanced in p_T.
- In GSP events, the $b\bar{b}$ pair will be very close in phase space, since both will tend to follow the direction of the gluon from the hard scatter interaction. The azimuthal distance $\Delta\phi$ peaks at low values.

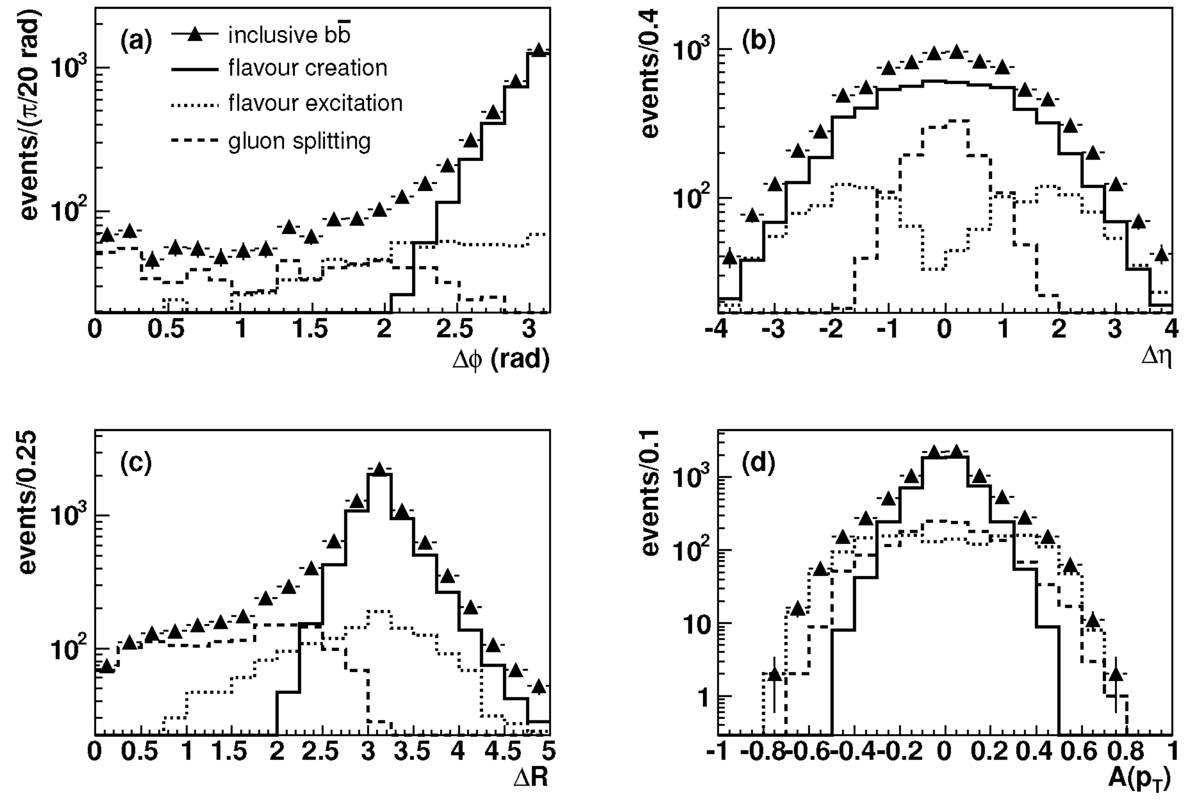

Figure 2.12: Correlations between two b quarks in PYTHIA 6.202 at $\sqrt{s} = 1.96$ TeV, for $p_T^{\mathrm{b},\bar{\mathrm{b}}} > 5$ GeV/c and $|\eta^{\mathrm{b},\bar{\mathrm{b}}}| < 4$.

- In FEX events, the b and $\bar{\mathrm{b}}$ quark are no longer strongly correlated in azimuth and the difference in azimuth shows a relatively uniform distribution. However, since one of the $\mathrm{b}\bar{\mathrm{b}}$ quark pair will tend to follow the direction of the initial state gluon, it will typically emerge relatively close to the beam at high $|\eta|$. The quark participating in the hard scatter will be more central. The p_T of the centrally produced quark is balanced by a recoil particle of arbitrary flavour rather than by the other heavy quark.

Angular correlations between the two quarks and the p_T asymmetry defined as

$$\mathcal{A}(p_T) = \frac{p_T^{\mathrm{b}} - p_T^{\bar{\mathrm{b}}}}{p_T^{\mathrm{b}} + p_T^{\bar{\mathrm{b}}}}$$

in simulated events are shown in Fig. 2.12.

The quark distributions will be distorted somewhat by the hadronisation process and by the presence of additional final state particles, specifically hard gluons radiating off the heavy quarks. These effects can largely be reduced by looking at jets carrying heavy flavour. By measuring the correlations between b flavoured jets in collision data, the relative contributions of FCR, GSP and FEX processes can be determined.

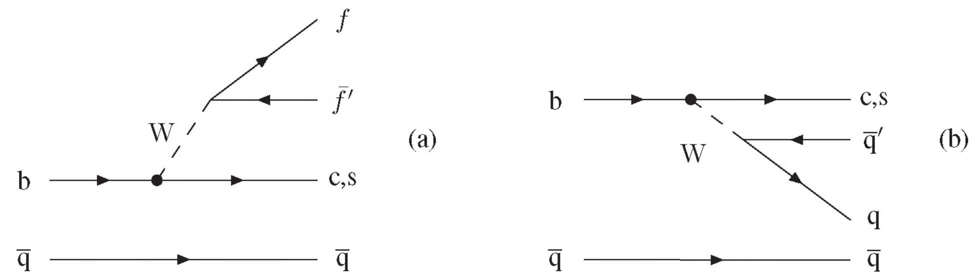

Figure 2.13: Spectator diagram for the decay of a B meson.

2.5 Decay of b flavoured hadrons

B flavoured hadrons decay to lighter flavours through the transition of the bottom quark to a lighter quark while emitting a W boson. The SU(2) quark eigenstates of the weak interaction are not identical to the mass eigenstates, allowing mixing between the three families; the dominant decay channel is b → Wc. (The top quark being too heavy.)

The simplest description of the decay of B hadrons is the spectator model. In this model, the b quark is treated as a free quark while the other quark has no influence on its decay. A diagram for spectator model decay of a B meson is shown in Fig. 2.13.

The W boson subsequently decays into either a lepton-neutrino pair or a $q\bar{q}'$ pair. B decays with the W decaying to a lepton-neutrino pair are referred to as semileptonic decays.

The weak force gets its name not from the magnitude of the coupling constant, but from the large mass of the W and Z^0 bosons. The mass enters through the propagator, which is proportional to $1/M^2$ as $q^2 << M^2$.

Without going into more detail (and ignoring other effects), it is clear that the time scales of the weak decay must be relatively long; typical time scales associated with the weak force are of the order of 10^{-12} s, compared to 10^{-23} s for the strong force. The experimentally measured average lifetime for all B hadrons is $\tau = 1.564 \pm 0.014$ ps [1]. The charged particle multiplicity for all B hadrons is 5.5 ± 0.5 [53], including secondary decay products from K^0_S and Λ decays. Excluding these secondary decays, the mean charged particle multiplicity of weakly decaying B hadrons is 4.97 ± 0.07 [54].

Other possibilities for the decay of the B hadron include W mediated flavour annihilation, W exchange and so-called penguin decays. Interference effects and soft gluon effects also affect the spectator model result. These non-spectator effects effectively decrease the lifetime and semileptonic branching ratios of the B hadrons. The effect is observed to be small [1].

Experimental signature of B decays

As B mesons and baryons decay, their large mass ($m_{B^\pm} = 5279.0 \pm 0.5$ MeV$/c^2$ [1]) imparts large momentum to their decay products in the plane perpendicular to the momentum of the original hadron. This relative transverse momentum (P_T^{Rel}), especially that of muons produced by the decay of the W, can be used to identify heavy flavour events in collision experiments. The hard fragmentation of the B hadron ensures that the jet containing the heavy flavour will be closely aligned with the hadron, so the large P_T^{Rel} imparted to the muon or electron can be measured with respect to the jet axis. By contrast, muons from the decay of charmed mesons (which have lower mass) or from decays-in-flight of charged pions and kaons inside jets will have lower average P_T^{Rel}. The higher P_T^{Rel} of muons from b quark decays will be exploited in this thesis to determine the number of b jets in a sample.

The long lifetime of B hadrons means that before decaying, the hadrons will travel on average $c\tau\beta\gamma \approx 450\beta\gamma\ \mu\mathrm{m}$. With the relativistic boost — for a 20 GeV B meson, $\beta\gamma$ is about 4 — this means that the B decay vertex is often displaced from the hard scatter or primary interaction vertex by several mm. The displaced decay vertex provides another strong experimental signature of b production.

Combined with the large opening angle of the decay products due to the large B mass, the long lifetime of B hadrons also means that trajectories of the decay products do not point back to the primary interaction vertex, but pass it at some distance. This distance, known as the impact parameter or distance of closest approach (dca) of a track, is used in this thesis to increase the fraction of b jets in the sample.

2.6 Backgrounds to $\mathrm{b\bar{b}}$ production

The cross section for $\mathrm{b\bar{b}}$ production at the Tevatron is of the order of 0.1 mb, less than 1% of the total hadronic cross section ($\sigma_{tot} \approx 75$ mb). The dominant background for a lifetime b tag comes from light quark jets faking a b jet. Decay vertices of long-lived neutral particles such as $\mathrm{K^0_S}$ and Λ or the large impact parameters of their decay tracks can lead to a false positive tag from either a secondary vertex tag or an impact parameter tag.

Fortunately, the mean life of these particles is much longer than that of B mesons: $c\tau \approx 2.68$ cm for $\mathrm{K^0_S}$ and $c\tau \approx 7.89$ cm for Λ [1]. However, they are produced about a few thousand times more frequently. Rejecting vertices with decay lengths significantly longer than the expected B meson decay length or tracks with very large impact parameters will help reduce this background.

More problematic is the background of (charged) charmed mesons. The mean life time of the $\mathrm{D^\pm}$ is $\tau = 1.040 \pm 0.007$ ps, $c\tau = 311.8\ \mu\mathrm{m}$ [1]. Although the mass is considerably less than that of B mesons ($m_{\mathrm{D^\pm}} = 1869.4 \pm 0.5\ \mathrm{MeV}/c^2$), the charged particle multiplicity of $\mathrm{D^\pm}$ meson decays is only 2.38 ± 0.06 [55], so the relative p_T of each individual track can still be large enough to get impact parameters in the same range as that for B meson decays. The $\mathrm{D^0}$ and $\mathrm{D^\pm}_s$ mesons have shorter lifetimes ($\tau = 0.4103 \pm 0.0015$ and $\tau = 0.490 \pm 0.009$ ps, respectively [1]) and slightly larger decay multiplicities (2.56 ± 0.05 and 2.7 ± 0.3 [55]) than $\mathrm{D^\pm}$ mesons and their decay tracks will have correspondingly smaller impact parameters.

The background for lepton based tags mainly comes from charmed meson decays and from the decay-in-flight of charged pions and kaons. Because of the lower mass of these particles, the P_T^{Rel} distribution will be much softer than for B decays.

2.7 Event generation and simulation

All Monte Carlo samples used in this thesis were generated using PYTHIA 6.202. The cross sections for the three classes of $\mathrm{b\bar{b}}$ production and the total cross section are shown in Fig. 2.11 as derived from PYTHIA 6.158.

In QCD production, only $2 \to 2$ processes are explicitly included. The CTEQ4L PDFs that were used include both charm and bottom quarks. However, through backward evolution of the initial state shower, the incoming hadrons are probed at a scale Q_0 much lower than the scale of the hard interaction, and heavy quarks are kinematically excluded. The higher order FEX and GSP contributions are generated through initial and final state shower simulations. To generate an inclusive $b\overline{b}$ sample, events containing b quarks are selected from a generic QCD sample. GSP events are selected by requiring the presence of a $b\overline{b}$ quark pair, pointing back to a common gluon parent. No b quarks should participate in the hard scatter interaction. For FEX, exactly one of the pair should participate in the hard scatter interaction; and both in the case of FCR.

The Peterson fragmentation model was used for b and c quarks, with $\epsilon_b = 0.00391$ and $\epsilon_c = 0.06$. The Lund symmetric fragmentation function was used for lighter quarks.

The decay of B hadrons is handled by the QQ package [56]. The decay tables contain the masses, lifetimes and decay modes of approximately 400 particles and are maintained to be as close to current measurements as possible.

2.8 Monte Carlo at Next-to-Leading Order

The realisation that certain $2 \to 3$ processes can be generated by showering off $2 \to 2$ hard processes, and that this will lead to overlap when NLO calculations are used, has led to an effort to understand the combination of NLO calculations with Monte Carlo shower models [44, 57].

As an example, the flavour excitation process (see Eq. 2.14) is treated as a leading order $\mathcal{O}(\alpha_s^2)$ process in standard Monte Carlos, with the heavy flavour either directly present in the parton distribution functions of the incoming hadrons or resulting from initial state showering. The process $gg \to Q\overline{Q}g$, for instance, has a contribution from initial state gluon splitting followed by the LO flavour creation process $gQ \to gQ$. However, the same configurations can arise in NLO computations. (This also makes the distinction between FCR and FEX ambiguous at NLO.) Since initial state gluon splitting forms part of the evolution of the PDFs of the incoming hadrons implemented through parton showers, there is a danger of double counting these events when NLO computations are combined with an initial state shower.

The MC@NLO approach [57] is a method for matching NLO calculations with parton shower Monte Carlo simulations, based on the subtraction method for NLO calculations. In MC@NLO, the subtraction is modified to take into account the terms that are generated by the parton shower. This results in a set of weighted LO and NLO parton configurations that can be fed into a parton showering generator without fear of double counting. The exact implementation depends on the shower model used, but is independent of the hard scatter process considered.

Fixed-order calculations fail or are less accurate when soft or collinear emissions are included. On the other hand, parton shower Monte Carlo simulations are less accurate in the hard scatter regime of high momentum transfer. MC@NLO combines the strong features of both: distributions of observables in simulated events tend to approach the shower model result in low p_T or collinear regions of phase space, but reproduce the NLO perturbative result in the high p_T region. The angular correlations between b quarks in MC@NLO are shown in Fig. 2.14.

The authors of [44] have used the MC@NLO method to simulate correlations between $b\overline{b}$ quark

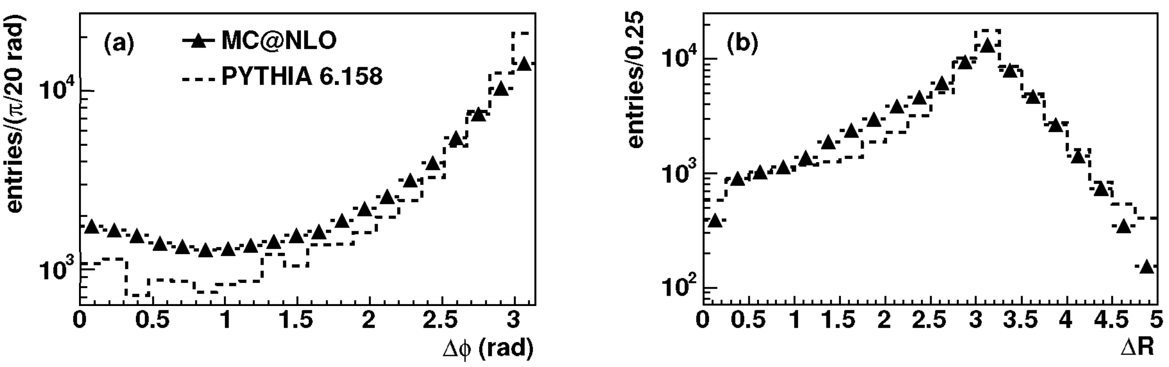

Figure 2.14: Angular correlations between b quarks in MC@NLO, for quarks with $p_T > 5$ GeV$/c$ and $|\eta| < 4$, compared to PYTHIA.

pairs in p$\bar{\text{p}}$ collisions at the Tevatron. As they remark in their conclusions, "An obvious next step would be to compare with Tevatron data on final state properties in top and bottom production." A measurement of the angular correlation between two b jets is presented in this thesis.

Chapter 3

Tevatron and the DØ detector

This chapter describes the experimental setup used for the measurement detailed in this thesis. The Tevatron accelerator is discussed in the first section. The remainder of this chapter describes the DØ detector, one of two collider experiments at Fermilab.

3.1 The Tevatron

The Tevatron is located on the grounds of the Fermi National Accelerator Laboratory (or Fermilab) in Batavia, Illinois, about 40 miles west of Chicago. The main accelerator is housed in a circular tunnel with a radius of about 1 km.

The Tevatron first came into operation in 1983 as the world's first superconducting synchrotron, colliding 800 GeV protons onto fixed targets. Since then, the Tevatron has been upgraded to collide beams of protons and antiprotons. Between 1992 and 1996, it delivered an integrated luminosity of $\int \mathcal{L}\mathrm{d}t = 120\ \mathrm{pb}^{-1}$ at $\sqrt{s} = 1.8$ TeV to the two collider experiments, the Collider Detector at Fermilab (CDF) and DØ. The highlight of this period of running, known as Run I, was the discovery of the top quark by the CDF and DØ collaborations in 1995 [58, 59].

In Run I, acceleration from 8 GeV to $120 - 150$ GeV took place in the "Main Ring", which was housed in the same tunnel as the Tevatron. Because the Main Ring ran through the DØ detector, this led to a long unavoidable dead time. For Run II, started in March 2001, the Tevatron was upgraded to deliver luminosities up to $\mathcal{L} = 2 \times 10^{32}\ \mathrm{cm}^{-2}\mathrm{s}^{-1}$ at a centre of mass energy of 1.96 TeV. The Main Ring has been replaced by the "Main Injector" housed in a separate tunnel and completed in 1999. It allows simultaneous operation of the Tevatron and other (fixed target) experiments such as NuMI [60]. The new tunnel also houses an Antiproton Recycler that will allow further increase of the total luminosity delivered by the accelerator.

The Fermilab accelerator system now consists of five stages of accelerators (see Fig. 3.1): a Cockcroft-Walton pre-accelerator, a 500-foot linear accelerator (Linac), the "Booster" synchrotron, the Main Injector and the Tevatron (originally called the Energy Doubler). In addition, the Antiproton Source uses two more storage rings, the Debuncher and the Accumulator, to select and accelerate antiprotons from the Target Station. The stages of acceleration are briefly detailed in the following sections.

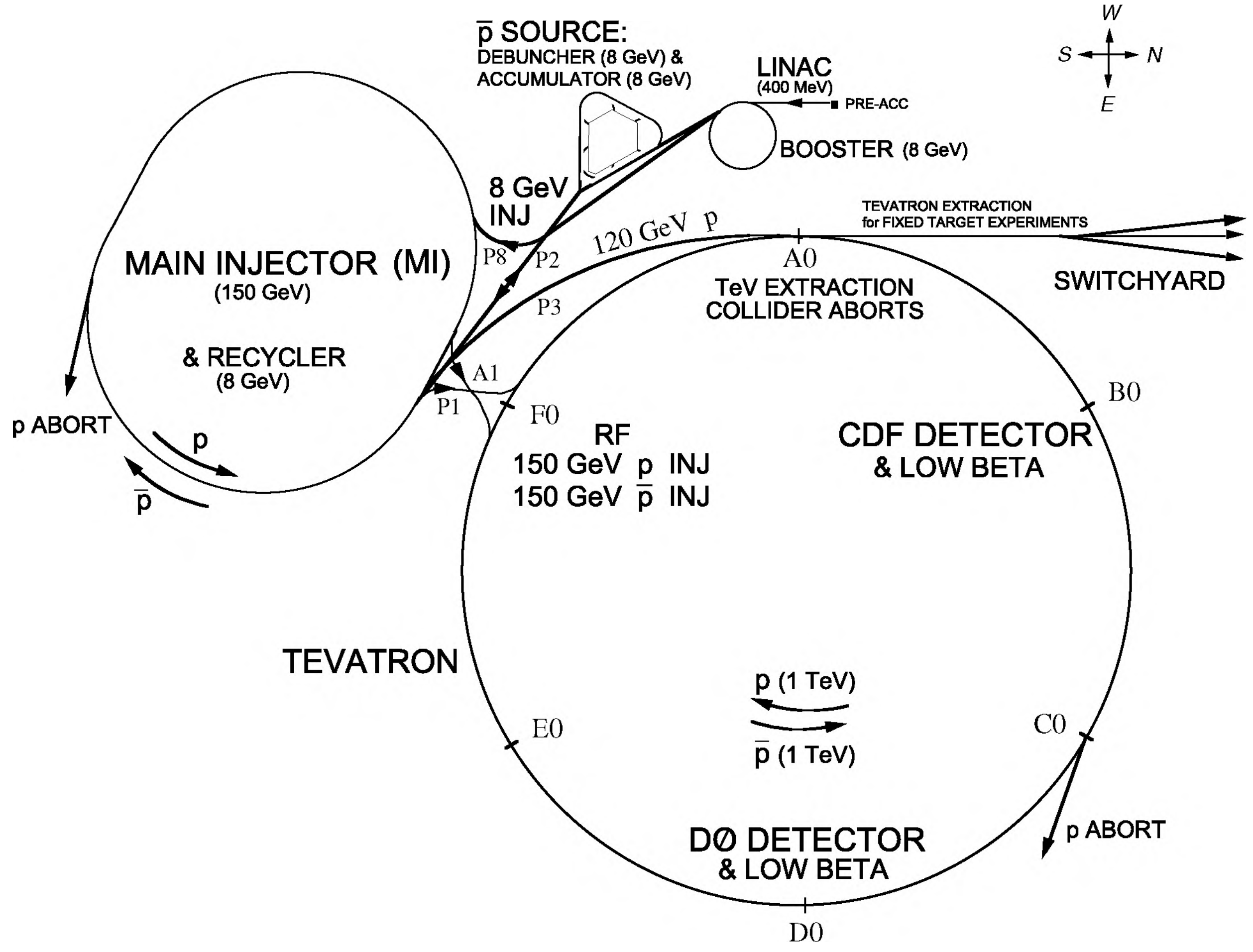

Figure 3.1: The Fermilab Accelerator Complex

3.1.1 Proton production and initial acceleration

Production of colliding beams starts with negative hydrogen ions (H^-) produced in a magnetron surface plasma source. The ions are produced from the interactions of electrons in the plasma with cesium atoms coating the cathode of the plasma source. The H^- ions escape the plasma chamber through an aperture and are electrostatically accelerated to 18 keV. Their energy is electrostatically increased to 750 keV (limited by the maximum potential difference) in the Cockcroft-Walton accelerator. In the Linac, they are further accelerated to 400 MeV. At 400 MeV, the hydrogen ions are relativistic enough so that they can be further accelerated in a synchrotron. The Booster, with a circumference of 475 m, strips the hydrogen ions of their electrons by passing them through a carbon foil and accelerates the protons to an energy of 8 GeV. Because the 20 ms Linac pulse is longer than the 2.2 ms Booster circumference, the pulse must be injected over several turns in the Booster. The negative charge of the hydrogen ions allows them to be merged with the proton beam already in the Booster. The protons are then injected into the Main Injector, where they are accelerated to energies sufficient for antiproton production and to feed the fixed target experiments (120 GeV) and for injection into the Tevatron at 150 GeV.

3.1.2 Antiproton production

To produce antiprotons, a single batch of up to 5×10^{12} protons is accelerated to 120 GeV in the Main Injector. The beam is extracted from the Main Injector and focused onto a nickel production target. The resulting cone of secondary particles is focused and rendered parallel by means of a lithium lens called the "Collection Lens". A pulsed dipole magnet bends all negatively charged particles of approximately 8 GeV kinetic energy into a transfer line while most of the other particles are absorbed in a beam dump.

The selected particles are transfered to the Debuncher. The Debuncher can make use of the time between Main Injector cycles — about 1.5 s — to reduce the transverse spread of the beam through stochastic cooling [61]. This greatly improves the efficiency of the following transfer to the Accumulator. A momentum cooling system further reduces the momentum spread of the beam.

Just before the next pulse arrives from the target, the antiprotons are extracted from the Debuncher and transfered to the Accumulator. Successive pulses of antiprotons from the Debuncher are stacked into the Accumulator over several hours or days. Cooling systems keep the antiprotons in the core of the stack, at the desired momentum and minimal transverse beam size.

When enough antiprotons have been accumulated, groups of four bunches of antiprotons are extracted from the Accumulator and transported to the Main Injector until the desired number of antiproton bunches, nominally 36, are in the Tevatron.

3.1.3 Final acceleration and collisions

In the Main Injector, proton and antiproton beams are accelerated to 150 GeV before they are injected into the Tevatron. In the Tevatron they are accelerated to their final energy of 980 GeV.

The beams in the Tevatron are each separated in 36 bunches of protons or antiprotons, each with a length of about 30 cm. The bunch spacing has been brought down to 396 ns, from 3.6 μs in Run I. The transverse width of the beam interaction region (the "beam spot") is about $\sigma_{xy} = 30\ \mu\mathrm{m}$ at design luminosity. The longitudinal size of the interaction region, dominated by the bunch length, is about $\sigma_z = 25\ \mathrm{cm}$. Collisions happen every 396 ns with a design instantaneous luminosity of $\mathcal{L} = 2 \times 10^{32}\ \mathrm{cm}^{-2}\mathrm{s}^{-1}$. The integrated luminosity goal for Run II is to deliver $4 - 8$ fb^{-1} by 2009.

3.1.4 The Antiproton Recycler

The Antiproton Recycler is a fixed-energy storage ring placed in the Main Injector tunnel directly above the Main Injector beam line. Using permanent magnets removes the need for expensive conventional iron/copper magnets along with their power supplies, cooling water system, and electrical safety systems. Because there are few power sensitive components, there are virtually no mechanisms for inadvertent beam loss.

The Recycler will function as a post-Accumulator storage ring. As the stack size in the accumulator ring increases, there comes a point when the stacking rate starts to decrease. By periodically emptying the contents of the Accumulator into the Recycler, the Accumulator is always operating in its optimum antiproton intensity regime.

3.2 The DØ detector

3.2.1 The DØ detector in Run I

The original DØ detector was designed for efficient lepton and jet identification, coupled to excellent hermeticity for missing energy measurements. This was achieved using finely segmented, hermetic electromagnetic and hadronic calorimetry, muon detection using thick magnetised iron, and inner tracking without a magnetic field. Of the original detector, only the calorimeter and part of the muon system have been kept for Run II. The central detector systems, which consisted of a vertex drift chamber, a transition radiation detector and forward and central drift chambers, have been completely replaced by new detectors. A more complete description of the DØ detector for Run I can be found in [62].

3.2.2 The DØ Run II detector

Figure 3.2 shows a cutaway view of the DØ Run II detector. It is 13 m high, 13 m wide and 20 m along the beam direction.

Physics goals for Run II, including top measurements and Higgs searches, have led to a new design of the inner volume of the DØ detector. High precision tracking and vertex information greatly improve the capabilities of the detector to detect b flavoured events. A 2 Tesla solenoid in the central volume allows precise momentum reconstruction for charged particles. The muon spectrometer, which had to be partially replaced because of the expected radiation damage at the higher Run II luminosities, has also been upgraded with scintillation counters. In addition, the higher luminosity and bunch crossing rate of the Tevatron in Run II have necessitated upgrades of the trigger and data acquisition systems.

From the inside out, the DØ Run II detector consists of the following subsystems:

- The Silicon Microstrip Tracker (SMT);
- The Central Fibre Tracker (CFT);
- The 2 Tesla superconducting solenoid;
- The forward and central preshower detectors;
- The uranium-liquid argon calorimeter;
- The muon spectrometer.

In addition to these systems, a set of forward proton detectors up- and downstream of the detector provide measurement of scattered protons at very small angles. A luminosity monitor provides measurements of the instantaneous and integrated luminosity.

Each of the subsystems of the new detector will be described in more detail in the following sections. The data acquisition and online event selection systems are treated in Chapter 4.

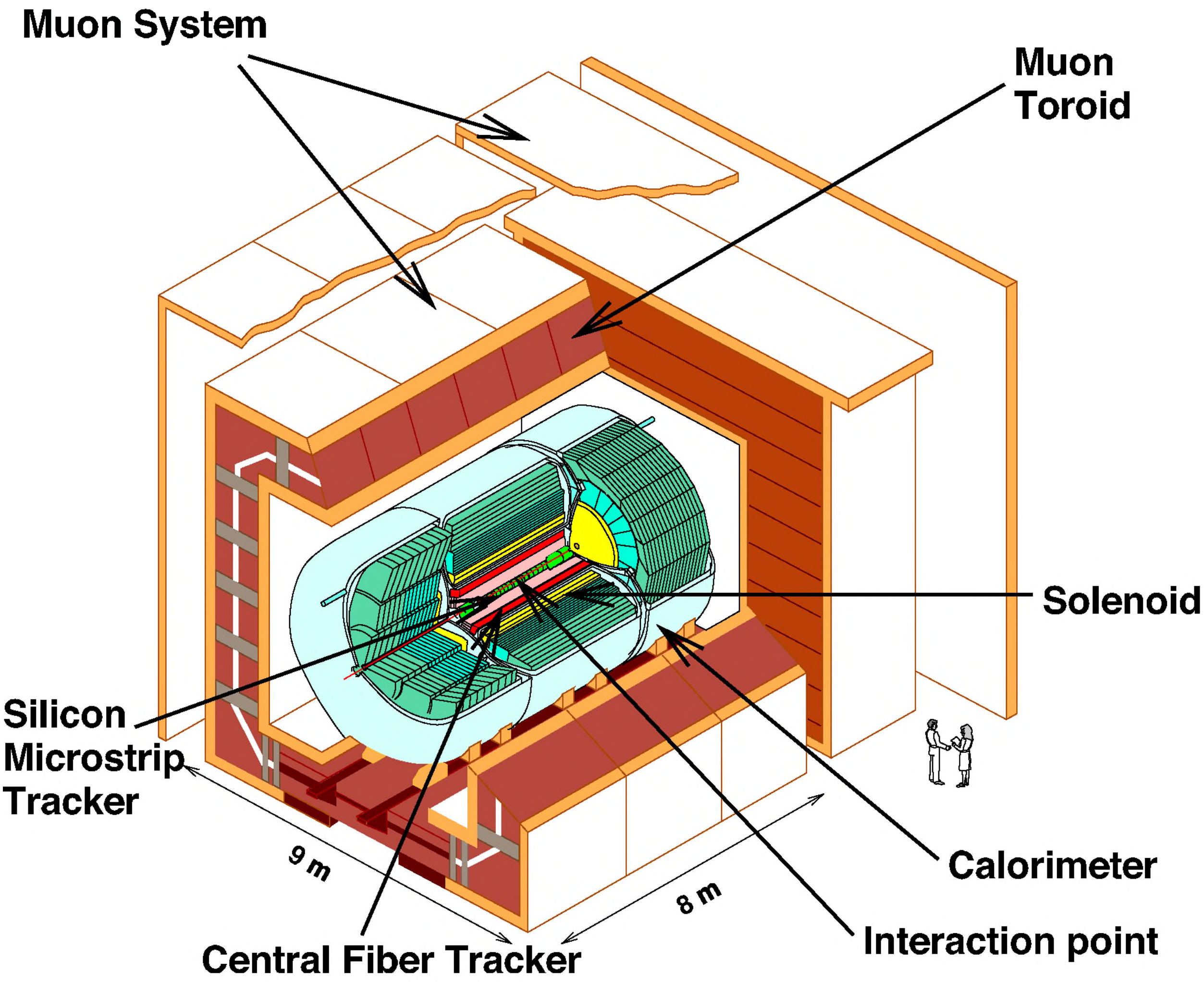

Figure 3.2: The DØ Detector for Run II.

3.3 Silicon Microstrip Tracker

The inner part of the DØ detector is shown in Fig. 3.3. The tracking volume now contains the Silicon Microstrip Tracker (SMT), the Central Fibre Tracker (CFT) and a 2 Tesla superconducting solenoid. Because the detection of b flavoured particles using their long lifetime depends crucially on the precision of the SMT, special attention is given to this detector.

The SMT was designed to provide precision track measurement in the inner part of the upgraded DØ detector. It consists of 6 barrels and 16 disks of silicon strip detectors with a total surface area of 3 m^2 and a total of about 800,000 readout channels. The SMT is shown in Fig. 3.4.

Because of the long interaction region of the Tevatron ($\sigma_z \approx 25$ cm) an extended design is needed to ensure perpendicular incidence of charged particles to the detector components over the entire region. The desire to cover a large rapidity range and to maximise acceptance for high p_T tracks have lead to a hybrid barrel-disk design with six barrels, twelve small area F-disks and four large area H-disks (see Fig. 3.4). The six barrels cover the region from -51 cm $< z <$ 51 cm.

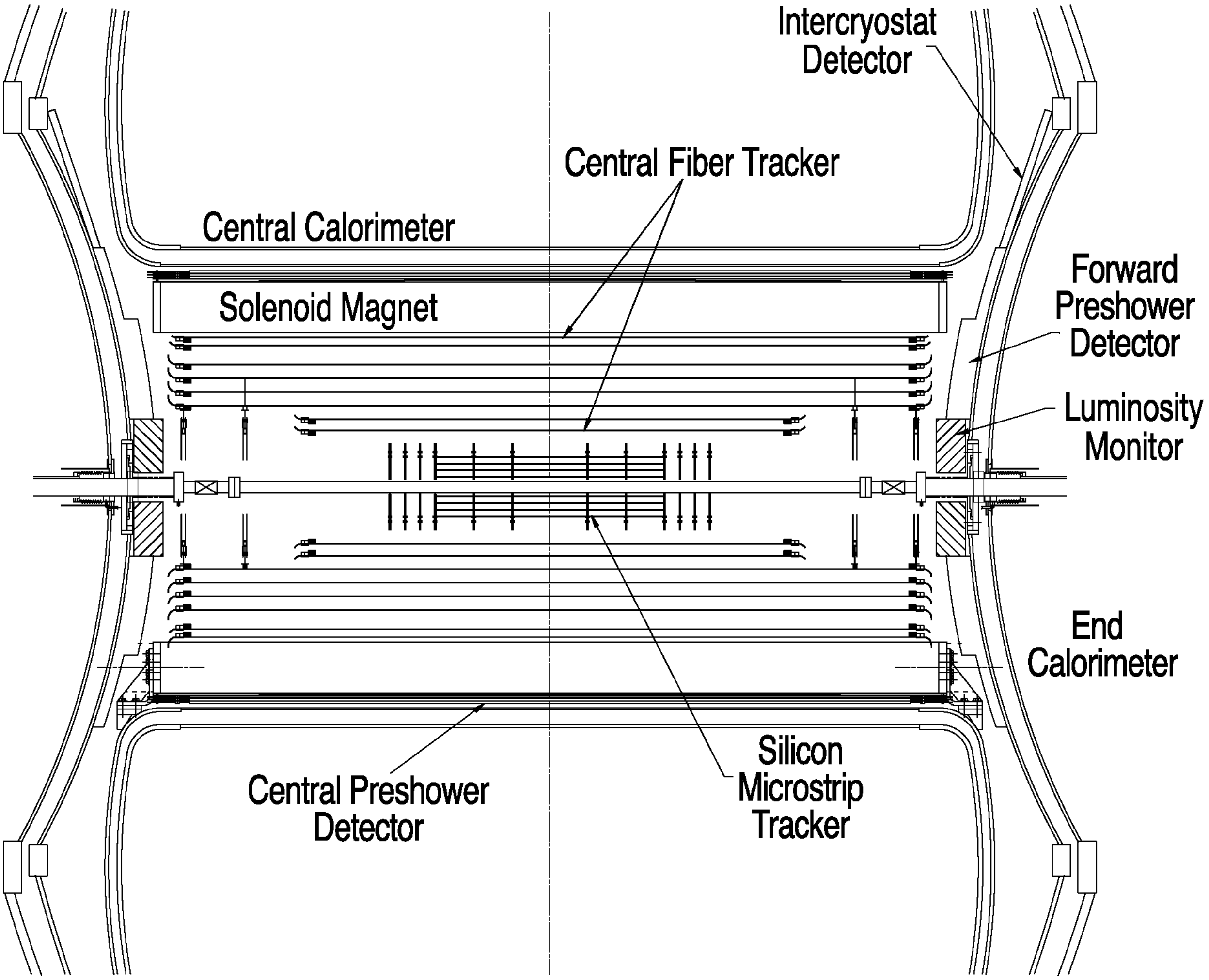

Figure 3.3: The central tracking systems of the DØ detector in Run II.

An F-disk is joined to the large $|z|$ end of each barrel. Three more F-disks at each end of the barrel region complete the central part of the detector. The four H-disks at $z = \pm 1004$ mm and $z = \pm 1210$ mm provide long-arm measurements to maintain good p_T resolution for tracks at high η. The H-disks were not used by the track reconstruction algorithms used in this thesis, but they will still be discussed in order to give a full description of the SMT.

The barrels consist of four superlayers of silicon “ladders”. Each superlayer has two sublayers of partially overlapping ladders, providing hermetic ϕ coverage (see Fig. 3.5). Each ladder is 12 cm long and made of two 6 cm long, 300 μm thick silicon sensors with readout strips on one or both sides. The single sided sensors are only used in the 1^{st} and 3^{rd} superlayers of the outermost barrel on each side of the detector. The readout strips on the two sides of each double sided sensor are at a relative angle of 90° for the 1^{st} and 3^{rd} superlayers of the central barrels and 2° for all other layers. The 90° ladders use a single, 12 cm long sensor. The sensor types for each layer are given in Table 3.1.

The disks are mounted perpendicular to the beam. The F-disks are made of twelve double sided

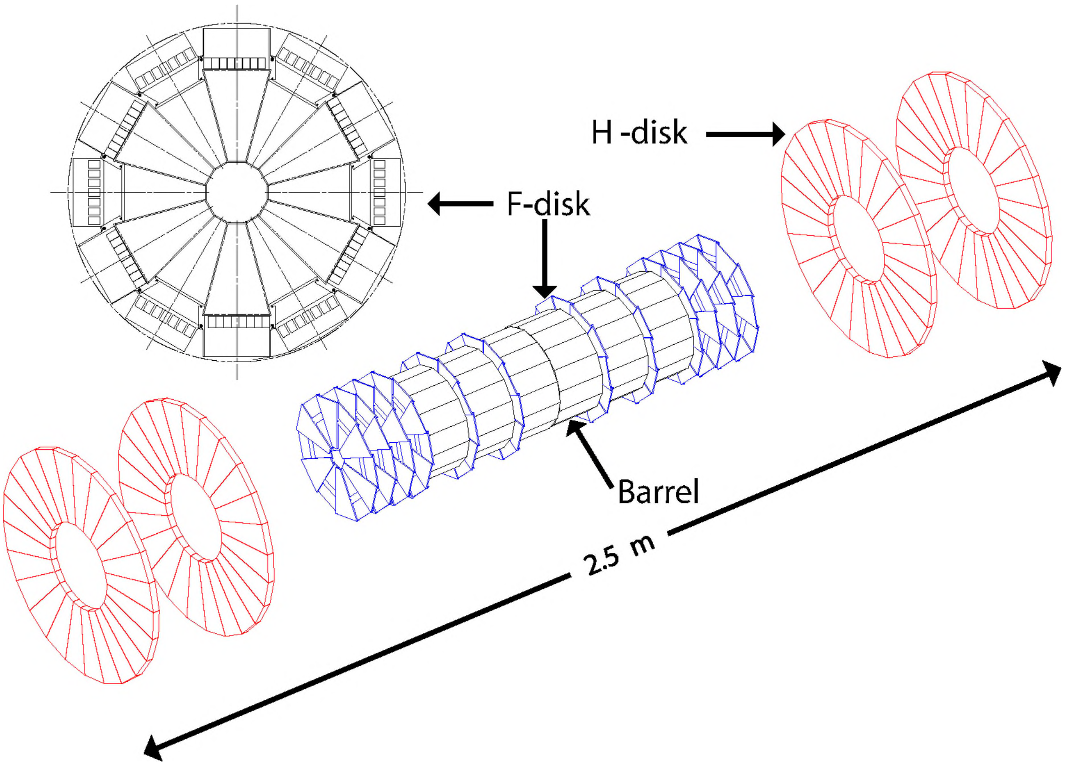

Figure 3.4: The DØ Silicon Microstrip Tracker.

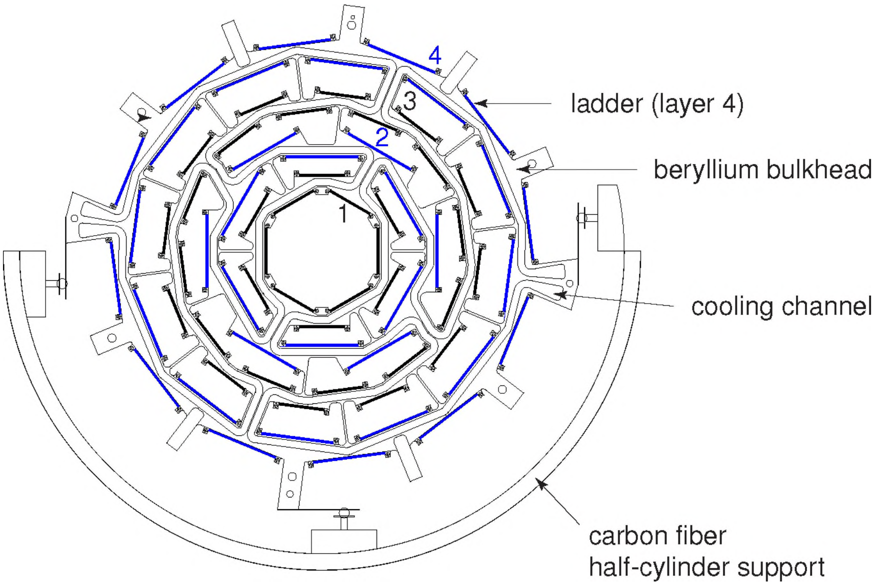

Figure 3.5: Side view of an SMT barrel showing the four superlayers and the overlapping ladders in each superlayer.

module	layer	stereo angle	readout pitch (μm) p/n	sensor length (cm)	inner radius (cm)	outer radius (cm)
F-disks	–	30°	50/62.5	7.93	2.57	9.96
H-disks	–	15°	80	14.6	9.5	26
central barrels (4)	1, 3	90°	50/153.5	12.0	2.715	7.582
	2, 4	2°	50/62.5	6.0	4.55	10.51
outer barrels (2)	1, 3	–	50	6.0	2.715	7.582
	2, 4	2°	50/62.5	6.0	4.55	10.51

Table 3.1: Readout parameters of the Silicon Microstrip Tracker.

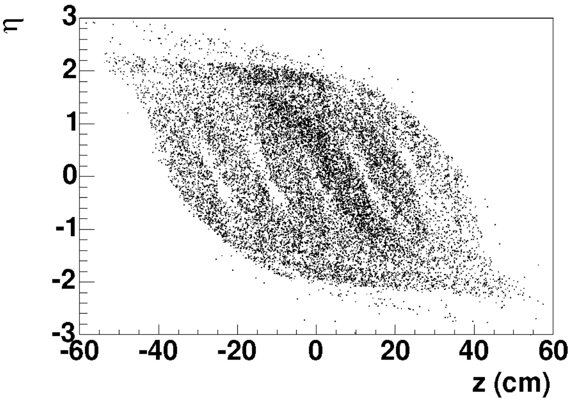

Figure 3.6: Acceptance of the SMT. Shown is the (z, η) distribution of all tracks with hits in all four barrel superlayers.

wedges which slightly overlap at the edges. The readout strips of the F-disk sensors make an angle of $\pm 15°$ with the symmetry axis of the wedge, providing a $30°$ stereo angle. The H-disks are each made of 24 single sided wedges, which are glued back-to-back in pairs. The readout strips of the H-disk sensors are at an angle of $7.5°$ with respect to the symmetry axis, providing an effective stereo angle of $15°$ for a pair of wedges glued back-to-back. The twelve pairs of wedges slightly overlap. The sensor types are summarised in Table 3.1.

The acceptance of the SMT barrels for tracks originating at the geometric centre of the detector is $|\eta| < 2$. Because of the long luminous region of the accelerator and the relatively short length of the detector, the actual acceptance depends on both the polar angle η and the point of origin z_0 of the track. The true coverage is determined by plotting the (z, η) distribution of all tracks with hits in all barrel superlayers and is shown in Fig. 3.6. The gaps between the barrels — an effect of the barrel-disk design — can be seen as white bands in the distribution.

Naively, the point resolution of a silicon strip detector is the pitch divided by $\sqrt{12}$. Because pulse height information is available, the resolution is improved by charge sharing among two or more readout strips and is proportional to the signal to noise ratio S/N. From beam tests, a 9 μm axial resolution is expected. The resolution in z depends on the detector type, and it is expected to

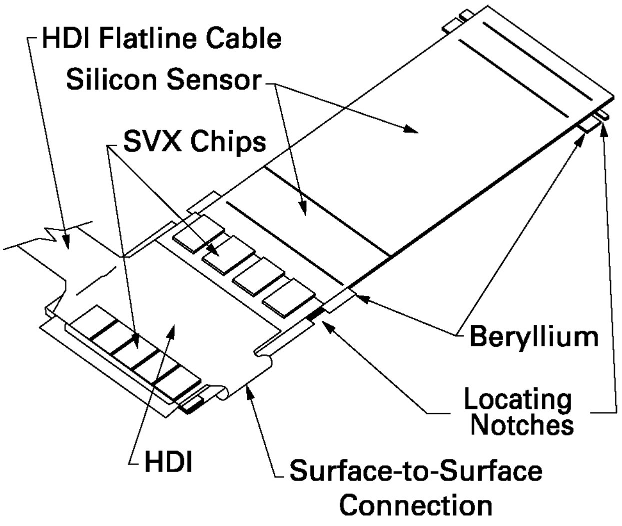

Figure 3.7: A double sided 2° silicon ladder.

be 35 μm for 90° stereo detectors and 450 μm for 2° stereo detectors. The expected p_T resolution $\sigma p_T/p_T$ within $|\eta| < 2$ ranges from 2-5% (5-10%, 20-30%) for 1 GeV (10 GeV, 100 GeV) tracks, and up to 20% (30%, 100%) at $\eta = 3$ [63].

3.3.1 Construction

The ladders are constructed by mounting two single or double sided silicon sensors (or one sensor in the case of the 90° ladders) on a rohacel-carbon fibre rail, creating a 12.4 cm long detector element (see Fig. 3.7). The readout electronics are mounted on kapton flexible circuits — High Density Interconnects or HDIs — which are laminated onto 300 μm thick beryllium substrates which provide support and a thermal path to the cooling channels. The sensors are glued to the HDIs and connected to the readout chips by wire bonding to complete a ladder. The double sided ladders are each read out through a single HDI, folded over one edge of the sensor to serve both surfaces. The F-disk wedges are read out by two HDIs, one on each side of the sensor.

The data from the axial strips will be used in the Level 2 Silicon Track Trigger [64]. Since not all alignment corrections can be applied in this trigger, the detector must be very accurately positioned. In particular, the relative alignment of the ladders within each barrel detector and the alignment of the barrel axis with the beam line need to be as good as 10 μm in the transverse plane. The beryllium substrates to which the HDIs are laminated contain precisely machined notches for positioning the ladders or wedges. Typically the position accuracy of the sensor with respect to these notches is in the range $2 - 5$ μm for ladders and $5 - 10$ μm for wedges. The ladders are positioned between two beryllium bulkheads (one of which is cooled) with a typical accuracy of about 20 μm [65, 66]. The wedges in the central and forward disks are mounted on alternate sides of a beryllium cooling ring. Positioning accuracy of the wedges with respect to the cooling ring is in the range $10 - 20$ μm for both x and y coordinates.

The detector is split longitudinally in two halves. Each half is installed in a carbon fibre and epoxy half cylinder, which aids in maintaining precise alignment, locates the SMT relative to the

CFT and supports the cabling and cooling channels. The relative alignment of the SMT and the CFT is $-28 \pm 37\ \mu\mathrm{m}$, determined by matching tracks found separately in each detector [65].

3.3.2 Production and testing

The silicon sensors and the HDIs were made at external companies, but final assembly of the ladders and wedges was done at Fermilab. Several electrical tests were performed at each stage of detector assembly [63, 67, 68]. Functionality problems at each step were analysed; most were due to bad chips, which were replaced at Fermilab. About 10% of all chips had to be replaced. Shorted AC coupling capacitors on the sensors necessitated the removal of 0.8% of all wirebonds connecting the sensor strips to the readout chips.

The final tests for all functioning detectors included a 72 hour burn-in test with full detector bias voltage, cooling and dry air, and a laser scan. During the burn-in test the leakage current, pedestals, gain and number of noisy channels were monitored for each detector. Noisy channels were identified in the burn-in test if they had pedestal widths of more than 6 ADC counts, compared to a typical uncorrelated noise of two ADC counts and an average pulse height for minimum ionising particles of 26 ADC counts. During the laser scan the silicon sensors were scanned with a 1064 nm infrared laser beam to identify dead channels and determine the depletion voltage. Channels were identified as dead if their response to the laser pulse was less than 1/3 of the pulse height expected for fully functional chips. Only detectors which satisfy mechanical specifications and have less than 5.2% dead or noisy channels are accepted for barrel and disk assembly. Averaged over all detectors, the SMT has 2% dead and 0.5% noisy channels.

Each ladder and each wedge was tested again as it was installed in a barrel or disk. After attaching the cables, readout was verified. Upon completion of the detector, 99.5% of all ladders and wedges were functional.

At the start of Run II, about 15% of the detectors could not be read out, due to problems ranging from bad cables and connections to failures of electronic board channels, HDIs and chips. Most were repaired during an extended shutdown. The exceptions are HDI or chip failures, which are unservicable due to their location within the enclosed tracking volume. When the data for this thesis were taken, less than 5% of the detectors were not read out [65].

3.3.3 Operation

Operating voltage

The sensors operate at a bias voltage which exceeds the depletion voltage by 20 V and ranges from 40 to 100 V. To account for changes due to radiation damage, split bias is applied to the double sided detectors. The voltage component applied to the junction side (the high electric field region, in this case the p side) is severely limited by the micro discharge effect [69]. Typically, the junction side bias component cannot exceed 25 V. Above this value, the noise and leakage current increase rapidly. Studies indicate that the micro discharge effect will move from p side to n side when type inversion occurs after an irradiation dose of about $0.3 - 0.4$ MRad. There is no evidence of breakdown if the voltage is applied to the ohmic side. To preserve the functionality of the detectors the p side bias component will be gradually increased. The leakage current is expected to increase from 10 μA to about 1 mA.

The SMT readout system

The silicon sensors are read out using the SVX IIe chip [70, 71]. The SVX IIe is fabricated in radiation hard 1.2 μm CMOS technology. Each chip has 128 readout channels, consisting of a preamplifier, a 32 cell deep analog pipeline and an 8 bit Wilkinson type ADC with sparsified readout. Digitisation is performed at 106 MHz and readout at 53 MHz. The chip contains many programmable features including adjustment of the ADC ramp and pedestal, preamplifier bandwidth, test pulse patterns, sparsification threshold, and polarity of the input pulse, which have been verified to work reliably [72].

The SVX IIe chips are mounted on the HDIs, which also contain passive electronics for supplying the chips and the silicon sensors with power. The control signals, digitised data, as well as chip and bias voltages are provided through the flexible tail of the HDI. Through low- and high-mass cables, the HDIs are connected to interface boards located adjacent to the detector. Each interface board handles up to eight HDIs. The boards refresh the signals and adjust the timing before the long transmission line (about 10 m) to the chips. They also perform power management and monitoring of voltages, currents and temperature, as well as the bias voltage distribution. From the interface boards, the signals are sent via a high-mass cable to sequencer boards located in six crates underneath the detector.

Each sequencer board is used to initialise the SVX IIe chips in up to 8 HDIs. It also performs the real-time management of the SVX IIe control lines to effect data acquisition, digitisation and readout based on the signals received from the trigger framework. Data acquisition by the SVX IIe chips is only performed upon a low level (Level 1) trigger accept signal. During readout of the SVX IIe chips, data from the HDIs are encoded and converted onto a serial optical line to VME readout buffers in the Movable Counting House. For every low level trigger accept, the data from every HDI are stored in a buffer memory. Once an event has been accepted at a higher trigger level, the correct buffer is scanned and the data are read out by a VME buffer driver board. The driver board stores the data from all readout buffers until they are sent to the online processing farm.

The maximum Level 2 trigger accept rate is about 1 kHz. Assuming a 5% occupancy, the data acquisition rate is of the order of 10^{10} bits per second. To ensure that the occurence of fatal readout errors will not be a limiting factor for the live time of the detector, a bit error rate of at most 10^{-14} can be tolerated. Tests have been made reading out up to 57 ladders (corresponding to approximately 60,000 channels) at a transfer rate of up to 250 Hz. Locking the data to a fixed value, an error free data transfer of 3×10^{13} bits was achieved.

In addition, tests of the noise and sparsification were made. For 132 ns bunch spacing settings, a mean pedestal width of two ADC counts was found, comparable with the results found using the stand alone DAQ system. Applying a six ADC count threshold then led to an occupancy of about 0.5%. Finally, a common mode noise of about 0.6 ADC counts, with little impact on the total noise, was observed. Therefore, provided that the coherent noise originating from external sources is manageable, the SMT data can be expected to be clean. The occupancy caused by noise hits should be sufficiently low such as not to affect the detector performance.

The whole readout chain was tested in a complete system of the final readout configuration. Data integrity was established with bit error rates down to 10^{-15}. The same test setup was used to test each barrel-disk assembly built. A detailed description of the readout system is given in [73].

3.3.4 Radiation monitoring

Extended exposure to high radiation levels will damage the SMT, mainly in the form of displacement damage to the crystal structure of the sensors. The radiation originates mainly from two sources:

1. Non ionising energy loss in the silicon by particles produced in the $p\bar{p}$ interactions. The flux of these particles follows the charged particle $r^{-1.68}$ dependence measured by CDF [74], where r is the distance to the beam line;

2. A neutron flux, approximately independent of r, originating mainly from interactions with the calorimeter.

The radiation dose at the smallest radii is mostly due to the charged particle flux (about 0.4 MRad per fb^{-1} [75]). Radiation damage will cause the leakage current to rise linearly with the total fluence. In addition, type inversion of the initially n type silicon bulk will occur after $0.3 - 0.4$ MRad, corresponding to about 1 fb^{-1}. After type inversion, the depletion voltage will rise to high values which limits the useful lifetime of the detector. Biasing the sensors from both sides, a total bias voltage of 120 to 130 V can be applied. Because a good charge collection efficiency requires the bias voltage to be about 20 V higher than the depletion voltage, the maximum depletion voltage at which the sensors can be operated is expected to be about 100 V. Significant loss of channels in Layer 1 is expected after about 3.6 fb^{-1} [76]. Operation of the second layer could also become impossible at a higher integrated luminosity; however, the loss of the innermost layer already severely impairs the detector performance for b tagging. To compensate for the loss of the first layer and to improve the b tagging capabilities of DØ, an additional "Layer Zero" will be installed inside the existing detector [77].

A significant part of the radiation exposure of the SMT may come from unexpected beam deviations and losses. To prevent unnecessary exposure to accidental radiation and to monitor the total radiation dose received by the SMT, two radiation monitoring and alarm systems have been installed. Four Beam Loss Monitors (BLMs) are mounted at each end of the detector, just outside the calorimeter end caps. Their main function is to provide an abort signal to the Beams Division if radiation levels are too high. A system consisting of 48 silicon diodes is located in the SMT volume itself. This system, similar to one previously used by the OPAL collaboration [78], provides an integrated dose measurement as well as a precise radiation history in the case of an abort. The diodes are known as the "radiation monitors". The radiation monitors can also send alarm signals to the control room and to the Beams Division. The location of the radiation monitors on one of the F-disks is shown in Fig. 3.8.

The Beam Loss Monitors have been used successfully by both CDF and the Beams Division in Run I [79]. The monitors are large argon filled gas counters with a large diameter anode cylinder, so no amplification occurs. The BLMs operate at 2 kV, well above their plateau region, to ensure a fast response time. This system is very robust and well understood, but not as sensitive to low radiation levels as the Radiation Monitors. In addition, their location makes it hard to correlate the measured dose to the dose at the SMT.

The sensors for the Radiation Monitors are small (1×1 cm) silicon diodes, cut from the SMT production wafers. They are mounted on small flexible circuits which are laminated onto beryllium support plates. Two diodes are mounted on one plate or "finger", one at the inner radius of the

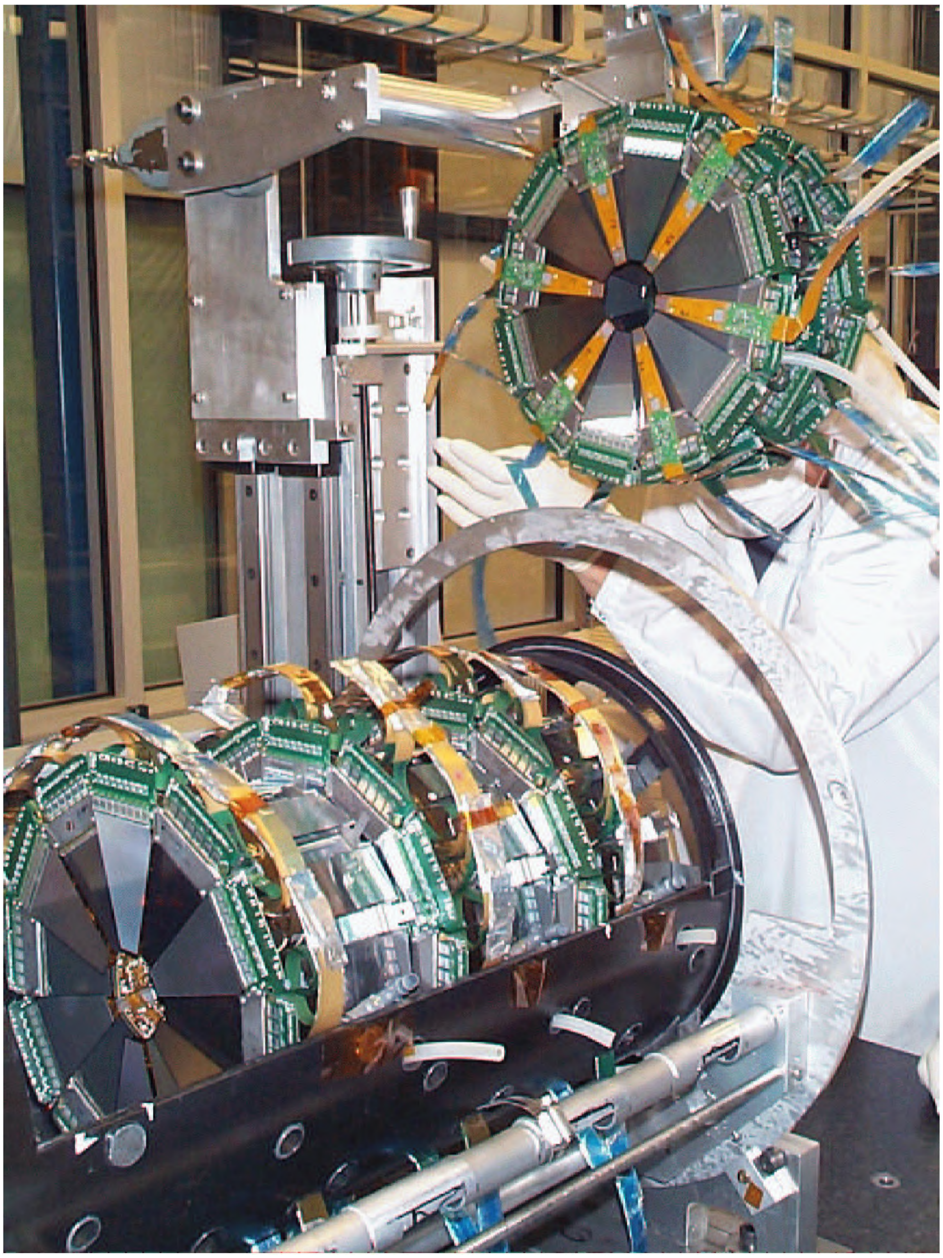

Figure 3.8: Location of the radiation monitors on one of the F-disks in the DØ detector. The picture shows one half of the SMT installed in the support cylinder. The three F-disks will be installed at the end of the central section at the left of the picture.

detector and one near the mounting point of the plate on the support ring. Six such modules are placed on each of the outer F- and H-disks, uniformly distributed in ϕ, for a total of 24 fingers. Charged particles traversing the 300 μm thick diodes generate a charge signal of about 3 fC which is amplified on the fingers. The flexible circuits contain two separate analog amplification circuits providing high and low gain output for each diode. The low gain signal provides an alarm signal for high radiation doses, while the high gain signal allows precise monitoring of the integrated

Figure 3.9: A radiation monitor finger installed on one of the H-disks.

dose. Both signals are integrated in a custom electronics crate. The high gain signal can be used to measure individual MIPs and to calibrate the signal. In addition, a precise record of the total received dose can be kept. A Radiation Monitor sensor module — or "finger" — is shown in Fig. 3.9, mounted on one of the H-disks.

The radiation monitoring systems are described in greater detail in [80, 81]. From the start of Run II until August 2004, during which time about 600 pb^{-1} was delivered to the DØ detector, the total effective radiation dose on the SMT inner barrel sensors was (123 ± 18) kRad [82]. About 25% of the accumulated dose was due to short periods of high radiation, usually connected to setting up the beams. The rest of the dose was due to stable running.

3.3.5 Single Event Effects

Because the SMT signals are digitised at the detector, the readout chips are subject to the same radiation levels as the rest of the vertex detector. Nuclear interactions of charged hadrons or neutrons can cause large local energy deposits, leading to disruptions in the operation of the readout chips. These disruptions are collectively known as Single Event Effects (SEE).

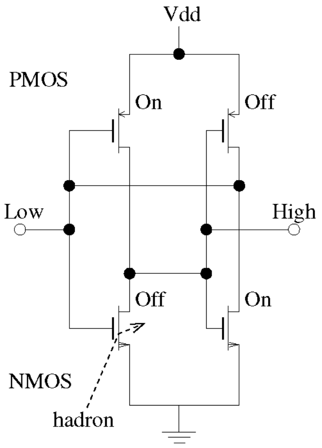

Figure 3.10: Simplified schematic of a CMOS memory cell showing a hadron interacting near the "off" PMOS transistor.

The energy deposition by heavy ions produced in the nuclear interaction can open current channels which affect the operation of the chip. A single event effect in a memory cell made of cross coupled inverters, as in the SVX IIe, can cause a change in the state of the cell if one of the transistors is affected. A simplified schematic of a nuclear interaction in a CMOS memory cell is shown in Fig. 3.10. Such nondestructive errors are known as Single Event Upsets (SEU) and can be recovered by re-initialising the chip. Destructive Single Event Latchups (SEL) are due to radiation induced turnon of parasitic transistors in the CMOS chips. The chip will draw a large current and may fail permanently if power is not switched off.

The likelihood of single event effects depends on the capacitive coupling between the features on the chip. The sensitivity of a chip therefore increases with decreasing feature size. Because of this, and because of the high radiation levels in DØ, single event effects become a serious concern. To estimate the rate at which these events may occur at DØ, the SEE cross sections were measured at the Crocker Nuclear Laboratory [83] at the University of California in Davis. Two hybrids of three SVX IIe chips were subjected to doses up to 16 MRad. The SEU cross section was measured by monitoring the state of the shift register, through which the digital initialisation pattern is downloaded to the chip. The cross section is plotted versus the incident beam angle in Fig. 3.11. The cross sections and expected SEU rates in Run II are given in Table 3.2 and Table 3.3, respectively. The upper limit on the SEU rate at DØ at design luminosity was found to be about one upset per hour, low enough for stable running. No latchups were observed during the test, giving an upper limit of 4.13×10^{-15} $\mathrm{cm}^2/\mathrm{chip}$ on the cross section at 95% Confidence Level. The Single Event Effect test is described in greater detail in [84].

Like the silicon detector itself, the chips suffer long term radiation damage. The deterioration of the bulk silicon manifests itself as a slow rise in the pedestal level, reducing the signal to noise ratio of the chips. Aside from this rise, the chips are stable up to integrated doses of just over 3 MRad. Above that, the pedestal level of the chips in the test rose to full saturation with a marginal increase in radiation, after which the readout logic started failing and the chips became unreliable.

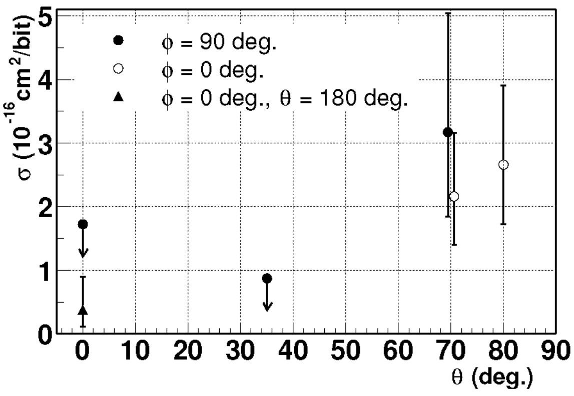

Figure 3.11: Single event upset cross section as a function of incident beam angle. The cross section is given as a cross section per bit for 63 MeV protons.

θ	ϕ	Fluence ($\times 10^{13}$ cm^{-2})	Upsets per 3×190 bits	σ (10^{-16} cm^2/bit)
0	90	3.05	0	< 1.72 (95%CL)
180	90	4.57	1	$0.38^{+0.52}_{-0.27}$
35	90	6.20	0	< 0.87 (95%CL)
70	90	2.21	4	$3.17^{+1.87}_{-1.33}$
70	0	4.88	6	$2.16^{+1.00}_{-0.76}$
80	0	3.90	6	$2.66^{+1.24}_{-0.94}$
0 + 180	90	7.62	1	$0.24^{+0.33}_{-0.17}$
70	0 + 90	7.09	10	$2.47^{+0.87}_{-0.70}$

Table 3.2: Single Event Upset cross section measured as a function of the incident beam angle.

3.4 Central Fibre Tracker

The Central Fibre Tracker (CFT) surrounds the SMT and completes the central tracking system. Together with the SMT, it enables track reconstruction and momentum measurement in the central region, $|\eta| < 2$. In addition, it provides fast trigger information within $|\eta| < 1.6$. By combining information from the tracker with the muon and preshower detectors, triggers for both single muons and electrons can be formed at the first trigger level.

The CFT consists of eight layers of scintillating fibres mounted on concentric cylinders at radii r = 19.5cm, 23.4cm, 28.1cm, 32.8cm, 37.5cm, 42.1cm, 48.8cm and 51.5cm. The two innermost cylinders are 166 cm long; the outer cylinders are 252 cm long. Each cylinder supports one doublet layer of fibres aligned with the beam, and one at a stereo angle of $+3°$ (odd cylinders) or $-3°$ (even cylinders). The doublet layers are made up of ribbons, made by placing the centre of the fibres in one "singlet" layer made of 128 adjacent fibres in the space between the fibres of a second singlet layer. This configuration compensates for the geometric gaps between adjacent fibres in a singlet layer and provides near unity detection efficiency per doublet layer (better than 99%). The double

	$r_\perp$ (cm)	$\lvert z \rvert$ (cm)	# SVX IIe chips	total flux ($\mathrm{cm}^{-2}s^{-1}$)	expected SEU rate ($\mathrm{s}^{-1} \times 10^{-4}$)
Layer 1	2.7	0 – 38	360	3×10^4 p; 1×10^6 $\mathrm{h}^\pm$	0.85
Layer 2	4.5	0 – 38	648	1×10^4 p; 3×10^5 $\mathrm{h}^\pm$	0.46
Layer 3	6.6	0 – 38	720	5×10^3 p; 2×10^5 $\mathrm{h}^\pm$	0.34
Layer 4	9.4	0 – 38	1296	1×10^3 p; 1×10^5 $\mathrm{h}^\pm$	0.30
F-disks	10	0 – 53	2016	1×10^3 p; 1×10^5 $\mathrm{h}^\pm$	0.47
H-disks	25	100, 120	1152	3×10^3 p; 1×10^4 $\mathrm{h}^\pm$	0.03
TOTAL			6192		2.5 ± 0.8

Table 3.3: Expected SEU rate at DØ in Run II.

clad fibres are 835 μm in diameter. The spatial resolution per doublet is about 100 μm.

The detector is divided into 80 sectors in ϕ. Each pie shaped slice has 960 fibres and the full detector has 76,800 channels. The axial fibres, which amount to one half of the fibres, are used to form the fast Level 1 trigger. All of the fibres are read out on a Level 1 trigger accept and are used for a Level 2 trigger.

The CFT signals are read out by Visible Light Photon Counters (VLPCs), which are located in cryostats on the platform under the central calorimeter. The VLPCs are connected to the scintillating fibres by clear fibre light guides with lengths of about 11 m. They can be operated at full efficiency with a noise rate of 0.1% or less, at a rate of at least 10 MHz. Readout of the VLPCs is handled by the same SVX IIe based readout system as the SMT. For the CFT, the SVX IIe chips are preceded by by a special trigger chip to provide a prompt Level 1 trigger pickoff. Each channel of this chip has a charge sensitive amplifier plus discriminator with TTL output and a buffer amplifier to put charge on an output capacitor which is read out by the SVX IIe.

Because the electronics for the CFT are located outside the detector volume, they are not subject to the high levels of radiation that the silicon sensors are exposed to. Only the scintillating fibres themselves are susceptible to any radiation damage. Studies indicate that no more than a 30% reduction in light yield is expected for the innermost layer during the course of Run II.

The acceptance of the CFT is defined in the same way as the SMT barrel acceptance (see Section 3.3 and Fig. 3.6). The acceptance for tracks originating at the centre of the detector is $|\eta| < 1.6$. The full (z_0, η) distribution is shown in Fig. 3.12.

3.5 Superconducting solenoid

The momenta of charged particles are determined by the curvature of their tracks in the magnetic field provided by a 2.8 m long superconducting solenoid. The magnet provides a field of 2 T inside the tracking volume. The solenoid is a two layered coil with a mean radius of 60 cm. The total energy stored is 5 MJ.

From the value of the field integral and the space point precision provided by the silicon and fibre tracking systems, a momentum resolution of $\Delta p_T/p_T^2 \approx 0.002$ can be reached. Within the tracking volume, the value of $\sin\theta \times \int B_z \mathrm{d}l$ along the trajectory of any particle reaching the solenoid is uniform to within 0.5% .

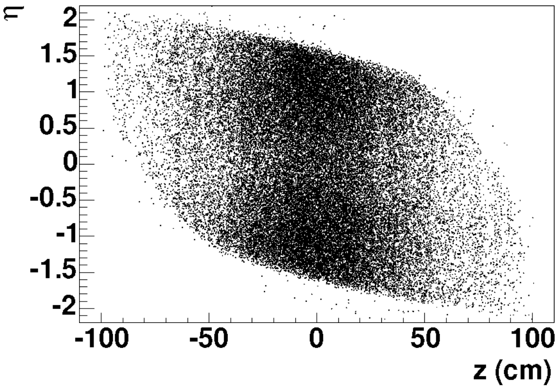

Figure 3.12: Acceptance of the CFT. Shown is the (z, η) distribution of all tracks with hits in all sixteen CFT layers.

The superconducting coil and cryostat represent about 1.1 radiation lengths of material. This is mostly due to aluminium which is distributed over 17cm of radial space. This configuration of material makes the solenoid a non-ideal preradiator. The low ratio of the radiation length and nuclear interaction length of aluminium means that the solenoid also consists of about 20% of the nuclear interaction length. Therefore, a significant fraction of charged pions start hadronic showers in the solenoid. Additionally, the thick solenoid allows electromagnetic showers in the solenoid to spread. Both effects will reduce the power of the detector to separate electrons from background.

3.6 Preshower detectors

The preshower detectors are designed to aid electron identification and triggering and to correct the electromagnetic energy measurement in the calorimeter for effects of the solenoid. The design includes two separate, but similar subdetectors: the Central PreShower detector (CPS) and the Forward PreShower detector (FPS).

Both the CPS and the FPS are made of triangular strips of scintillator with embedded wavelength shifting fibres. Readout is done by visible light photon counters (VLPCs). By early energy sampling, they can help minimise the loss of energy resolution due to the addition of about 1.1 radiation lengths (X_0) of material in the solenoid coil, allowing precise matches between track and shower position. While the DØ calorimeter will provide superior position resolution for high E_T electrons, the finely segmented preshower detectors will contribute significantly to the position measurement of low E_T electrons, such as those from b quark decays.

The Central Preshower detector is placed in the 51 mm gap between the solenoid cylinder and the central calorimeter cryostat at a radius of 72cm, and covers the region $-1.2 < \eta < 1.2$. The detector consists of three layers of scintillator strips arranged in an axial-u-v geometry, with a stereo angle of $\pm 23^\circ$. The average measured pitch is 3.54 mm. A lead absorber is placed before the detector so the solenoid plus lead total two radiation lengths of material for particles at normal incidence, increasing to about four radiation lengths for the largest angles.

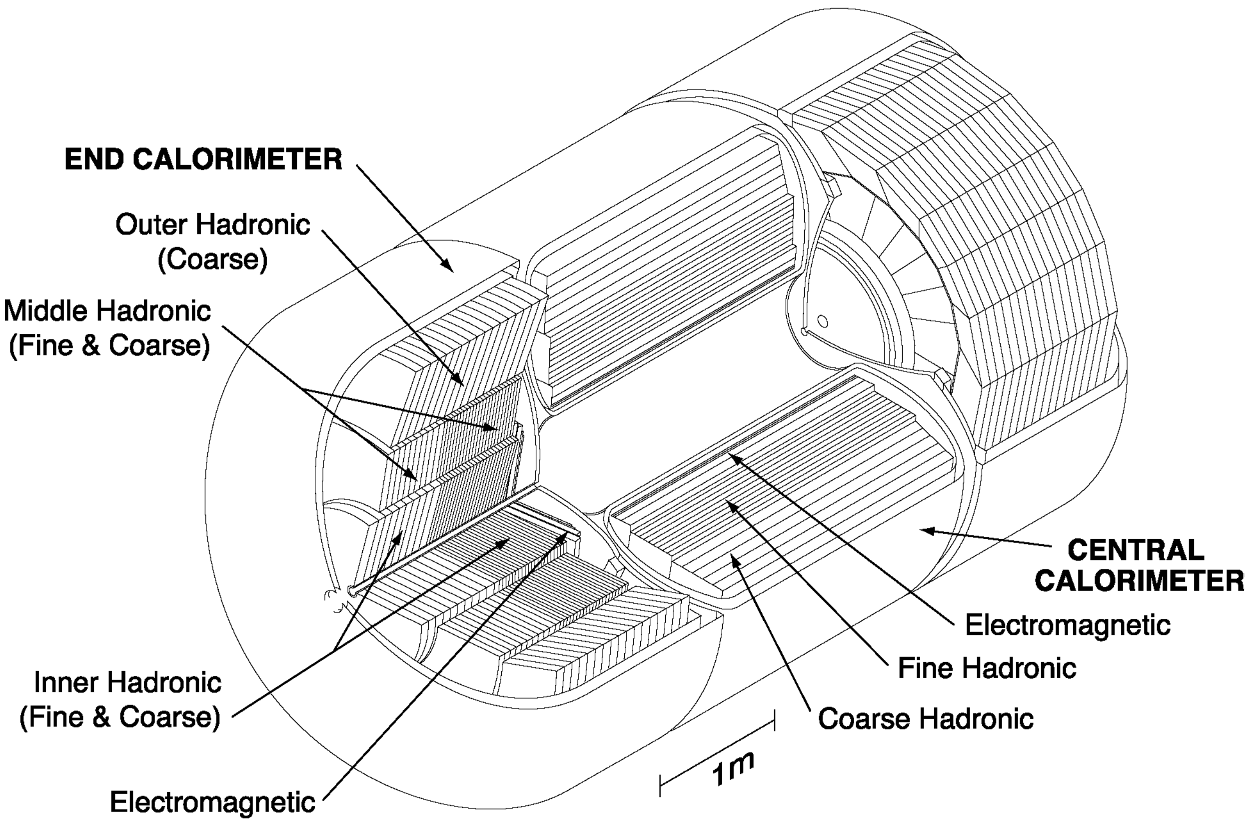

Figure 3.13: The DØ calorimeter.

Two Forward Preshower detectors cover the pseudorapidity range $1.4 < |\eta| < 2.5$, with one detector mounted on the inner face of each of the end calorimeter cryostats. Each detector is composed of a $2X_0$ thick layer of lead-stainless steel absorber sandwiched by two active scintillator planes. Each of the planes consists of two layers of scintillating fibres, with a stereo angle of $22.5°$. The average measured pitch of the fibres is 3.65 mm.

Neither preshower detector was used in the jet reconstruction for the analysis presented in this thesis. More information can be found in the technical design reports [85, 86] and in [87].

3.7 Calorimeter system

The full calorimeter detector from Run I has been kept for Run II, limiting modifications to the front end electronics. The calorimeter is shown in Fig. 3.13.

The calorimeter is contained in three separate cryostats. The central calorimeter covers the region $|\eta| < 0.8$, while the end calorimeters extend the coverage to $|\eta| \lesssim 4$.

The calorimeter is a sandwich design with uranium, copper and stainless steel as the absorbing materials and liquid argon as the sensitive material. Each layer of absorber material is followed by a 2.3 mm liquid argon gap on either side of a 1.3 mm signal board. The signal board contains copper pads surrounded by a resistive coating. The absorber and the copper pads are grounded

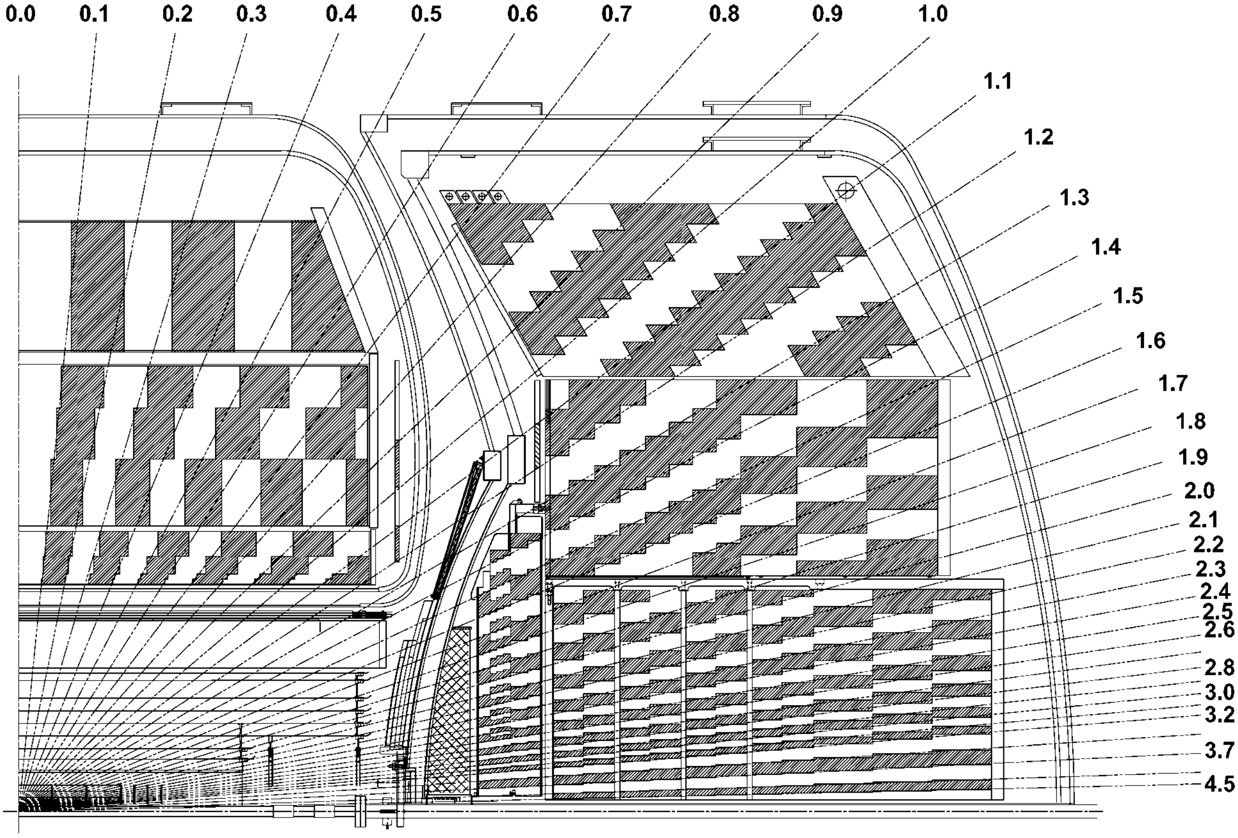

Figure 3.14: Side view of the calorimeter showing the segmentation and coverage in η.

while the resistive coating is connected to a high voltage source to create an electric field of about 9 kV/cm across the liquid argon gap. The copper pads in different layers are aligned such that their centres are radially aligned with the centre of the detector.

The segmentation of the calorimeter is shown in Fig. 3.14. The transverse segmentation of the calorimeter is determined by the size of the readout towers which is 0.1×0.1 in $\Delta\eta \times \Delta\phi$ for $|\eta| < 3.2$. This is fine enough to probe the transverse shape of a jet, which is typically contained in a cone with $R = \sqrt{(\Delta\eta)^2 + (\Delta\phi)^2} \lesssim 0.8$. In the very forward region, $|\eta| > 3.2$, the segmentation is 0.2×0.2, because the physical shower size in that region is much wider in $(\eta \times \phi)$ space than in the central region. The longitudinal segmentation is determined by the number of successive pads at different depths in the calorimeter that are read out together.

Looking out from the interaction region, the DØ calorimeter consists of a thin electromagnetic calorimeter followed by a thicker hadronic calorimeter. The electromagnetic calorimeter uses uranium absorbers of 3 mm thickness in the central region and 4 mm in the forward region. It has a total thickness of about 20 radiation lengths, grouped into four readout layers. The third layer, which spans the region of maximum electromagnetic energy deposition, has a segmentation of 0.05×0.05 instead of 0.1×0.1. This allows a more precise determination of the direction of electromagnetic showers.

The hadronic section uses 6 mm thick uranium-niobium (2%) alloy absorbers in the inner layers and 46.5 mm thick copper (central calorimeter) or steel (forward calorimeters) plates in the outer layers. The layers with 6 mm absorbers are known as the "fine hadronic layers" and are used for hadronic shower shape measurements; the outer layers are known as the "coarse hadronic layers" and are used to contain the showers of high energy jets. The outer layers are called the "coarse hadronic" layers. The total thickness of the hadron calorimeters is about 6 nuclear interaction lengths (λ_I) in the central calorimeter and about 9 λ_I in the forward calorimeters.

The readout electronics of the calorimeter have been completely replaced for Run II. To minimise the effects of pileup in the calorimeter, the shaping times have been reduced with respect to Run I to 200 ns, matching both the charge drift times and the 396 ns bunch crossing time in Run II. Because this short shaping time increases the sensitivity to noise and reflections on the signal cables, the old cables from the calorimeter cryostat have been replaced.

The Run I preamplifier hybrids have been replaced with new hybrids which have better noise performance and increased output drive capability. The shaper circuitry incorporates an analog pipeline using a switched capacitor array originally developed for the Superconducting Super Collider and modified to match DØ trigger specifications. The performance of the system with regard to pileup has been simulated, and the capability of the upgrade detector is found to be comparable to that of the old detector at lower Run I luminosities.

3.7.1 The intercryostat detector

An InterCryostat Detector (ICD) is located between the central and forward calorimeter cryostats to compensate for the loss in resolution in the overlap region, $0.7 < |\eta| < 1.4$. The ICD plays an important role in DØ calorimetry, both in terms of measuring jet energy as well as missing transverse energy ($\not{E}_T$). In order to preserve the Run I calorimeter resolution, the ICD has been modified for Run II by relocating the photo detection readout outside of the high magnetic field environment in the intercryostat region.

Each ICD consists of a single layer of 384 scintillator tiles of size (0.1×0.1) in $(\eta \times \phi)$, matching the liquid argon calorimeter cells. The light signals, picked up by wavelength shifting fibres in the tiles, are transported along clear fibres to the photo detection readout, located about 8 m from the tiles.

In addition to the ICD, separate readout cells called "Massless Gaps" are installed just inside both the central and forward calorimeter cryostats. The cells are similar to the cells of the liquid argon calorimeter, except the absorber plates are replaced with thin ground planes. Each 1.5 cm thick cell consists of two signal boards, three ground planes and four liquid argon gaps. The central Massless Gaps cover the region $0.7 < |\eta| < 1.2$; the forward cells cover the region $0.7 < |\eta| < 1.3$. The addition of the ICD and the Massless Gaps makes the calorimeter nearly hermetic over the full η coverage.

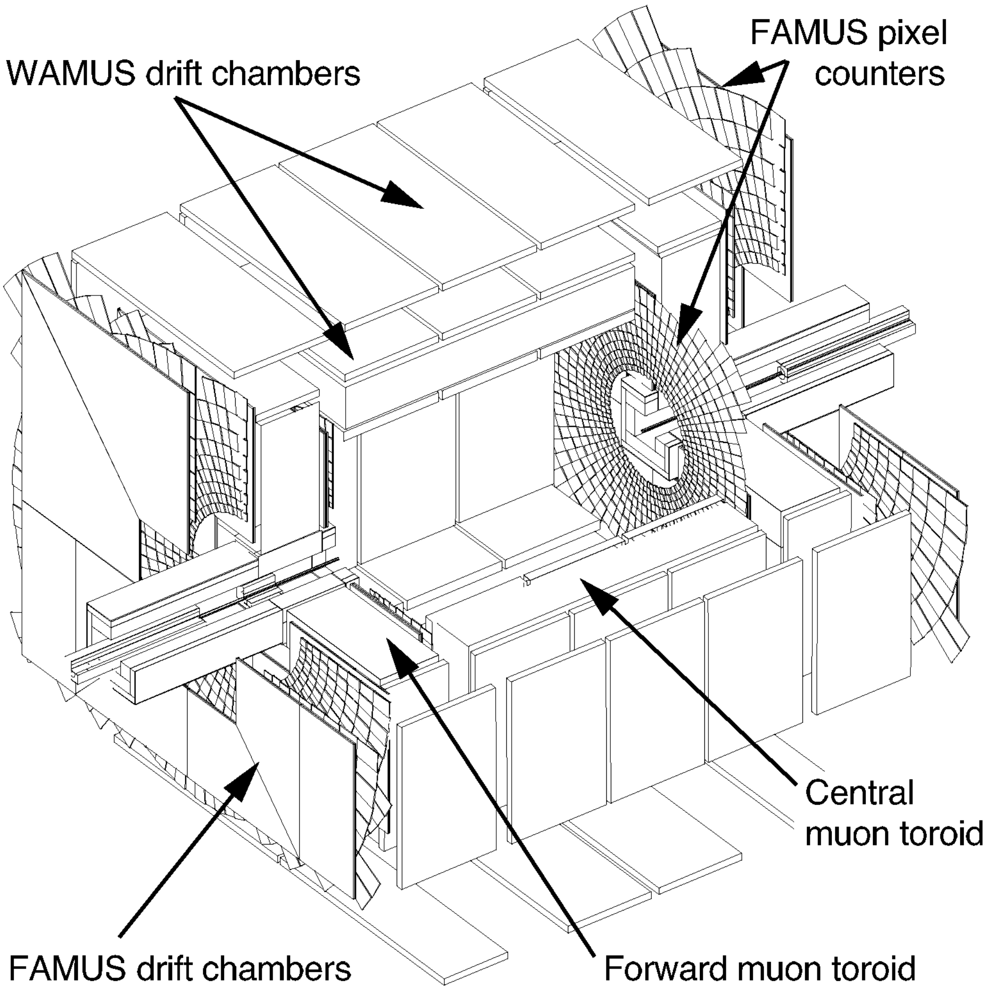

Figure 3.15: Cutaway view of the DØ Muon Spectrometer.

3.8 Muon system

The DØ muon system is divided in the central muon system, which covers the $|\eta| \lesssim 1$ range, and the forward muon system, which covers the range $1 < |\eta| < 2$. Both regions use three layers of drift tubes designated A, B and C, where the A layer is closest to the interaction region. Toroidal magnets are located between the A and B layers. In addition, scintillation detectors in each region provide timing and triggering. The complete muon system is shown in Fig. 3.15. The central and forward regions are discussed in more detail separately.

3.8.1 The central muon system

The central muon system or WAMUS (Wide Angle MUon System) consists of three detector systems: the drift chambers, the Cosmic Cap and Bottom scintillators, and the $A\phi$ scintillation counters. Between layer A and layers B+C, a toroidal magnet provides a field of about 2 T with field lines running in the plane perpendicular to the beam axis.

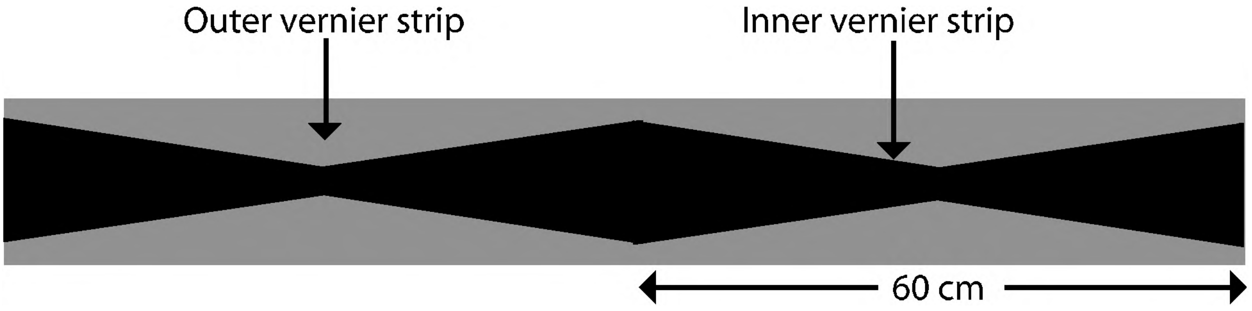

Figure 3.16: Schematic view of part of a vernier pad showing the diamond pattern. The black and grey sections correspond to the inner and outer pads.

WAMUS drift chambers

The WAMUS drift chambers are the same Proportional Drift Tubes (PDTs) as used in Run I. The drift chambers are large, typically 100×220 in^2, and are made of rectangular extruded aluminium tubes. The anode wires are oriented along the magnetic field lines of the toroid. Approximately 55% of the central region is covered by three layers of PDTs, and close to 90% is covered by at least two layers. The PDTs in layers B and C outside the toroid have three decks of drift cells; layer A has four decks with the exception of the layer underneath the detector, which has three. The cells are 10.1cm across, with typically 24 columns of cells per chamber.

For each hit, the drift chambers provide the drift time T to the anode wire and the difference ΔT between the arrival times of the hit in the cell and of a hit in the neighbour connected to it at the far end. The drift distance resolution is $\sim 500\ \mu\mathrm{m}$. The ΔT measurement provides the distance along the wire with a resolution of about $10 - 50$ cm, depending on whether the muon passes close to or far from the electronics. To improve the accuracy along the wire, vernier cathode pads are inserted at the top and bottom of each tube. The insulating pads are coated with copper cladding, separated into inner and outer regions in a repeating diamond pattern with a period of 60 cm(see Fig. 3.16). The ratio of the charge deposited on the inner and outer pads can be used to locate the hit within about 3 mm modulo half the repeat period. The expected momentum resolution of the drift chambers is $\sigma(1/p) = 0.18(p-2)/p^2 \oplus 0.005$ (p in GeV$/c$), the first term due to multiple scattering in the toroid iron and the second due to spatial resolution and alignment errors. Figure 3.17 shows a cutaway view of the 3-deck and 4-deck extrusions as well as an end view of a drift tube showing the wire and vernier pads.

To reduce the number of crossings which occur during one drift interval, a fast, non flammable mixture of 80% argon, 10% methane and 10% CF_4 is used as the drift gas. At approximately 2.5 kV operating voltage for the pads and 5 kV for the wires, the drift velocity is $\sim 10\ \mathrm{cm}/\mu\mathrm{s}$, for a maximum drift time of $\sim$ 500 ns.

WAMUS scintillation counters

The "Cosmic Cap" scintillation counters were already used in Run I and cover the top and sides of the WAMUS C-Layer. They provide a fast trigger signal outside the toroid magnet for identifying muons from cosmic rays. In addition, they provide a time stamp for muons which pass through the

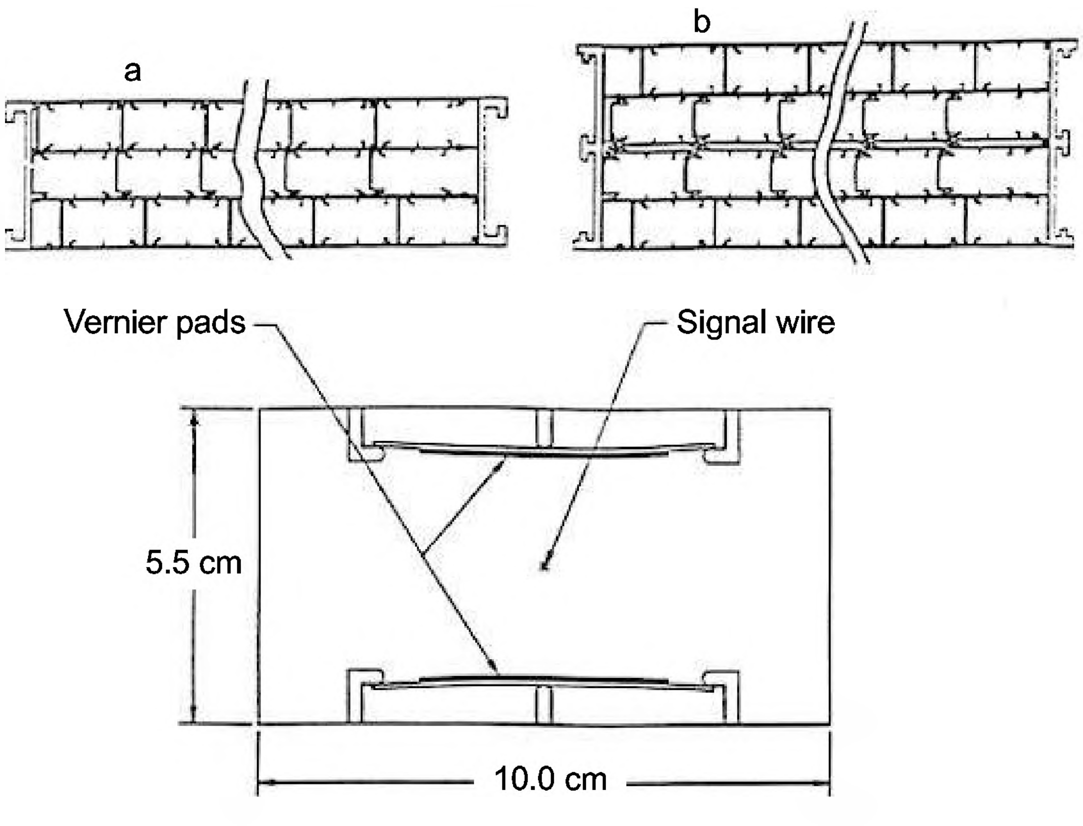

Figure 3.17: The WAMUS Drift Chambers.

WAMUS PDTs to determine in which crossing the muons were produced. After offline corrections, a resolution of 2.5 ns was achieved in Run I. Online, the counters have a timing resolution of about 5 ns. The efficiency was 98%. The counters have three sizes depending on the size of the WAMUS chamber on which they are mounted. There are 12 divisions in ϕ and 20 divisions in η for a total of 240 counters, with the long counter dimension along ϕ. The counters are made from grooved scintillator material. Wavelength shifting fibres are glued into the grooves and are read out by photomultiplier tubes.

The coverage of the Cosmic Cap is completed in Run II by 132 Cosmic Bottom counters. These counters are located underneath the B- or C-Layer of the bottom WAMUS detector, depending on their location in η. Their design is similar to that of the Cosmic Cap counters. One important difference is that the orientation of the bottom counters has the narrow dimension along ϕ and the long dimension along η. This orientation is preferred because it has better matching in ϕ with the inner tracking chamber trigger. The widths are approximately $4.5°$ in ϕ.

The $A\phi$ counters cover the WAMUS PDTs mounted between the calorimeter and the toroid magnet, just in front of the WAMUS A-Layer. They provide a fast measurement for triggering and identifying muons and for rejecting out-of-time backscatter from the forward direction. In addition, they provide a time stamp for muons passing through the WAMUS PDTs, particularly important for low p_T muons which do not penetrate to the Cosmic Cap or Bottom counters. The ϕ segmentation is $\sim 4.5°$, appropriate for the expected multiple scattering for high p_T muons. The longitudinal segmentation is $33\frac{1}{4}$ inches. The timing resolution is better than 4 ns at the trigger level and better than 2.5 ns offline.

3.8.2 The forward muon system

Since ageing studies of the WAMUS chambers used in the forward region in Run I showed that these chambers would not survive the high radiation doses in Run II, a new design for the Forward Angle MUon System (FAMUS) has been developed.

The forward muon system consists of three layers of Mini Drift Tubes, three layers of scintillation counters, and extensive shielding to reduce trigger rates, fake track reconstruction and ageing of the detectors. The forward toroid magnet provides the magnetic field for momentum determination.

FAMUS drift chambers

Muon tracks in the forward region are reconstructed using Iarocci-type Mini Drift Tubes (MDTs). The A-layer consists of 4 planes of rectangular tubes; the B- and C-layers have 3 planes each. The tubes are made from aluminium extrusions and consist of eight adjacent $9.4 \times 9.4\ \mathrm{mm}^2$ cells with a 50 μm anode wire in the centre. The tubes are oriented along the magnetic field lines of the forward toroid. A fast gas mixture provides a maximum electron drift time of about 60 ns.

The track position can be determined by drift time measurements with a position accuracy of $\sigma_x \approx 700\ \mu\mathrm{m}$ in each layer. The tubes are approximately 100% efficient in the active area. Due to the walls, the actual efficiency is about 94% for perpendicular tracks. Dead zones at the ends of the tubes contribute to the inefficiency. The overall reconstruction efficiency of the FAMUS detector is around 90%.

FAMUS scintillation counters

Three planes (A, B and C) of scintillation counters are installed just inside the corresponding FAMUS MDT layers on each side of the detector. Each counter is made of a trapezoidal scintillator plate with two wavelength shifter bars for light collection and read out by a single photomultiplier tube. The counters are arranged in (r, ϕ) geometry. The ϕ segmentation is $4.5°$ and matches the trigger sectors for the CFT. The η segmentation is 0.12 for the inner nine rows of counters and 0.07 for the outer three. The total η coverage matches that of the FAMUS MDTs. Beam tests have shown that the detection efficiency at the high voltage plateau is 99.9% and that time resolutions below 1 ns can be reached. The scintillators are used to reduce the number of background hits and provide a fast trigger signal that can be used in combination with the CFT.

3.8.3 Shielding

The upgrade of the DØ muon system includes the addition of shielding material. This shielding blocks non-muon background particles origination from the three hottest sources. The main source is scattered proton and antiproton fragments which interact with both the exit of the calorimeter (producing background in the A-layers of both WAMUS and FAMUS) and the beam pipe and low beta quadrupoles (producing showers in the FAMUS B and C-layers).

The main feature of the B and C-layer shield is a thick iron, lead, and polyethylene casing surrounding the beam pipe and the final low beta quadrupole magnet. This casing extends from the calorimeter to the accelerator tunnel. The shield is approximately 170 cm wide on the outside and has an inside hole ~ 50 to 65 cm wide for the accelerator equipment. The appropriate thickness of the casing was determined by Monte Carlo simulations (GEANT [88] and MARS [89]) for various shielding configurations [90]. The new shielding is expected to reduce the number of hits in the counters by about a factor of 40.

3.9 Forward Proton Detector

The Forward Proton Detector (FPD) is a series of momentum spectrometers which make use of accelerator magnets along with points measured on the track of a scattered proton or antiproton to calculate its momentum and scattering angle. The FPD was added to the DØ detector to study hard diffraction physics.

The points are measured using detectors located in Roman pots, which are stainless steel containers that allow the detectors to function close to the beam. The particles traverse a thin steel window at the entrance and exit of each pot. The pots are remotely controlled and can be moved close to the beam (within a few mm) during stable beam conditions. Each pot contains a scintillating fibre detector which measures the (x, y) coordinate of the deflected proton or antiproton at the position of the pot.

A dipole spectrometer consisting of two Roman pots is located about 57 m downstream of the interaction point along the outgoing $\bar{\mathrm{p}}$ beam. In addition there are four stations that use the quadrupole magnets to measure the proton trajectory. These stations are located at $|z| \approx 23$ m and $|z| \approx 31$ m.

The FPD was not used for this study. It is described in more detail in [91, 92].

3.10 Luminosity monitors

The accelerator luminosity at DØ is monitored by measuring the rate of nondiffractive inelastic collisions in the interaction region. The luminosity monitors consist of 24 scintillator wedges surrounding the beam at $z = \pm 135$ cm and covering the pseudorapidity region $2.7 < |\eta| < 4.4$. The wedges are read out by fine mesh photomultipliers directly on the faces.

In the case of a nondiffractive collision, charged particles produced in the interaction generate a signal in the luminosity monitor scintillators. The luminosity monitor counts once for each beam crossing with such an interaction and measures the fraction of crossings with no interactions. The average number of interactions per crossing is calculated using Poisson statistics for the probability of zero interactions $P_0 = e^{-\langle n \rangle}$. The luminosity can then be determined using the total inelastic and diffractive cross sections, which are taken from [93]. The acceptance for detecting nondiffractive inelastic collisions is $(98 \pm 1)\%$, estimated from Monte Carlo studies.

In Run I, an error of 5.3% was attained on the luminosity measurement, which included a 2.6% contribution related to uncertainties in the detector acceptance and efficiency and a 4.6%

contribution due to uncertainties in the inelastic and diffractive cross section measurements. The estimated uncertainty for Run II is 6.5% [94].

In addition to the luminosity measurement, the luminosity monitors also provide a time of flight measurement for charged particles hitting the scintillators. The time of flight is used to determine the position of the primary interaction vertex and to detect multiple interactions, which can be rejected using trigger electronics. The measurement also allows a clear separation between beam-beam interactions and the principal background from beam halo. A time of flight resolution of 250 ps in Run I allowed determination of the longitudinal vertex position to an accuracy of 3.5cm for single interaction beam crossings. A resolution of $\sim$ 200 ps is expected for Run II [95].

3.11 Monte Carlo modelling of detector response

Interactions in the DØ experiment are simulated in three steps. First, an event generator is used to simulate the beam-beam interaction. The interaction of particles with the detector is simulated using DØGSTAR (DØ GEANT Simulation of the Total Apparatus Response). DØGSTAR is a full simulation of the DØ detector including all detector elements and passive material and is based on GEANT [88].

A third program, called DØSim, is used to add minimum bias events, calorimeter pileup and noise to the events simulated by DØGSTAR. The resulting output is a simulation of the real data of the experiment and can be analysed with the same reconstruction and analysis software used for real data.

Chapter 4

Data acquisition and online event selection

An *event* is defined as a beam crossing in which at least one inelastic interaction occurs. At a beam crossing rate of 2.5 MHz (for 396 ns bunch spacing) and at the design luminosity of $\mathcal{L} = 2 \times 10^{32}\ \mathrm{cm}^{-2}s^{-1}$, the mean number of inelastic interactions per crossing is $\langle n \rangle = 3.9$ (using the total inelastic $\mathrm{p\bar{p}}$ cross section $\sigma_{\mathrm{p\bar{p}}} = 49$ mb [1]). The probability that no inelastic interactions occur is about two percent. At this rate, not every event can be permanently stored. To fully realise the potential of the data, an online filtering system is employed to select the most interesting events to be recorded to tape for further analysis. This trigger system makes decisions based on the presence of particular signals in the event, such as the detection of high energy jets and muons.

The data presented in this thesis have been selected with a trigger requiring the presence of a jet and a muon in the event, internally known by the codename MU_JT20_L2M0. The terms making up this trigger are discussed in detail in this chapter. Triggers used for background studies, efficiency studies and trigger efficiency studies are also mentioned. The description of specific triggers is preceded by an overview of the trigger framework employed by the DØ experiment. A more extensive description of the trigger hardware and algorithms can be found in [96].

4.1 The trigger framework

To minimise dead time, the trigger framework has three separate selection levels. The output rate or decision frequency at each level is dictated by the maximum input rate of the next level and, ultimately, by the rate at which events can be written to tape. In addition, the limited depth of pipelines (at Level 1) and buffers (at Level 2) imposes an upper limit on the average time available to make each decision.

At the first level (L1), fast information from the front-end readout of the detectors is used to make a trigger decision within 4.2 μs. Each subdetector has its own L1 system; the final decision is made by the trigger framework as an AND/OR combination of the various subdetectors' L1 trigger terms. If selected, events are passed from Level 1 to the second level (L2) trigger, where the information is refined and combinations are made to form rudimentary "physics objects" (e.g. jets, muons or electrons). A single global processor combines the information to make a decision within an average 100 μs decision time. Events passing L2 initiate a full detector readout and are reconstructed in the third level trigger (L3), a computer farm, for final selection. The event rate can in this way be reduced to maximally 10 kHz at L1, 1 kHz at L2 and finally to an output rate to tape

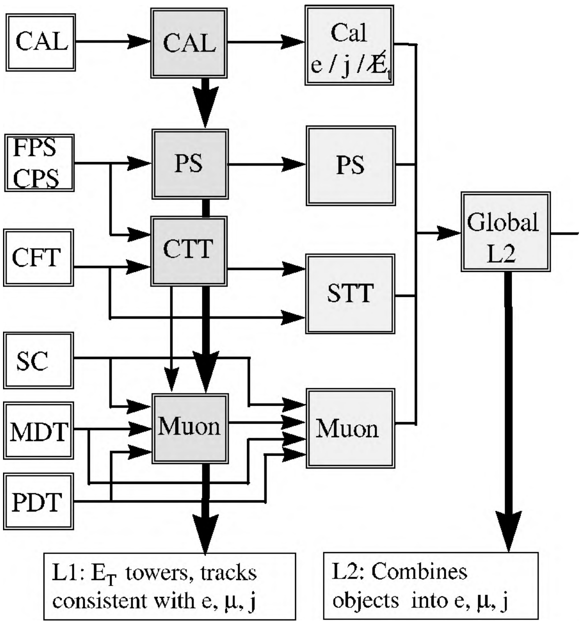

Figure 4.1: Overview of the Level 1 and Level 2 trigger framework.

of 50 Hz or less. The actual rates achieved when the data presented in this thesis were collected were about 1 kHz at L1, 300 Hz at L2 and 50 Hz at L3. The rates were limited by the available algorithms at higher levels of the trigger and fine tuning of the electronics.

4.1.1 Level 1

At Level 1, trigger decisions are based on geometric cuts and coincidences consistent with electrons, muons and jets, using fast front-end output of the detectors. The calorimeters (CAL), muon scintillators (SC) and wire chambers (MDT and PDT), forward and central preshower detectors (FPS and CPS) and central fibre tracker (CFT) can all be used. The layout of the Level 1 (and Level 2) framework is shown in Fig. 4.1.

The trigger decisions made by each of the subdetectors are collectively known as “AND/OR” or L1 Framework terms and are combined into a global decision by the L1 framework. There are 256 L1 Framework bits available that can be dynamically assigned to trigger results from the L1 trigger detectors, the luminosity monitoring system and the L1 Framework itself. A typical L1 trigger is a coincidence (AND) of two or more L1 framework terms such as a deposit in the calorimeter and hits in the muon system. The framework supports 128 unique L1 trigger bits, each of which is preprogrammed to require a specific combination of AND/OR terms. Logic OR is supported as well as coincidences.

Each front-end crate has a pipeline to retain the data from 32 crossings. A series of field programmable gate arrays examines the list of terms from the luminosity monitors and the detector triggers to determine whether a specific L1 bit has been set. If so, the framework issues an accept and the event data is digitised and moved from the pipeline into a series of 16 event buffers to await a L2 trigger decision.

Level 1 calorimeter triggers

The calorimeters are used to trigger on jets or electromagnetically interacting (EM) objects (photons and electrons), based on energy deposits in the whole depth of the calorimeter or only in the first four layers, respectively. The trigger terms have the general form CJT(N, X) for jets and CEM(N, X) for EM objects, requiring N calorimeter towers with an energy deposit greater than X GeV. No hadronic tower energy veto is applied for CEM triggers used in this thesis. The trigger towers are 0.2×0.2 structures in (η, ϕ) space, consisting of 2×2 readout towers in the central region and 1×1 in the forward region, radially aligned with the centre of the detector (see Fig. 3.14). The L1 calorimeter triggers cover the range $|\eta| < 2.4$. Typical multi-jet trigger terms would require a combination of terms such as CJT(3,3)CJT(2,5), this example requiring the presence of three or more towers with E_T greater than 3 GeV, of which at least two must be above 5 GeV. The term used in this analysis is CJT(1,5), requiring a single tower above 5 GeV.

Level 1 muon triggers

The muon triggers at L1 can make use of both scintillator and wire hits in the muon system, as well as tracks in the central fibre tracker, to form L1 objects. These objects contain the p_T of the central (CFT) track, the η region and the object quality. The formed stubs are collected by the muon trigger crate manager and sent to the trigger framework. A L1 muon AND/OR term has the general form *muNptxRQxx*, where N is the number of muon candidates required above a p_T threshold indicated by ptx. The variable R indicates the region of the detector: a = all ($|\eta| < 2$), b = between ($1 < |\eta| < 2$), c = central ($|\eta| < 1$) and w = wide ($|\eta| < 1.5$). The quality requirement Q can take the values t (tight) or l (loose) and the final two characters are reserved for additional options (e.g. dimuon sign or mass, or restricting the hits to a single layer). The L1 muon term used in this thesis is *mu1ptxatxx*, requiring one tight muon in any region ($|\eta| < 2.0$) with no p_T threshold. The central tracker was not used; the *tight* quality selection requires both A- and BC-layer scintillator hits lying in the same region (forward or central) and octant of the detector. The times associated with the scintillator hits are required to lie within a programmable trigger gate. The hit time is calibrated such that a muon from a p$\overline{\text{p}}$ collision would hit the scintillator at $t = 0$. In the forward system, the gate is $|t| < 15$ ns. The A-layer gate in the central muon system is $|t_A| < 12$ ns; the BC-layer gate is $|t_{BC}| < 23$ ns. The BC-layer counters need a larger window because of their longer length and decay time, leading to a lower timing resolution. A small number of BC-layer counters have even wider timing gates to account for different geometric design as well as less-well measured resolutions.

Other triggers at Level 1

Aside from the muon system and the calorimeter, the central fibre tracker and the forward proton detector can also be used to trigger events at L1. Neither trigger was operational when the data presented in this thesis were taken.

Several additional terms are defined at Level 1, to enable selection of events based on the presence of beam crossings or of interactions (luminosity). These include the *AliveBX* ("Live Accelerator Beam Crossing"), which marks the window of time in which beam crossings may occur, *Afastz*, *ALMNorth* and *ALMSouth*. The *ALMNorth* and *ALMSouth* terms use the hodoscopes of luminosity monitor scintillation counters mounted on the front surfaces of the end calorimeters, signalling the presence of an event in the interaction region. *Afastz* compares the time difference between the summed north and south signals to distinguish between collisions and beam halo. The time difference between the north and south hits is also used to measure the z-position of the interaction; the *Afastz* modules have a resolution of 6.25 cm in z.

Zero Bias and Minimum Bias triggers

Triggers which do not rely on any specific "physics" terms can be employed to study some detector effects (including offset energy in the calorimeter, see Section 5.1.4) and effects of the triggers themselves. A "Zero Bias" trigger accepts every bunch crossing, regardless of whether or not an actual collision occurred. The Zero Bias trigger uses the *ALiveBX* L1 Framework term. A "Minimum Bias" trigger requires an inelastic collision in which both the proton and the antiproton break up. These events are triggered using the *AFastz* L1 Framework term.

Prescaling

Triggers whose accept rate would exceed the bandwidth assigned to them are prescaled by only activating the trigger once every *n* events, where *n* is the prescale factor. In this case, the L1 requirement will only be tested once every *n* events. In all other events, the specific trigger is not considered.

4.1.2 Level 2

The Level 2 trigger system is designed to further reduce the input rate from L1 to maximally 1 kHz, within, on average, 100 μs decision time, and introducing less than 5% dead time. The L2 trigger operates in two stages. The first stage or preprocessor stage prepares data from each L1 trigger for use in the second or global processor stage. The global processor combines objects from the L2 preprocessors to make a trigger decision. Data flow is simplified by 16 buffers in front of each transfer point in the system.

Specific L2 triggers run only on specific L1 accepts; the L2 muon triggers are run only when a L1 muon trigger has fired, for example. The relations between L1 and L2 trigger elements are shown in Fig. 4.1.

In the preprocessor phase, each detector system separately builds a list of trigger information. Individual preprocessors are used for the calorimeter, fibre tracker, muon system, and the preshower detectors. A separate preprocessor, the Silicon Track Trigger (STT), is being designed to use information from the silicon microstrip tracker to signal tracks consistent with long-lived particles, in much the same way as described in Chapter 6.

Each preprocessor combines information from the L1 framework with additional detector information to form improved trigger objects such as energy clusters or tracks. The time required for the formation of preprocessor objects is about 50 μs.

The global processor makes a final L2 trigger decisions within 75 μs (much of the average total decision time of 100 μs available for the L2 trigger is taken up by the preprocessor stage.) The decisions are based on correlations among multiple detector systems. For example, spatial correlations between track segments, preshower depositions and calorimeter energy depositions may be used to select electron candidates. As at Level 1, 128 pass/fail bits can be configured to select events. The global processor reports the result to the L2 framework. The framework, using the same FPGA logic as the L1 framework, coordinates the operation of L2 and reports the trigger decisions to Level 3.

Level 2 calorimeter triggers

All the Level 2 calorimeter algorithms use a low-threshold reference set of L1 trigger towers as input for clustering. L2 calorimeter objects are formed by adding the energy of adjacent towers in a 3×3 grid around the seed tower. (The grid size was changed to 5×5 after the data presented in this thesis were taken.)

A complete L2 jet trigger requires N jets with transverse energy E_T greater than *Y* GeV and is denoted L2J(*N,Y*). No merging or splitting (see Section 5.1.1) of these (0.6×0.6 in η, ϕ) jets can take place, due to time constraints.

A missing transverse energy ($\not{E}_T$) algorithm returns a vector sum of all tower E_T values and may apply a variety of threshold and fiducial cuts in the calculation.

No Level 2 jet selection was used for the acquisition of the data presented in this thesis. The efficiency of jet triggers at Level 2 has been studied in [97].

Level 2 EM Triggers

In addition to the total cluster energy, the Level 2 EM trigger computes the following quantities:

- E_T^{EM}, the sum of the energy contained in the first four layers of the seed tower and the highest-E_T tower among the four nearest neighbours;
- E_T^{Tot}, the sum of the energy contained in all layers of the seed tower and the highest-E_T nearest neighbour.

Cuts are then applied on E_T^{EM}, the fraction of energy deposited in the first four layers E_T^{EM}/E_T^{Tot} and on the isolation, the total energy deposit in the two leading towers (E_T^{Tot}) divided by the total energy deposited in the 3×3 cluster. A matched central track and matching preshower hits can also be required. No Level 2 EM triggers were used in this thesis.

Level 2 muon Triggers

At Level 2, the muon candidates are improved by using calibration and more precise timing information. The L2 muon preprocessor receives the L1 muon output and uses most of the information available from the muon system: timing from the forward and central scintillators and the central drift tubes (PDTs), as well as the hit information from the forward drift tubes (MDTs). A quality is assigned to the muon candidates found and the transverse momentum is extracted from the kink of the tracks in the toroidal magnetic field.

Muon tracks are formed separately for the A and the B+C layers. The resulting “stubs” are matched into muon objects if the A- and BC- stub line up within a geographical window of $\Delta\eta < 0.3$ and $\Delta\phi < \pi/4$. If a stub in either the A- or BC- layer cannot be matched to a stub in the complementary layers, the stub itself becomes a L2 muon object of lowest quality. The quality of “matched” L2 muon objects is based on the number of hits in A- and BC-stubs. The L2 muon trigger mu(1,med,0.) is used in this thesis, requiring a single muon of medium quality with no p_T threshold.

The *medium* qualification requires in the forward region ($|\eta| > 1$):

- An A-layer stub with hits in two MDT planes AND a matching scintillator hit, OR hits in three or more MDT planes. If the stub has hits in only two planes, the other two planes are not allowed to have any hits near this stub;
- A B-, C- or B/C layer stub with hits in at least two MDT planes in either of the two layers,

and in the central region ($|\eta| < 1$):

- Three or more PDT wire hits in the A-layer with a valid hit pattern in the reconstruction look-up table;
- Three or more PDT wire hits in layers B and C with a valid hit pattern (the hits may be contained in a single layer or spread between the two).

The requirements for *loose* and *tight* L2 muons are summarised in [98].

4.1.3 Level 3

Upon receipt of a L2 accept from the global processor, L3 initiates a full detector readout and moves the event data into eight transfer buffers. The data are reconstructed on a processor farm and filtered with a suite of “physics tools”, which have access to all the data in the event to search for electron, muon and jet candidates. The output of these tools is used by a set of filters to select interesting event topologies. Like at Level 2, specific Level 3 filters run only on certain L1/L2 accepts. The system has a maximum event input rate of 1 kHz and up to 50 Hz accept rate. It is characterised by parallel data paths (“switches”) which transfer data from the front-end crates to a farm of processors. Any event meeting the L3 filter requirements will be transferred to tape storage for later offline reconstruction. Available triggers include jet, electron, muon and track triggers as well as harder to identify objects such as τ leptons.

Level 3 jet triggers

A list of towers with energy deposits sorted by E_T is used to define Level 3 jets using a simple cone algorithm [99]:

1. Define a list of seeds, initialised with the highest E_T tower above threshold;
2. Calculate $\Delta R = \sqrt{\Delta\phi^2 + \Delta\eta^2}$ between the highest E_T unassigned tower and the seeds;
3. Add the tower to the first seed in the list with $\Delta R < R_{cone}$;
4. If there is no match, add the tower to the list of seeds as a new entry;
5. Proceed with 2. until all towers above threshold are processed.

The jet centroid position is calculated as the energy-weighted sum of the jet's tower positions.

Level 3 jet trigger names are constructed as "jet(N,X)", requiring N jets with $E_T > X$ GeV.

The specific Level 3 jet trigger used for this analysis required a single jet with $E_T > 20$ GeV in the region $|\eta| < 3$. The adjustable cone size and seed threshold energy were $R_{cone} = 0.7$ and $E_T > 0.5$ GeV, respectively. The jet direction was calculated using the centre of the detector rather than a reconstructed primary vertex.

Comparing the Level 3 jets to Monte Carlo simple cone jets, the reconstructed energy was found to be about 20% lower than the true Monte Carlo jet energy, which is in agreement with what is observed for the offline reconstruction (see section 5.1.4).

Level 3 electron triggers

At Level 3, electrons are identified by the shape of their energy deposition in the calorimeter. In addition, a matching track or matching preshower hits may be required.

Calorimeter energy deposits are clustered using the same simple cone algorithm used by the Level 3 jet algorithm. Cuts are then applied on the total energy of the cluster, the fraction of the energy deposited in the first four layers of the calorimeter, and on the transverse shape of the shower. The cone size used to cluster the energy deposits is 0.4 (in $\eta \times \phi$-space) for all Level 3 EM triggers used in this thesis.

The only requirement for a "very loose" Level 3 electron is that the fraction of energy deposited in the EM layers of the calorimeter (*EMF*) is at least 0.8; "loose" electrons must have *EMF* > 0.9.

A Level 3 electron trigger term is denoted as "ele(N,X,sh/vl)", requiring N "loose" electron objects of at least X GeV transverse energy. The optional third argument indicates additional cuts on the transverse shower shape ("sh") or relaxation of the "loose" requirement to "very loose" ("vl").

The additional "shower shape" cut requires a width of less than (0.09, 0.08, 0.05) in the first three calorimeter layers, respectively.

4.1.4 Complete trigger terms

The overall trigger name covers the requirements at all three levels for that specific combination of L1, L2 and L3 triggers. The names aim to describe the requirements at all three levels. The MU_JT20_L2M0 trigger, for instance, requires a coincidence of a muon and a jet trigger term at Level 1, a refinement of the muon trigger at Level 2 and a 20 GeV jet cluster at Level 3. This trigger is designed to select heavy quark jets, using the muon decay mode of heavy quarks as described in Section 2.5. The "trigger list" of active triggers that are used to filter collision data can be modified to reflect physics interests and to acquire data samples for specific studies.

At levels 2 and 3, "Mark And Pass" filters are available in addition to the specific trigger requirements. The Mark And Pass filter is assigned to a specific trigger name and accepts every event that passes the requirement of the previous levels. A Mark And Pass filter at L3 will accept all events fulfilling the L1 and L2 requirements of that trigger. The result of the corresponding L3 trigger is also recorded. The Mark And Pass filters are typically set to accept only one in every *n* events and are used to study the efficiencies of the L3 filters.

4.2 Efficiency of the muon plus jets trigger

The trigger used for the selection of data used in this thesis is called MU_JT20_L20 and requires the presence of a jet and a muon in the event. The L1, L2 and L3 terms are:

- Level 1: mu1ptxatxx_CJT5;
- Level 2: mu(1,med,0.);
- Level 3: jet(1,20.).

The L1 term requires a single "tight" muon in the region $|\eta| < 2.0$ and a tower with 5 GeV transverse energy. The muon and jet requirements are refined at L2 and L3, respectively. The individual terms, their efficiencies and the overall efficiency for objects passing offline selection criteria are discussed in the following sections.

Since this thesis concerns an exclusive measurement of angular correlations, the overall efficiencies of the triggers are of less importance than the dependence of the efficiency on the kinematic variables of the objects. Dependence of the triggers on the E_T and p_T of the jet and the muon, and on their pseudorapidity η, affects the selection of events in the final data sample. Any ϕ dependence of the jet trigger will bias the angular correlation measurement itself.

4.2.1 Efficiency of Level 1 terms

Assuming the muon and jet triggers at L1 are uncorrelated, the efficiency of the L1 mu1ptxatxx and CJT5 triggers can be calculated separately. In fact, correlations may arise from punch-through of jet particles through the calorimeter (leading to a false muon signal) or by energy deposition above threshold of a muon in the calorimeter. The correlations turn out to be insignificant and are discussed at the end of this section. In both the muon and the jet case, the efficiency can be determined by studying the L1 AND/OR bits in a reference sample that has been selected with a different trigger.

Level 1 muon efficiency

The efficiency for the mu1ptxatxx trigger is determined from a sample of events that has been selected with jet and EM triggers and in which an offline reconstructed muon is present. The trigger requires a scintillator hit in both the A- and in the B- or C- layer. The muon was required to have at least one scintillator hit and two wire hits in the A layer and at least one scintillator hit and three wire hits in the BC-layers, and a converging fit of the two segments. (The same requirements are used to select muons in Chapters 5-7.) If a segment was shared by more than one muon track, the track with the lowest fit χ^2 was selected. In only 6% of the events a second muon meeting these requirements that did not share any segments with the selected muon was found; these events were discarded.

Cosmic muons with scintillator hit times outside the trigger gate may still be reconstructed offline. The contribution of cosmic muons is estimated by looking at the offline scintillator hit time distributions. The time distributions of hits in the A- and BC-layers of the muon system for

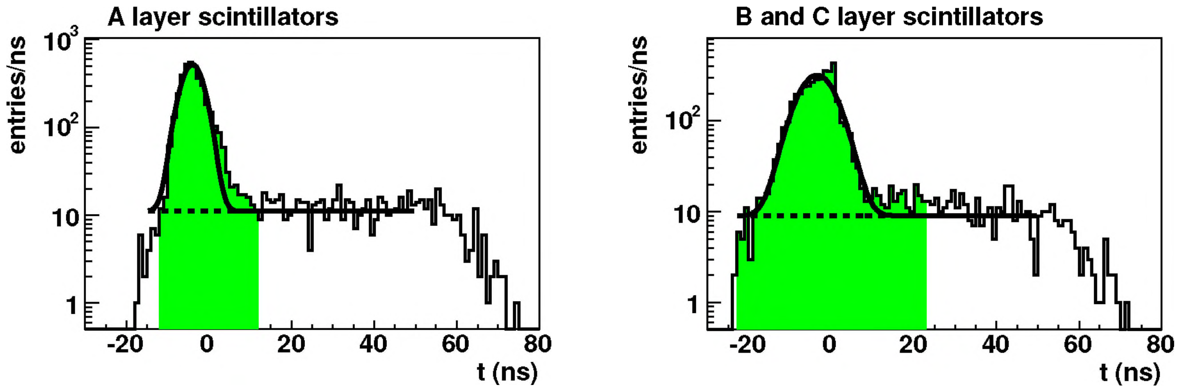

Figure 4.2: Scintillator hit timing distributions for good offline muons in the central region. The shaded bands indicate the trigger gate.

p_T (GeV/c)	$f_{cosmics}$	$f_{cosmics}(\lvert t_A\rvert > gate_A \vee \lvert t_{BC}\rvert > gate_{BC})$
$p_T < 6$	$(8.4 \pm 0.2)\%$	$(4.2 \pm 0.2)\%$
$6 < p_T < 10$	$(11.5 \pm 0.3)\%$	$(6.7 \pm 0.4)\%$
$10 < p_T < 15$	$(20.3 \pm 0.7)\%$	$(11.1 \pm 0.8)\%$
$15 > p_T > 20$	$(28 \pm 1)\%$	$(17 \pm 2)\%$
$20 < p_T < 30$	$(40 \pm 1)\%$	$(31 \pm 2)\%$
$p_T > 30$	$(57 \pm 1)\%$	$(44 \pm 2)\%$
$p_T > 6$	$(22.9 \pm 0.4)\%$	$(16.4 \pm 0.4)\%$

Table 4.1: Contribution of cosmic muons in the central region. The middle column shows the total estimated fraction of cosmic muons in the sample. The right column shows the estimated fraction of cosmic muons with at least one hit time outside the trigger gate.

central muons ($|\eta| < 1$) are shown in Fig. 4.2. The trigger windows are indicated by the shaded regions.

The distributions are fitted with the sum of a Gaussian function and a horizontal line, describing the hit time distributions for signal muons and cosmic muons, respectively. The number of signal muons is determined by integrating the Gaussian part of the fit function. The remaining muons are deemed to be cosmic muons. The overall fraction of cosmic muons is determined as the average of the A- and BC-layer results. The number of cosmic muons with hit times outside the trigger gate is determined by counting the total number of muons with hit times outside the gate and subtracting the number of signal muons with hit times outside the gate, as given by the fit.

The fraction of cosmic muons depends strongly on the transverse momentum of the muons. The fraction was therefore estimated in several bins of muon p_T. The results per bin are given in Tables 4.1 and 4.2. Other than the difference between the central and forward muon systems, no dependence on η was found.

The efficiency of the L1 muon trigger is then measured by looking at the L1 Framework bit for

p_T (GeV/c)	$f_{cosmics}$	$f_{cosmics}(\|t_A\| > gate_A \vee \|t_{BC}\| > gate_{BC})$
$p_T < 6$	$(1.69 \pm 0.07)\%$	$(0.96 \pm 0.08)\%$
$6 < p_T < 10$	$(3.0 \pm 0.2)\%$	$(1.6 \pm 0.2)\%$
$10 < p_T < 15$	$(6.9 \pm 0.6)\%$	$(3.4 \pm 0.6)\%$
$15 > p_T > 20$	$(20 \pm 1)\%$	$(13 \pm 2)\%$
$20 < p_T < 30$	$(29 \pm 2)\%$	$(19 \pm 2)\%$
$p_T > 30$	$(52 \pm 2)\%$	$(35 \pm 2)\%$
$p_T > 6$	$(10.4 \pm 0.4)\%$	$(7.4 \pm 0.4)\%$

Table 4.2: Contribution of cosmic muons in the forward region.

the mu1ptxatxx term and is defined as:

$$\epsilon = \frac{N(\mu;\text{ mu1ptxatxx set})}{N(\mu) - N(\text{cosmics})}$$

where $N(\mu;$ mu1ptxatxx set$)$ is the number of events with an offline muon in which the mu1ptxatxx trigger bit is set, $N(\mu)$ is the number of events in which an offline muon is present and $N(\text{cosmics})$ is the estimated number of events with a cosmic muon with scintillator hit times outside the trigger gate.

The efficiency is plotted as a function of the p_T, η and ϕ of the offline muon in Fig. 4.3. The bottom region of the detector ($|\eta| < 1.1$ and $4.25 < \phi < 5.15$), which has reduced detector coverage (see Section 3.8.1), is excluded from the efficiency measurements. The integrated efficiency for muons with $p_T > 6$ GeV/c is $(99.4 \pm 0.4(\text{stat}) \pm 0.5(\text{cosmics}))\%$ in the central region and $(96.2 \pm 0.5(\text{stat}) \pm 0.4(\text{cosmics}))\%$ in the forward region.

Level 1 jet efficiency

The efficiency of the L1 jet trigger is determined from a data sample selected with muon triggers with no jet requirements. An offline jet passing "good" quality cuts was required in each event. The cuts were on the fractions of energy deposited in the electromagnetic (*EMF*) and coarse hadronic (*CHF*) (outer) layers of the calorimeter; the ratio of the energy contained in the hottest tower to the next hottest tower *HotF*; and on the number (n_{90}) and fraction (f_{90}) of towers totalling 90% of the total energy. The efficiency is then defined as the fraction of events in which the jet trigger L1 AND/OR term CJT(1,5) was set:

$$\epsilon = \frac{N(\text{jet;CJT(1,5) set})}{N(\text{jet})}$$

where N(jet) is the number of events with at least one good jet and N(jet;CJT(1,5) set) is the number of events in which the trigger bit was set.

The efficiency is measured as a function of the scale corrected E_T, η and ϕ of the leading-E_T jet in the event. Especially at lower values of the E_T of the leading jet, the trigger may have been fired by another jet in the event. The quoted efficiency is therefore an "event efficiency" rather than the true jet efficiency. The jet efficiency can be measured by taking the additional jets into account

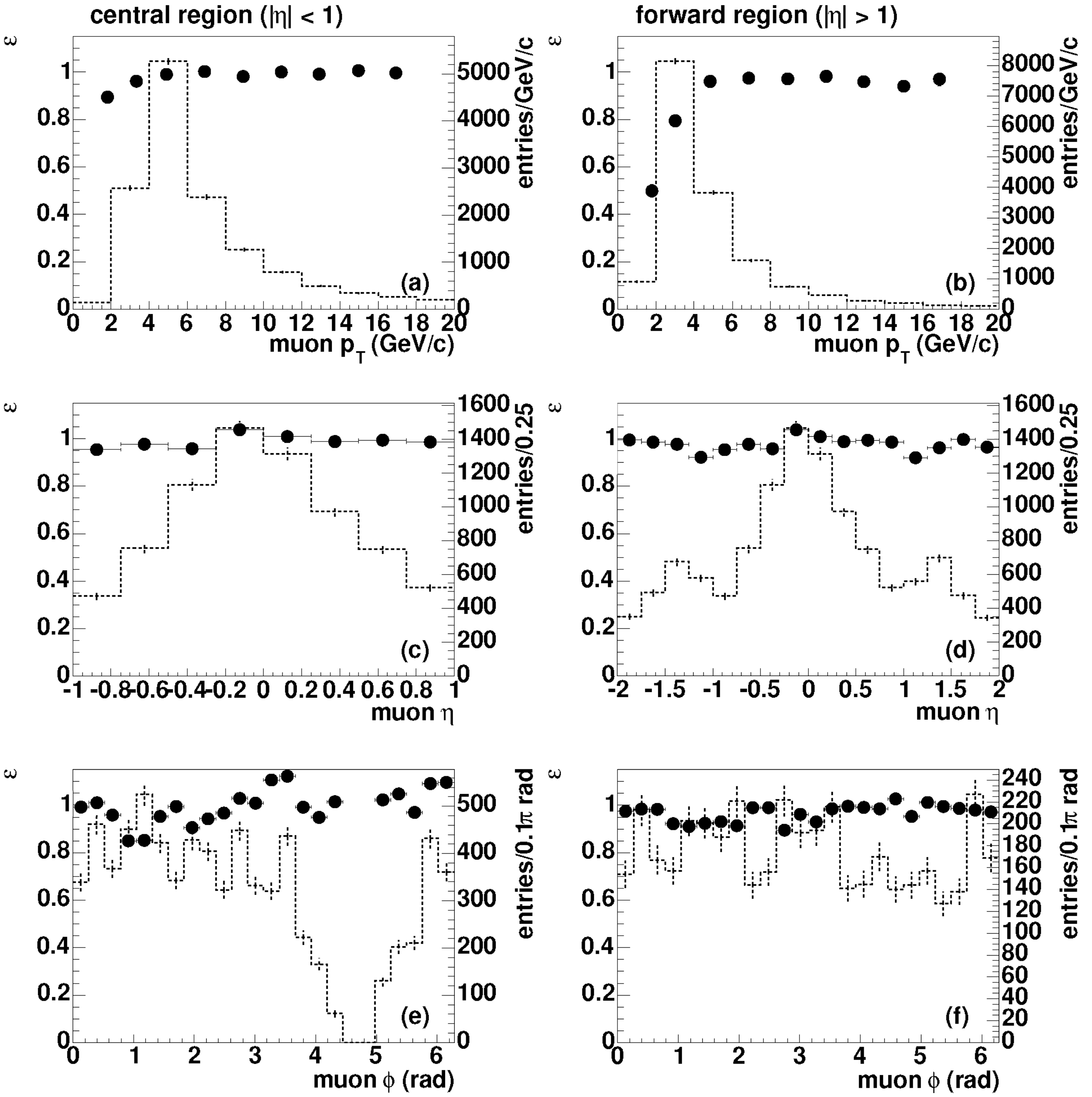

Figure 4.3: Efficiency of the Level 1 muon trigger as a function of muon p_T, η and ϕ for central (left) and forward (right) muons. The dashed histograms show the distribution of offline muons.

or by looking for the Level 1 energies of the towers associated with each jet. This last approach has been used in [97].

A low online zero-suppression threshold leads to additional noise jets characterised by energy distributed over many towers (see Section 5.1.5). Even after the cut on $f_{90} < 0.8 - 0.5 \times CHF$, a large number of these jets remain. The L1 jet trigger, requiring at least one tower with relatively high E_T, is inefficient for these noise jets. To determine the efficiency for good jets, the cut on f_{90} was tightened to $f_{90} < 0.6$ for the determination of the trigger efficiency only.

	central region	forward region
p_0	24.4 ± 0.1	24.6 ± 0.2
p_1	2.44 ± 0.04	2.80 ± 0.07
p_2	0.988 ± 0.004	0.997 ± 0.006
χ^2_λ/ndf^1	$50.8/22$	$18.8/22$

Table 4.3: Parameters of the fit (Eq. 4.1) to the L1 jet trigger efficiency as a function of jet E_T (Fig. 4.4).

Because this cut is tighter than the nominal offline cut, a bias may be introduced in the trigger efficiency. The noisy jets are somewhat clustered in (η, ϕ). To estimate the bias, the noisiest regions were removed by hand and the efficiency and turn-on were determined with and without the $f_{90} < 0.6$ cut. The difference between the two measurements was taken as an uncertainty on the low side of the efficiency. The efficiency is plotted in Fig. 4.4, as a function of the energy scale corrected jet E_T (see Section 5.1.4), and as a function of the η and ϕ coordinates of the leading jet, for the complete sample as well as for jets with $E_T > 20$ GeV. The trigger is more than 98% efficient for jets with $E_T > 55$ GeV in the central region and above $E_T > 56$ GeV in the forward region. In Fig. 4.4(2), an excess of jets can be seen found for $3.4 < \phi < 3.8$. These jets are probably noise jets that are reconstructed offline but do not cause the trigger to fire. This leads to an underestimation of the trigger efficiency in the same bin.

The turn-on as a function of jet E_T is parametrised as

$$\epsilon = \frac{p_2}{2}\left(1 + \mathrm{erf}\left(\frac{E_T - p_0}{p_1\sqrt{E_T}}\right)\right). \tag{4.1}$$

The resulting parameters of the fit are shown in Table 4.3. The efficiency for jets with (energy scale corrected) $E_T > 20$ GeV in the central region is (63.2±0.4)%.

The parametrisation is only used to give an indication of the efficiency and turn-on curve; therefore, no systematic uncertainty due to the choice of parametrisation is given.

Correlation of L1 trigger terms

Correlations between the L1 muon and jet triggers may arise from two sources:

1. Punch-through of particles in a jet can cause hits in the muon system which may fire the trigger;
2. The energy deposition of muons in the calorimeter may be large enough to fire the jet trigger.

Since any particle inside a jet that punches through the calorimeter with enough energy to cause the Level 1 muon trigger to fire is indistinguishable from a real muon offline, the first correlation becomes irrelevant. The fake muons arising from this effect are taken into account at a later stage, when the fraction of b-flavoured jets is extracted from a sample of jets with associated muons.

---

[1] The goodness-of-fit parameter χ^2_λ is defined as $\chi^2_\lambda = -2\ln(\lambda)$, where λ is the likelihood ratio (see Appendix A).

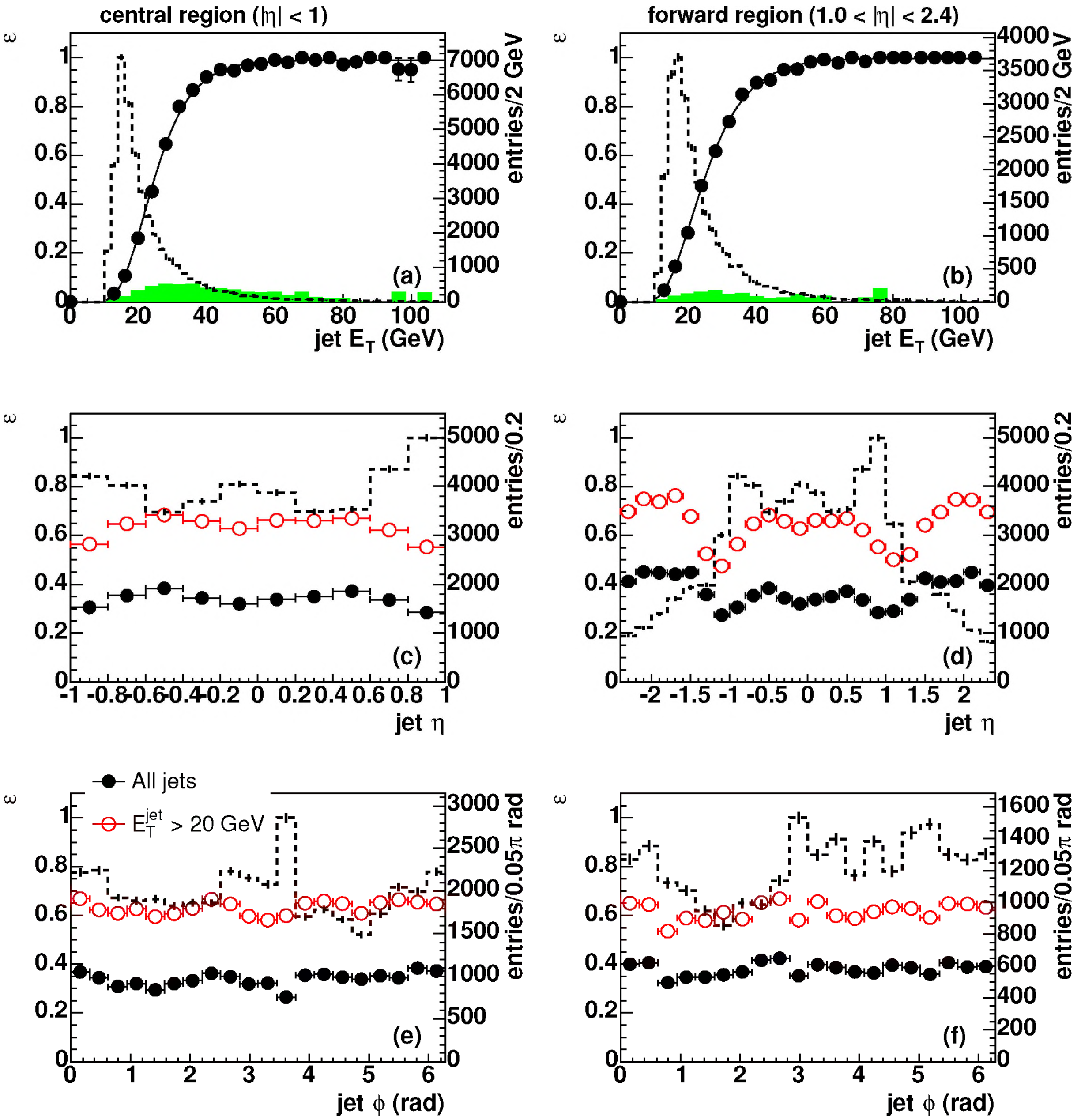

Figure 4.4: Efficiency of the Level 1 jet trigger as a function of E_T, η and ϕ of the leading jet in the event. The solid points show the efficiency for all jets. The open circles show the efficiency for jets with $E_T > 20$ GeV. The dashed curves indicate the offline distributions of jets in the sample. The shaded histogram in plots (a) and (b) indicates the systematic uncertainty due to the $f_{90} < 0.6$ cut.

To study the correlation due to the second effect, the energy deposition of isolated muons in the calorimeter was studied [100]. Only $(0.23 \pm 0.03)\%$ of all muons caused an energy deposit of more than 5 GeV in a 3×3 grid of towers. Since the jet trigger requires a 5 GeV deposit in a single tower, this fraction is an overestimate of the fraction of muons that will cause the jet trigger to fire. If the muon is near a jet, however, even a lower energy deposit may cause a tower that is already near threshold to exceed the 5 GeV threshold and fire the trigger.

To exclude any possible bias from the muon on the jet trigger, the jet trigger efficiency is determined separately for jets with an associated muon. The muon was not taken into account in the energy correction. The resulting efficiency for jets with an associated muon was compatible with that for jets without a matched muon, showing that the presence of a muon does not affect the jet trigger in a significant way.

4.2.2 Efficiency of the Level 2 muon trigger

The efficiency of the L2 muon trigger is determined from a sample selected with a trigger that has the same Level 1 requirements as the MU_JT20_L2M0 trigger but has no requirements at levels 2 and 3 and is therefore essentially a "Mark And Pass" filter for the L2 muon term. This trigger is known by the codename mu1ptxatxx_CJT5.

The output of the L2 muon trigger system can be studied off line. The efficiency is defined as the probability to match an offline reconstructed muon to a Level 2 muon of medium quality. The separation between L2 muons and offline muons is shown in Fig. 4.5. Level 2 muons are required to be closer to an offline muon than the octant size, $\Delta\phi < \pi/4$, and closer than $\Delta\eta < 0.7$ in η. The efficiency is then defined as:

$$\epsilon = \frac{N(\mu;\text{matched L2 }\mu)}{N(\mu)}$$

where $N(\mu)$ is the number of events with a tight offline muon and $N(\mu;\text{matched L2 }\mu)$ is the number of events in which a medium L2 muon is matched to the offline muon.

After the L1 scintillator hit requirement, very few out-of-gate cosmic muons remain. In addition, a matching scintillator hit is only required for central medium Level 2 muons if wire hits are found in fewer than three A-layer MDT planes. Since fewer than 0.1% of all central medium muons fail this requirement, the contribution of cosmic muons becomes irrelevant for the determination of the trigger efficiency.

The efficiency is plotted as a function of p_T, η and ϕ of the offline muon in Fig. 4.6 for the central muon system and the forward muon system separately. For muons with $p_T > 6$ GeV, the efficiency as determined by a straight line fit is (92.0±0.6)% in the central region and (89.8±0.8)% in the forward region.

A bias may be introduced by the somewhat arbitrary matching parameter $\Delta\eta$. Matching the offline and online muons in ϕ only, the efficiency for muons with $p_T > 6$ GeV is $(92.4\pm0.6)\%$ and $(91.3\pm0.7)\%$ in the central and forward region, respectively. The larger discrepancy in the forward region can be explained by the lower η resolution at high η, as a result of the "compression" of that angle.

4.2.3 Efficiency of the Level 3 jet trigger

The efficiency of the Level 3 jet trigger is studied using events that have been selected with the "Mark and Pass" filter for the MU_JT20_L2M0 trigger. Events that have been selected in this way

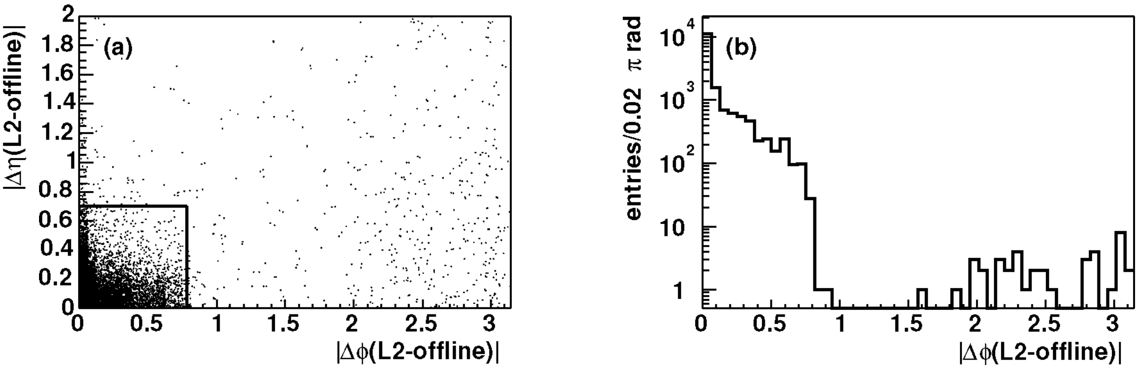

Figure 4.5: (a) (η, ϕ) and (b) azimuthal separation between a tight offline muon and the closest Level 2 muon.

meet all the requirements of the L1 and L2 triggers, so the efficiency of the L3 term *after* L1 and L2 requirements can be measured by counting the number of events in which the trigger actually fired, given an offline reconstructed good jet. The resulting turn-on curve and η and ϕ dependence of the L3 jet(1,20.) jet trigger have been plotted in Fig. 4.7, for the complete sample as well as for jets with $E_T > 20$ GeV. The calorimeter-only scale corrected jet energy was used.

As for the Level 1 jet trigger, this efficiency does not take into account additional jets in the event and is therefore an "event efficiency" rather than the true jet efficiency.

The L3 jet trigger efficiency dependence on the jet E_T is parametrised as

$$\epsilon = \frac{p_2}{2}\left(1 + \mathrm{erf}\left(\frac{E_T - p_0}{p_1\sqrt{E_T}}\right)\right) + p_3, \qquad (4.2)$$

where the mean transverse energy in each bin was taken as the E_T for that bin. The parameters of the fit are given in Table 4.4. The algorithm is 99% efficient for jets with $E_T > 39$ GeV in the central region ($|\eta| < 1$) and $E_T > 44$ GeV in the forward region ($1 < |\eta| < 3$). The efficiency for jets with $E_T > 20$ GeV in the central region is (72.2±0.5)%.

The algorithm is slightly efficient even for very low energy jets. The offset is caused by the presence of bad jets in the sample which are removed by jet quality cuts and are therefore not taken into account in the efficiency calculation. Most of these jets are the result of many noisy towers (see Section 5.1.5.) These "noise jets" may still accumulate enough energy at L3 to cause the trigger to fire.

4.2.4 Overall efficiency of MU_JT20_L2M0

Since the efficiencies at each level of the trigger are determined given that the requirements of all previous levels were satisfied, the overall trigger efficiency can simply be determined as

$$\epsilon_{trigger} = \epsilon^{\mu}_{L1} \times \epsilon^{jet}_{L1} \times \epsilon^{\mu}_{L2} \times \epsilon^{jet}_{L3}.$$

The efficiencies of the four triggers for jets with $E_T > 20$ GeV and muons with $p_T > 6$ GeV, both in the central region ($|\eta| < 1$) are listed in Table 4.5. The overall efficiency for an event

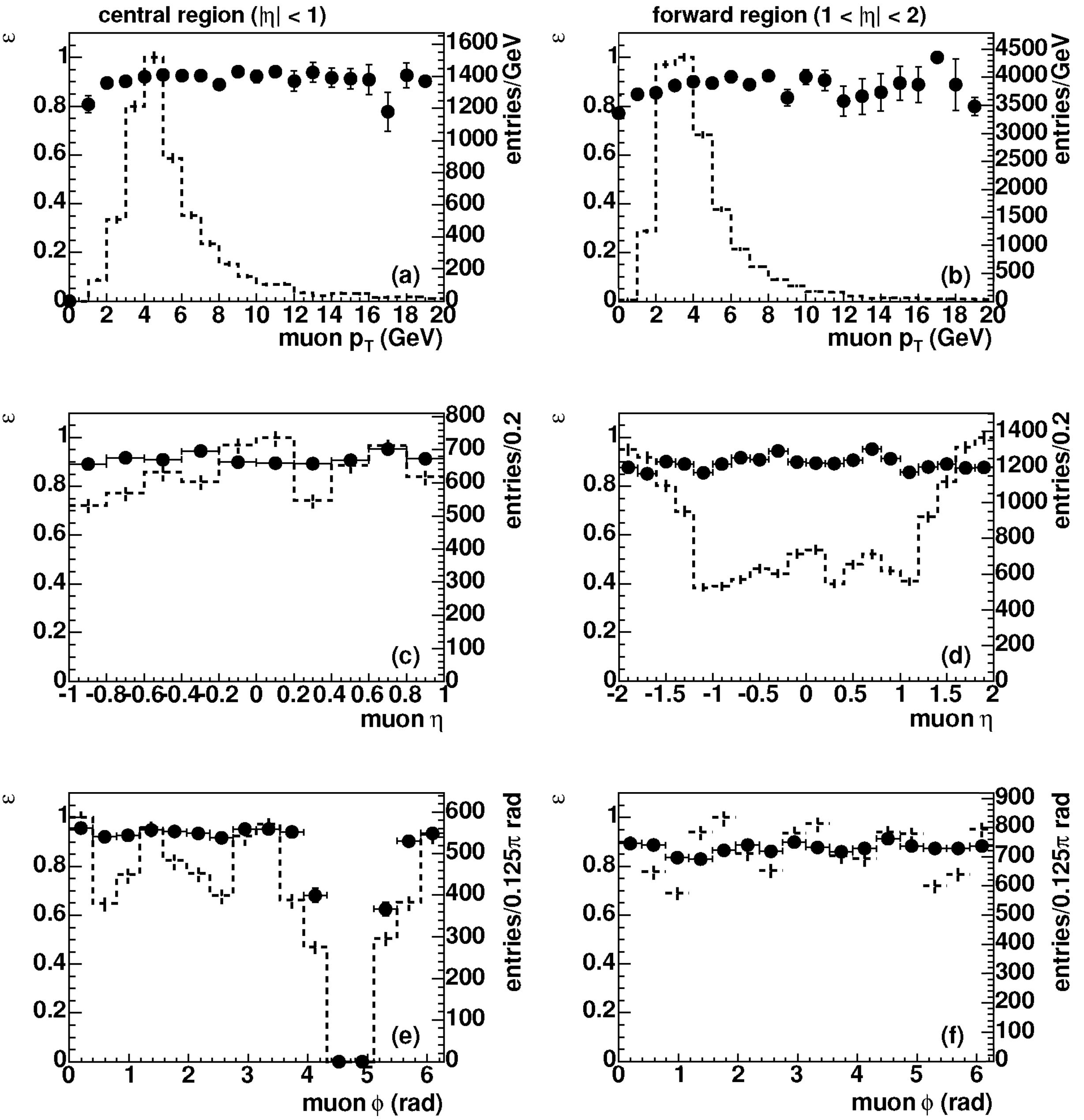

Figure 4.6: Efficiency of the Level 2 muon trigger as a function of muon p_T, η and ϕ in the central (left) and forward (right) muon systems (black points with error bars). The dashed histograms show the distributions for all offline muons.

with a muon and jet passing these requirements is (41±1)%. The turn-on curve for such events as a function of the leading jet E_T is shown in Fig. 4.8. The error bars cover all the statistical and systematic uncertainties discussed in the previous sections.

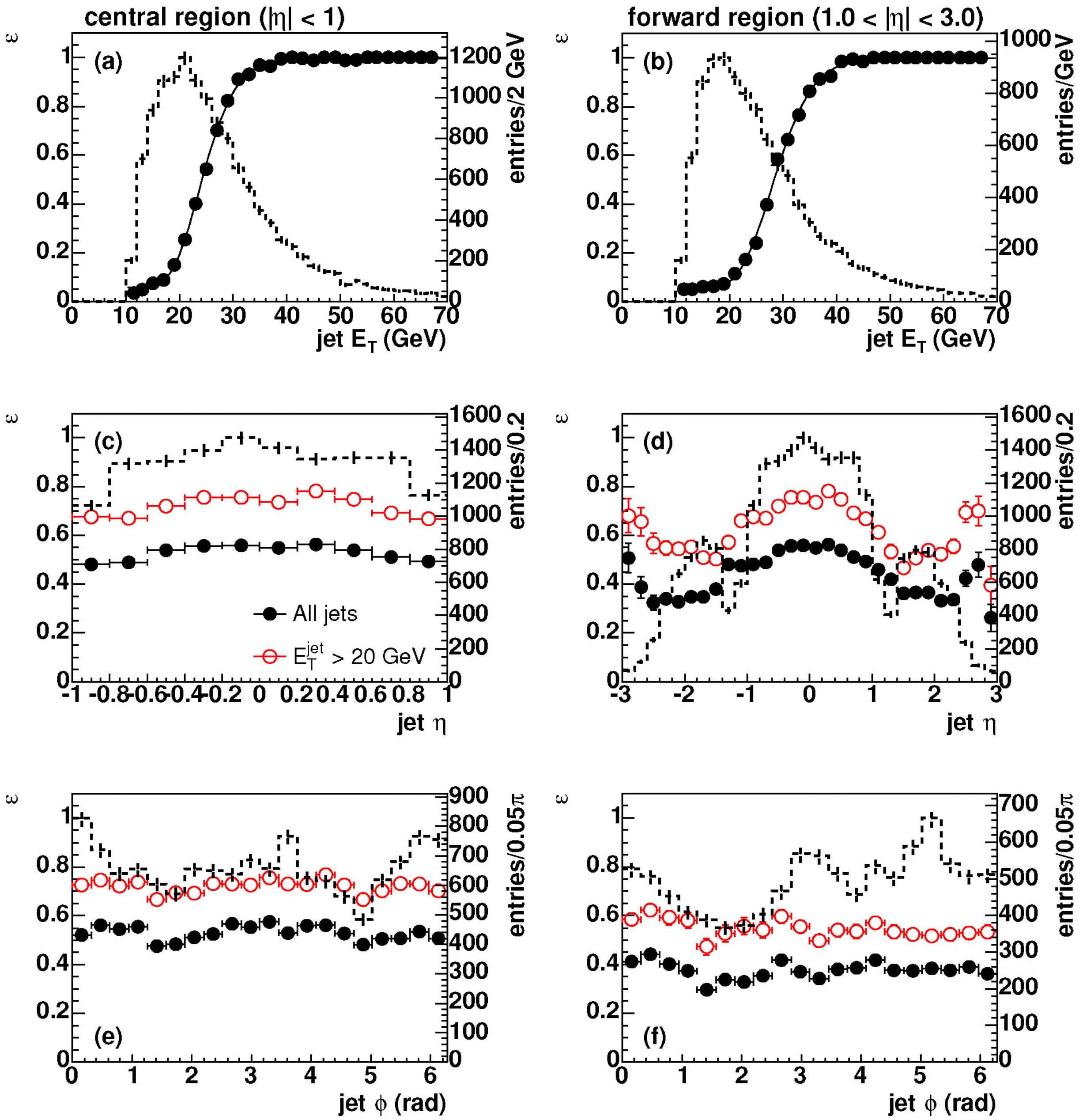

Figure 4.7: Efficiency of the Level 3 jet trigger as a function of E_T, η and ϕ of the leading jet in the event. The solid points show the efficiency for all jets. The open circles show the efficiency for jets with $E_T > 20$ GeV. The dashed histograms show the distribution of the leading offline-reconstructed jet.

	central region	forward region
p_0	24.6 ± 0.3	28.8 ± 0.2
p_1	1.36 ± 0.10	1.42 ± 0.05
p_2	0.94 ± 0.03	0.939 ± 0.001
p_3	0.06 ± 0.03	0.059 ± 0.001
χ^2_λ/ndf	$30.0/26$	$20.7/26$

Table 4.4: Values of the parametrisation of the Level 3 jet efficiency in the central ($|\eta| < 1$) and forward ($1 < |\eta| < 3$) regions of the calorimeter.

Trigger term	Efficiency
ϵ^{μ}_{L1}	$(99.4 \pm 0.6)\%$
ϵ^{jet}_{L1}	$(63.2 \pm 0.4)\%$
ϵ^{μ}_{L2}	$(92.0 \pm 0.6)\%$
ϵ^{jet}_{L3}	$(72.2 \pm 0.5)\%$
ϵ(MU_JT20_L2M0)	$(41 \pm 1)\%$

Table 4.5: Efficiency of the MU_JT20_L2M0 trigger for jets with $E_T > 20$ GeV and muons with $p_T > 6$ GeV in the central region.

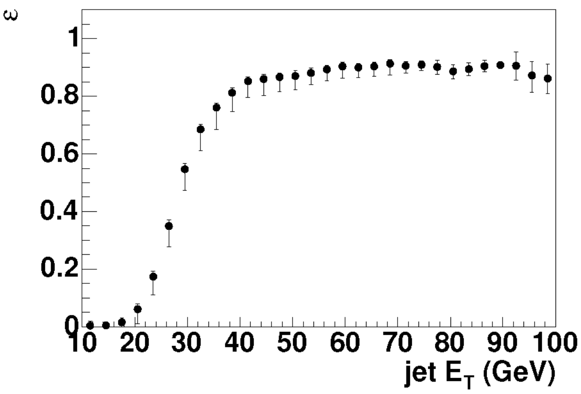

Figure 4.8: Overall trigger efficiency for events with a central muon ($p_T > 6$ GeV/c) and jet as a function of jet E_T.

Chapter 5

Data reconstruction

The partons produced in the primary interaction are never observed directly. Instead, their properties are reconstructed from their energy deposits in the detector.

In the tracking detectors, ionisation by charged particles passing through the detector material leads to small electrical signals which are digitised and recorded as hits. The hits are combined by tracking algorithms to reconstruct the trajectory of the particle. Combining all tracks in the event, the location of the primary interaction vertex can be determined.

Most particles — muons and neutrinos being the notable exceptions — deposit all their remaining energy in the calorimeter. The energy deposits are clustered by the jet reconstruction algorithm.

The reconstruction algorithms used to find tracks, jets, vertices, muons, photons and electrons are presented and their efficiencies and resolutions are discussed. The focus will be on jets, tracks and muons in the central region ($|\eta| < 1$), which will be used to identify b flavoured events in Chapter 7.

5.1 Jet reconstruction

The hadronisation and decay of quarks and gluons produced in a collision lead to collimated “jets” of particles pointing back to the original particles produced in the primary interaction. Hadronisation describes the emission and absorption of gluons by partons in the final phase of the collision and quark pair production from the gluons. The gluons and quarks all carry colour charge; during the hadronisation process, they are combined to form colourless hadrons.

At the particle level, a jet is defined as a collection of particles originating from the fragmentation and hadronisation processes. The true particle jet will never be observed in this form because it gets distorted when it interacts with the calorimeter material.

At reconstruction level, a jet is an object formed by clustering associating nearby energy deposits in the detector, in DØ in the calorimeter (although jets can also be made from tracks).

Several clustering algorithms are available. Ideally, the algorithm should be applicable to both Monte Carlo particle jets and detector jets, and the detector jet should give a known representation of the particle jet.

5.1.1 Jet reconstruction algorithm

In DØ jets are reconstructed from energy deposits by particles showering in the calorimeter, using the Improved Legacy Cone Algorithm [101]. Cone algorithms form jets by associating together particles whose trajectories or energy deposits lie within a circle of fixed radius R in $(\eta \times \phi)$ space around the jet axis.

In DØ the energy deposited by particles is recorded by calorimeter cells which the algorithm treats as massless particles with four-momenta

$$p_{\text{cell}} = E_{\text{cell}}(1, \vec{n}), \tag{5.1}$$

where $\vec{n}$ is the unit direction vector from the interaction point (the event primary vertex). The cell four-momenta are summed in towers with a size of 0.1×0.1 in $(\eta \times \phi)$ space, according to the transverse segmentation of the calorimeter (see Fig. 3.14). Jet reconstruction then proceeds according to the following steps:

1. Starting from the highest p_T tower with $p_T^{\text{tower}} > 0.5$ GeV$/c$, clusters are formed by adding towers with $E^{\text{tower}} > 1$ MeV, in order of decreasing p_T, in a cone of size $R = 0.3$ in $(\eta \times \phi)$ space around the seed tower. After adding each new tower, the seed axis is recalculated using the four-vector or E-scheme recombination scheme:

$$p = (E, \vec{p}) = \sum_i (E^i, p_x^i, p_y^i, p_z^i), \tag{5.2}$$

$$p_T = \sqrt{p_x^2 + p_y^2}, \tag{5.3}$$

$$y = \frac{1}{2} \ln \frac{E + p_z}{E - p_z}, \tag{5.4}$$

$$\phi = \tan^{-1} \frac{p_y}{p_x}. \tag{5.5}$$

   Additional variables are defined as:

$$\theta = \tan^{-1}(p_T/p_z), \tag{5.6}$$

$$\eta = -\ln(\tan(\theta/2)), \tag{5.7}$$

$$E_T = E \sin(\theta). \tag{5.8}$$

   The sum over i in Eq. 5.2 runs over calorimeter towers. Towers associated with the cluster remain in the cluster even if they are outside the new cone. The list of towers is only run through once. All towers used by the cluster are then removed from the list of towers and an attempt to find additional clusters is made starting at the highest p_T remaining tower, until no towers with $p_T > 0.5$ GeV$/c$ remain. Clusters with $p_T < 1$ GeV$/c$ and clusters consisting of only a single tower are rejected. The same cluster finding algorithm, called the *simple cone algorithm*, is also used to reconstruct electromagnetically interacting particles (see Section 5.2).

2. Starting with the highest p_T cluster above 1 GeV$/c$, jets are formed by summing all tower four-momenta within a cone of fixed radius R — in (y, ϕ)-space this time — around the seed

axis. In this analysis $R = 0.5$. After the list of towers is run through, a new centroid is calculated according to Eq. 5.2–5.5 and a new cone is formed around the new centre. The process is repeated until the cones are stable. Reconstruction then proceeds with the next highest p_T cluster until no clusters with $p_T^{\text{cluster}} > 1$ GeV$/c$ remain.

3. In case two stable jets are separated by more than R but less than $2R$, a new jet axis is defined at the midpoint of the two stable jets. This new axis is then used as an additional seed for jet formation.

4. If two jets share energy in towers, they are merged if the shared energy exceeds 50% of the energy of the lowest p_T jet. Otherwise, each of the shared towers is assigned to the closest jet. After merging and splitting is completed, all jets with $p_T < 8$ GeV$/c$ are discarded.

5.1.2 Hot cell suppression

Hot (noisy) cells in the calorimeter are identified and suppressed at three levels [102]:

- Cells with pedestal values below 400 or above 800 ADC counts or a zero suppression threshold above 100 counts[1] are automatically suppressed;

- After pedestal calibration a zero-bias run is taken. Cells with a pedestal value greater than 1 GeV, a sigma greater than 1 GeV or an occupancy exceeding 30% for energies above 500 MeV are suppressed;

- During the offline reconstruction, the NADA algorithm [103, 104] identifies hot cells on an event by event basis.

The pedestal level is determined for each channel separately and is on average about 600 counts. The zero suppression threshold is determined for each channel as $x \times \sigma$, where σ is the pedestal RMS in ADC counts and x is the zero suppression threshold factor. The pedestal RMS is typically in the range 2–7 counts. The zero suppression factor was set to 1.5 when the data presented in this thesis were collected. An additional offline zero suppression was applied with a nominal threshold of 2.5σ. Due to a mistake in the software, the effective offline threshold was $2 - 2.3\sigma$ depending on the calorimeter layer.

The NADA algorithm identifies hot cells by looking at the isolation of high E_T cells. Candidate cells are rejected if the total energy of neighbour cells is below a certain threshold. The neighbour cells are defined as those within a cube surrounding a candidate cell within 0.3×0.3 in $(\eta \times \phi)$ space and in either the same or a directly adjacent layer.

The energy of the cube is the sum of the energies of all cells in the cube except the hot cell candidate and any cell with $E^i_{\text{cell}} < E^{\text{cut}}_{\text{cell}}$ in order to avoid the contribution of cells with low energy due for example to electronics noise. The candidate cell is marked as a hot cell if the energy in the cube is lower than the parameter $E^{\text{cut}}_{\text{cube}}$.

Due to the geometry of the calorimeter some layers need special treatment. The third electromagnetic layer has a finer segmentation in $(\eta \times \phi)$ than the other layers (0.05×0.05 rather than

---

[1] The conversion from counts to energy depends on the layer and on the individual cell. One count corresponds to about 30 MeV in the coarse hadronic layers of the calorimeter and to about 10 MeV in all other layers.

0.1×0.1). Therefore, the cells are first merged by groups of four to form 0.1×0.1 "cells". The first fine and the first coarse hadronic layers have higher energy depositions due to their higher nuclear interaction lengths and require specific values of the NADA algorithm parameters. The intercryostat and Massless Gap detectors also need specific parameter values because of relatively large amounts of uninstrumented material in those regions.

In this analysis, the following cuts are used:

- Cells with $E_T < -1$ GeV or $E_T > 500$ GeV are always rejected;
- If the candidate cell transverse energy is within $1 < E_T^{\text{candidate}} < 5$ GeV, $E_{\text{cell}}^{\text{cut}} = E_{\text{cube}}^{\text{cut}} = 100$ MeV;
- If the candidate cell transverse energy is within $5 < E_T^{\text{candidate}} < 500$ GeV, dynamic thresholds depending on the candidate cell energy are used: $E_{\text{cell}}^{\text{cut}} = E_{\text{cube}}^{\text{cut}} = 0.02 \times E^{\text{candidate}}$.

The efficiency of the NADA algorithm using the static (100 MeV) threshold only, for candidate cells with $E_T^{\text{candidate}} > 10$ GeV, was about 60% [103], but not all layers of the calorimeter were considered. The parameter set used in this analysis finds about three times as many hot cells per event [104]; if only hot cells in layers considered by the static threshold algoritm are counted, 27% more cells are found. The misidentification rate is about 0.04 cells per event.

5.1.3 Jet reconstruction efficiency

Since the search for a jet primarily depends on the existence of a precluster with at least 1 GeV transverse energy inside the jet cone and at least one tower with a $p_T > 0.5$ GeV$/c$ in the precluster, the jet reconstruction efficiency can be determined from the p_T distributions of seed towers and preclusters for jets in various p_T ranges,

$$\epsilon_{\text{jet}} = \epsilon_{\text{precluster}} \times \epsilon_{\text{tower}}. \tag{5.9}$$

From a fit $f(p_T^{\text{seed}})$ to the the seed p_T distribution, the efficiency can be calculated as:

$$\epsilon(E_T^{\text{jet}}) = \frac{\int_{1\ \text{GeV}}^{\infty} f(p_T^{\text{seed}}) \mathrm{d}p_T^{\text{seed}}}{\int_{-\infty}^{\infty} f(p_T^{\text{seed}}) \mathrm{d}p_T^{\text{seed}}}. \tag{5.10}$$

In other words, the efficiency is the probability for a jet of given E_T to contain a seed tower above 0.5 GeV and a cluster above 1 GeV. The measurement is only valid if the fit of the seed distribution gives a reasonable representation of the seed distribution in the extrapolated region.

The p_T distribution for the leading tower in reconstructed jets is shown in Fig. 5.1 for two jet E_T bins, together with a Gaussian fit with a logarithmic argument. Even for very low jet E_T ($E_T > 10$ GeV), the seed tower requirement does not introduce any significant loss of efficiency.

The p_T distribution for the leading cluster in each jet is shown in Fig. 5.2. The cluster momentum is fitted with a Gaussian function. The 1 GeV cut does not introduce any inefficiency for jets with $E_T > 10$ GeV.

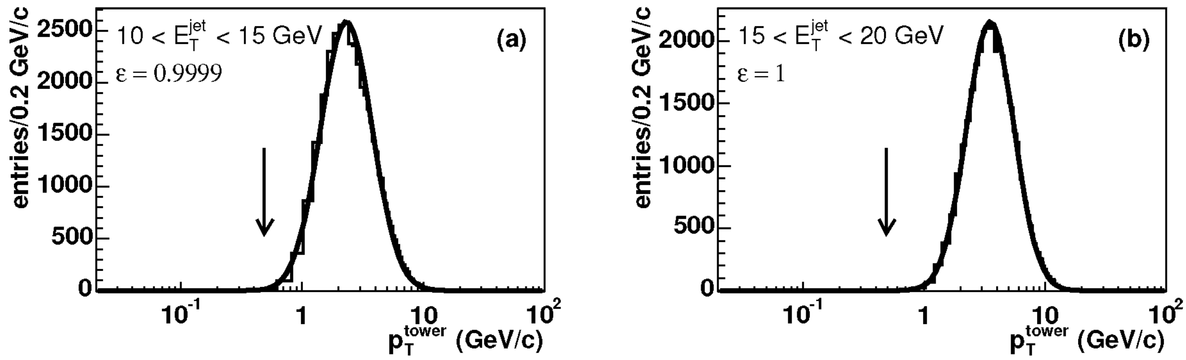

Figure 5.1: Distribution of the leading tower E_T in each jet for jets with $10 < E_T < 15$ GeV (a) and $15 < E_T < 20$ GeV (b). The arrows indicate the minimum seed energy.

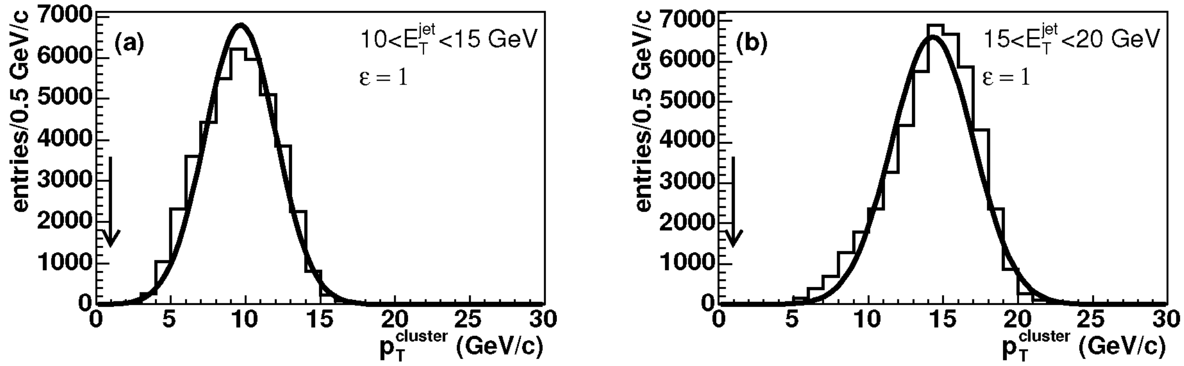

Figure 5.2: Distribution of leading cluster p_T in each jet for jets with $10 < E_T < 15$ GeV (a) and $15 < E_T < 20$ GeV (b). The arrows indicate the minimum seed energy.

5.1.4 Jet energy scale

The jet energies measured by the calorimeter must be corrected to the energies of the jets of particles before entering the calorimeter. This correction consists of three parts:

- subtraction of the offset energy that does not originate from the hard scattering;
- correction for the calorimeter response to the particles constituting the jet;
- correction for the showering inside and outside the jet cone.

After corrections, the jet energy is equal to:

$$E_{\text{jet}} = \frac{E_{\text{jet}}^{\text{cal}} - E_{\text{offset}}}{R_{\text{jet}} \times F_S}, \tag{5.11}$$

where $E_{\text{jet}}^{\text{cal}}$ is the jet energy measured in the calorimeter, E_{offset} is the offset energy, R_{jet} is the response of the calorimeter to particle jets, and F_S is the fraction of the jet energy contained within the cone. The energy scale corrections used in this thesis have been determined by the Jet Energy Scale group [105, 106]. A summary of the method is given below.

Offset energy

Multiple p$\overline{\text{p}}$ interactions during a single beam crossing, pileup of events from previous beam crossings, spectator parton interactions (*physics underlying event*) and uranium noise all contribute to the offset energy. The first two contributions depend on the instantaneous luminosity and somewhat on background conditions, while the underlying event contribution is a function of the centre-of-mass energy.

The highest instantaneous luminosity during data taking was $\mathcal{L} = 30 \times 10^{30}\ \text{cm}^{-2}\text{s}^{-1}$. (For most of the data set, the luminosities were in the range $\mathcal{L} = (10-20) \times 10^{30}\ \text{cm}^{-2}\text{s}^{-1}$.) The mean number of inelastic interactions per crossing is given by

$$\langle n \rangle = \mathcal{L} \times \sigma_{\text{p}\overline{\text{p}}} \times \Delta t,$$

where $\sigma_{\text{p}\overline{\text{p}}}$ is the total inelastic cross section and Δt is the beam crossing interval. Using a total inelastic cross section of 49 mb [1] and a bunch crossing interval of 396 ns, the mean number of interactions per crossing at a luminosity of $\mathcal{L} = 30 \times 10^{30}\ \text{cm}^{-2}\text{s}^{-1}$ is $\langle n \rangle = 0.59$. The probability to have more than one (inelastic) interaction is only about 12%, so the contribution from multiple interactions was not included in the determination of the jet energy scale corrections. The remaining contributions to the offset energy are determined from minimum bias data.

Energy response

The energy response of the calorimeter is determined from events with a jet opposite a photon (γ+jet events), using the energy balance of the event in the nearly hermetic DØ calorimeter. The missing transverse energy $\not{E}_T$ is defined as

$$\vec{\not{E}}_T = -\left(\sum_i E_{x_i}, \sum_i E_{y_i} \right), \tag{5.12}$$

where $E_{x_i} = E_i \sin\theta_i \cos\phi_i$, $E_{y_i} = E_i \sin\theta_i \sin\phi_i$ and E_i, θ_i, ϕ_i are the energy and angular position of each calorimeter tower. In γ+jet events, $\not{E}_T$ corresponds to the overall imbalance of transverse energy in the detector due to differences in the response to photons and jets. This can be used to measure the calorimeter response to jets relative to the precisely known photon response R_{EM}, which can be determined from $\text{Z}^0 \to \text{e}^+\text{e}^-$, J/ψ and π^0 samples, using the known masses of these resonances (see e.g. [107]).

In γ+jet events, the true photon and recoil transverse energies $\vec{E}_{T\gamma}$ and $\vec{E}_{T\text{recoil}}$ satisfy

$$\vec{E}_{T\gamma} + \vec{E}_{T\text{recoil}} = 0. \tag{5.13}$$

In a real calorimeter, however, the photon and jet responses are both less than unity, and the equation is modified to:

$$\vec{E}_{T\gamma}^{\text{meas}} + \vec{E}_{T\text{recoil}}^{\text{meas}} = -\vec{\not{E}}_{T}^{\text{meas}}, \tag{5.14}$$

where $\vec{E}_{T\gamma}$, $\vec{E}_{T\text{recoil}}$ and $\vec{\not{E}}_{T}^{\text{meas}}$ are the measured energies. The photon and jet responses R_{EM} and R_{recoil} are defined by $\vec{E}_{T\gamma}^{\text{meas}} = R_{\text{EM}}\vec{E}_{T\gamma}$ and $\vec{E}_{T\text{recoil}}^{\text{meas}} = R_{\text{recoil}}\vec{E}_{T\text{recoil}}$. If $\vec{E}_{T\gamma}^{\text{meas}}$ is corrected for energy scale in the γ+jet sample, Eq. 5.14 transforms into

$$\vec{E}_{T\gamma} + R_{\text{recoil}}\vec{E}_{T\text{recoil}} = -\vec{\not{E}}_{T}^{\text{meas}} \qquad \Rightarrow \tag{5.15}$$

$$E_{T\gamma} + R_{\text{recoil}}(\hat{n}_{T\gamma} \cdot \vec{E}_{T\text{recoil}}) = -(\hat{n}_{T\gamma} \cdot \vec{\not{E}}_{T}^{\text{meas}}) \qquad \Leftrightarrow \tag{5.16}$$

$$1 + R_{\text{recoil}}\frac{\hat{n}_{T\gamma} \cdot \vec{E}_{T\text{recoil}}}{E_{T\gamma}} = \frac{-\hat{n}_{T\gamma} \cdot \vec{\not{E}}_{T}^{\text{meas}}}{E_{T\gamma}}, \tag{5.17}$$

where $\hat{n}_{T\gamma} = \vec{E}_{T\gamma}/|\vec{E}_{T\gamma}|$ and $\vec{\not{E}}_{T}^{\text{meas}}$ is the missing transverse energy recalculated after the photon correction. Rewriting equation 5.13 as $E_{T\gamma} = -\hat{n}_{T\gamma} \cdot \vec{E}_{T\text{recoil}}$, R_{recoil} can be determined as

$$R_{\text{recoil}} = 1 + \frac{\vec{\not{E}}_{T}^{\text{meas}} \cdot \hat{n}_{T_\gamma}}{E_{T_\gamma}}. \tag{5.18}$$

In the special case of a γ+jet two body process and in the absence of offset and showering effects, R_{recoil} would be equal to the ratio $E_{T\text{jet}}^{\text{meas}}/E_{T\text{jet}}^{\text{particle}}$ of measured to particle jet transverse energies. In the presence of offset and showering losses, R_{recoil} is the response of the calorimeter to jets, R_{jet}, where "jet" refers to the leading (highest E_T) jet of the event. This is a good approximation if the difference in azimuth between the jet and the photon is close to π.

Measuring R_{recoil} as a function of $E_{\text{jet}}^{\text{meas}}$ is complicated by the relatively low resolution of the jet energy measurement, which causes biases due to trigger and reconstruction thresholds and event topology. Most of these biases and smearing effects are reduced to negligible levels by measuring the response R_{recoil} not as a function of $E_{\text{jet}}^{\text{meas}}$ but instead as a function of the jet energy estimator E', defined as

$$E' = E_{T_\gamma}\cosh(\eta_{\text{jet}}), \tag{5.19}$$

where E_{T_γ} includes the electromagnetic scale correction. Both E_{T_γ} and η_{jet} are measured with high resolution compared to $E_{\text{jet}}^{\text{meas}}$. The dependence of R_{recoil} on $E_{\text{jet}}^{\text{meas}}$ is then determined by measuring the average $E_{\text{jet}}^{\text{meas}}$ in each E' bin.

A cryostat factor $F_{\text{cry}} = \frac{R_{\text{recoil}}(\text{EC})}{R_{\text{recoil}}(\text{CC})}$ is determined from data in the overlapping E' region between the central cryostat (CC) and the end cryostats (EC). The cryostat factor is found to be $F_{\text{cry}}^{\text{data}} = 1.047 \pm 0.060$, where the error is statistical. The cryostat factor is used to scale the response points in the EC in order to combine them with those in the CC. The full cryostat factor correction was applied to jet energies for $|\eta_{\text{jet}}| > 1.8$, no cryostat factor correction was applied for $|\eta_{\text{jet}}| < 0.7$ and the correction was linearly interpolated in the intermediate region.

In the intercryostat (ICR) region, the response can be determined by plotting the response as a function of $|\eta_{\text{jet}}|$ in different photon E_T bins. In each E_{T_γ} bin, the response is fitted in the range $|\eta_{\text{jet}}| < 0.5$ and $2.0 < |\eta_{\text{jet}}| < 2.5$ in order to factor out the energy dependence. The measured response is then divided by the fit in order to calculate the correction in the ICR. The ICR correction is determined from events with $E_{T_\gamma} > 30$ GeV, and applied for $0.6 < |\eta_{\text{jet}}| < 1.85$.

Out of cone showering

The showering correction is measured from the showering profiles of jets in the photon+jet data used for the response analysis. The correction was determined in three *physics* η regions[2]: $|\eta| < 0.7$, $0.7 < |\eta| < 1.8$ and $1.8 < |\eta| < 2.5$. The average pseudorapidity in these bins is $\langle|\eta_{\text{jet}}|\rangle = 0.34,\ 1.19,\ 2.10$, respectively. The analysis procedure is as follows:

1. Around each jet axis, concentric rings are defined with $r_{j+1} - r_j = 0.1$ in $(\Delta\eta, \Delta\phi)$;
2. The average energy within each ring is computed using all calorimeter cells whose central axis lies within the ring. Both positive and negative energy cells, after pedestal subtraction, are used;
3. The average energy density as a function of r is determined for each ring by dividing the average energy by the ring area;
4. The offset and baseline energy are calculated in each pseudorapidity region by fitting the energy densities in three r bins around the *jet limit* (defined below), using a horizontal line;
5. The offset and baseline are subtracted from each showering profile;
6. The fraction of the jet energy contained within the reconstruction cone is calculated. The fraction of the jet energy contained within the cone is defined as:

$$F_S = \frac{E_{\text{cone}}}{E_{\text{jet limit}}}.$$

The *jet limit* is the distance in (η, ϕ) space from the jet centroid to where the jet ends and is based on Run I studies. The limit is 1.0 for $0 < |\eta| < 0.7$, 1.2 for $0.7 < |\eta| < 1.8$ and 1.5 for $|\eta| > 1.8$. The corrections are calculated at the average pseudorapidity $\langle|\eta_{\text{jet}}|\rangle$ for each bin and interpolated between the values; for $|\eta| < 0.34$ and $|\eta| > 2.10$ the correction is set equal to the values at $|\eta| = 0.34$ and $|\eta| = 2.10$, respectively.

Energy correction in semileptonic b jets

A special energy correction is needed for jets originating from heavy quarks that decayed semileptonically. This correction accounts for the true energy of the muon, E_μ, as well as for the energy carried by the neutrino, E_{ν_μ}, after subtracting the small average fraction of the muon energy deposited in the calorimeter, E_μ^{cal}.

To better estimate the direction of the decaying B hadron, the full muon four-vector was added to the jet. To avoid double counting the muon energy, the muon energy is not taken into account in the scalar jet energy scale correction. The correction then consists of two consecutive corrections:

$$\begin{aligned} E_{\mu\,\text{jet}} &= E_{\text{jet}} - \langle E_\mu^{\text{cal}}\rangle + \langle E_{\nu_\mu}\rangle && (5.20)\\ p^\lambda_{\mu\,\text{jet}} &= p^\lambda_{\text{jet}} + p^\lambda_\mu, && (5.21) \end{aligned}$$

---

[2] $Physics\ \eta$ is defined with respect to the reconstructed primary vertex of the event (see Section 5.4).

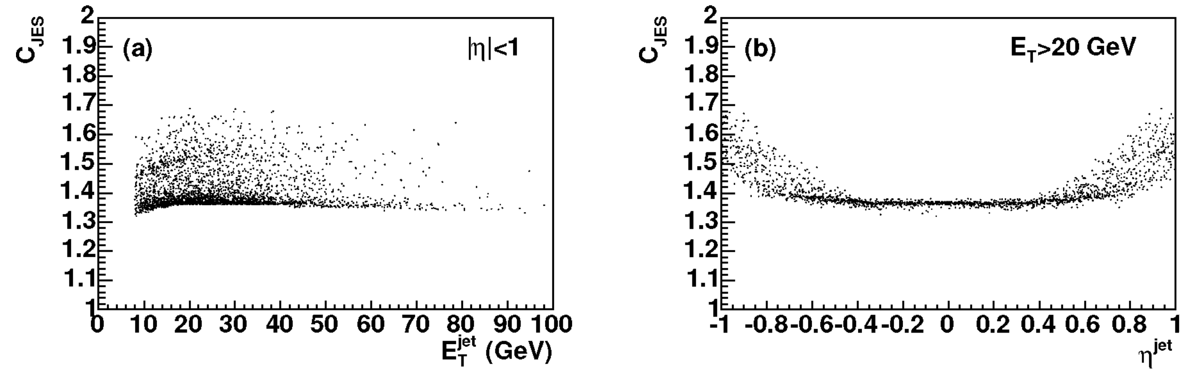

Figure 5.3: Jet Energy Scale correction factor $C_{\rm JES}$ as a function of jet energy (a) and pseudorapidity (b).

where $E_{\mu\,\rm jet}$ and $p^{\lambda}_{\mu\,\rm jet}$ are the energy and four-vector of the corrected semileptonic jet, $E_{\rm jet}$ and $p^{\lambda}_{\rm jet}$ are the energy and four-vector of the jet before applying the muon and neutrino energy correction and p^{λ}_{μ} is the measured four-vector of the muon. The mean neutrino energy $\langle E_{\nu_\mu}\rangle$ and the average energy loss of the muon in the calorimeter $\langle E^{\rm cal}_{\mu}\rangle$ were both estimated from Monte Carlo in two bins each of $E_{\rm jet}$ and P_T^{Rel}, the transverse momentum of the muon with respect to the jet axis.

Uncertainties on the jet energy scale correction

The statistical uncertainty on the jet energy scale has mostly been determined from the uncertainties on the parameters of fits used to determine the correction.

The systematic uncertainty on the offset was set equal to 40% of the measured minimum bias E_T density, based on Run I studies. The systematic uncertainty on the response is determined from the difference between different fits, with a minimum of 5% to account for the fact that a full systematic error analysis has not yet been performed. Below 20 GeV, the uncertainty was multiplied by a factor to account for low E_T bias. This factor has been chosen so that it gives a systematic error of 10% at $E_{\rm jet} = 15$ GeV. For jet energies above 150 GeV, the systematic uncertainty was further increased linearly by $3\%/100$ GeV, to account for the fact that there was not enough data at high energies to cross check the scale in this regime. A 5% contribution was added in quadrature to the response systematic energy to account for the fact that the photon energy has not yet been corrected with the electromagnetic scale correction (expected to be in the range from 1% to 6%). A more complete description of the error analysis is given in the jet energy scale documentation [106].

The final correction factor and uncertainty are determined for each jet, based on its E_T, η and detector η values. The correction factor and uncertainty for a sample of jets are shown in Fig. 5.3 and Fig. 5.4.

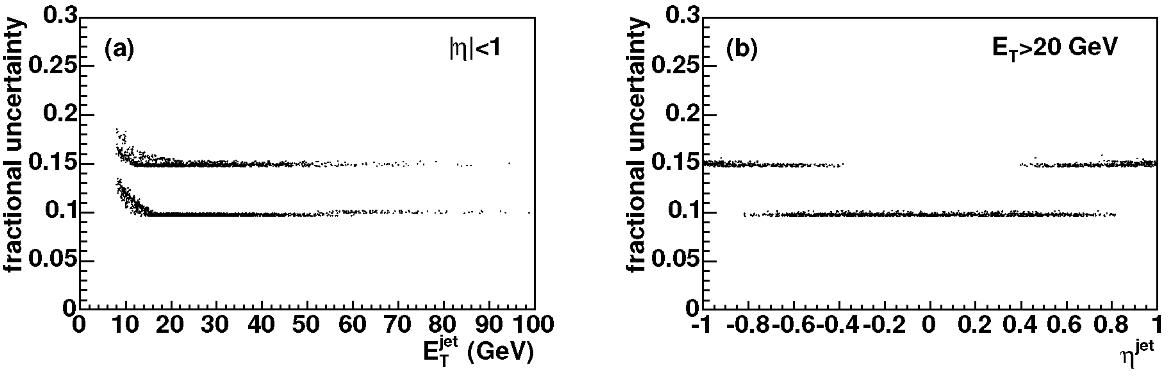

Figure 5.4: Jet Energy Scale correction uncertainty for semileptonic jets as a function of jet energy (a) and pseudorapidity (b). The upper distribution in each scatter plot corresponds to jets in the intercryostat region, defined by $0.6 < \eta_{\mathrm{det}} < 1.85$.

5.1.5 Jet quality

To eliminate fake jets resulting from hot calorimeter cells, pedestal fluctuations and misidentification of non-jet particles, cuts are applied on the following variables:

- *HotF*, the ratio of energies in the hottest and next hottest towers;
- *CHF*, the fraction of the total jet energy deposited in the coarse hadronic (outer) layer of the calorimeter;
- n_{90}, the number of towers containing 90% of the total jet energy;
- $f_{90} = n_{90}/n_{\mathrm{tot}}$, the number of towers containing 90% of the jet energy divided by the total number of towers in the jet;
- *EMF*, the fraction of the total jet energy deposited in the electromagnetic layers of the calorimeter.

The exact cuts applied and their efficiency, as well as the total jet selection efficiency, are listed in Table 5.1.

The cuts on *HotF* and n_{90} are designed to remove fake jets that are caused by large energy fluctuations or permanent hot cells in a single tower. The cut on *CHF* removes jets that arise from noise in the coarse hadronic layers of the calorimeter, which are more prone to noise.

Due to the low online zero suppression threshold of 1.5σ and the softer offline cut of $2 - 2.3\sigma$ (see Section 5.1.2) when the data for this thesis were taken, many additional seed towers were present in the data. Fluctuations of cells in the coarse hadronic layers and in the intercryostat region are amplified by relatively large weights — because of their larger size — and larger intrinsic noise. A cell in the coarse hadronic layer passing the 2.3σ cut has at least about 700 MeV of energy. Since jet reconstruction starts from 500 MeV towers, noise in these regions results in large numbers of additional jet seeds, some of which gather enough energy in the jet cone to pass the 8 GeV jet

	data	Monte Carlo
$HotF < 10$	0.9961 ± 0.0006	0.9965 ± 0.0008
$CHF < 0.4$	0.987 ± 0.001	0.980 ± 0.002
$n_{90} > 1$	1	0.999 ± 0.001
$f_{90} > 0.8 - 0.5 \times CHF$	0.955 ± 0.002	0.916 ± 0.004
$0.05 < EMF < 0.95$	0.9904 ± 0.0008	0.963 ± 0.003
combined	0.924 ± 0.002	0.845 ± 0.005

Table 5.1: Jet quality selection criteria and selection efficiency for data and Monte Carlo.

reconstruction threshold. These fake jets are removed by a cut on f_{90} as a function of the fraction of the total jet energy found in the coarse hadronic layers.

The lower cut on *EMF* removes fake jets resulting from noise in the other layers of the calorimeter. The upper cut, as well as removing fake jets resulting from noise, rejects misidentified photons and electrons.

Efficiency of quality cuts

To determine the efficiency of these selection criteria for real jets, reconstructed jets in a dijet sample are used. The presence of a reconstructed, good quality jet in one hemisphere of the detector indicates (from conservation of momentum) that recoil particles or jets should be present in the opposite hemisphere. Requiring no other high energy objects or missing E_T to be present in the event, a jet reconstructed in the opposite hemisphere should be a real jet.

The efficiency of the $EMF < 0.95$ cut did not change when the additional requirement of two or more associated tracks in the jet was applied. This indicates that the fraction of fake jets due to misreconstructed electrons and photons can safely be ignored.

The distributions of the criteria used for jet selection, before and after selection, are shown in Fig. 5.5 and 5.6 for jets in a data sample selected with a muon+jet trigger. The efficiency of the selection cuts for central data and Monte Carlo jets is plotted as a function of jet E_T in Fig. 5.7 and as a function of η in Fig. 5.8. The f_{90} cut dominates the inefficiency. The inefficiency due to the *CHF* cut increases with E_T. This is expected as higher E_T jets will also deposit a larger fraction of their energy in the outer layers of the calorimeter. The efficiency of the selection criteria as a function of E_T is not very well described by the Monte Carlo. For jets with $E_T > 15$ GeV the ratio of the efficiencies in data and Monte Carlo does not significantly depend on E_T. Since an overall scale factor between the data and the Monte Carlo does not affect the analysis presented in this thesis, no attempt to correct the discrepancy is made.

The efficiency of the jet quality cuts was found to be independent of ϕ^{jet}. Figure 5.8 shows a decrease in efficiency for the *CHF* and *EMF* cuts for jets in the intercryostat region. Aside from an overall scale factor, the η dependence in Monte Carlo describes the data well.

The jet quality cuts and the efficiency of each cut for jets with $E_T > 20$ GeV are summarised in Table 5.1. The efficiency was determined from a horizontal line fit in the range $20 < E_T < 100$ GeV.

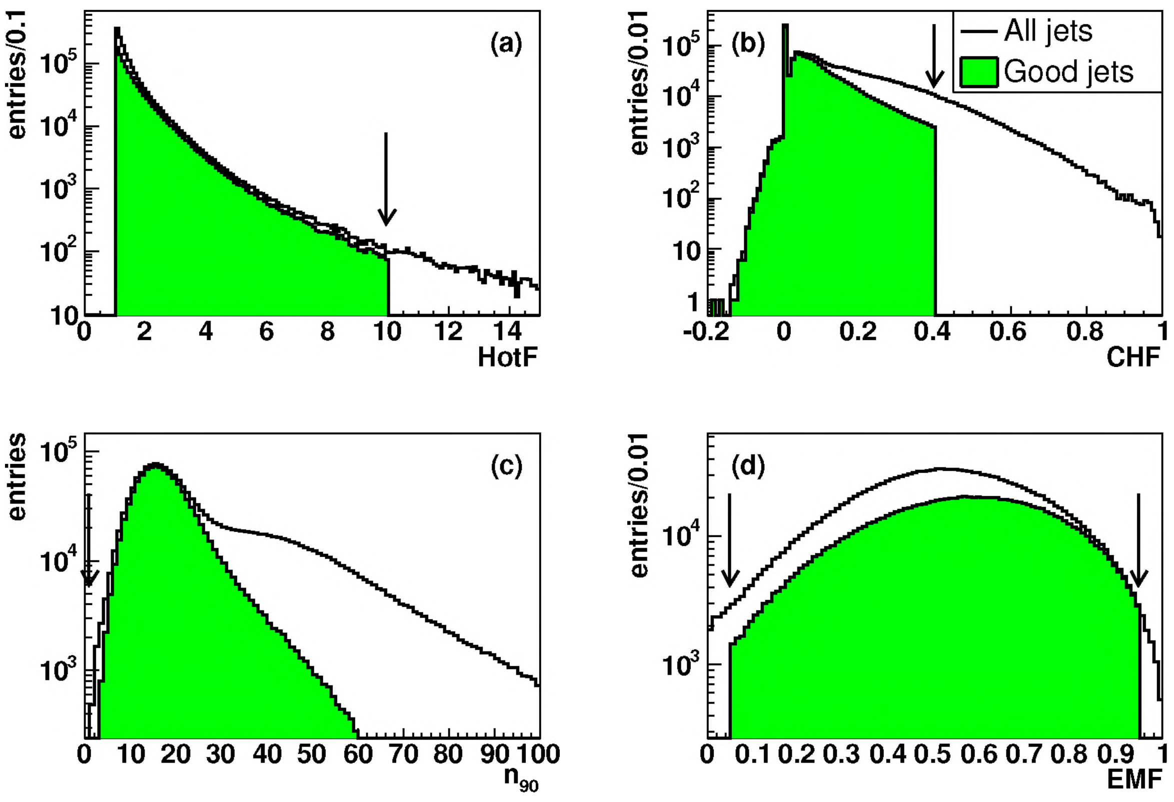

Figure 5.5: Distributions of jet selection parameters *HotF* (a), *CHF* (b), n_{90} (c) and *EMF* (d) for jets before and after selection. The arrows indicate the cut values.

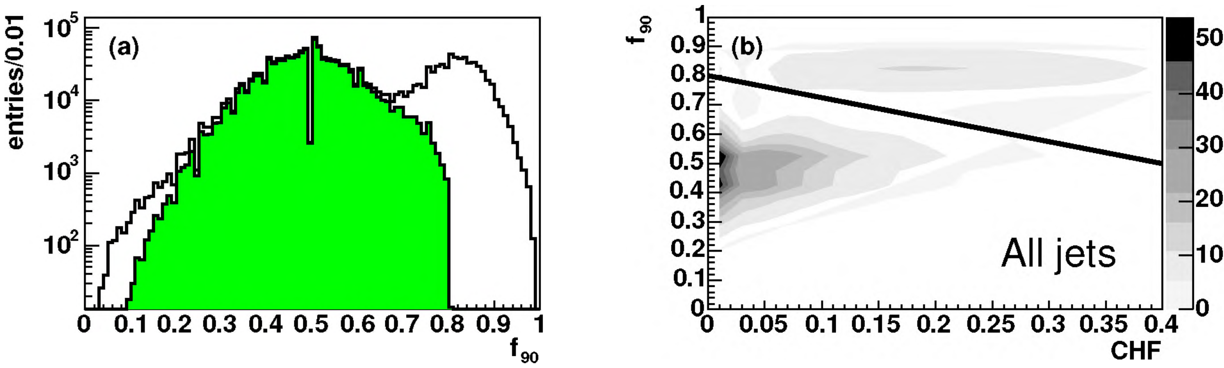

Figure 5.6: Distributions of n_{90} (a) and f_{90} as a function of *CHF* (b). Jets above the solid line in (b) are dominated by noise and are removed.

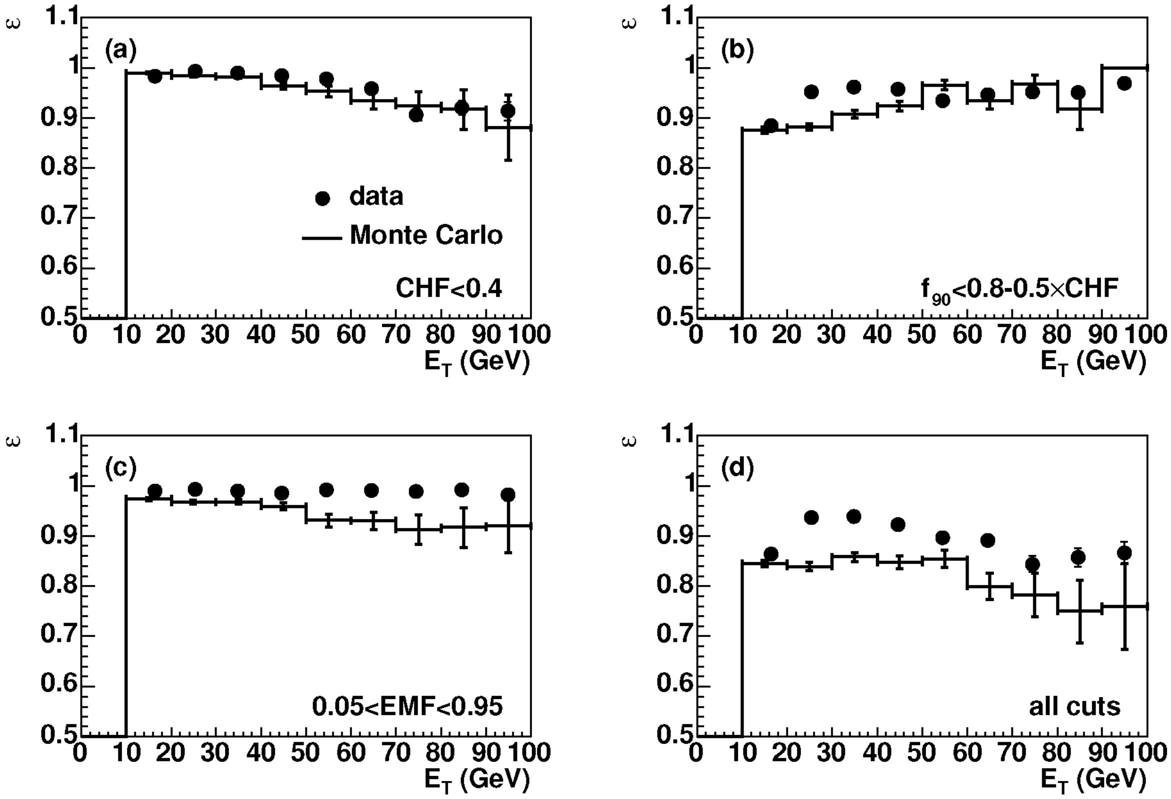

Figure 5.7: Efficiency of jet selection criteria. The plots show the efficiency for the cuts on *CHF* (a), f_{90} (b), *EMF* (c) and all cuts combined (d) as a function of jet E_T in data (solid markers) and Monte Carlo (histogram).

5.1.6 Energy resolution

The energy resolution of the energy scale corrected jets is determined from dijet events exploiting the energy balance in the event. The asymmetry variable $\mathcal{A}$ is defined as

$$\mathcal{A} = \frac{E_T^{(1)} - E_T^{(2)}}{E_T^{(1)} + E_T^{(2)}}, \tag{5.22}$$

where $E_T^{(i)}$ is the transverse energy of each jet. Plotted in different bins of the average E_T of the two jets, the distribution of $\mathcal{A}$ exhibits a Gaussian shape with width $\sigma_{\mathcal{A}}$. The relative uncertainty on the reconstructed jet energy, $\sigma(E_T)/E_T$ can now be expressed as

$$\frac{\sigma(E_T)}{E_T} = \sqrt{2}\sigma_{\mathcal{A}}. \tag{5.23}$$

To measure the asymmetry variable, events have been selected in which both jets pass the standard jet quality criteria and with additional requirements to ensure good energy balance:

- Runs with bad tracking, calorimetry or muon measurement [108] were rejected;

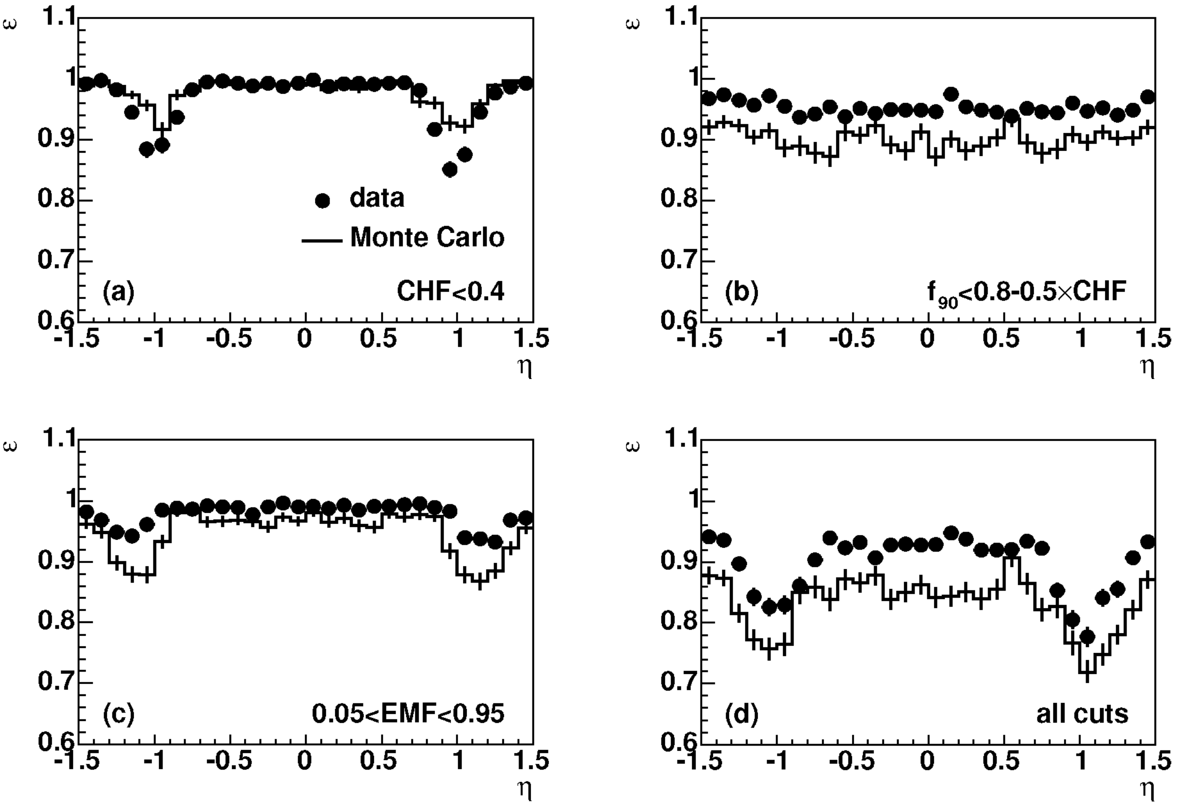

Figure 5.8: Efficiency of jet selection criteria for the cuts on *CHF* (a), f_{90} (b), *EMF* (c) and all cuts combined (d) as a function of jet η in data (solid markers) and Monte Carlo (histogram).

- The jets are separated by more than 2.8 rad in azimuth;
- Missing E_T does not exceed 70% of the E_T of the leading (highest E_T) jet;
- If electromagnetically interacting particles (γ,e) were present, the leading p_T EM particle must satisfy $p_T^{\text{EM}}/E_T^{\text{leading jet}} < 0.2$;
- No reconstructed muon was present in the event.

The asymmetry variable was fitted with a Gaussian with mean fixed at zero in several bins of the average E_T of the two jets in the event. The resulting energy resolution is shown in Fig. 5.9 for data and Monte Carlo jets. Both resolution curves were fit with a function of the form

$$\frac{\sigma_{E_T}}{E_T} = \sqrt{\frac{N^2}{E_T^2} + \frac{S^2}{E_T} + C^2}, \tag{5.24}$$

where the term N^2/E_T^2 corresponds to noise fluctuations in the low energy range, the S^2/E_T term corresponds to the effect of the nature of the showering interactions and signal sampling and C is the resolution limit at high energies due to calibration errors. The shape of the function is based on

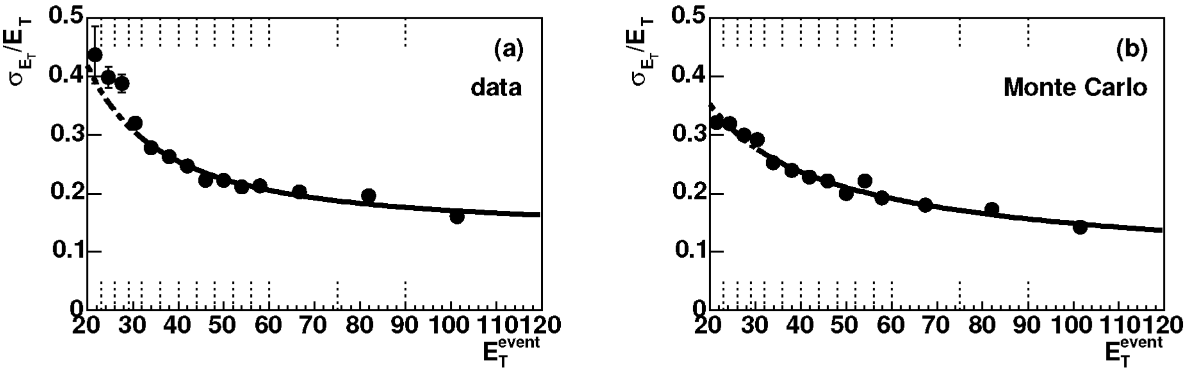

Figure 5.9: Jet energy resolution as a function of jet E_T in data (a) and Monte Carlo (b). The first three measurements in data (a) are affected by the trigger efficiency and are not included in the fit.

	data	Monte Carlo
N	7.1 ± 1.2	3.4 ± 5.7
S	0.8 ± 1.12	1.36 ± 0.24
C	0.134 ± 0.022	0.05 ± 0.10
χ^2/ndf	$24/8$	$11/8$

Table 5.2: Values of the fit parameters of the jet energy resolution fit (see Eq. 5.24).

experience from Run I and on first principles. Because of trigger biases, the resolution cannot be measured for jets with $E_T < 30$ GeV and the fit is only performed for $E_T > 30$ GeV for both data and Monte Carlo. The values of the fit parameters of the fits in Fig. 5.9 are shown in Table 5.2. The fit uncertainties allow unphysical negative values for some of the parameters. Since at this point the interpretation of the parameters is not directly important, the parametrisation is used as given by the fit.

5.1.7 Angular resolution

The angular resolution of reconstructed jets is studied using dijet events passing the same criteria as in Section 5.1.6, without the requirement on the azimuthal separation but requiring that the asymmetry parameter $\mathcal{A}(p_t) < 0.2$. Since Monte Carlo templates will be used to fit to the data in Chapter 6, the difference in angular resolution between data and Monte Carlo is especially important. To account for E_T dependence of the resolution, the Monte Carlo events were weighted to match the distribution of the average E_T of the two jets in data. Figure 5.10 shows the distributions of $\Delta\phi$ (a) and $\Delta\eta$ (b) between two jets in data and Monte Carlo, for jets with $|\eta| < 1.0$.

The azimuthal difference $\Delta\phi$ is directly sensitive to the resolution as it depends on the deviation of each jet to the back-to-back axis. The resolution can be expressed as

$$\sigma_\phi = \frac{\sigma(\Delta\phi)}{\sqrt{2}}, \tag{5.25}$$

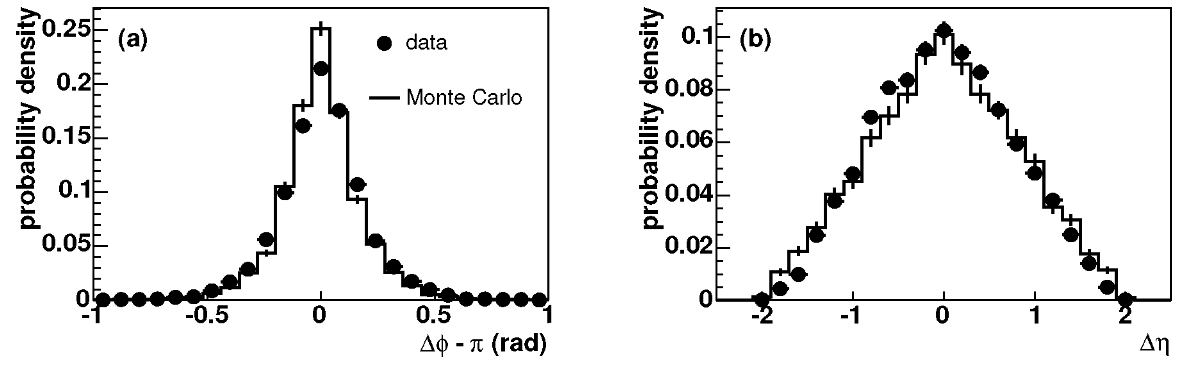

Figure 5.10: $\Delta\phi$ (a) and $\Delta\eta$ (b) angular difference between two jets in dijet data and QCD Monte Carlo.

where $\sigma(\Delta\phi)$ is the width of the distribution. The distribution is well described by a sum of two Gaussians. The resolutions, determined from the width of the narrow Gaussian, are 0.076 ± 0.004 rad and 0.063 ± 0.004 rad for data and Monte Carlo jets respectively, for $E_T^{\text{jet}} > 20$ GeV.

The narrow Gaussian contains about 65% of all jets in data and 63% in Monte Carlo. The widths of the wider Gaussian are 0.24 ± 0.01 rad in data and 0.203 ± 0.008 rad in Monte Carlo. The resolution in data is significantly lower than in the Monte Carlo; this may be due to underestimation of the noise in the simulation and to pileup and the presence of overlying minimum bias events in data.

The difference in pseudorapidity $\Delta\eta$ is not as sensitive to the resolution as events may be boosted along the direction of the beam and no energy balance is required in that direction. However, since the calorimeter segmentation in η is roughly equal to that in ϕ the resolutions for each angle are assumed to be identical.

5.1.8 Monte Carlo jet corrections

Due to a geometry mismatch in the Monte Carlo generation of the $b\overline{b}$ samples, the calorimeter jets were shifted in η with respect to the Monte Carlo particle jets. (The particle jets are defined by clustering Monte Carlo particles using the same cone algorithm used for calorimeter jet reconstruction.) In addition, the calorimeter jet energy showed a dependence on the particle jet energy different from that in Monte Carlo samples with correct geometry.

To correct this bias, the profiles of $\eta^C - \eta^P$ as a function of η^C and of $E_T^C - E_T^P$ as a function of E_T^C in a sample with the geometry mismatch were compared to those in a similar sample without the mismatch. Here, η^P and E_T^P are the pseudorapidity and transverse energy of the particle jet, and η^C and E_T^C are the pseudorapidity and transverse energy of the calorimeter jet. The calorimeter jets in the mismatched sample were shifted in η as a function of η^C and their four-vectors multiplied by a scale factor as a function of E_T^C so that the η and E_T profiles matched those in the correct-geometry sample. The corrections were applied before the jet energy scale correction.

5.2 EM object reconstruction

Electromagnetically interacting objects — photons and electrons — are reconstructed using their energy deposits in the preshower detectors and in the calorimeter. (Electrons can also be reconstructed starting from tracks in the central tracking detectors [109].) The reconstruction algorithm is described in [110]. The calorimeter based photon reconstruction is briefly discussed here.

Reconstruction of EM objects in the calorimeter proceeds along the following steps:

1. Initial clusters are found in the calorimeter using the simple cone algorithm described in Section 5.1.1, using a cone size of $R < 0.4$. Clusters with *EMF* < 0.9 or $p_T < 1.5\ \mathrm{MeV}/c$ are rejected.

2. For selected clusters, the isolation is computed as

$$r_{\text{iso}} = \frac{(E^{\text{tot}} - E^{\text{core}})}{E^{\text{core}}}, \tag{5.26}$$

   where E^{tot} is the total energy in towers within a cone of radius $R < 0.4$ around the cluster axis and E^{core} is the total energy within $R < 0.2$. Only towers within a distance $\sqrt{(i_\eta)^2 + (i_\phi)^2} < 4$ from the highest p_T tower in the initial cluster are used, where $i = 1$ for the nearest neighbour, $i = 2$ for the next-to-nearest neighbour and so on. The cluster is rejected if $r_{\text{iso}} > 0.2$.

3. The initial clusters are used to build final EM clusters. If the highest p_T tower in the initial cluster has detector $|\eta| > 1.3$, a forward cluster is built; a central cluster is built otherwise.

   For central clusters, all cells in the towers within $\sqrt{(i_\eta)^2 + (i_\phi)^2} < 2$ of the leading p_T tower define an EM cluster.

   For forward clusters, the highest energy cell and the highest energy cell in the third layer (EM3) of the calorimeter are found. All cells within a cone of radius $10\ \mathrm{cm}$ at EM3 and origin at (0, 0, 0) are included in the cluster. If the energy of the highest energy EM3 cell is more than 10 times smaller than that of the overall highest energy cell, the latter is used as the cone axis; otherwise, the highest energy EM3 cell is used.

4. Central preshower clusters are added to the cluster if they match the final calorimeter cluster within a $\Delta\eta \times \Delta\phi = 0.05 \times 0.05$ window. The cluster position is updated using the position of the preshower cluster. The forward preshower detector is not used.

5. Tracks with $p_T > 1.5\ \mathrm{GeV}/c$ are matched to the cluster if they match the cluster within $\Delta\eta < 0.05$, $\Delta\phi < 0.05$ and $\Delta(1/p) < 2/3$. If a matched track is found, the cluster is identified as an electron; otherwise, it is assumed to be a photon.

5.3 Track reconstruction

As charged particles pass through the central tracker, they deposit energy in sensitive elements of the detector. The resulting signals are called hits. Track reconstruction starts with clusters of hits found in the SMT and CFT detectors. Each cluster represents a position measurement with known uncertainty and a measurement of the energy deposited by the passing particle.

The task of the tracking algorithm is to assign clusters to tracks, i.e. to determine the ordered list of clusters associated with the passage of each particle, and to determine the kinematic parameters of the particle creating the track.

Tracks in DØ are reconstructed using hits in both the SMT and the CFT. A road method algorithm (GTR) is used to find the tracks starting from seeds in either the SMT or CFT.

Trajectories of muons penetrating the calorimeter and the muon toroid are reconstructed independently in the central trackers and in the muon system. The central tracking for muons is therefore identical to that for other charged particles. The reconstruction of muon tracks in the muon system is described in Section 5.6.

5.3.1 The GTR track finding algorithm

An overview of the GTR track finding method is given in [111] with more DØ specific information given in [112]. A short summary is presented here.

The GTR algorithm uses several components to define tracks:

- Surfaces
  GTR uses a model of the tracking detectors using abstract surfaces. To describe the DØ detector, two types of surface are needed: cylindrical surfaces for the CFT and flat planes for the SMT.

- Paths
  A road or path is an ordered list of the surfaces that a particle originating in a $p\bar{p}$ collision will encounter. The paths define the starting point and search direction for tracks. The first few surfaces are used to build a "seed" track with approximate parameters and uncertainties. Reconstruction algorithm parameters (most notably the maximum track fit χ^2 and number of missed surfaces) are defined for each road.

- Propagators
  Propagators are used to extrapolate the seed tracks to other surfaces in the path. The propagator solves the equations of motion for a charged particle in the magnetic field inside the detector, updating the track parameters and uncertainties for the energy loss and the uncertainties for the effects of multiple scattering in any material crossed while reaching the target surface.

- Fitters
  At each new surface, a Kalman fitting algorithm attempts to match clusters on that surface to the track. The track and cluster uncertainties are combined into a match χ^2. The combination is rejected if the χ^2 value is too large; otherwise, the cluster is added to the track and new track parameters and uncertainties are computed. If no matching cluster is found, this information is also stored, as well as the probability for this miss to occur.

- Filters
  After moving through the list of surfaces in a path, several filters are applied to clean the list of candidate tracks. Tracks are rejected based on the overall fit χ^2 and the number of missed surfaces. If tracks share four or more clusters, the track with the best χ^2 is kept.

Paths used in DØ track reconstruction

Five paths are used in the standard DØ track reconstruction, each covering a different angular region of the detector. The regions are:

- *Central*, the region covered by the SMT and all layers of the CFT;
- *Overlap*, the region covered by the SMT and at least five but fewer than all layers of the CFT;
- *Gap*, covered by at least one but fewer than five layers of the CFT;
- *Forward*, covering the forward region of the H-disks; and
- *SMT Extended* (explained below).

In the *central* region, track finding is done in three steps: axial fibre tracking; stereo fibre tracking; and silicon extension.

Track seeds are built from three clusters in the outer three axial layers of the CFT. The seeds are required to be consistent with particles coming from the interaction region and to have curvatures corresponding to momenta greater than $0.4\ \text{GeV}/c$. The seeds are then propagated through the remaining axial layers. If more than one cluster matches the track in a single layer, multiple tracks are produced.

After passing all eight axial CFT layers, the list is filtered to remove duplicate tracks. The remaining tracks are passed to the next stage of the algorithm, which looks for clusters in the stereo layers of the CFT. Only two clusters are needed to define the stereo parameters of the track; the two-cluster seeds are required to be in the outer two stereo layers of the CFT. The seeds are then propagated through the remaining stereo layers, which are filtered after reaching the innermost layer.

The remaining tracks are extrapolated to the SMT to match SMT hit clusters to the track. Unlike in the CFT, a track is allowed to pass any silicon layer without picking up a cluster. The only requirement is that a minimum of four clusters are picked up.

In the *overlap* region, track finding also begins in the CFT, but clusters from the axial and stereo fibres in each layer are combined to speed up the process. The combined clusters are required to have a z position consistent with a track exiting the edge of the CFT. Tracks can begin in the seventh, sixth or fifth layer but are not allowed to miss any other layers.

In the *gap* and *forward* regions, track finding begins in the outer sublayers of the silicon barrels and works inward. The F-disks covering the radial gap between the sublayers are also included in each step. Tracks are allowed to “miss” any silicon layer they cross, as long as at least four matching clusters are found. In the *forward* region, candidate tracks can be extended to the H-disks; however, these were not used when the data presented in this thesis were taken.

Because the SMT was operational before the CFT, the silicon-only track finding intended for use in the *gap* region was used in all regions. In addition, the *SMT extended* path was introduced to gain efficiency for finding tracks with both SMT and CFT clusters. Tracks found in the SMT were extended into the CFT, picking up fibre clusters. The tracks were allowed to miss one axial fibre layer and all stereo layers.

GTR output

The five GTR paths each produce a list of candidate tracks. These lists are merged into a final list of tracks for the event.

During merging, the lists are checked for duplicate tracks; of all tracks sharing more than four clusters, only the longest track is kept. Of tracks equal in length, the track with the lowest fit χ^2 was selected.

Five parameters are normally required to define a track: two position parameters, two direction parameters and a charge signed curvature (q/p_T). The track parameters used in this thesis are:

- d_0, the impact parameter or *distance of closest approach* to the beam in the transverse plane;
- z_0, the z coordinate of the track at the point of closest approach;
- ϕ, the azimuthal angle of the track direction at the point of closest approach;
- $\tan\lambda = \cot\theta$, where θ is the polar angle of the track direction and $\lambda = \pi - \theta$;
- q/p_T, the charge signed curvature defined as the charge of the track over the transverse momentum $p_T = \sqrt{p_x^2 + p_y^2}$.

The impact parameter d_0 also holds a geometrical sign definition. The sign of d_0 is chosen by convention. In DØ it is defined by the direction of the track and the relative position of the point of closest approach:

$$sign(d_0) = sign(\phi_{\text{track}} - \phi_{\text{pca}}), \tag{5.27}$$

where ϕ_{track} is the direction of the track and ϕ_{pca} the direction of the vector from the interaction point to the point of closest approach, the point on the track where it passes closest to the interaction point. The sign of d_0 is referred to as the "detector sign" of the impact parameter, since it does not depend on the physics process. The detector signed impact parameter is expected to be symmetrically distributed around zero, reflecting the azimuthal symmetry of the detector.

The same sign is obtained if the distance of closest approach is defined as

$$d_0 = y_{\text{PV}} \cdot \cos(\phi_{\text{track}}) - x_{\text{PV}} \cdot \sin(\phi_{\text{track}}), \tag{5.28}$$

where $(x_{\text{PV}}, y_{\text{PV}})$ are the coordinates of the production vertex of the track. While these coordinates are generally not known, this definition of d_0 can be used to determine the width of the beam (see Section 5.5.2.)

5.3.2 Hit efficiency

For tracks within the acceptance of the detector, the hit efficiency can be determined by looking at the number of hits associated to good tracks. The efficiency defined in this way includes both the efficiency of the detector to register a passing charged particle and the efficiency of the track finding algorithm to associate hits with tracks.

The number of CFT hits per track with $|z_0| < 30$ cm and $|\eta| < 1.3$ is shown in Fig. 5.11. Further criteria applied to the tracks are: $|d_0| < 0.1$ cm, $p_T > 1$ GeV/c, presence of a jet within a $\Delta R < 0.5$ cone around the track, and hits in all four SMT superlayers. From this distribution,

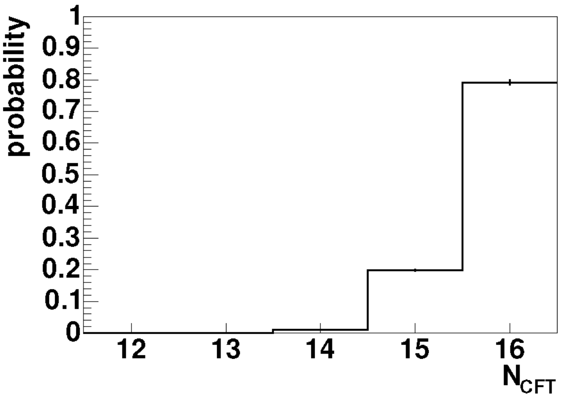

Figure 5.11: Number of CFT hits per track within the acceptance of the tracker.

	data	Monte Carlo
Layer 1	82%	91%
Layer 2	75%	94%
Layer 3	81%	93%
Layer 4	84%	95%

Table 5.3: SMT hit efficiency per superlayer, for data and Monte Carlo tracks.

the single hit efficiency for the CFT is found to be 98.5%. The efficiency in the Monte Carlo simulation is 100%. The mean number of CFT hits per track does not depend strongly on η and ϕ for tracks in the central region. The estimate of the hit efficiency is biased by the requirement that a track is found; however, tracks with hits in all four SMT superlayers can be found using the *SMT extended* GTR path in which case the only requirement on the number of CFT hits is that a hit was found in at least seven of the eight axial layers.

Because of overlapping modules within the superlayers, the SMT hit efficiency is harder to determine. The efficiency *per superlayer*, however, can be measured by looking at tracks with hits in the other three superlayers and at least 8 CFT hits. The efficiencies per superlayer, for tracks with hits in all CFT layers and in the three other superlayers, $p_T > 1$ GeV$/c$, $|d_0| < 0.1$ cm, $|z_0| < 22$ cm, $|\eta| < 1.3$ and with a matched jet within a $\Delta R < 0.5$ cone, are shown in Table 5.3. These efficiencies include an inefficiency due to the gaps between the barrels in the z direction. The statistical uncertainties are about 0.1%. Because of recoverable readout and bias problems, the run-to-run variation in efficiency can be of the order of $1 - 2\%$. The efficiency is clearly overestimated in the Monte Carlo simulation. The higher inefficiency in data is caused by a higher fraction of dead and noisy strips on the silicon sensors and by failures of entire modules due to readout or bias problems. The mean number of superlayers with hits per track does not depend strongly on η and ϕ for tracks in the central region.

The distribution of the number of hits in each SMT superlayer is shown in Fig. 5.12(a). Figures 5.12(b)–(d) show the superlayer in which the innermost hit is found for tracks with hits in three, two and one superlayer(s), respectively. It is clear that the Monte Carlo simulation overesti-

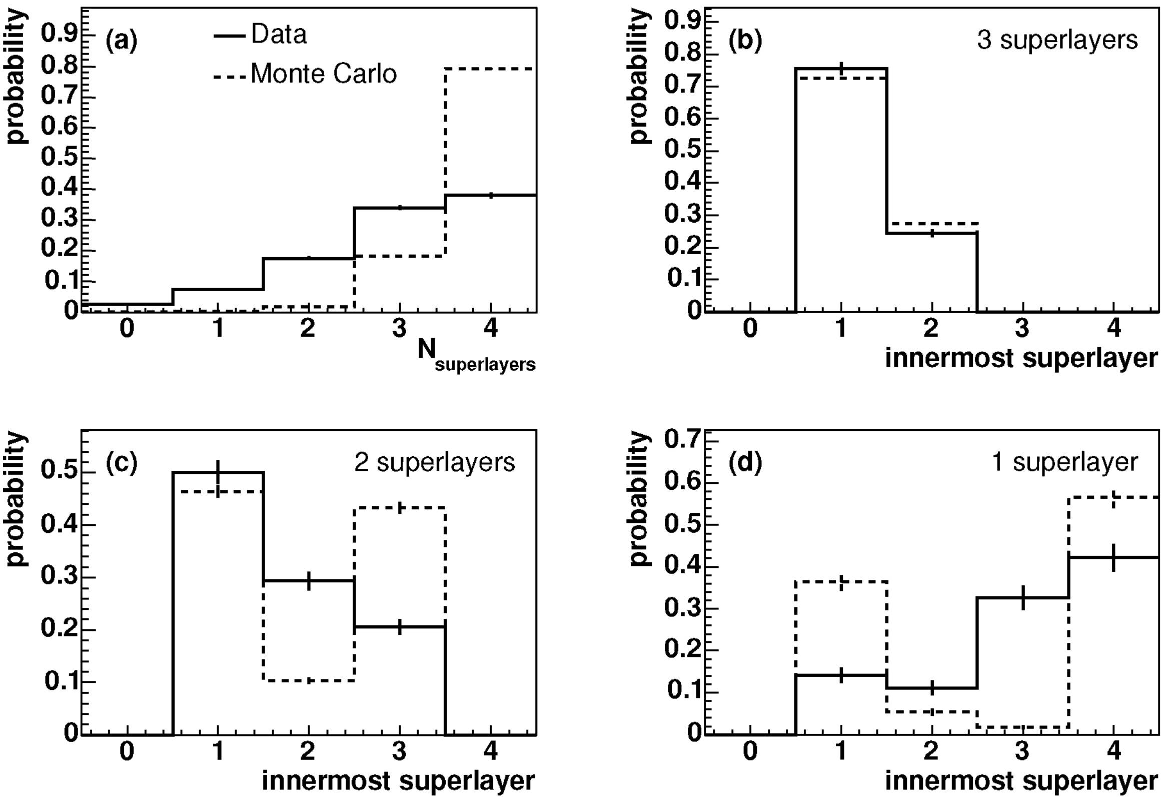

Figure 5.12: Number of SMT layers with hits (a) and radius of innermost hit for tracks with hits in three (b), two (c) or one layer (c). The solid histograms show the distributions in data, the dashed histograms those in the Monte Carlo simulation.

mates the hit efficiency and the quality of the reconstructed tracks.

5.3.3 Tracking efficiency in jets

Because of the higher particle density, pattern recognition for tracks inside jets is more difficult than for isolated tracks. Figure 5.13 shows the numbers of reconstructed tracks with $p_T > 800\ \mathrm{MeV}/c$ inside a $\Delta R < 0.5$ cone around a reconstructed jet in Monte Carlo as and data, as a function of the E_T (a) and of the η (b) and ϕ (c) coordinates of the jet. The tracks were required to have at least 8 CFT hits and hits in at least 2 SMT superlayers. The primary vertex was constrained to the region $-22 < z < 22$ cm. The Monte Carlo distributions were weighted to match the jet E_T distribution in data.

The number of charged Monte Carlo particles with $p_T > 800\ \mathrm{MeV}/c$ inside the jet cone is also shown. Charged particles that decayed before reaching the outer layer of the CFT were not included. The track reconstruction efficiency in Monte Carlo, taken as the number of reconstructed tracks divided by the number of charged particles in each jet, is about 70% and does not depend on η and ϕ of jets with $|\eta| < 1$. The efficiency decreases slightly with increasing jet E_T.

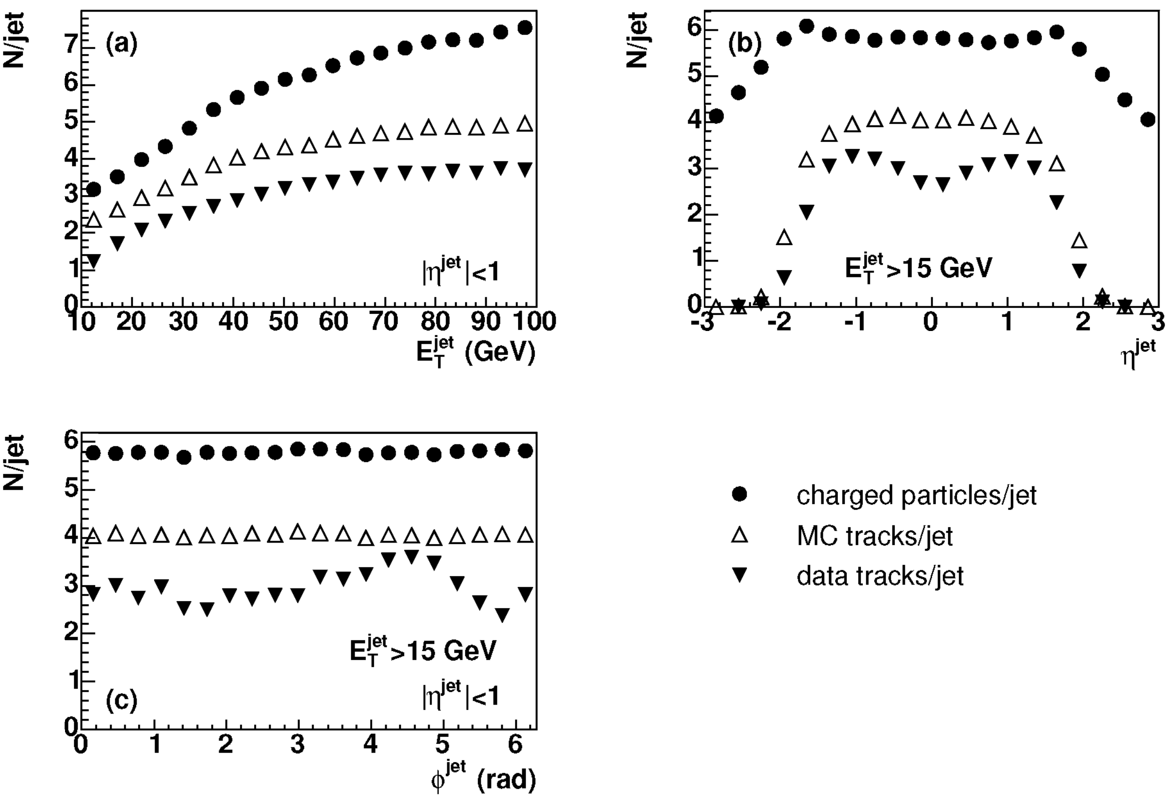

Figure 5.13: The number of reconstructed tracks with $p_T > 800$ MeV/c associated with a reconstructed jet in Monte Carlo and data, as a function of jet E_T, η and ϕ. The number of charged Monte Carlo particles with $p_T > 800$ MeV/c per jet is also shown. Tracks were required to have at least 8 CFT hits and hits in at least 2 SMT superlayers.

The mean number of tracks for jets in the central region is about 2.9 tracks per jet. In Monte Carlo, the mean number of tracks per jet in the same region is 4.1 tracks per jet. Releasing the requirements on the numbers of CFT and SMT hits, the mean number of tracks per jet is 3.6 in data and 4.1 in Monte Carlo. The simulation clearly overestimates both the quantity and the quality of reconstructed tracks.

The dependence of the number of tracks per jet in data as a function of ϕ^{jet} is related to the different lengths of the clear fibres connecting the CFT to the VLPCs as a function of ϕ. This effect has been corrected in later versions of the reconstruction software.

5.3.4 Momentum resolution

The momentum resolution of the tracker is determined by the strength of the magnetic field, the radius of the tracker, the accuracy of measurement of the helix and the amount of multiple scattering. The SMT provides an accurate measurement of the track angle at small radius, but the measurement of the sagitta and outer points in the central rapidity region are dominated by the fi-

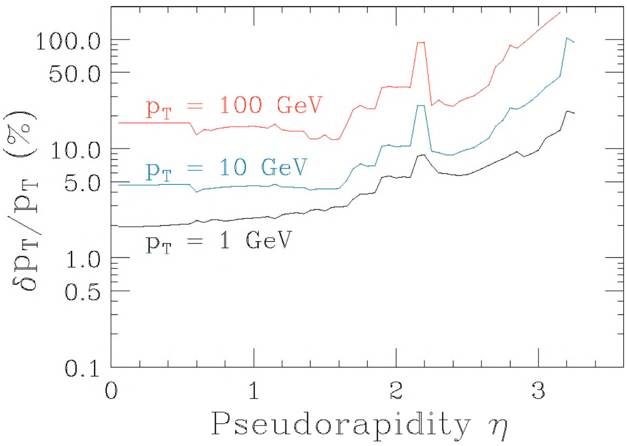

Figure 5.14: Momentum resolution in the central tracker as a function of $|\eta|$ (taken from [113]).

bre tracker, because of its longer lever arm. At high $|\eta|$ (beyond 1.8) tracks miss the outer layers of the CFT and the momentum resolution decreases rapidly. The SMT H-disks, which cover radii less than $26\ \mathrm{cm}$ at large $|z|$, can provide high resolution measurement points for very forward tracks to improve the momentum resolution but are not used in this analysis. The design p_T resolution (including H-disks) is shown as a function of $|\eta|$ in Fig. 5.14 (taken from [113]).

5.3.5 Transverse impact parameter resolution

The impact parameter is defined as the distance of closest approach of a track to the primary interaction point. Unless indicated otherwise, the beam position is used as the primary interaction point in the transverse plane. (A motivation is given in Section 5.4.3.)

The longitudinal (r, z) position of the tracks can only be accurately ($\mathcal{O}(100\ \mu\mathrm{m})$) measured with detectors incorporating a large stereo angle and by the disks. For less accurate measurements required to separate multiple event vertices ($\mathcal{O}(1\ \mathrm{mm} - 1\ \mathrm{cm})$) a small stereo angle is sufficient. As the longitudinal impact parameter is not used in this thesis, the rest of this section only concerns the transverse impact parameter d_0 .

Ideal impact parameter resolution

The impact parameter resolution mostly depends on the resolution of the "support point", the innermost hit on the track, and on the angular resolution σ_ϕ. The latter measurement depends on the distance between the inner- and outermost hits as well as on their resolutions, and on multiple scattering.

The effect of the hit resolution on the impact parameter resolution can be naïvely understood by considering a simple two layer system with identical resolutions at the inner and outer radii, r_1 and r_2. The impact parameter resolution of this system can be modelled as

$$\sigma = \sigma_{\mathrm{meas}} \times \frac{\sqrt{1 + (r_1/r_2)^2}}{1 - (r_1/r_2)}. \tag{5.29}$$

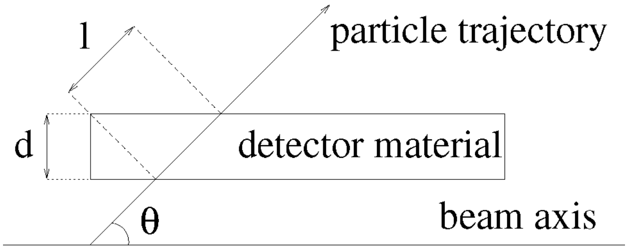

Figure 5.15: Particle trajectory through detector material.

A similar formula holds for disks where r_1 and r_2 are the radii of the first and last hits on a track passing through several disks.

The radii of the SMT layers at DØ are 2.7 cm, 4.5 cm, 6.6 cm and 9.4 cm. Combined with an expected axial point resolution of about 9 μm (see Section 3.3), the expected impact parameter resolution for tracks with hits in both the inner- and outermost layer is 13 μm. In reality, the resolution is lower, due to finite alignment accuracy, imperfect understanding of the hit cluster resolution, and, for low p_T tracks, multiple scattering in the detector and imperfect description of the material distribution. Since the point resolution of the CFT is only about 100 μm, it does not contribute significantly to the impact parameter resolution, even despite the larger radii of the hits.

True impact parameter resolution

The impact parameter resolution can be measured from a sample of zero-lifetime events. The width of the d_0 distribution is then taken as a measure of the resolution of the tracker. This width still includes the width of the beam spot, however:

$$\sigma_{d_0} = \sqrt{(\sigma_{d_0}^{\text{track}})^2 + (\sigma_{\text{beam}})^2},$$

where σ_{d_0} is the width of the d_0 distribution measured with respect to the nominal beam position, σ_{beam} is the width of the beam spot and $\sigma_{d_0}^{\text{track}}$ is the resolution of the tracker. The width of the beam spot can be determined from correlations of track pairs (see Section 5.5.2) and depends on z; for the determination of the impact parameter resolution in this section only tracks with $|z_0| < 10$ cm were used and the beam width in this region was treated as constant.

Multiple scattering

Multiple scattering will degrade the impact parameter resolution for low p_T tracks. The contribution to the transverse impact parameter uncertainty from multiple scattering is inversely proportional to the transverse momentum p_T and proportional to the square root of the length of material traversed. Assuming most of the material is distributed along cylinders around the beam axis (as is the case in the middle of a barrel), this length is inversely proportional to $\sin\theta$ (see Fig. 5.15). The amount of multiple scattering can then be described by a single parameter

$$p_{\text{scat}} = p_T \times \sin^{1/2}\theta = p \times \sin^{3/2}\theta. \tag{5.30}$$

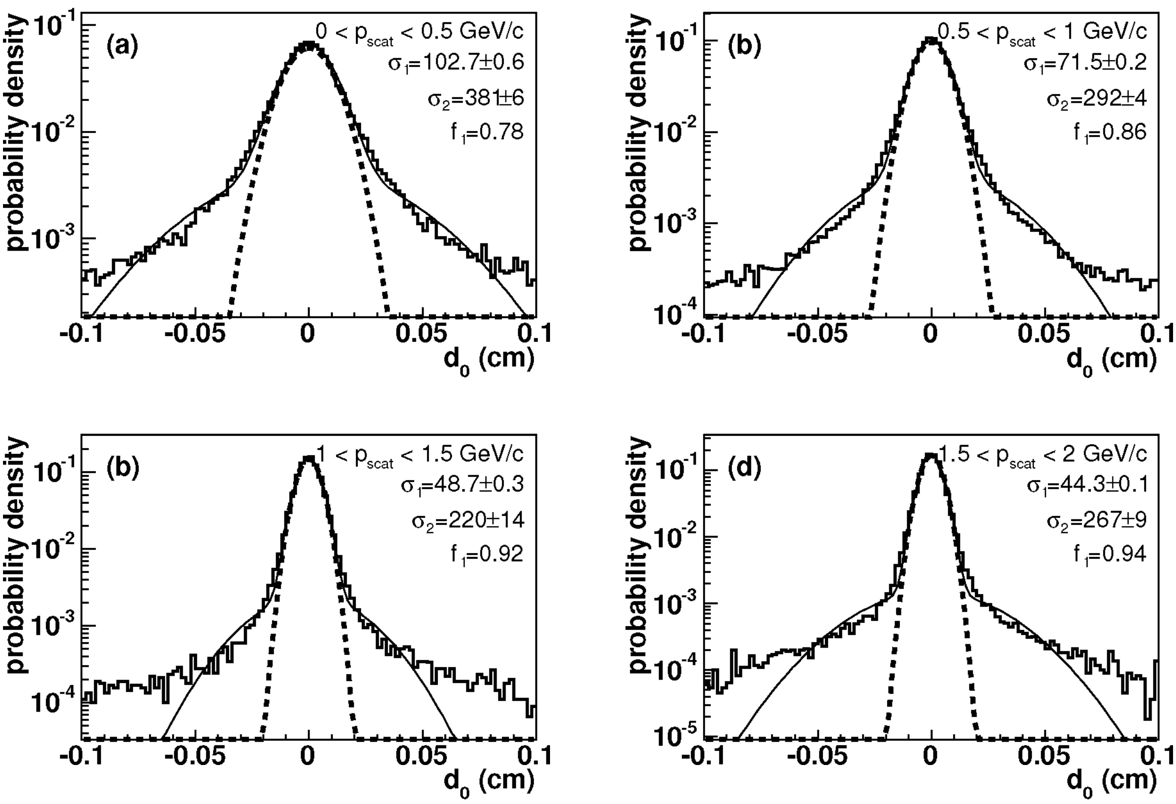

Figure 5.16: Impact parameter distribution in four bins of p_{scat}. The width of this distribution implicitly includes the width of the beam.

The d_0 distributions for tracks with hits in all four SMT superlayers in four bins of p_{scat} are shown in Fig. 5.16.

The impact parameter uncertainty can be parametrised as [114]:

$$\sigma_{d_0}^2 = A^2 + \frac{B^2}{p_{\text{scat}}^2}. \tag{5.31}$$

The first term describes the finite d_0 resolution in the absence of multiple scattering, and the second term describes the degradation of the resolution resulting from multiple scattering.

The d_0 resolutions as a function of p_{scat} for tracks with at least 8 CFT hits and hits in 1 to 4 SMT superlayers are shown in Fig. 5.17. The tracks were matched to jets within $\Delta R < 0.5$. The beam width (determined in Section 5.5.2) was quadratically subtracted from the width of the d_0 distribution for each data point. The values for the fit parameters in Eq. 5.31 are given in Table 5.4.

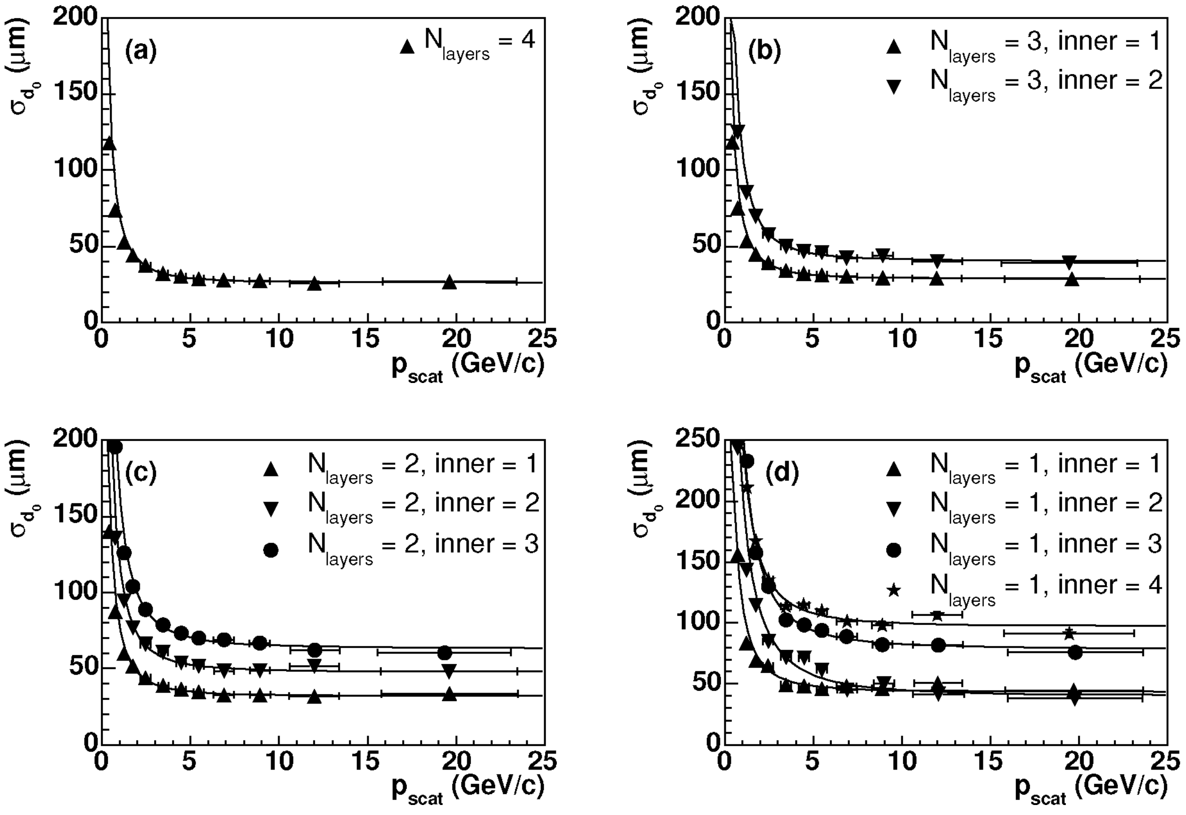

Figure 5.17: Impact parameter resolution as a function of $p_{\text{scat}} = p_T \times \sin^{1/2}\theta$, for tracks with hits in 4 (a), 3 (b), 2 (c) or 1 (d) superlayer(s). The width of the beam has been quadratically subtracted from the width of the d_0 distribution for each data point.

superlayers	innermost layer	A (μm)	B (μm GeV/c)	χ^2/ndf
4	1	26.0 ± 0.2	65 ± 3	22.0/10
3	1	28.6 ± 0.2	63 ± 3	9.0/10
3	2	40.2 ± 0.4	104 ± 5	19.3/10
2	1	31.8 ± 0.4	71 ± 3	12.3/10
2	2	47.8 ± 0.6	110 ± 5	14.8/10
2	3	63.4 ± 0.9	153 ± 8	11.4/10
1	1	43.3 ± 0.9	107 ± 6	28.5/10
1	2	40 ± 2	206 ± 11	23.0/10
1	3	79 ± 2	254 ± 13	6.9/10
1	4	97 ± 1	236 ± 13	18.5/10

Table 5.4: d_0 resolution for tracks categorised by number of SMT superlayers with hits, and the layer in which the innermost hit was found.

5.4 Primary vertex reconstruction

A vertex is the production point of two or more particles and can be due to a particle collision or to a particle decay. The primary collision point of an event is known as the primary vertex. Vertices can be reconstructed by fitting tracks to a common point of origin. The vertex finding and fitting algorithm is described in [115].

5.4.1 Vertex reconstruction algorithm

The primary vertex position is first estimated by fitting all charged tracks with impact parameter significance (the impact parameter divided by its uncertainty) smaller than 3 into a single vertex. Tracks with a high χ^2 contribution to the fit are excluded one by one in decreasing order of their χ^2 contribution and the vertex is re-fitted after each removal. This process is iterated until all remaining tracks have a χ^2 contribution below a cutoff. Once a vertex has been found, the algorithm is applied to the remaining tracks and the process is repeated until no more vertices can be reconstructed. The event primary vertex is selected from the reconstructed vertices as the vertex with the highest $\sum_i \log(p_T^i)$ [116], where p_T^i is the transverse momentum of a track i attached to the vertex.

5.4.2 Vertex reconstruction efficiency

The primary vertex reconstruction and selection efficiency has been studied in Monte Carlo $\mathrm{t\bar{t}}$, $\mathrm{Z}^0 \to \mathrm{b\bar{b}}$ and $\mathrm{Z}^0 \to \tau\bar{\tau}$ samples. The efficiency to reconstruct a Monte Carlo vertex within the region $|z| < 40\ \mathrm{cm}$ that has at least 3 reconstructed charged particle tracks is better than 97% for all samples studied [116]. In data, 83% of all events selected with a muon+jet trigger have a primary vertex with at least 3 tracks. 1.7% of all events have no reconstructed primary vertex. In most of those events, no reconstructed tracks are found.

5.4.3 Primary vertex resolution

The uncertainty on the vertex position depends very strongly on the quality of the vertex fit and on the number of tracks associated with the vertex. The mean resolution as a function of the number of tracks is shown in Fig. 5.18, along with the distribution of the number of tracks per vertex. To achieve a resolution competitive with the uncertainty on the beam position — nominally 30 μm, dominated by the width of the beam (see Section 5.5) — at least 8 tracks are needed. Only 47% of all primary vertices pass this requirement, leading to an unacceptable loss of events. Therefore, the primary vertex will only be used in this thesis as a constraint on the longitudinal position of the primary interaction, ensuring that the interaction is fully covered by the central tracking detectors. The requirement on the number of tracks can then be relatively loose.

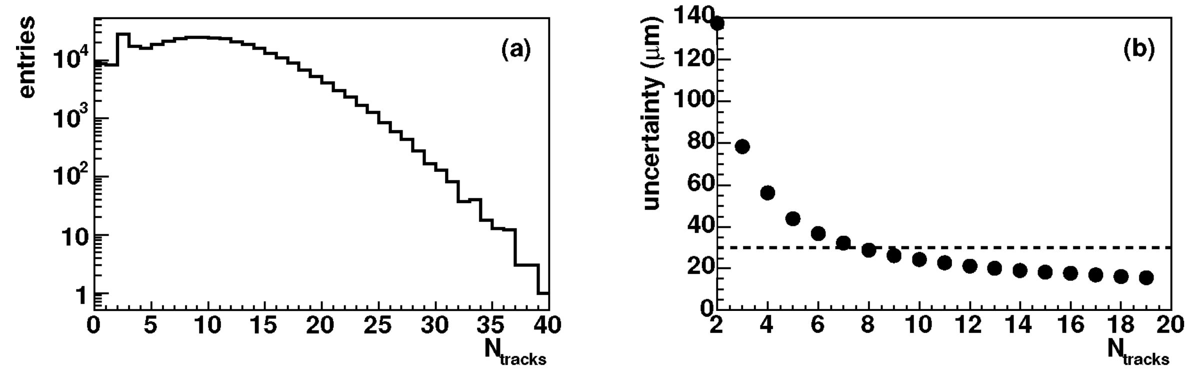

Figure 5.18: Number of tracks attached to the event primary vertex and the uncertainty $(\sigma_x + \sigma_y)/2$ on the vertex position. The dashed line indicates the nominal beam width (30 μm).

5.5 Beam width and position

5.5.1 Beam position

The actual beam position in DØ varies according to accelerator conditions. While variations within a Tevatron store are small, large changes in the (x, y) position and the slope along z are sometimes observed between Tevatron stores. To determine the impact parameter of tracks with respect to the beam, the position needs to be known with high accuracy.

The beam position for a run is determined as the mean x and y position for all primary vertices reconstructed for that run. By determining the mean position for several z regions along the beam, the slope of the beam through the detector is also determined.

If the wrong reference coordinates for the track helix parameters are chosen, the track impact parameter will show a periodic dependence on the azimuthal track direction ϕ. This dependence can be used to extract the offset of the reference coordinates to the true interaction point but is used here only as a cross check. In Fig. 5.19, the $d_0 - \phi$ distribution is shown for a sample of tracks from one run, with respect to $(0, 0)$ and with respect to the beam position determined by averaging vertex positions. The (x, y) position of the beam is determined at the z coordinate of the track at the point of closest approach to $(0, 0)$. After choosing the correct reference coordinates, there is no residual dependence of the mean of the d_0 distribution on ϕ.

5.5.2 Beam width

The width of the beam can be determined from the impact parameter correlations between track pairs [117]. Assuming straight tracks, the impact parameter of a track can be parametrised by Eq. 5.28,

$$d_0 = y_v \cdot \cos(\phi) - x_v \cdot \sin(\phi).$$

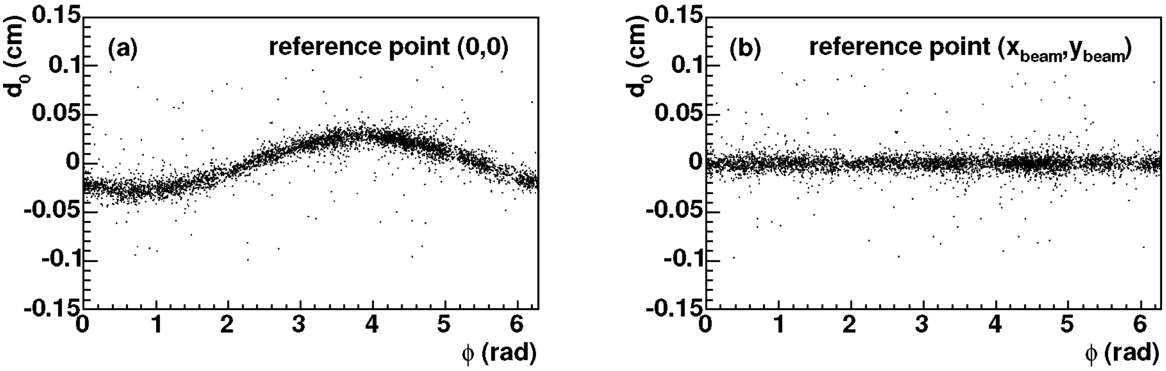

Figure 5.19: Track d_0 as a function of ϕ, with respect to (0,0) (a) and with respect to the fit beam position (b).

Ignoring the uncertainty on the d_0 measurement[3], the correlation between two tracks coming from the same vertex is then given by

$$\langle {d_0}^{(1)} {d_0}^{(2)} \rangle = \langle (y_v \cdot \cos(\phi^{(1)}) - x_v \cdot \sin(\phi^{(1)})) \times (y_v \cdot \cos(\phi^{(2)}) - x_v \cdot \sin(\phi^{(2)})) \rangle. \tag{5.32}$$

The angular brackets indicate averaging over all track pairs. Introducing two new angular variables, $\Delta\phi = (\phi^{(1)} - \phi^{(2)})$ and $\Phi = \frac{1}{2}(\phi^{(1)} + \phi^{(2)})$, Eq. 5.32 can be rewritten as

$$\langle {d_0}^{(1)} {d_0}^{(2)} \rangle = \frac{1}{2}(\langle y_v^2 \rangle - \langle x_v^2 \rangle) \cos(2\Phi) - \langle x_v y_v \rangle \sin(2\Phi) + \frac{1}{2}(\langle y_v^2 \rangle + \langle x_v^2 \rangle) \cos(\Delta\phi). \tag{5.33}$$

Choosing the reference such that the correlation between the primary vertex coordinates is zero, and assuming the beam is circular, Eq. 5.33 can be simplified and written as

$$\langle {d_0}^{(1)} {d_0}^{(2)} \rangle = \sigma_F^2 \cdot \cos(\Delta\phi). \tag{5.34}$$

The beam width σ_F is extracted from a fit on the distribution of ${d_0}^{(1)} {d_0}^{(2)}$ as a function of $\cos(\Delta\phi)$ in several z regions along the beam. This distribution is shown for a small z region in Fig. 5.20. A cut of $p_T > 0.5$ GeV$/c$ was applied to validate the straight line approximation.

Using Eq. 5.33, the widths of the beam in the x and y directions were determined separately to verify the roundness of the beam. Within the uncertainties of the fit, the widths were equal in both directions.

The beam is nominally focused at the centre of the detector ($z = 0$). Away from the focal point, the width increases. The width as a function of z can be described by a second order polynomial, as shown in Fig. 5.21. In fact, the narrowest part of the beam is displaced by a few centimetres from $z = 0$. The second order polynomial description of the beam width, determined for separate running periods, is used throughout this thesis. The results of the fit are shown in Table 5.5.

---

[3] The uncertainties can safely be ignored if the measurements of the impact parameters of two tracks ${d_0}^{(1)}$ and ${d_0}^{(2)}$ are uncorrelated and unbiased.

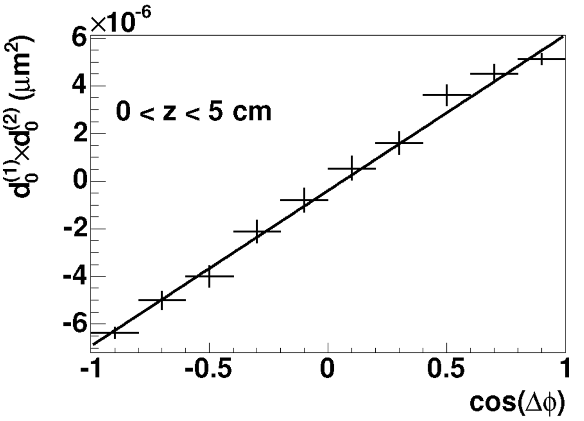

Figure 5.20: The product $d_0{}^{(1)} d_0{}^{(2)}$ as a function of $\cos(\Delta\phi)$ for a small region along the beam axis.

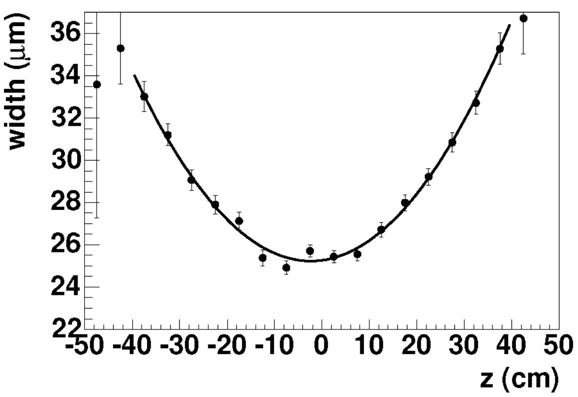

Figure 5.21: Width of the beam as a function of z. The fit function is a second order polynomial.

Run period (in 2002)	p_0 (μm)	p_1 (μm/ cm)	p_2 (μm/ cm^2)	χ^2/ndf
August 22 to September 9	24.1 ± 0.2	0.05 ± 0.01	0.0062 ± 0.0005	24.7/13
September 13 to October 8	24.2 ± 0.2	0.011 ± 0.008	0.0076 ± 0.0004	12.2/13
October 8 to October 25	25.3 ± 0.1	0.030 ± 0.005	0.0064 ± 0.0003	10.1/13

Table 5.5: Parameters of the beam width parametrisation $\sigma_{\text{beam}} = p_0 + p_1 \times z + p_2 \times z^2$ for three running periods in 2002.

5.6 Reconstruction of muon trajectories

Muon trajectories are reconstructed using information from the central tracking, calorimeter and muon subdetectors. In this thesis, only "local" muon tracks — using only information from the muon system — are used. Tracks reconstructed in the central volume of the detector are matched to local muons to determine the local muon resolution. Muons with central track information are referred to as "global" muons. A full description of the local muon reconstruction algorithm can be found in [100]. A summary is presented here.

The reconstruction of muon trajectories in the muon system proceeds in three steps:

1. Reconstruction of the time and position of scintillator hits and of the position and drift distance of wire hits;

2. The combination of reconstructed wire and scintillator hits in each layer into straight track segments;

3. Fitting reconstructed segments in the A-layer to reconstructed segments in the B- and C-layers to reconstruct the momentum of the muon.

The kinematic parameters of a local muon are determined as follows:

- $\phi^{\rm local} = \tan^{-1}(y_A/x_A)$, where (x_A, y_A) are the average hit positions in the A layer;

- $\eta^{\rm local}$ is determined from a fit to the hits in the local muon system;

- if a B/C-layer segment can be matched to an A-layer segment, a fit through the toroid is attempted to determine $p^{\rm local}$. (Strictly speaking, the component perpendicular to the toroid field is measured.) The values of $\eta^{\rm local}$ and $\phi^{\rm local}$ are then also updated.

5.6.1 Hit reconstruction

Muon trajectories are reconstructed from hits in the muon scintillators and in the drift tubes. The scintillators provide a time stamp as well as a position measurement. The drift tubes are used to find track segments in the muon system.

In the central region, the dual readout of the Proportional Drift Tubes (PDTs) provides a measurement of the drift time as well as the axial time. The axial time determines the position of the passing particle along the wire. The drift time, together with the angle of the track (which is taken into account during the segment reconstruction stage), determines the distance of the particle perpendicular to the wire. The scintillator hit position improves the axial (ϕ) resolution in the central system.

In the forward muon system, the Mini Drift Tubes (MDTs) only provide one time measurement, which is the sum of the drift and axial times. Because the MDTs do not provide an independent axial measurement, a matching scintillator hit is required to determine the axial position of the track. If the position along the wire is known from a matching scintillator hit, the drift time can be determined and used to calculate the perpendicular distance of the particle trajectory to the wire.

5.6.2 Segment reconstruction

After the hits have been reconstructed from raw data, straight track segments are reconstructed in each layer of the muon system. The algorithm can be separated in 5 distinct steps:

1. Pattern recognition;
2. Straight line fit;
3. Scintillator hit match;
4. Match of B- and C-layer segments to form a single BC-layer segment;
5. Selection of the best resulting segment.

The pattern recognition process uses a linked list algorithm [118]. Straight lines, called links, are made between each pair of wire hits. The links are matched recursively to form straight line segments; whenever two links are found to be compatible with a straight line segment they are merged into a new link containing all the hits of the previous links. The process is repeated until an attempt has been made to match each link with all other links. The resulting segments are then fit as straight lines.

After the fit has converged, the segment is extrapolated to the scintillator position in the drift plane of the wire hits. If a matching hit is found, the segment is re-fitted, now taking into account the scintillator hit. In the central region, the dual readout of the PDTs yields an axial resolution of about $10\ \mathrm{cm}$. In the forward region, the scintillator hit provides the only axial measurement. Without a scintillator hit, the axial resolution is equal to the length of a MDT wire divided by $\sqrt{12}$, resulting in a resolution of $60 - 90\ \mathrm{cm}$. If a matching scintillator hit is found, the position of the segment is set to the centre of the scintillator, resulting in a resolution of about $7\ \mathrm{cm}$.

Because of the absence of a magnetic field between the B- and C-layers, segments in these layers are expected to be parts of the same straight line segment. The B- and C-layer segments are therefore matched within each octant and region, and a new fit is performed using all hits on both segments.

The algorithm can find multiple segments from a collection of hits. The best segments are selected by lowest χ^2/ndf. From segments with only two hits, the segment that is best compatible with the primary vertex is selected.

5.6.3 Local muon track reconstruction

The local track reconstruction matches segments in the A-layer, in front of the toroid, with segments in the B- and C-layers, and performs a fit to determine the momentum of the particle. The segments are matched by relating the directions of the segments in the ϕ and η directions with their positions. A first estimation of the momentum is made by comparing the angles of the two segments in the drift plane

$$P_{\text{drift}} = \frac{0.3BD}{|\tan\theta|}, \tag{5.35}$$

where P_{drift} is the momentum in GeV/c in the plane perpendicular to the wires, B is the toroid magnetic field (1.8 T), D is the distance in meters that the muon travels in the toroid and θ is

category	A-layer wire hits	A-layer scintillator hits	BC-layer wire hits	BC-layer scintillator hits	fit status
medium	>1	>0	>1	>0	
tight	>1	>0	>2	>0	successful

Table 5.6: Muon selection criteria for tight and medium muons.

the angle difference between the two segments. Using initial parameters from this estimation, a nonlinear fit is performed to find the best momentum compatible with the positions and directions of the two segments. Starting with the position of the B/C-layer segment, the track is propagated stepwise through the toroid to the A-layer along a helical path, accounting for the energy loss at each step and taking into account multiple scattering modelled by two planes in the toroid.

5.6.4 Local muon track quality

Based on the number of hits associated with a muon track, and on convergence of the fit between A- and B/C-layer segments, a “loose”, “medium” or “tight” quality designation is defined. The criteria for “medium” and “tight” quality muons are summarised in Table 5.6. For “loose” muons, one of the tests is allowed to fail, with the A-layer scintillator and wire chamber hits together treated as one test. “Global” muons have the additional requirement of a matched central track. The criteria for loose, medium and tight muons were established based on muons in real data [119].

5.6.5 Improving η resolution using the primary vertex

In the muon system, η is determined by a fit through the hits in the A-layer. The hit resolution and short reconstruction arm limit the resolution to $\sigma_\eta \approx 83 \times 10^{-3}$ in data and $\sigma_\eta \approx 56 \times 10^{-3}$ in Monte Carlo. The resolutions are determined by matching muons to tracks reconstructed in the central tracking system (see Section 5.6.8).

The η coordinate can also be determined using the primary vertex and the position of the muon on the A-layer. The η coordinate is then given by

$$\theta = \tan^{-1}\left(\frac{r_A}{z_A - z_{\mathrm{PV}}}\right), \tag{5.36}$$

where z_A and $r_A = \sqrt{x_A^2 + y_A^2}$ give the position of the muon on the A-layer and z_{PV} is the z coordinate of the primary vertex. With an uncertainty of $\mathcal{O}(0.1 - 0.01\ \mathrm{mm})$ on the primary vertex position (depending on the number of attached tracks), the resolution can be improved to 36×10^{-3} in data and 31×10^{-3} in Monte Carlo. The locally measured and improved η resolutions for central data and Monte Carlo muons are shown in Fig. 5.22.

The muon momentum was kept constant when updating the muon η information. This leads to a small change in the transverse momentum p_T. The local muon parameters are now determined as follows:

- η^{local} is determined from the position on the A-layer and the z coordinate of the primary vertex;

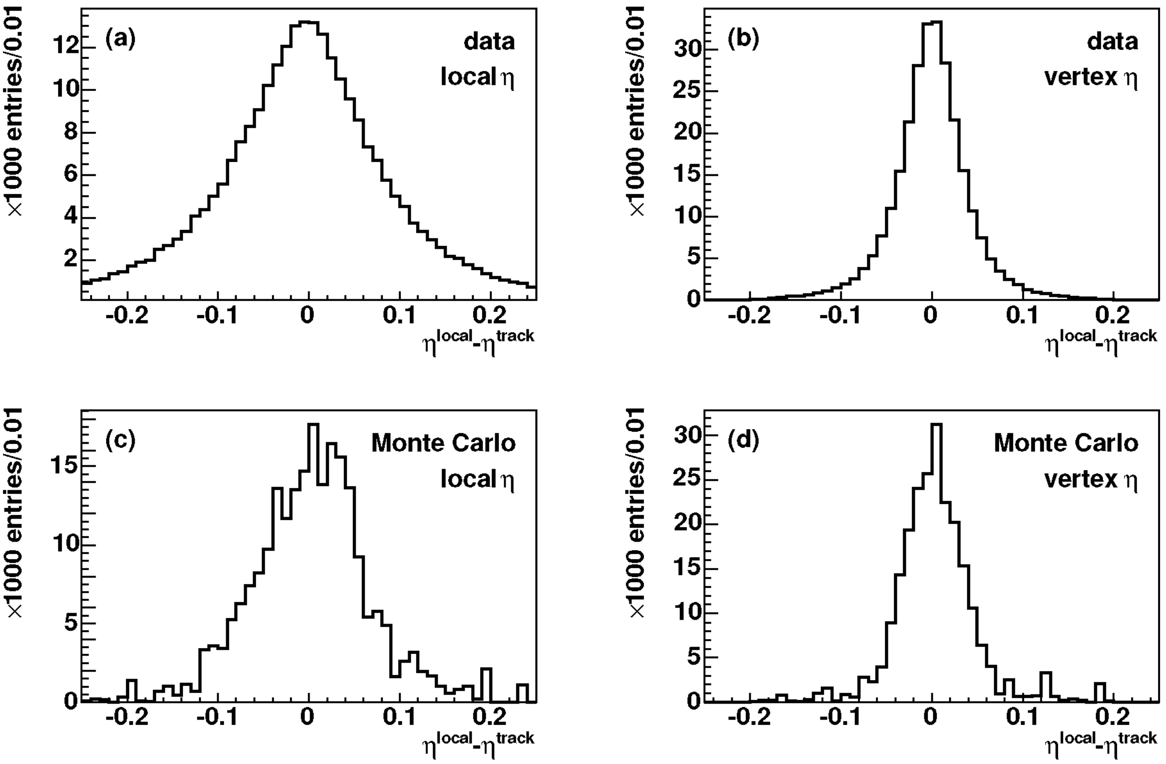

Figure 5.22: Locally measured and improved η resolutions for central data (a, b) and Monte Carlo muons (c, d).

- ϕ^{local} is determined from the position on the A-layer and the nominal beam position (0,0);
- p^{local} is determined from the local muon track fit through the toroid.

5.6.6 Muon extrapolation

The kinematic parameters of local muons are given at the A-layer of the muon system. To match muons to objects in the inner part of the detector, the ϕ coordinate must be corrected to account for the bending in the magnetic field of the solenoid.

In principle, the change in ϕ should be proportional to $1/p_T$. However, the method of determining ϕ in the local muon system, combined with the finite region of the magnetic field, makes the extrapolation more complicated. Instead of an analytical solution, an ad hoc parametrisation of the shift in ϕ with respect to a matched central track as a function of local muon p_T is used:

$$\delta\phi = \alpha + \beta/p_T^{\gamma}, \tag{5.37}$$

where $\delta\phi = \phi^{\text{local}} - \phi^{\text{track}}$ and p_T is the locally measured muon momentum. The result of the fit for a Monte Carlo sample of muons is shown in Fig. 5.23. The parameters of the fit for data and Monte Carlo are shown in Table 5.7, for central muons with no nearby reconstructed jet ($\Delta R > 1.0$).

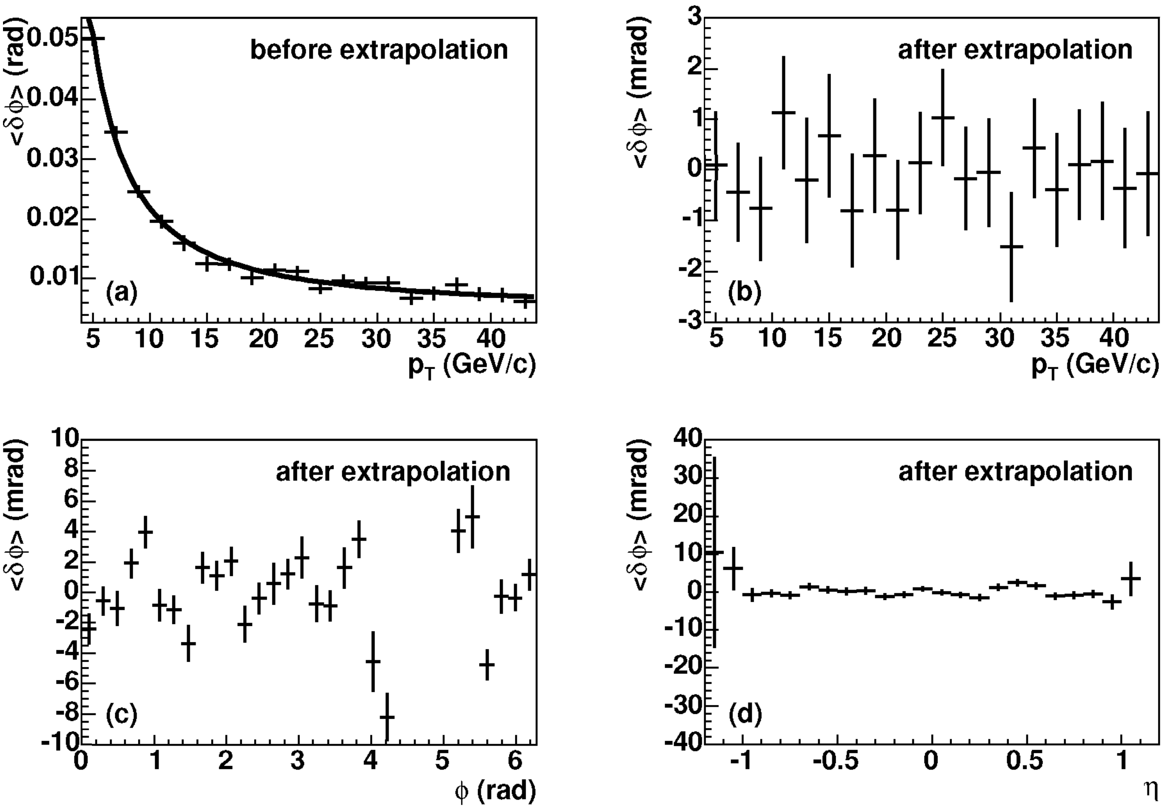

Figure 5.23: Extrapolation of the local muon ϕ coordinate to the centre of the detector. Figure (a) shows the result of the fit (see Eq. 5.37). Figures (b) through (d) show the difference between locally and centrally measured ϕ as a function of p_T, ϕ and η, respectively, after extrapolation.

	α (rad)	β (rad/(GeV/c)$^\gamma$)	γ	χ^2/ndf
WAMUS data	-0.014 ± 0.004	0.217 ± 0.006	0.67 ± 0.05	$17/17$
WAMUS MC	0.0051 ± 0.0006	0.52 ± 0.06	1.50 ± 0.08	$25/17$

Table 5.7: Parameters for the extrapolation (Eq. 5.37) of locally measured muon azimuth to the centre of the detector.

The large difference between data and MC is mostly due to the strong correlation between the fit parameters.

5.6.7 Muon reconstruction efficiency

The muon reconstruction efficiency in Monte Carlo was determined by matching reconstructed muons to the Monte Carlo muons in a cone of size $\Delta R < 0.3$. The reconstruction efficiencies in the central and forward local muon systems as a function of p_T, η and ϕ are shown in Fig. 5.24. The overall efficiency for muons with $p_T > 6$ GeV/c in the central region is $(48.0 \pm 0.4)\%$.

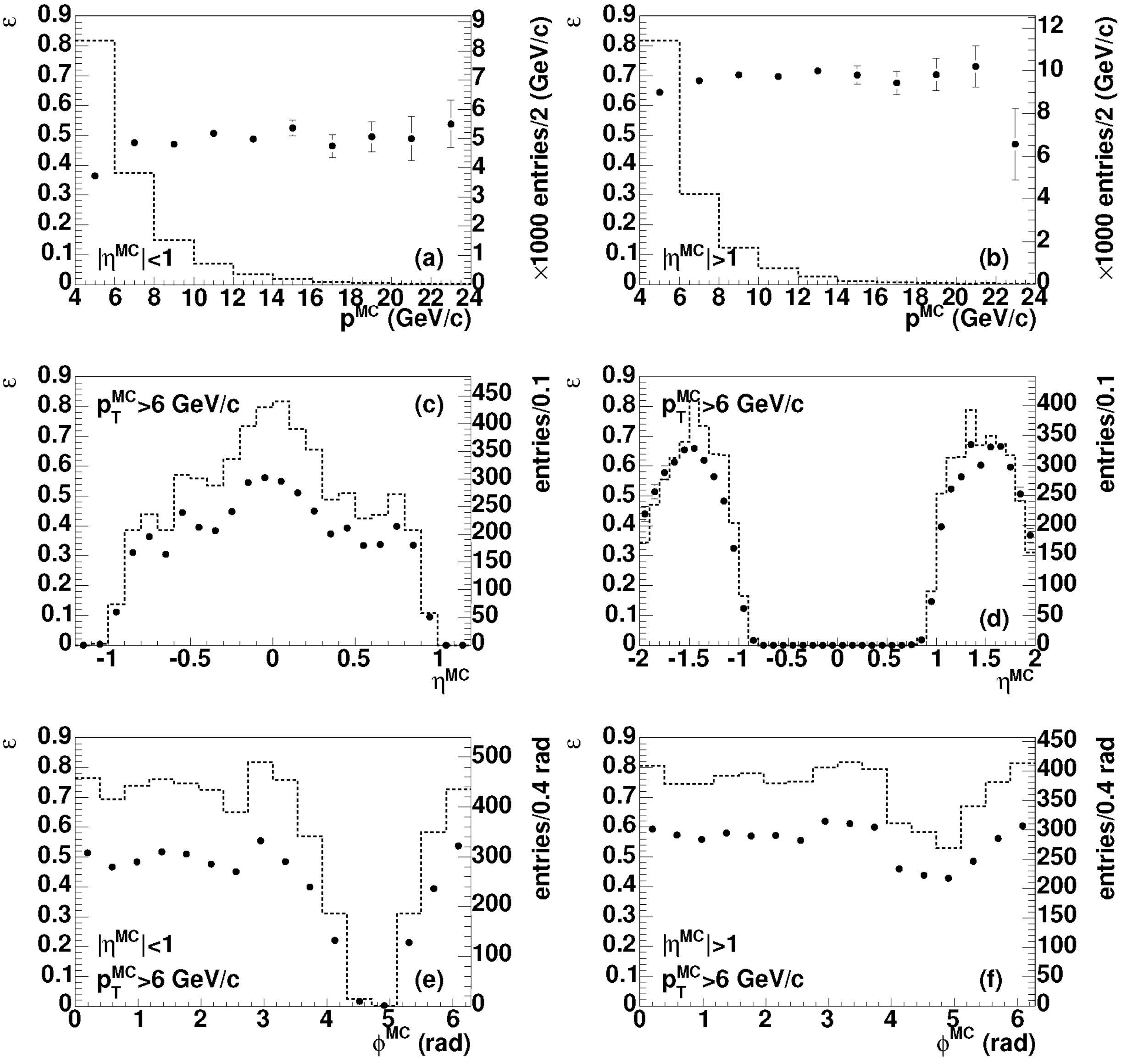

Figure 5.24: Muon reconstruction efficiency in WAMUS (left) and FAMUS (right) in the Monte Carlo simulation as a function of p_T (a,b), η (c,d) and ϕ (e,f). A cut of $|\eta^{\mathrm{MC}}| < 1$ (WAMUS) and $|\eta^{\mathrm{MC}}| > 1$ (FAMUS) was applied for the efficiencies as a function of p_T^{MC} and ϕ^{MC} and a cut of $p_T > 6$ GeV$/c$ for the efficiencies as a function of ϕ^{MC} and η^{MC}. The dashed histograms show the distributions of reconstructed muons.

The muon reconstruction efficiency in data can be determined by looking for decay muons of resonances reconstructed in the central tracker. Because of the limited efficiency of the central tracking systems, it was not possible to perform this analysis on the present data set. In a previous study[100], the reconstruction efficiency has been determined from the separate hit, segment finding and track fitting efficiencies. The reconstruction efficiency in Monte Carlo was found to describe the data well.

5.6.8 Muon resolution

The resolution of local muons is measured with respect to matched central tracks in an isolated muon sample ($\Delta R(\mu - \text{jet}) > 1.0$). The resolution of the central tracker is far better than that of the local muon system. Neglecting the finite resolution of the central tracker, the relative deviation of the measured momentum from the true momentum can be characterised as [120]

$$\Delta = \left(\frac{p}{q}\right)^{\text{track}} \times \left(\left(\frac{q}{p}\right)^{\text{track}} - \left(\frac{q}{p}\right)^{\text{local}}\right), \tag{5.38}$$

where q^{track} and p^{track} are the charge and transverse momentum measured in the central tracker and q^{local} and p^{local} are measured in the muon system. The momentum resolution is then given by the width of the distribution of Δ,

$$\frac{\sigma(p)}{p} = \frac{\sigma(q/p)}{q/p} = \sigma(\Delta). \tag{5.39}$$

By performing the measurement in several bins of global muon p, the dependence of the resolution on p is determined. The resolution as a function of the p of tight muons reconstructed in the forward and central muon systems is shown in Fig. 5.25.

To avoid any bias due to the track matching method, the tracks were matched in $(\eta \times \phi)$ only. The track and the muon were required to match within $\Delta\phi < 0.1$ and $\Delta\eta < 0.1$. No other tracks were allowed to be present within $\Delta R < 0.3$.

From Run I, the functional form of the resolution as a function of p was found to be [120]

$$\frac{\sigma(p)}{p} = \frac{\alpha(p - \beta)}{p} \oplus \gamma p, \tag{5.40}$$

where α is the multiple scattering contribution, β accounts for the energy loss in the calorimeter and γ is the contribution due to the finite position resolution of the muon chambers, with p in GeV/c. Based on the expected energy loss in the detector, β was fixed to a value of 2 GeV. The results of the fit are shown in Table 5.8. The results for the fit with β as a free parameter are also shown and validate the use of the fixed value[4]. The resolutions for the central and forward systems as a function of p are shown in Fig. 5.25.

The angular resolution is determined by comparing the direction of the local muon track with the direction of the matched central track. The tracks were matched within a cone of $\Delta R < 0.5$, with no additional track present within $\Delta R < 0.6$. An additional cut on the momentum of the track of $p^{\text{local}}/3 < p^{\text{track}} < \frac{5}{3} \times p^{\text{local}}$ was used. The distributions for $(\eta^{\text{local}} - \eta^{\text{track}})$ and $(\phi^{\text{local}} - \phi^{\text{track}})$ for tight muons with $p_T > 6\ \text{GeV}/c$ are shown in Fig. 5.26 (ϕ) and Fig. 5.27 (η). The resolutions are determined from Gaussian fits to the distributions. The resolutions are given in Table 5.9.

---

[4] A priori, a higher value for β might indeed be expected for the forward muon system.

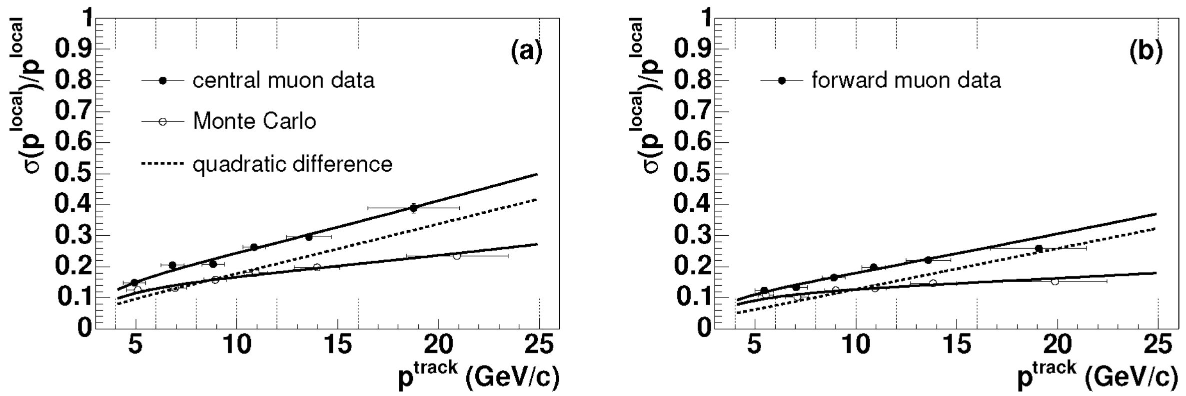

Figure 5.25: Momentum resolution in the forward (a) and central (b) muon system. The functional form of the fit is given in Eq. 5.40 and the fit parameters are given in Table 5.8. The dashed lines indicate the quadratic difference between the data and Monte Carlo resolutions.

	α	β (GeV/c)	γ (GeV/c)$^{-1}$	χ^2/ndf
WAMUS data	0.20 ± 0.03	2	0.019 ± 0.001	5.6/4
WAMUS MC	0.18 ± 0.01	2	0.009 ± 0.001	2.5/4
WAMUS data	0.20 ± 0.07	2.1 ± 1.0	0.018 ± 0.003	5.6/3
WAMUS MC	0.19 ± 0.06	2.3 ± 1.1	0.008 ± 0.003	2.5/3
FAMUS data	0.14 ± 0.02	2	0.014 ± 0.001	3.8/4
FAMUS MC	0.147 ± 0.009	2	0.005 ± 0.001	5.3/4
FAMUS data	0.22 ± 0.09	3.1 ± 1.0	0.010 ± 0.006	3.5/3
FAMUS MC	0.17 ± 0.03	2.5 ± 0.6	0.002 ± 0.004	4.8/3

Table 5.8: Parameters of the fit to the muon resolution (Eq. 5.40). The results are shown both with a fixed value of $\beta = 2$ GeV and with β as a free parameter. The graphic representations of the fits are shown in Fig. 5.25.

	σ_ϕ (mrad)	σ_η ($\times 10^{-3}$)
WAMUS data	46.72 ± 0.09	35.60 ± 0.07
WAMUS MC	39.27 ± 0.07	30.82 ± 0.05
FAMUS data	47.83 ± 0.06	34.41 ± 0.05
FAMUS MC	53.69 ± 0.08	34.89 ± 0.05

Table 5.9: Muon angular resolutions in data and Monte Carlo. The fit region was constrained to the mean $\pm 3\sigma$. The non-Gaussian tails are small (see Fig. 5.26 and 5.27).

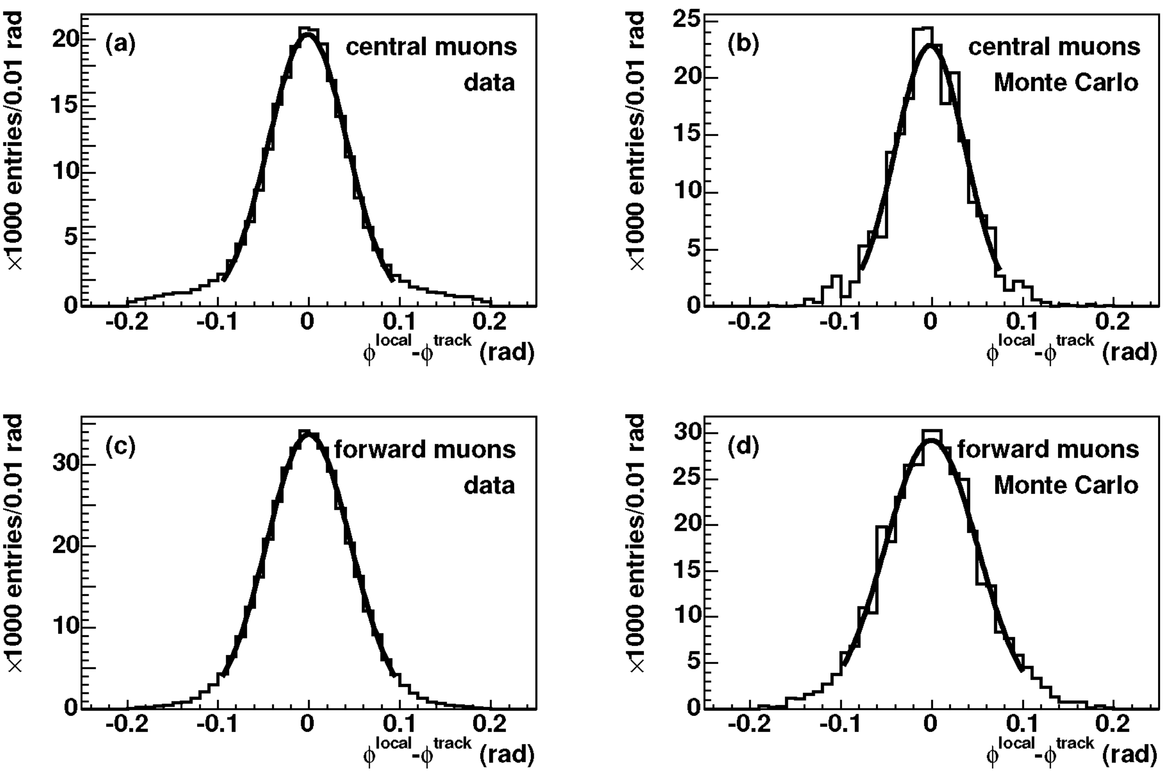

Figure 5.26: Azimuthal angle (ϕ) resolution of local muon tracks in data. Plots (a) and (b) show the ϕ resolution in the central muon system for data and Monte Carlo, plots (c) and (d) show the resolution in the forward muon system.

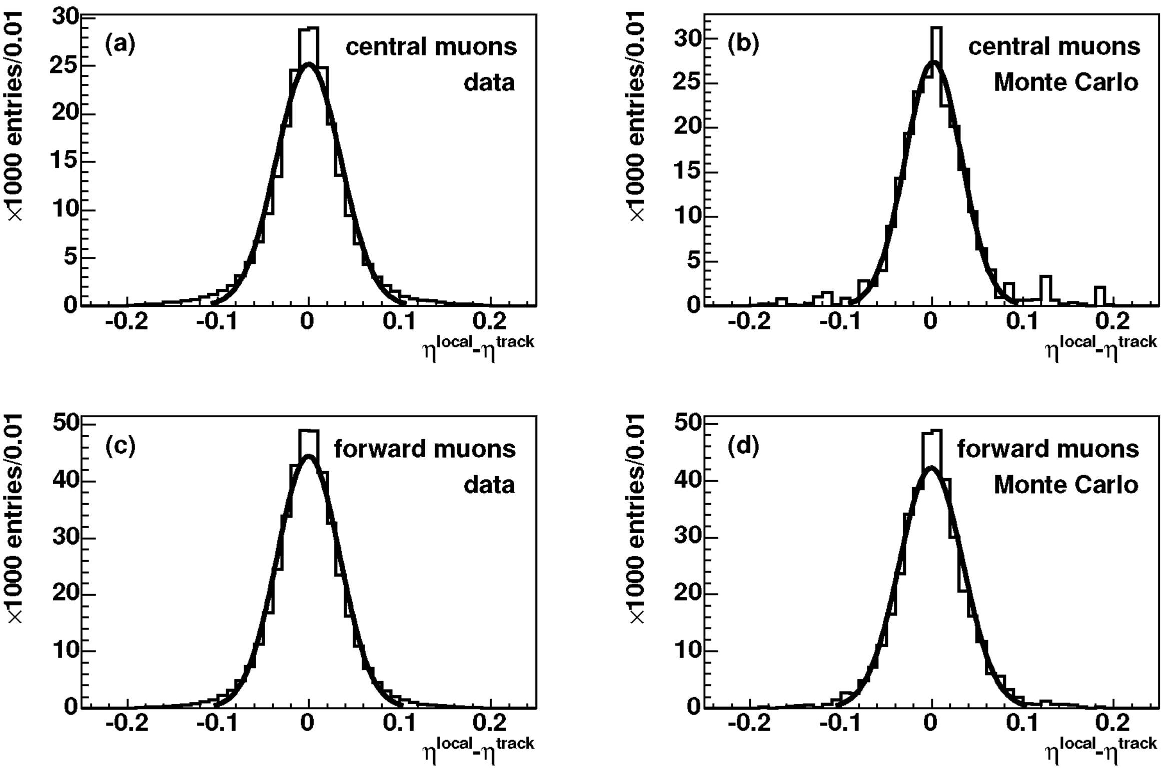

Figure 5.27: Polar angle (η) resolution of local muon tracks in data. Plots (a) and (b) show the η resolution in the central muon system for data and Monte Carlo, plots (c) and (d) show the resolution in the forward muon system.

Chapter 6

Identification of b jets

Two distinct properties of B decays are commonly used to identify b jets. *Lepton* tags employ the properties of the lepton resulting from the decay of the $\mathrm{W}^{\pm}$ boson emitted by the decay of the b quark (see Fig. 6.1.) Because of the heavy mass of the B hadron, this lepton has a large average transverse momentum relative to the flight direction of the B hadron. Since the hard fragmentation of the b quark ensures that most of the available momentum is carried by the B hadron, this relative transverse momentum can be directly measured with respect to the jet resulting from its decay. Muon tagging has been used successfully by DØ in Run I [33, 35, 36, 47], and will be discussed in more detail below. Electrons can also be used but are harder to identify in a jet environment. The primary backgrounds are charm jets and decays-in-flight of charged particles in light quark and gluon jets. The lepton tag method suffers mostly from the low branching fraction $BR(\mathrm{b} \to \ell\nu_\ell \mathrm{X}) = (10.7 \pm 0.2)\%$ [1]. The muon tagging method used in this thesis is described in Section 6.1.

Because of their relatively long lifetime, the decay vertex of B hadrons is displaced from the primary vertex. *Lifetime* tags use the long lifetime of B hadrons ($\tau = 1.56 \pm 0.01$ ps [1] for a typical admixture of bottom particles at high energies) by looking for particles in a jet that do not originate from the primary interaction point in the event. This can be done either by reconstructing the decay vertex of the B hadron, or by using the lifetime information carried by individual tracks: the trajectories of the decay products of a long-lived particle do not point back directly to the primary vertex but have a large impact parameter. The information from individual tracks can be combined by simply counting the number of tracks with large impact parameters or in a more sophisticated probabilistic manner. In this thesis, a jet lifetime probability tag will be used to identify b jets in a sample that has been enriched by requiring that a muon tag is also present. The jet lifetime probability tag is described in Section 6.2.

6.1 Muon tag

The decay of a high-energy B hadron to a μX final state leads to a jet of fragmentation and decay particles and an associated muon. The jet and the associated muon are referred to as a “muon jet”. Because of the large mass of the B hadron the muon has a large average transverse momentum with respect to the jet axis.

Muons inside jets are also produced by decays of charmed hadrons, $\tau \to \mu$ decays and by the

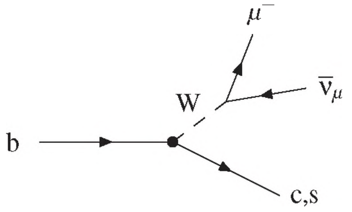

Figure 6.1: Semileptonic decay of a b quark.

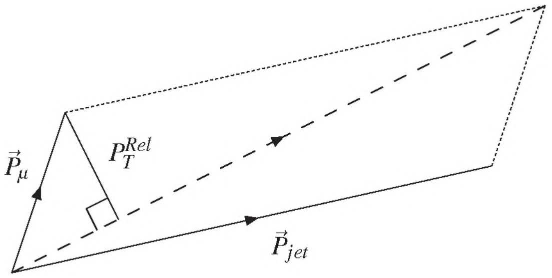

Figure 6.2: Definition of the P_T^{Rel} tagging variable. The dashed line represents the μ+jet axis.

decays-in-flight of charged pions, kaons and other light mesons inside a jet. To distinguish the B hadron decays from these background processes, the P_T^{Rel} variable is used.

The P_T^{Rel} tagging method was first described in [6], and in DØ Run II in [100]. The P_T^{Rel} distribution in data is compared with distributions (*templates*) derived from Monte Carlo simulations to determine the fraction of b jets in a sample of muon jets. The fraction is determined by a fit which weighs the templates to match the data distribution, taking into account the statistical uncertainty of both the data and the templates.

The templates must match the expected distributions in data for the signal and background sources. To this end, the differences between resolutions and efficiencies in data and those in the Monte Carlo simulation must be correctly taken into account. The generation of the templates, the template fit and the results in a sample of muon jets are described in the following sections.

6.1.1 P_T^{Rel} templates

The P_T^{Rel} tagging variable is defined as the transverse momentum of the muon with respect to the combined μ+jet axis (see Fig. 6.2). Due to the large mass difference of the b quark and its decay products, the value of P_T^{Rel} is on average higher for B decays than for background processes. The P_T^{Rel} distributions of Monte Carlo muons with respect to an associated particle jet are shown in Fig. 6.3, for $\mathrm{b} \rightarrow \mu$ (including $\mathrm{b} \rightarrow \mathrm{c} \rightarrow \mu$), $\mathrm{c} \rightarrow \mu$ and $\pi/\mathrm{K} \rightarrow \mu$ decays. Even at this level, it is nearly impossible to separate the $\mathrm{c} \rightarrow \mu$ and $\pi/\mathrm{K} \rightarrow \mu$ decays. The finite muon and jet momentum and angular resolutions result in further smearing of these distributions. These processes are therefore treated as a single background source. The P_T^{Rel} distribution for $\mathrm{b} \rightarrow \mathrm{c} \rightarrow \mu$ decays is almost identical to that of $\mathrm{c} \rightarrow \mu$ decays. For a statistical determination of the fraction of b jets in a sample they are included in the b signal template.

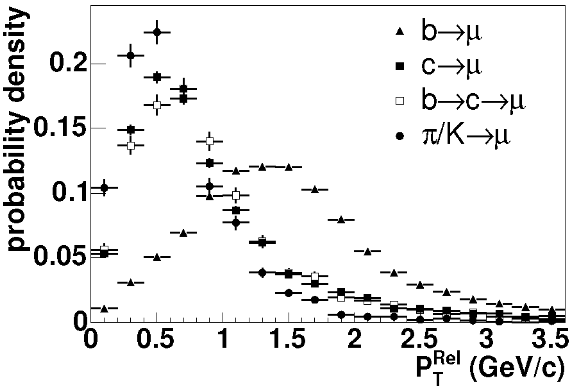

Figure 6.3: True Monte Carlo P_T^{Rel} distributions for muons from various decay processes.

The templates used in the fit are generated by matching a reconstructed muon to a reconstructed jet in the Monte Carlo simulation. The muon is required to lie within a cone of $\Delta R < 0.7$ around the jet in $(\eta \times \phi)$ space. Each muon can only be assigned to the jet closest to it; if more than one muon can be associated with a jet, only the best reconstructed muon (by lowest local fit χ^2) is used. The matching criteria used in data and in the simulation are identical.

Especially in gluon splitting events, two jets may be very close together in ΔR. In that case, it is possible that the muon is assigned to the wrong jet. This effect was evaluated in Monte Carlo. Defining the b jet as the jet closest to the B hadron decaying semileptonically, the decay muon was associated with another jet in only $(0.38 \pm 0.09)\%$ of all cases. For all other processes leading to muons in jets, this fraction was significantly lower.

6.1.2 Signal template

The signal template was generated by fully simulating and reconstructing $\mathrm{b\bar{b}}$ events with at least one of the b quark decays resulting in a muon. Jets were identified as b jets by requiring the presence of a B hadron within a $\Delta R < 0.5$ cone around the jet axis. To reject fake muons and muons originating from light particle decays, the reconstructed muon was matched to a Monte Carlo muon originating from a b flavoured parent within a cone of $\Delta R < 0.3$.

Muons from "cascade" b → c → μ decays are included in the signal template. While the P_T^{Rel} distribution for cascade decays is much more similar to that for c → μ decays than that for b → μ decays, the total fraction of b jets including cascade decays can still be determined on a statistical basis by the fit. Because all hadrons containing a b were forced to decay directly to μX or τX, the cascade decays have been given a weight to recover the correct fraction of b → c → μ decays with respect to the total number of b → μX decays. The weight is derived from the branching fractions $BR(\mathrm{b} \to \mu)$ and $BR(\mathrm{b} \to \mathrm{c} \to \mu)$.

The P_T^{Rel} distributions of muons with respect to the parent B hadron are identical for gluon splitting, flavour excitation and flavour creation processes. In high-energy gluon splitting events, however, the presence of $\mathrm{b\bar{b}}$ jets (where both the b and $\mathrm{\bar{b}}$ quark decay products end up in the same reconstructed jet) leads to an enhanced tail in the P_T^{Rel} distribution with respect to the MC particle

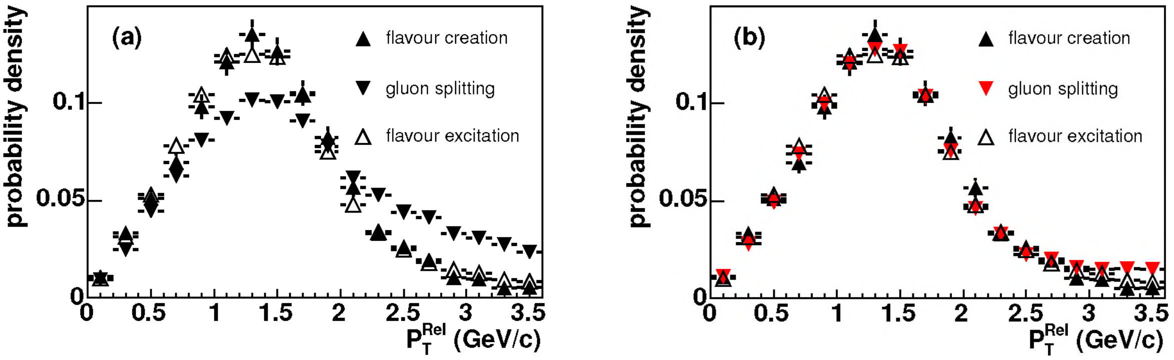

Figure 6.4: Muon P_T^{Rel} distribution with respect to an MC particle jet with $E_T > 20$ GeV. Distribution (a) shows an enhanced tail for gluon splitting events, due to the presence of b$\bar{\text{b}}$ jets. In distribution (b), b$\bar{\text{b}}$ jets have been explicitly removed.

jet (see Fig. 6.4(a)). This effect is more pronounced at higher values of jet E_T. Requiring that only one of the b$\bar{\text{b}}$ quark pair is found within a $\Delta R < 0.5$ cone around the jet axis, the difference between the templates disappears (see Fig. 6.4(b)).

In Chapter 7, the presence of a second tagged jet in the event helps to reduce the contribution of b$\bar{\text{b}}$ jets, so they are explicitly excluded from the P_T^{Rel} templates. Even without the requirement of a second tagged jet, the contribution of b$\bar{\text{b}}$ jets is small; no discrepancy was found between the P_T^{Rel} templates derived from inclusive b$\bar{\text{b}}$ and flavour creation only samples in [100], using fully reconstructed muons and jets.

6.1.3 Background template

Two separate background templates were generated. A c $\longrightarrow \mu$ template was generated in the same way as the b $\longrightarrow \mu$ template. Jets were identified as c jets by requiring the presence of a charmed hadron within a $\Delta R < 0.5$ cone around the jet axis. The reconstructed muon was matched to a Monte Carlo muon originating from a c flavoured parent within a cone of $\Delta R < 0.3$.

The main background from non-heavy flavour events comes from in-flight decays of charged pions and kaons. Because the PYTHIA event generator treats these particles as stable particles, the full simulation must be run for each event. To efficiently generate a large sample of decay-in-flight events, a random charged pion or kaon above a threshold of $p_T > 4$ GeV$/c$ was forced to decay inside the detector volume. The decay took place during the detector simulation step. To account for the probability of the decay to occur naturally, each event is weighed with the decay probability as a function of the pion or kaon p_T. The resulting weighted muon p_T and P_T^{Rel} distributions are shown in Fig. 6.5, together with the distributions in a Monte Carlo sample without forced decays. The small discrepancy in the p_T distributions can be ascribed to the p_T cutoff used for the generation of the samples in PYTHIA.

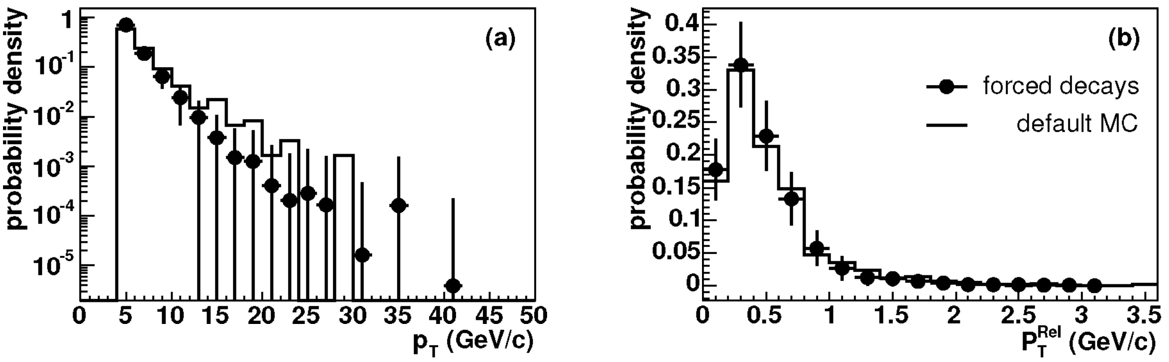

Figure 6.5: Weighted muon p_T (a) and P_T^{Rel} (b) distributions in the light jet background Monte Carlo simulation.

6.1.4 Resolution smearing

To be able to fit Monte Carlo distributions to data, the Monte Carlo must be corrected to account for the difference in resolution in the simulation and in the real experiment. The P_T^{Rel} variable depends on the transverse momentum of the jet and the muon and their angles. These are smeared according to the resolutions measured in Chapter 5.

The azimuthal direction (ϕ) of Monte Carlo jets was smeared with a Gaussian function determined from the difference between the data and Monte Carlo distributions measured in Section 5.1.7, keeping η and E constant. Because the resolution depends on the parametrisation, the amount of smearing was chosen such that a Kolmogorov test yielded a maximum probability for the match between the data and Monte Carlo distributions. The η resolution is assumed to be the same as the ϕ resolution. The η coordinate was therefore smeared with the same function as the ϕ coordinate.

The jet E_T resolution was measured in Section 5.1.6 (see Eq. 5.22). Because the E_T resolution depends on the η resolution as well as the energy resolution, the E_T resolution in Monte Carlo was remeasured after smearing the angular coordinates of the jets. The remaining difference between the E_T resolutions was taken into account by smearing the jet energy E with a Gaussian uncertainty determined by the squared difference between the data and the new Monte Carlo resolutions given in Table 6.1, keeping the jet angle unchanged.

The muon p resolutions in data and Monte Carlo are given in Section 5.6.8 (see Eq. 5.38). The momentum of muons in Monte Carlo was smeared according to the quadratic difference between the data and Monte Carlo resolutions as a function of p, given in Table 5.8. The muon ϕ and η directions were smeared with a Gaussian function with a width equal to the quadratic difference between the data and Monte Carlo resolutions measured in Section 5.6.8, keeping p constant. After smearing, the p, η and ϕ resolutions in Monte Carlo closely resemble those in data (see Fig. 6.6 and 6.7).

	data	Monte Carlo	Monte Carlo η smeared	Monte Carlo η and E smeared
N	7.1 ± 1.2	3.4 ± 5.7	5.5 ± 2.4	5.8 ± 2.3
S	0.8 ± 1.12	1.36 ± 0.24	1.0 ± 0.6	1.02 ± 0.55
C	0.134 ± 0.022	0.05 ± 0.10	0.11 ± 0.04	0.099 ± 0.047
χ^2/ndf	$24/8$	$11/8$	$13/8$	$11/8$

Table 6.1: Values of the fit parameters (see Eq. 5.24) of the jet energy resolution fit for data and Monte Carlo. The Monte Carlo jet η and ϕ coordinates were smeared before the E_T resolution measurement.

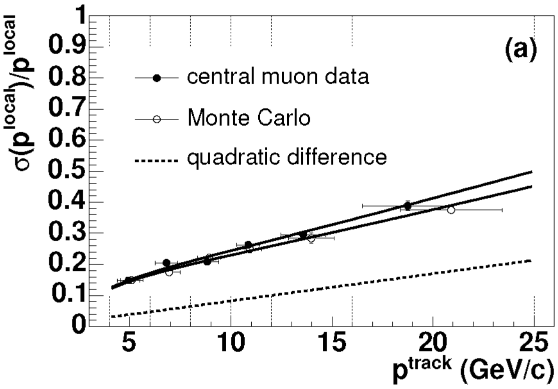

Figure 6.6: Muon momentum resolution in data (solid points) and smeared Monte Carlo (open circles).

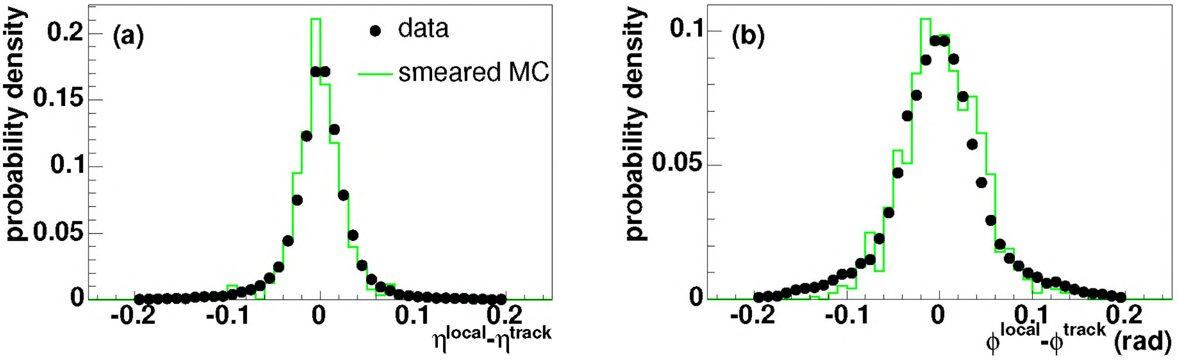

Figure 6.7: Muon η (a) and ϕ (b) resolution in the central muon system for muons with $p_T >$ 6 GeV$/c$ in data (solid points) and smeared Monte Carlo (line).

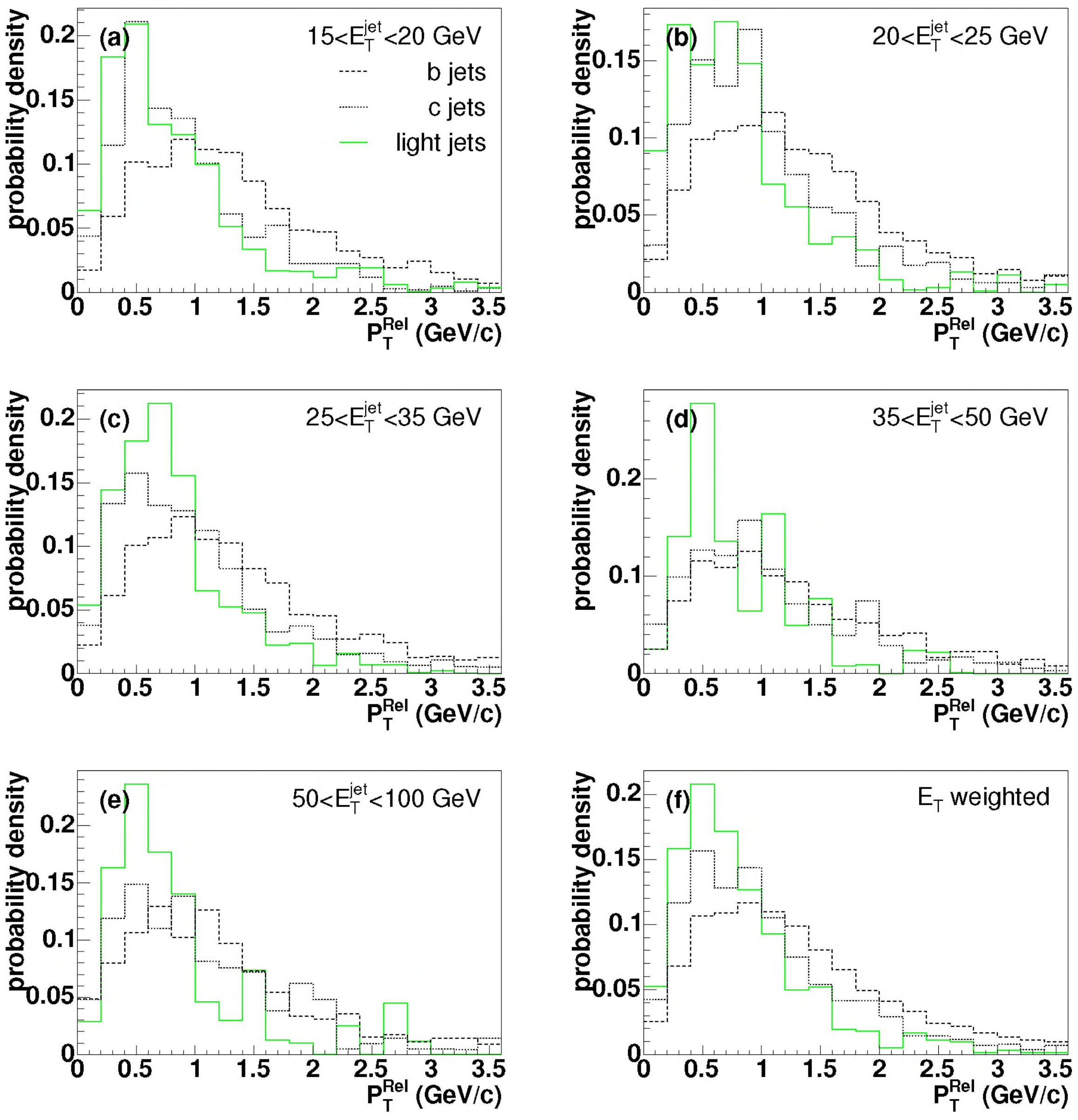

Figure 6.8: P_T^{Rel} templates in five E_T bins with edges $E_T = 15, 20, 25, 35, 50, 100$ GeV (a–e) and for the full E_T range, weighted with the trigger efficiency as a function of E_T (f).

6.1.5 Jet E_T and trigger efficiency dependence

Despite the fact that P_T^{Rel} is a boost-invariant quantity, the resolution dependence of the detector on the E_T of the jet and the p_T of the muon may affect the P_T^{Rel} distributions. For the determination of the efficiency of the lifetime tag in Section 6.2.10, this is taken into account by generating templates in several bins of jet E_T. The final templates in these five bins are shown in Fig. 6.8.

In Chapter 7, a measurement over the entire E_T range is done and a single template is used, with each jet assigned a weight according to the measured trigger efficiency (see Section 4.2.4).

6.1.6 Template fit results

The proportions of b jets and background jets in the data sample are determined by fitting the Monte Carlo P_T^{Rel} distributions to the data. A binned maximum likelihood fit is used, taking into account the finite size of the Monte Carlo samples. The method is fully described in [121]. A few important issues are discussed below.

The number of data events in bin i is denoted by d_i. The predicted number of events in each bin is given by the number of Monte Carlo events a_{ji} from source j in bin i and is given by

$$f_i = N_D \sum_{j=1}^{m} P_j a_{ji}/N_j, \tag{6.1}$$

where N_D is the total number in the data sample, and N_j the total number in the Monte Carlo sample for source j. The P_j are the proportions of the different sources and should sum to unity. Writing $p_j = N_D P_j/N_j$, Eq. 6.1 becomes

$$f_i = \sum_{j=1}^{m} p_j a_{ji}. \tag{6.2}$$

Using Poisson statistics, the log likelihood to be maximised is

$$\ln \mathcal{L} = \sum_{i=1}^{n} d_i \ln f_i - f_i. \tag{6.3}$$

In the case of limited Monte Carlo statistics, the distribution $\{a_{ji}\}$ for each sample is generated from the (unknown) *true* distribution $\{A_{ji}\}$. The correct prediction for the number of events in bin i is then

$$f_i = \sum_{j=1}^{m} p_j A_{ji}. \tag{6.4}$$

The total log likelihood to be maximised is then the combined likelihood of the observed $\{d_i\}$ and the observed $\{a_{ji}\}$

$$\ln \mathcal{L} = \sum_{i=1}^{n} d_i \ln f_i - f_i + \sum_{i=1}^{n}\sum_{j=1}^{m} a_{ji} \ln A_{ji} - A_{ji}. \tag{6.5}$$

The number of predicted events is automatically normalised to the number of data events by maximising the likelihood. Likewise, the proportions P_j correctly sum to unity. The quality of the fit can be estimated using a likelihood ratio (see Appendix A.)

Event weights

Event weights in the Monte Carlo samples are taken into account by determining the bin-by-bin weights w_{ji} of the P_T^{Rel} distribution for each sample. They are included in the fit by changing Eq. 6.4 to

$$f_i = \sum_{j=1}^{m} p_j w_{ji} A_{ji}. \tag{6.6}$$

	this analysis		Reference [100]	
E_T range	b jet fraction	background	b jet fraction	background
15-20 GeV	0.60 ± 0.03	0.40 ± 0.03		
20-25 GeV	0.65 ± 0.02	0.36 ± 0.03	0.39 ± 0.06	0.61 ± 0.07
25-35 GeV	0.61 ± 0.02	0.41 ± 0.03	0.22 ± 0.07	0.78 ± 0.08
35-50 GeV	0.70 ± 0.03	0.33 ± 0.04	0.24 ± 0.06	0.76 ± 0.07
50-100 GeV	0.49 ± 0.10	0.58 ± 0.10	0.14 ± 0.08	0.86 ± 0.1
Overall	0.63 ± 0.01	0.37 ± 0.01		

Table 6.2: The b jet fraction in five E_T bins of the muon+jet sample.

In the code, the proportions P_j are normalised to the observed Monte Carlo distributions $\{a_{ji}\}$. If the weights w_{ji} for a sample vary widely between bins *and* the distribution $\{a_{ji}\}$ for that sample is very different from the distribution $\{A_{ji}\}$ (which is the case if the size of the Monte Carlo samples is much smaller than that of the data sample), the normalisation is no longer automatically correct and the P_j may sum to a value different from unity. This can be seen most pronounced in Fig. 6.9(e).

Fit results

The fit is performed separately in each E_T bin. The results of the fits are shown in Fig. 6.9. The fraction of b $\rightarrow \mu$ decays in each bin is given in Table 6.2.

The fractions of b jets are compared to those found in [100] in Table 6.2. The fractions found here are larger than those found in [100], but unlike that reference include b $\rightarrow$ c $\rightarrow \mu$ decays. In addition, the data from [100] do not use a Level 3 jet trigger term.

The fit is also performed on the entire data set using the weighted templates. The result of the fit is shown in Fig. 6.9(f). The overall b jet fraction as determined by this fit is consistent with the results obtained using the E_T-binned templates (see Table 6.2).

6.1.7 Systematic uncertainties

Smearing of Monte Carlo distributions

In principle, smearing the Monte Carlo distributions introduces a sensitivity to errors in the parametrisation of resolutions in data and Monte Carlo. The resulting uncertainty is small since only the *difference* between data and Monte Carlo has to be taken into account. In addition, as the resolutions improve, the room for differences between data and Monte Carlo decreases. The uncertainty due to the smearing procedure is deemed negligible for the rest of this thesis.

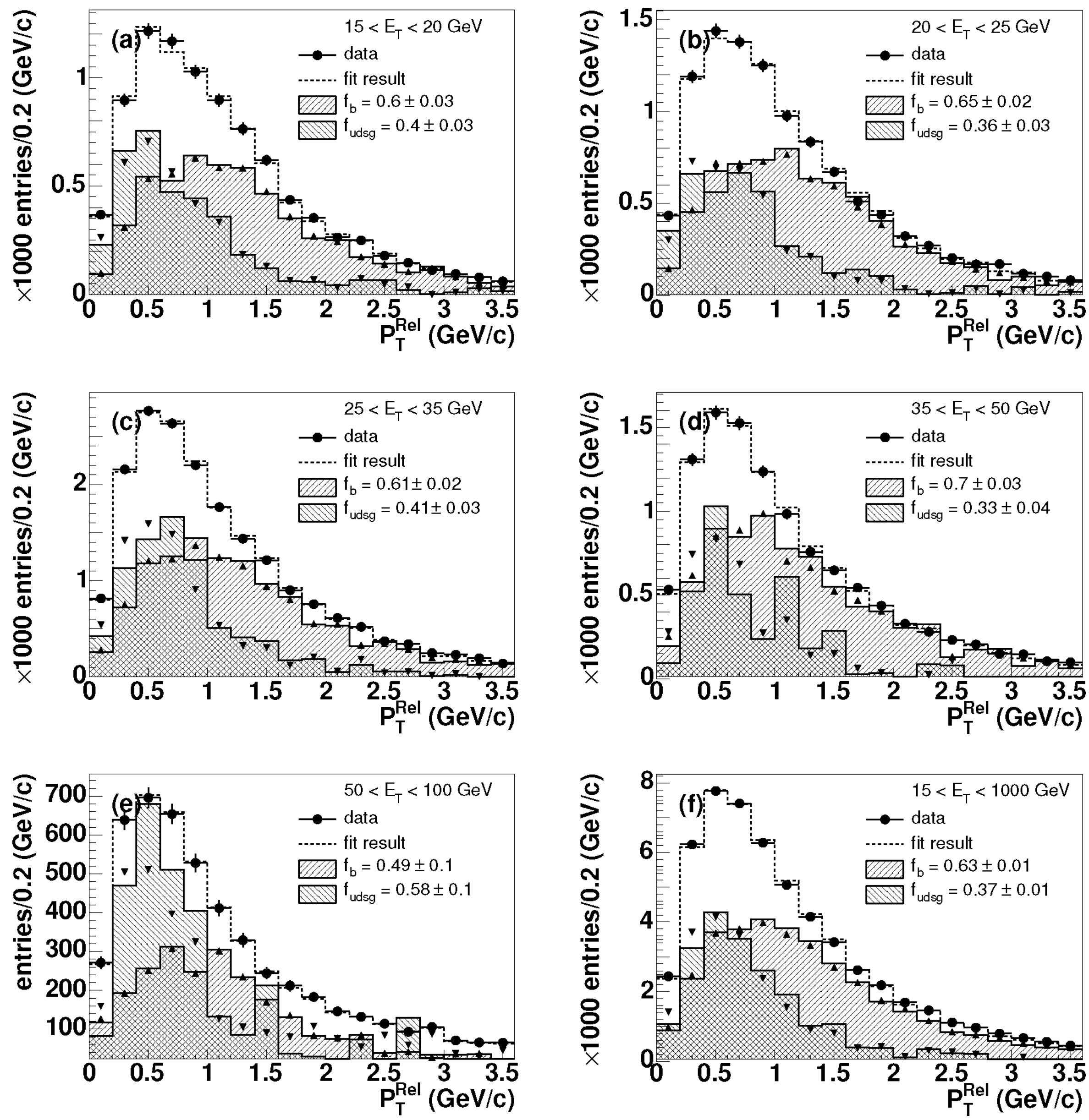

Figure 6.9: Results of the P_T^{Rel} fit to the muon+jet sample in five bins of jet E_T (a–e) and over the entire range (f). The dashed line histogram shows the result of the fit. The data are indicated by the solid circles. For each Monte Carlo sample, the dashed histogram shows the observed distribution a_{ji}; the triangular markers show the "true" distribution A_{ji} estimated by the fit procedure. The uncertainties include the effects of both data and Monte Carlo statistics.

Fragmentation

The modelling of the fragmentation of the b quarks affects the P_T^{Rel} distribution in two ways:

- In the case of hard fragmentation, most of the available energy is carried by the B hadron and the jet momentum vector is very strongly correlated with that of the B hadron. If the fragmentation is softer, the b jet is not as good a representation of the momentum vector of the B hadron;
- If the fragmentation is hard, there is more energy available for the muon resulting from the decay of the B hadron.

The effect of changing the fragmentation function parameter is evaluated in Section 7.5.6.

Monte Carlo tuning

As a final remark, the P_T^{Rel} distributions also depend on other inputs of the Monte Carlo simulation. For example, the transverse fragmentation function is approached in PYTHIA by a Gaussian with a fixed width. An optional second Gaussian can be added to describe long tails. The background P_T^{Rel} distribution (including $c\bar{c}$) is very sensitive to the transverse momentum distribution of primary hadrons. The width of the transverse momentum distribution and other parameters are tuned to the results of other experiments. In this thesis, the default parameters for PYTHIA 6.202 are used [122].

6.2 Jet lifetime probability tag

The relatively long lifetime and heavy mass of B hadrons lead to a significant displacement of their decay products from the primary interaction point. This displacement can be quantified by the transverse impact parameter (d_0) of the reconstructed tracks, defined as the distance of closest approach in the transverse plane of the tracks to the interaction point (see Section 5.3.1). To first order, the impact parameter does not depend on the boost of the system but only on the lifetime of the decaying particle and on the transverse kick it imparts to its decay products.

The probability that a track originates from the primary interaction point is determined by comparing its impact parameter to a resolution function determined from the distribution of background tracks in data. From the background probabilities of all tracks associated with a jet, the probability that the jet originates from a (zero-lifetime) background process can be computed. A cut on this probability is used to tag b jets.

6.2.1 Signed impact parameter significance

Instead of using the detector signed (see Section 5.3.5) impact parameter d_0, a “physics signed” impact parameter b_0 is defined for each track based on the position of the virtual crossing point of the track and the associated jet with respect to the interaction point (see Fig. 6.10). The sign is negative if the track crosses the jet axis behind the interaction point and positive if this virtual crossing occurs in front of of the interaction point. “Behind” and “in front” are defined by the direction of the jet. For particles produced at the primary interaction point, the distribution of b_0

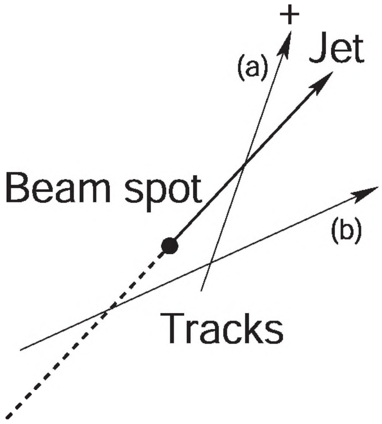

Figure 6.10: Definition of the physics signed impact parameter b_0. The impact parameter is defined as positive if the track crosses the jet axis downstream of the beam position (a). If the track crosses the jet axis behind the beam position, the impact parameter is negative (b).

is symmetrically smeared around the origin. For the decay products of long-lived particles, the distribution has an enhanced positive tail.

Because of the finite resolution of individual tracks, which may be degraded by multiple scattering, missing hits or a poor track fit, the impact parameter itself is a poor discriminant between long-lived particle decay tracks and background tracks. Instead, the impact parameter significance is used, defined as the impact parameter divided by the uncertainty

$$S = b_0/\sigma_{b_0}. \tag{6.7}$$

The impact parameter and significance can be defined in three as well as in two dimensions, but the inclusion of the longitudinal dimension is only useful if the longitudinal resolution is not much worse than that in the transverse plane. As the resolution of the DØ SMT is much worse along the beam direction than in the transverse plane and use of a 3D impact parameter requires the use of a primary vertex as the reference point, only the 2D impact parameter with respect to the beam position is used in this thesis.

6.2.2 Track background probability

The probability that a track with significance S is consistent with zero-lifetime background processes can be determined by comparing the significance to the distribution for background tracks. Since all tracks with lifetime greater than zero are expected to have positive impact parameters, the distribution of background tracks can be derived from the negative significance distribution in data. The probability that a track with $S > 0$ comes from a zero-lifetime process is defined as

$$P(S) = \frac{\int_S^\infty f_{\text{res}}(S')\mathrm{d}S'}{\int_0^\infty f_{\text{res}}(S')\mathrm{d}S'}, \tag{6.8}$$

where $f_{\text{res}}(S)$ is the resolution function. In this analysis, no parametrisation of the resolution function is used but instead the negative significance distribution itself is used as the resolution

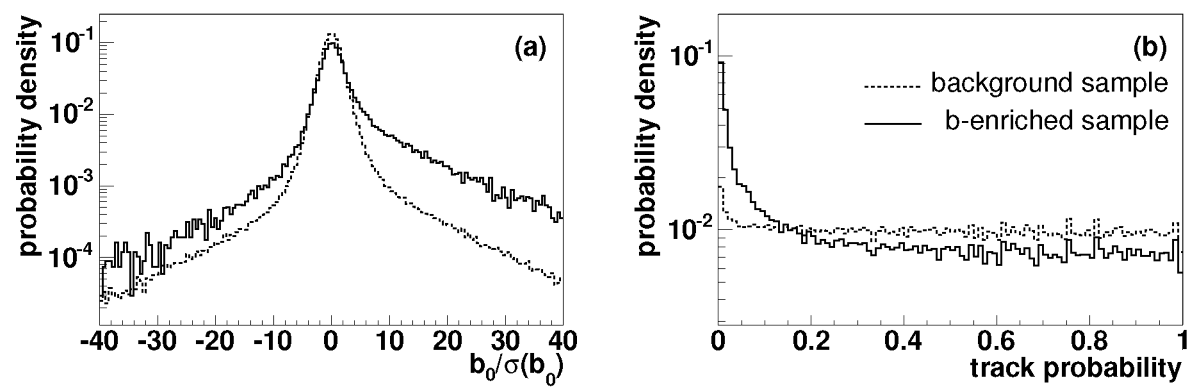

Figure 6.11: Signed impact parameter significance (a) and track background probability (b) in data for tracks from a background sample (dotted lines) and from a sample with high b jet content (solid lines).

function. The integral over f_{res} in Eq. 6.8 then becomes an integral over the distribution of $-b_0$. The resolution function is determined separately for several categories of track quality (see Section 6.2.6).

De facto, the larger significance of tracks from decays of long-lived particles is transformed into a peak at low background probability. The track significance and probability distributions are shown in Fig. 6.11 for tracks from a background sample and from a sample of muon jets in which the fraction of b jets has been enhanced by requiring $P_T^{Rel} > 1$ GeV/c for the muon.

Because of the finite resolution of especially the jet direction, the physics sign assigned to the impact parameter of a track may be incorrect. Since the distribution is symmetric for tracks coming from the primary vertex, the net effect is zero for background tracks. Tracks from long-lived particle decays, however, which have large positive impact parameters, may acquire an incorrect negative sign. This can lead to “lifetime contamination” of the resolution functions determined from the distribution of negative impact parameter tracks.

This effect is reduced by determining the resolution functions from a sample low in heavy flavour events (see Section 6.2.7). In addition, since mis-signing is most likely for tracks that are almost parallel to the jet, a cut on the azimuth between the track and the jet can be applied when the resolution functions are determined. The performance of the tag was not improved by the latter requirement.

6.2.3 Jet probability

Based on the background probabilities of associated tracks, the probability that a jet is compatible with zero-lifetime processes can be determined as a simple product of individual track probabilities

$$\Pi = \prod_{i=1}^{N} P_{\text{track},i}, \tag{6.9}$$

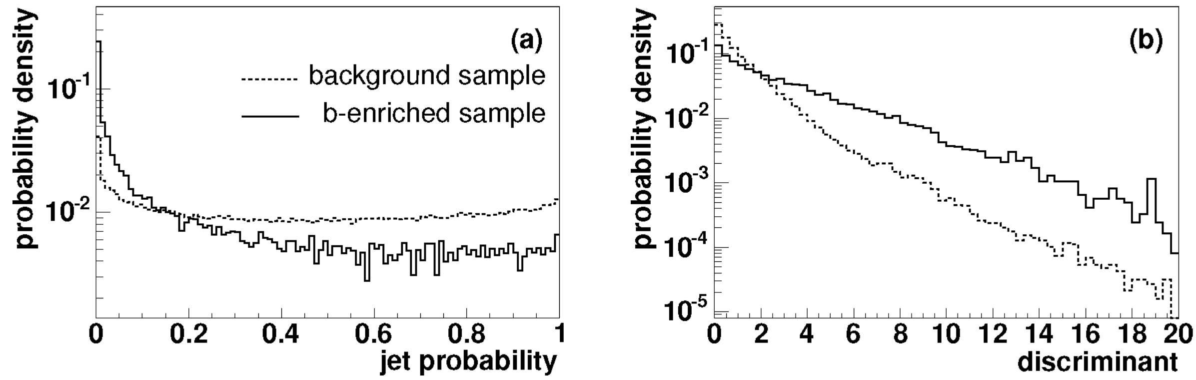

Figure 6.12: Jet background probability (a) and discriminant (b) in data for jets in a background sample (dotted lines) and in a sample with high b jet content (solid lines).

where $P_{\text{track},i}$ is the background probability for track i. As for tracks, jets coming from long-lived particles have probabilities close to zero, while background jets are less peaked.

The simple product will automatically yield smaller values as the number of tracks used in the products increases. While by itself the number of tracks can also lead to a distinction between b and light quark jets, a more explicit distinction and more uniform behaviour of the jet probability is desirable. To this end the probability $\mathcal{P}$ is defined as

$$\mathcal{P}_{\text{jet}} = \Pi \cdot \sum_{i=0}^{N-1} \frac{(-\ln \Pi)^i}{i!}, \tag{6.10}$$

with Π defined as before and N the number of associated tracks. For a uniform distribution of track probabilities, Eq. 6.10 yields a uniform distribution of P_{jet} independent on the number of tracks, given that the individual track probabilities are uncorrelated.

Because b flavoured jets have probabilities concentrated near zero, the jet discriminant $\mathcal{D}$ is defined as

$$\mathcal{D} = -\ln \mathcal{P}_{\text{jet}}. \tag{6.11}$$

The value of the discriminant is large if compatibility with the primary interaction point is small. An enriched b jet sample can be obtained by applying a cut on the value of the discriminant.

The jet probability and discriminant in data are shown in Fig. 6.12, for the same background and b enriched samples as used in Fig. 6.11.

A single misreconstructed track with a large impact parameter or a single reconstructed track from a V^0 decay particle may cause a false tag of a light background jet. Since the probability to have two such tracks is much lower than the probability to have only one, at least two good tracks with $b_0 > 0$ are required to tag a jet. The performance of the tag is further improved by explicitly rejecting poorly reconstructed tracks and large-d_0 tracks that are unlikely to come from b decays. The discriminating power of each individual track is enhanced by correcting the impact parameter uncertainty of the tracks for residual effects and by determining the resolution functions for several track quality categories.

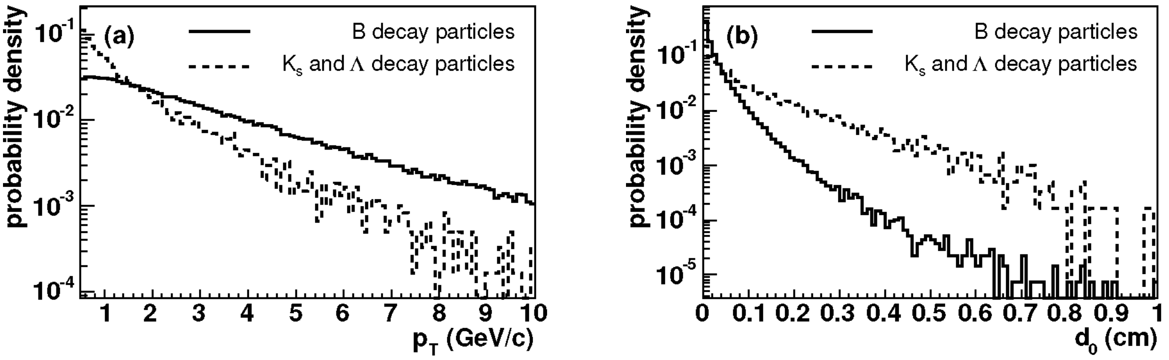

Figure 6.13: The p_T spectrum (a) and impact parameter distribution (b) for B decay particles and particles from decays of Λ and $\mathrm{K^0_S}$ particles.

6.2.4 Track selection

To reduce the influence of fake or misreconstructed tracks with artificially large impact parameters and tracks originating from the decay of long-lived neutral particles, several selection criteria are applied.

Transverse momentum and distance of closest approach

Long-lived neutral particles like $\mathrm{K^0_S}$ and Λ (also known as $\mathrm{V^0}$s, after their signature in bubble-chamber pictures) can lead to a significant tagging efficiency for light jets. The best way to reduce this background would be to fully reconstruct these particles and reject the tracks of their decay particles. The tracking efficiency in the data used here was too low to efficiently reconstruct $\mathrm{V^0}$ decay tracks (see Section 5.3.3). The different p_T and d_0 distributions of tracks can be used to reduce the influence of $\mathrm{V^0}$ decay particles on the background efficiency.

A cut on track p_T is employed to reduce the number of real background tracks as well as the number of tracks with too low resolution due to multiple scattering. Figure 6.13(a) shows the p_T distribution in Monte Carlo for charged particles from either a B hadron (solid line) or $\mathrm{V^0}$ decay (dashed line), excluding $\mathrm{V^0}$ that come from B decays themselves. The particles have been selected from either an inclusive $\mathrm{b\bar{b}}$ sample or an inclusive QCD sample (both generated with a cutoff of $p_T > 10$ GeV on particles produced in the hard scatter interaction) and matched to a particle jet in a cone of $\Delta R < 0.5$. The particles were required to cross all layers of the tracker before decaying.

An implicit cut of $p_T > 400\ \mathrm{MeV}/c$ is applied by the track reconstruction algorithm, so particles with $p_T < 400\ \mathrm{MeV}/c$ are not reconstructed in any case. A cut of $p_T > 800\ \mathrm{MeV}/c$ rejects 22% of the $\mathrm{V^0}$ decay particles and 12% of the B decay particles above $400\ \mathrm{MeV}/c$.

The lifetime of B mesons is much shorter than that of important $\mathrm{V^0}$s ($\tau = 89.53 \pm 0.06$ ps for $\mathrm{K^0_S}$, $\tau = 26.3 \pm 0.2$ ps for Λ). An upper limit on d_0 can therefore be used to reject a large fraction of the tracks coming from $\mathrm{V^0}$ decays. Figure 6.13(b) shows the d_0 distribution for stable charged particles originating from B decays (solid line) and $\mathrm{V^0}$s (dashed line). A cut of $d_0 < 1$ mm, after the $p_T > 800\ \mathrm{MeV}/c$ cut, rejects 22% of the remaining $\mathrm{V^0}$ decay particles, while keeping 97% of the B decay particles.

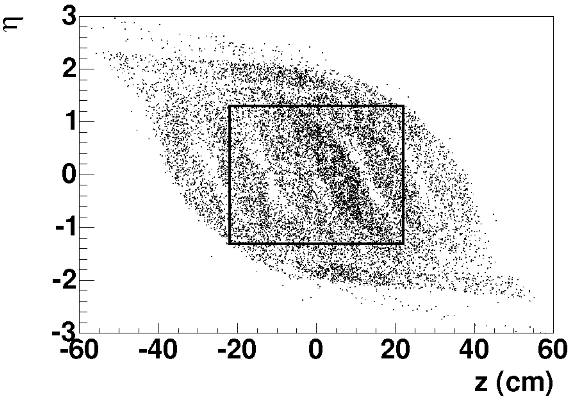

Figure 6.14: The (z_0, η) distribution of tracks with hits in all four SMT barrel superlayers. The box indicates the region of full acceptance.

SMT hits

The dominant contribution to the impact parameter resolution is made by the innermost hit (see Section 5.3.5) in the SMT. To make sure most tracks associated with jets with $|\eta_{\text{jet}}| < 1$ traverse all four SMT barrel layers, the region in which events are accepted is limited to $|z| < 22$ cm. This region was found by plotting the (z_0, η) distribution of all tracks with hits in all four superlayers and looking at the region $|\eta| < 1.3$ to allow for the jet-track match distance. The distribution is shown in Fig. 6.14. The box indicates the region of acceptance. The dark bands in the plot indicate the coverage of each of the six barrel segments; the clear bands correspond to the space between the barrels reserved for the F-disks. The best tracks have hits in all four SMT superlayers. Tracks with hits in only three or two superlayers can still contribute to a lifetime signal, especially if the innermost hit is in the first or second layer; tracks with hits in only a single superlayer are rejected.

CFT hits

While the CFT does not contribute to the d_0 resolution, a requirement on the number of CFT hits can help reduce fakes and misreconstructed tracks. In addition, the CFT is very important for the p_T measurement of the track.

To be reconstructed in the CFT, without SMT hit requirements, eight hits are required on a track. The distribution of CFT hits in data is shown in Fig. 6.15(a). Tracks with fewer than eight CFT hits are reconstructed by defining a track in the SMT and adding matching hits in the CFT. Figure 6.15(b) shows the significance distribution for tracks with hits in all four SMT superlayers and fewer than eight (dashed line) or eight or more (solid line) CFT hits. The distribution for tracks with fewer than eight CFT hits clearly shows more dominant tails. These tracks are rejected.

To ensure uniform behaviour of the tag, the analysis is limited to the region of full acceptance of the SMT barrels, $|z| < 22$ cm and $|\eta| < 1.3$. The bounds of this region are plotted in Fig. 6.16(a) which shows the (z_0, η) distribution of tracks with the maximum number of CFT hits. The CFT does not limit the region of full acceptance for the tag. Figure 6.16(b) shows the number of CFT hits per track in this region. No additional rejection based on the number of CFT hits is needed.

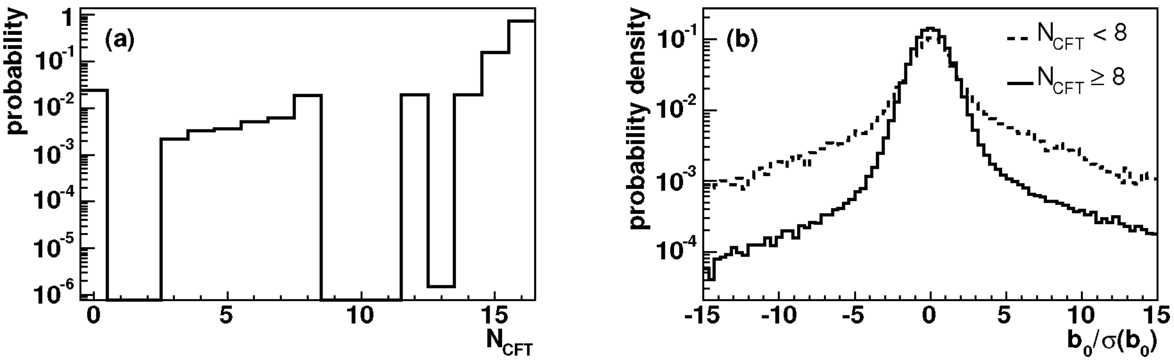

Figure 6.15: Distribution of the number of CFT hits per track (a) and dependence of d_0 significance on the number of CFT hits (b).

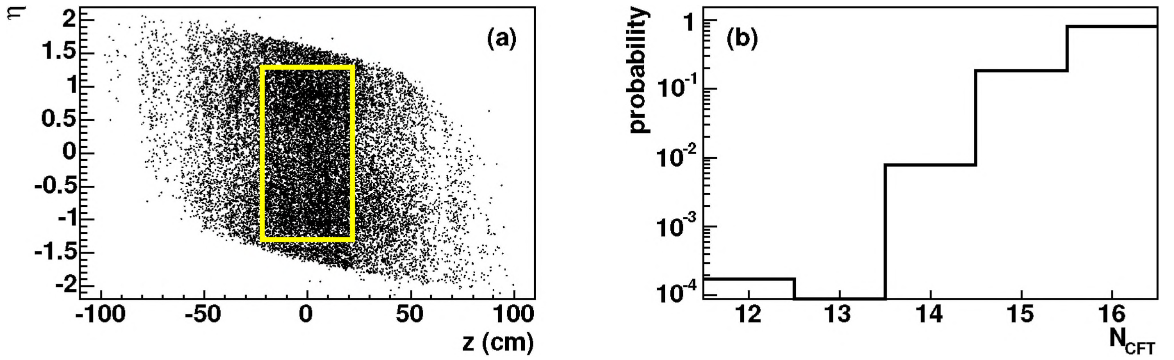

Figure 6.16: Region of full acceptance of the CFT (a) and number of CFT hits per track in the acceptance region (b).

6.2.5 Correction of track impact parameter uncertainty

Beam width

Because of the poor resolution of vertices with few tracks, the beam position is used as the reference point for track impact parameters. The uncertainty on this reference point is dominated by the width of the beam; the uncertainty of the position measurement itself is only a few microns (see Section 5.5.1). To compute the correct significance for each track, the width of the beam at the z-position of the track must then be added in quadrature to the uncertainty given by the track fit. The beam width parametrisation used for this purpose is given in Section 5.5.2.

Residual uncertainty corrections

After subtraction of the beam width, the track fit uncertainty still underestimates the impact parameter resolution. Imperfect understanding of the SMT alignment and of the hit cluster resolutions leads to a constant additional contribution to the uncertainty. At low values of p_{scat} (see Eq. 5.30), the complexity of the material distribution in the detector leads to an additional residual dependence of the uncertainty on p_{scat}. To correctly take into account the uncertainty on the impact parameter of each track, the uncertainty given by the track fit must be corrected for these effects. For simplicity, they are treated as a single correction.

The size of the effects is determined by comparing the uncertainty given by the track fit with the width of the impact parameter distribution after beam width subtraction. If the track description were perfect, the mean uncertainty for a sample of tracks would be equal to the impact parameter width of those tracks. In Fig. 6.17 the width and uncertainty are plotted along with their quadratic difference. Only a small z-region is used to be insensitive to the z-dependence of the beam width. At large p_{scat}, the correction is dominated by the imperfect alignment and understanding of the hit resolutions. At low p_{scat} values, it is clear that a small dependence on p_{scat} remains in the uncertainty. The discrepancy is taken into account by adding a correction to the track fit uncertainty in quadrature. This correction is determined as the quadratic difference between the measured width and the calculated uncertainty as

$$\sigma_{\text{scat}}^2 = \sigma_{d_0}^2 - \sigma_{\text{fit}}^2,$$

where σ_{d_0} is the measured width of the d_0 distribution after quadratically subtracting the beam width, σ_{fit} is the uncertainty given by the track fit error matrix and σ_{scat} is the correction. The correction, plotted as the solid squares in Fig. 6.17, is fitted with the same functional form of Eq. 5.31 as the impact parameter resolution as a function of p_{scat}. The correction is determined separately for eight possible SMT hit configurations, based on the number of superlayers with at least one hit and on the layer with the innermost hit. The hit configurations used for the uncertainty correction are not identical to those used for track quality categorisation in Section 6.2.6.

6.2.6 Track quality categorisation

If the resolution of each track were perfectly understood, and in the absence of long-lived particles, the distribution of the significance S would be a Gaussian with a width of one and a mean of zero. In reality, the distribution depends on track properties including p_{scat} and the number and location of hits in the SMT. If these effects are not taken into account, the efficiency and purity of the tag are adversely affected. The inclusion of tracks with poorly understood resolutions (resulting in wider significance distributions and longer tails) in the resolution functions decreases the discriminating power of well-understood tracks. Conversely, poorly understood tracks are assigned an artificially low background probability when compared with a resolution function dominated by better tracks. By dividing the tracks in several *quality categories* based on the SMT hit configuration and the value of p_{scat}, the resolution functions are determined with more accuracy.

The tracks were first categorised according to the number of SMT superlayers with hits (two, three or four) and whether the track has a hit in the innermost superlayer. The radius of the inner sublayer and the span, defined as the difference in radius between the innermost and outermost layers with hits, were also considered. Despite the fact that the latter two criteria strongly affect the impact parameter resolution, no difference in the significance distributions was observed, indicating that they are properly taken into account in the track fit uncertainty.

Even after correcting the uncertainty for multiple scattering (see Section 6.2.5), a dependence of the tails in the significance distribution on the value of p_{scat} can be seen for tracks with fewer

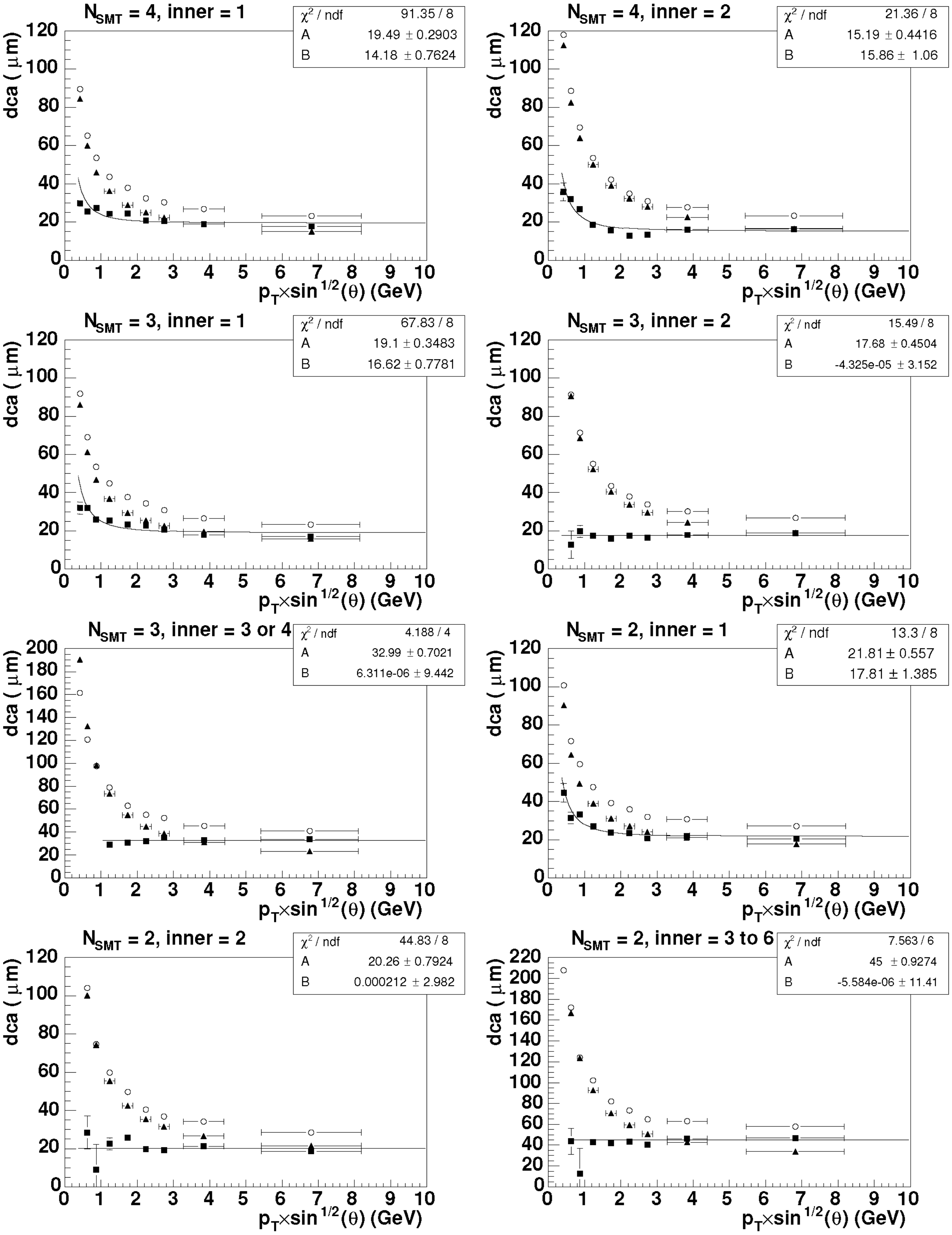

Figure 6.17: Residual dependence of the track impact parameter uncertainty on the multiple scattering variable p_{scat}, for all hit configurations considered. The uncertainty is plotted as solid triangles, the true width is shown as open circles. The solid boxes indicate the quadratic difference between the two.

N_{SMT}	Hit in Layer 1	$p_{\text{scat}} < 1$ GeV$/c$	$1 < p_{\text{scat}} < 1.5$ GeV$/c$	$p_{\text{scat}} > 1.5$ GeV$/c$	all
4	yes	25.9%	8.4%	7.4%	41.6%
3	yes	18.9%	6.2%	5.4%	30.6%
3	no	5.8%	1.9%	1.6%	9.2%
2	yes	6.2%	2.0%	1.6%	9.8%
2	no	5.6%	1.8%	1.5%	8.8%

Table 6.3: Track quality category definitions and the fraction of tracks in each category.

than the maximum possible number of SMT hits. This is probably due to the larger margin for errors in the track fit for tracks that are not maximally constrained in the SMT, but have a smaller radius of curvature and a larger probability to deviate from their ideal trajectory. Three bins of p_{scat} are used: $p_{\text{scat}} < 1$ GeV$/c$, $1 < p_{\text{scat}} < 1.5$ GeV$/c$ and $p_{\text{scat}} > 1.5$ GeV$/c$

The definition of the track quality categories is shown in Table 6.3, along with the fraction of the total track sample in each bin. The number of bins is kept small to keep enough statistics in each bin.

6.2.7 Background sample: photon plus jets

To minimise the contamination of B decay tracks in the resolution function, a sample low in heavy flavour content is used to determine the resolution functions. Because of the limited trigger bandwidth assigned to multi-jet triggers (especially at low E_T), the use of an all jet sample is not feasible. In addition, in a generic jet sample heavy flavour jets are only suppressed by the larger quark masses.

Instead, a sample of events selected with EM triggers is used. Offline, the events were required to have a reconstructed photon opposite a jet. Photon+jet events arise when a photon scatters of a quark. This interaction is suppressed for down-type quarks (including b quarks), which have a charge of $-\frac{1}{3}$, with respect to up-type quarks, which have a charge of $\frac{2}{3}$.

The triggers used to acquire the sample are listed in Table 6.4. Offline, events were required to have exactly one reconstructed photon and no more than three good reconstructed jets. The azimuthal separation between photon and jet was required to be larger than 1.5 rad.

The fraction of heavy flavour jets in this sample is estimated by looking for the presence of jets with an associated muon in the sample. Only $f_\mu = (0.10 \pm 0.04)\%$ of all jets in the sample have an associated muon with $p_T^\mu > 6$ GeV$/c$. The muon P_T^{Rel} distribution is shown in Fig. 6.18(a). From a P_T^{Rel} template fit to the distribution, the estimated fraction of b jets in this subsample of muon jets is $f_{\text{b}} = 0.82 \pm 0.07$.

The total fraction of b jets in the photon+jets sample is estimated by taking into account the branching ratio $BR(\text{b} \to \mu X)$ and the muon reconstruction efficiency $\epsilon^\mu_{\text{reco}}$ and correcting for the acceptance of the muon momentum cut

$$f_{\text{b}}^{\text{tot}} = C_{p_T} \times \frac{f_\mu \times f_{\text{b}}}{BR(\text{b} \to \mu X) \times \epsilon^\mu_{\text{reco}}}, \tag{6.12}$$

where C_{p_T} is the correction factor to account for the muon p_T cut. The correction factor was obtained from the p_T distribution of Monte Carlo muons from b decays in Monte Carlo, shown in

name	Level 1	Level 2	Level 3
EM_LO	CEM(1,5)		ele(1,10.)
EM_LO_SH	CEM(1,5)		ele(1,7.,sh)
EM_HI_EMFR8	CEM(1,10)		ele(1,40.,vl)
EM_HI	CEM(1,10)		ele(1,30.)
EM_HI_SH	CEM(1,10)		ele(1,20.,sh)
EM_HI_L2	CEM(1,10)	em(1,11)	ele(1,30.)
EM_MX_EMFR8	CEM(1,15)		ele(1,40.,vl)
EM_MX	CEM(1,15)		ele(1,30.)
EM_MX_SH	CEM(1,15)		ele(1,20.,sh)

Table 6.4: Triggers used for the photon+jets sample. The trigger terms are explained in Chapter 4.

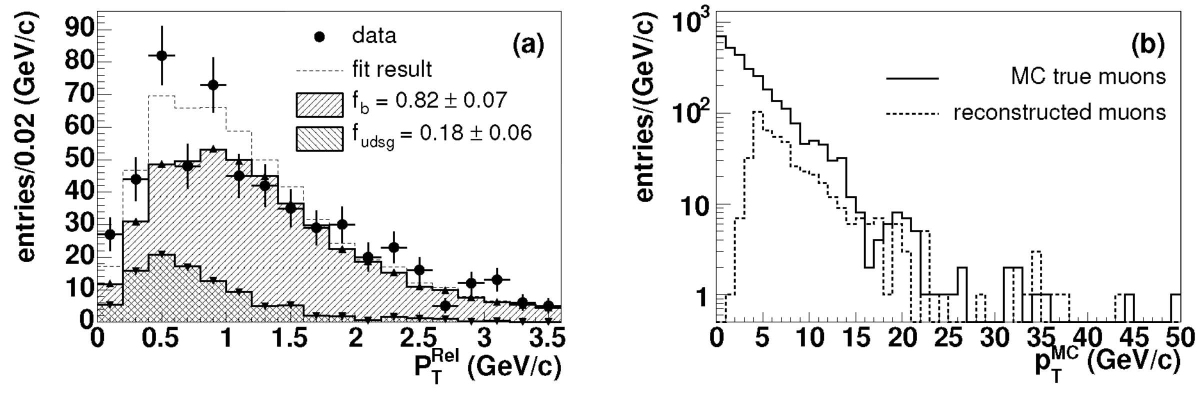

Figure 6.18: Muon P_T^{Rel} distributions for muon jets in the photon+jets sample (a) and the p_T distribution of muons from b decays in Monte Carlo (b).

Fig. 6.18(b). The muons were matched to a reconstructed jet with $E_T^{\mathrm{CAL}} > 15$ GeV and $|\eta^{\mathrm{CAL}}| < 1$ satisfying all quality cuts. The correction factor is equal to one over the fraction of Monte Carlo muons with $p_T > 6$ GeV$/c$, $C_{p_T} = 5.1 \pm 0.2$.

Given the branching ratio $BR(\mathrm{b} \to \mu X) = 0.195 \pm 0.006$ (including b $\to$ c $\to$ μ decays) and the muon reconstruction efficiency $\epsilon^{\mu}_{\mathrm{reco}} = 0.480 \pm 0.004$, the fraction of b jets in the photon+jets sample is $f_{\mathrm{b}}^{\mathrm{tot}} = 0.04 \pm 0.01$.

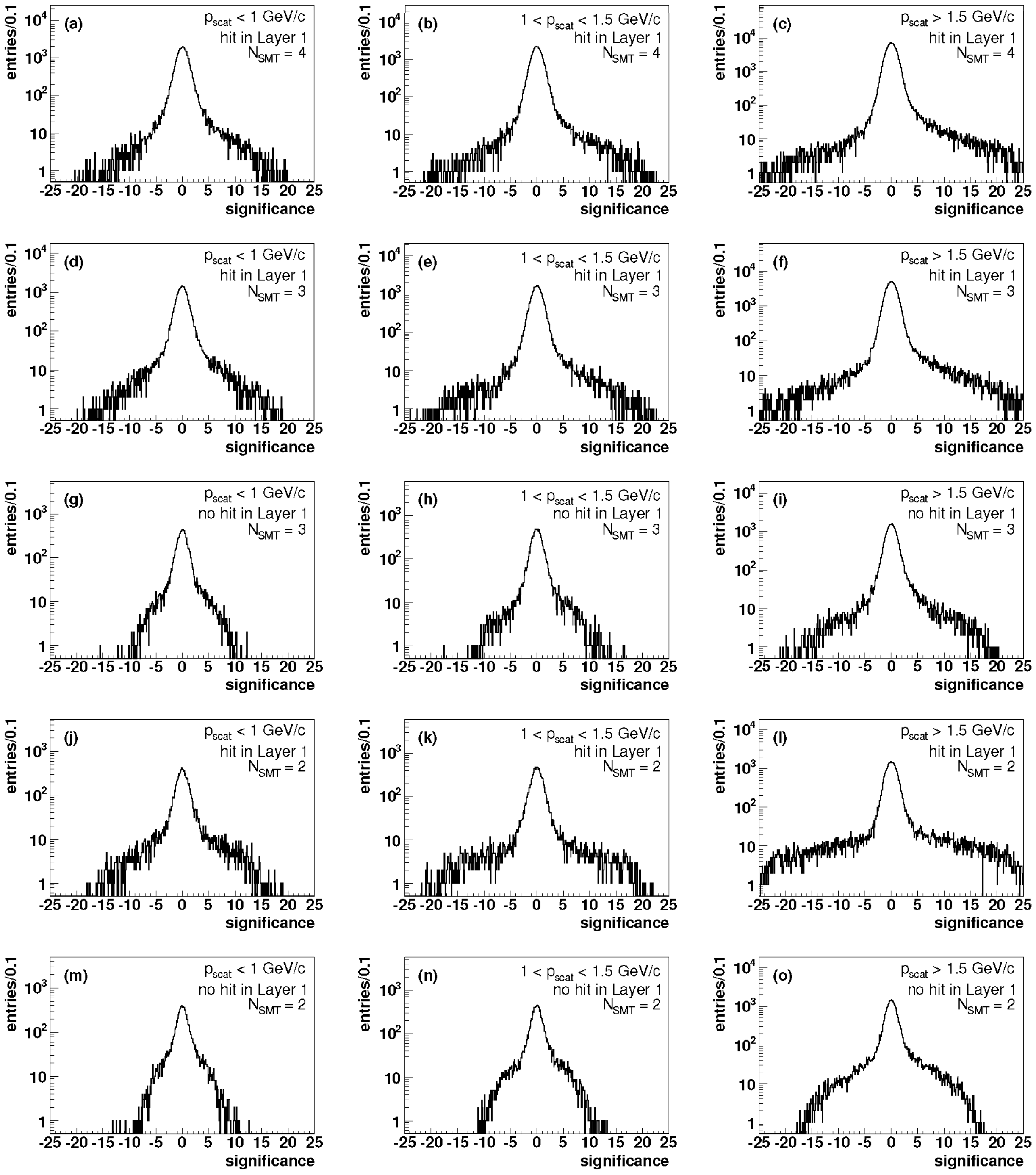

Figure 6.19: Physics signed significance distributions for all track categories.

6.2.8 Resolution functions

The resolution functions were determined from the significance distribution of negative b_0 tracks in the photon+jets sample. All the corrections and categorisations discussed in this chapter were applied. The same track selection criteria used for the resolution functions are applied for the tag itself. The criteria are summarised below.

- $\Delta R(\text{track-jet}) < 0.5$;
- $p_T^{\text{track}} > 800\ \text{MeV}/c$;
- $|d_0| < 0.1\ \text{cm}$;
- $N(\text{CFT hits}) \geq 8$;
- $N(\text{SMT layers}) \geq 2$.

The distributions of b_0 for all track categories are shown in Fig. 6.19. For the resolution functions, a finer binning of 0.001 was used.

6.2.9 Efficiency

The efficiency of the jet lifetime probability tag is defined as

$$\epsilon_{\text{b}} = \frac{N(\text{tagged b jets})}{N(\text{b jets})}. \tag{6.13}$$

This efficiency implicitly includes tracking efficiency and charged particle multiplicity. The requirement of two good tracks with $b_0 > 0$ already includes an implicit lifetime tag, as tracks from B decays are more likely to have $b_0 > 0$. The fraction of jets with at least two matched good tracks irrespective of their impact parameter is not directly sensitive to long-lived particle decays. In the following, N_{tracks} denotes the total number of matched good tracks.

The efficiency of the jet lifetime probability tag is determined using the known number of b jets present in the muon+jet sample before and after applying the tag. The number of b jets in both instances is determined using a muon P_T^{Rel} fit. The jet lifetime probability tag efficiency is calculated as

$$\epsilon_{\text{b}} = \frac{f_{\text{b}}^{\text{tag}} N^{\text{tag}}}{f_{\text{b}}^{\text{tot}} N^{\text{tot}}}, \tag{6.14}$$

where N^{tot} is the total number of muon jets in the sample, $f_{\text{b}}^{\text{tot}}$ is the fraction of b jets in the untagged sample, and N^{tag} and $f_{\text{b}}^{\text{tag}}$ are the number of tagged jets and the fraction of b jets in the tagged sample. The P_T^{Rel} fits for six different values of the impact parameter discriminant cut for jets with $E_T > 15$ GeV are shown in Fig. 6.20. The resulting efficiency as a function of the discriminant cut is shown in Fig. 6.21.

The possibility that the muon is reconstructed as a high-p_T track in the central tracking system may bias the lifetime tag to higher efficiencies; on the other hand, the charged particle multiplicity for semileptonic B decays is lower than for fully hadronic decays. Both effects will be diminished by the low track reconstruction efficiency in jets. In a version of the jet lifetime probability tag used

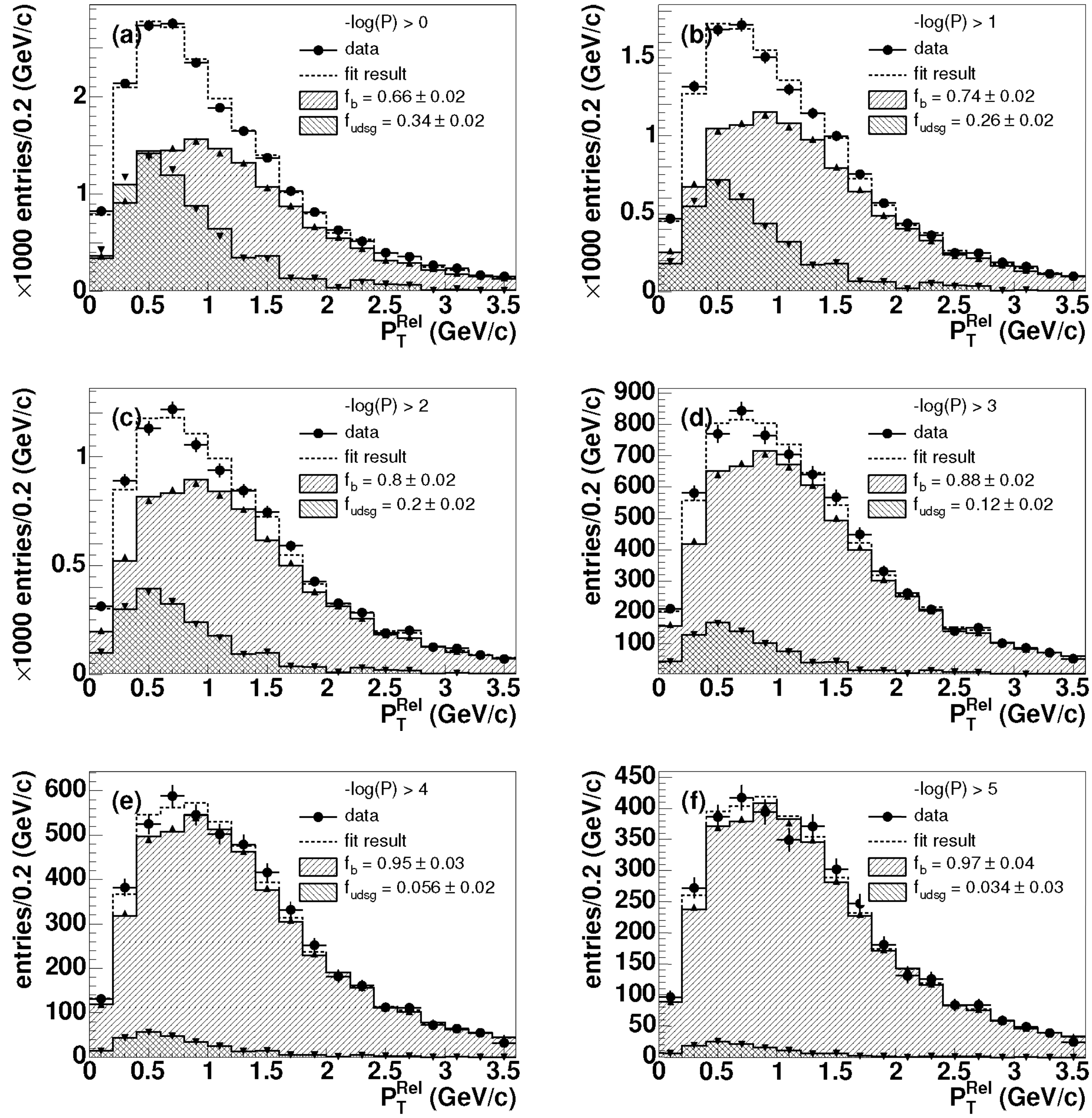

Figure 6.20: P_T^{Rel} Distribution of muon jets after applying a cut on the jet discriminant.

for more recent data, no effect of the presence of a semileptonic B decay on the tagging efficiency was found [123].

The efficiency as a function of jet E_T is determined by dividing the sample in five different E_T bins, as was done in Section 6.1.5, and performing the P_T^{Rel} fits in each bin. The dependence of the fraction of jets with at least two matched tracks and the efficiency on jet E_T are shown in Fig. 6.22(a) and (b), respectively, for a discriminant cut of $\mathcal{D} > 5$. No dependence of the efficiency on E_T is observed. This may be due to the large uncertainties caused by limited statistics in the Monte Carlo templates.

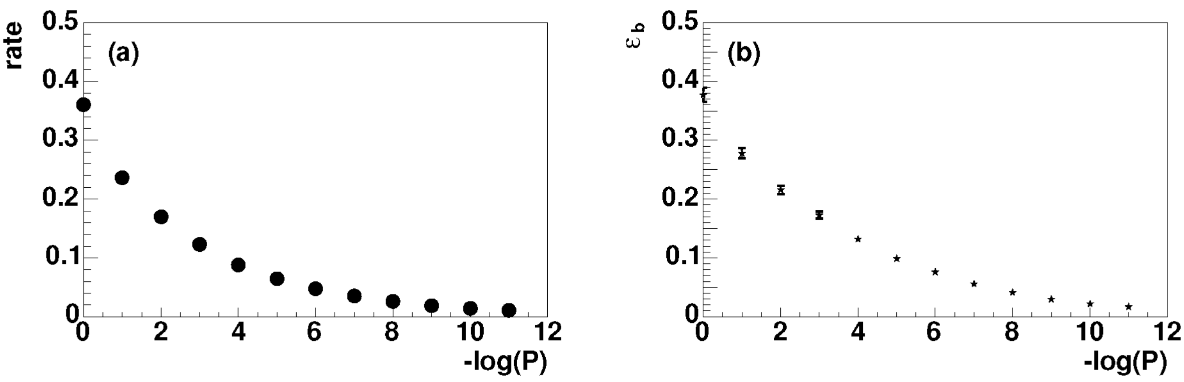

Figure 6.21: Muon jet tag rate (a) and jet lifetime probability tag efficiency (b) as a function of the discriminant cut for jets with $E_T > 15$ GeV.

The dependence of the fraction of jets with $N_{\text{tracks}} \geq 2$ and efficiency on η and ϕ are shown in Fig. 6.22(c–f). The efficiencies were determined by performing the P_T^{Rel} fits in bins of η and ϕ. The η dependence of the efficiency is described by a parabola with its maximum at $\eta = 0$. The strong ϕ dependence is a result of the tracking efficiency ϕ dependence caused by the different lengths of the clear fibre light guides connecting the CFT to the VLPCs which were not correctly taken into account in the version of the reconstruction software used [124]. A sine fit was used for the dependence of the efficiency on ϕ, with the phase and period fixed to the values obtained from a fit to the fraction of jets with $N_{\text{tracks}} \geq 2$.

6.2.10 Background efficiency

Ideally, the fake rate can be predicted from first principles: if the probability for background jets is uniformly distributed the fake rate is simply equal to the cut applied on the probability. In reality, imperfect understanding of the resolutions, possible correlations between tracks and especially the presence of real long-lived particles in background jets all increase the fake rate. To solve these problems, either the *negative tag rate* or the tag rate in a pure background sample can be used.

The negative tag rate is determined using all negative b_0 tracks associated with a jet. The negative track and jet probabilities are defined the same way as the "normal" probabilities, using negative instead of positive b_0 tracks. If the resolution is correctly parametrised, the probabilities of negative b_0 tracks should be uniformly distributed by definition. Because of mis-signing effects (see Section 6.2.2), the negative tag rate will still be higher in samples that contain a lot of signal. On the other hand, the presence of real long-lived particles in background jets means that the negative tag rate will in general be an optimistic estimate of the fake rate.

Instead, the background efficiency is determined from a sample known to contain few heavy flavour jets. The photon+jets sample used to determine the resolution functions (see Section 6.2.7) has a lower b jet contamination than a pure multi-jet sample and is used to measure the fake rate. The total fraction of b jets in this sample is $f_{\text{b}}^{\text{tot}} = 0.04 \pm 0.01$. The fake rate is then determined as:

$$\epsilon_{\text{background}} = \frac{N(\text{tagged jets})/N(\text{jets}) - \epsilon_{\text{b}} \times f_{\text{b}}^{\text{tot}}}{1 - f_{\text{b}}^{\text{tot}}}, \tag{6.15}$$

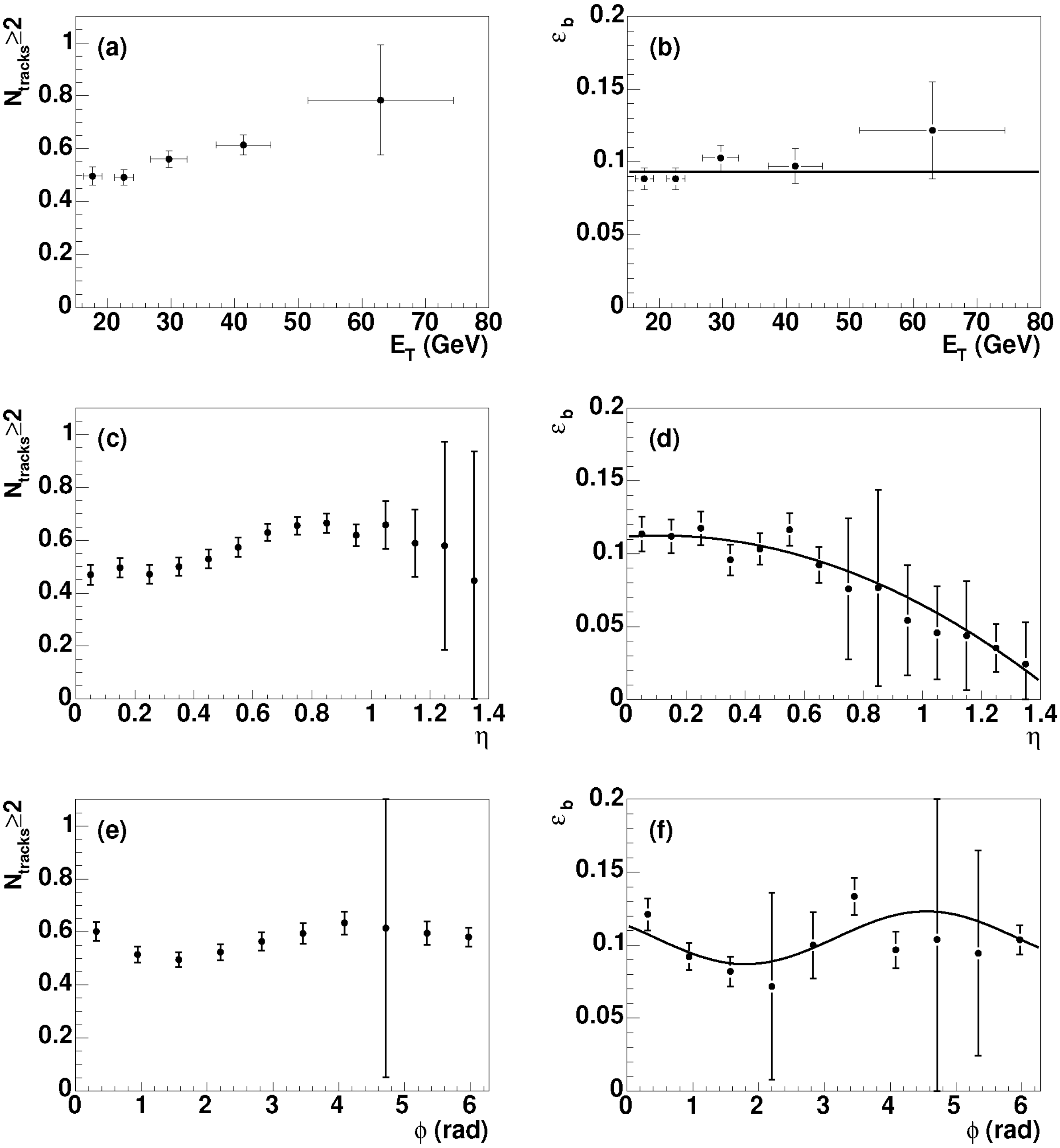

Figure 6.22: The fraction of jets with $N_{\text{tracks}} \geq 2$ (left) and the efficiency of the jet lifetime probability tag for a cut of $\mathcal{D} > 5$ (right) as a function of jet E_T, $|\eta|$ and ϕ.

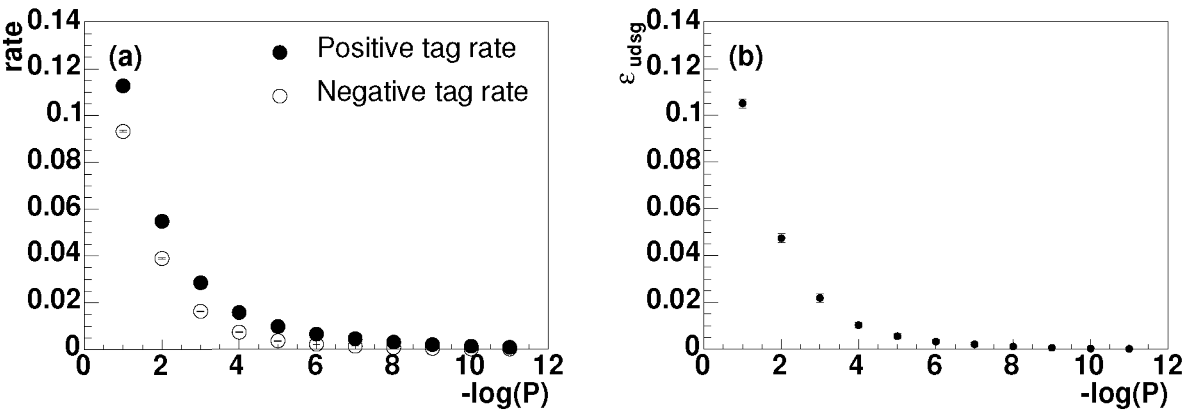

Figure 6.23: Tagging rate and negative tag rate for jets in the photon+jet sample as a function of the discriminant cut (a), and light jet tagging efficiency (b). The statistical uncertainties are smaller than the symbol size.

where ϵ_b is the b jet efficiency. This neglects the fact that the efficiency for c jets is also higher than for light jets. However, the efficiency for c jets is also *lower* than the efficiency for b jets and the presence of charm in the background sample will have a smaller impact on the measured light jet efficiency.

The light jet tagging efficiency as a function of the discriminant cut is shown in Fig. 6.23(b). The efficiency determined using Eq. 6.15 is lower than the positive tag rate shown in Fig. 6.23(a), but slightly higher than the negative tag rate. The efficiency for a cut of $\mathcal{D} > 5$ and the fraction of jets with $N_{\text{tracks}} \geq 2$ for light jets as a function of E_T, η and ϕ are shown in Fig. 6.24.

6.2.11 Overall tagging performance

The overall performance of the tag can be characterised by a performance curve. The efficiency for b jets is plotted as a function of the efficiency for light jets in Fig. 6.25. The efficiencies for b jets and light jets are also shown in Table 6.5.

A cut of $\mathcal{D} > 5$ corresponds to a nominal background efficiency of $\mathcal{P} < e^{-5} \approx 0.0067$. The measured background efficiency at that operating point is 0.006 ± 0.001. This efficiency includes the probability that at least two good tracks with $b_0 > 0$ are matched to the jet and must be corrected for that probability. The efficiency for jets with at least two such tracks is 0.022 ± 0.004, which is much higher than the nominal background efficiency. This is probably due to presence of real long-lived particles in background jets.

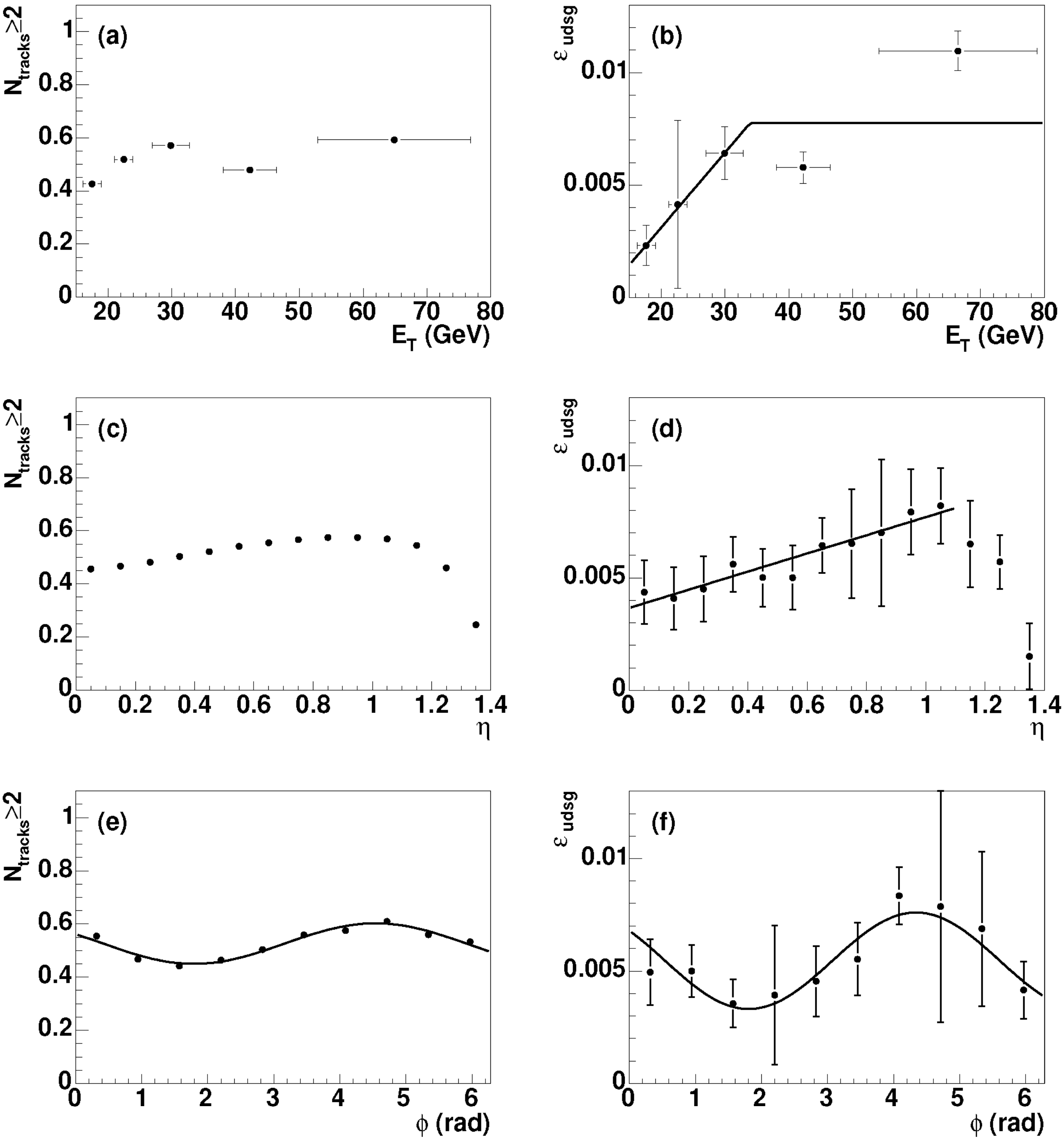

Figure 6.24: The fraction of jets with $N_{\text{tracks}} \geq 2$ (left) and the efficiency of the jet lifetime probability tag for a cut of $\mathcal{D} > 5$ (right) as a function of jet E_T, $|\eta|$ and ϕ for jets in the photon+jet sample .

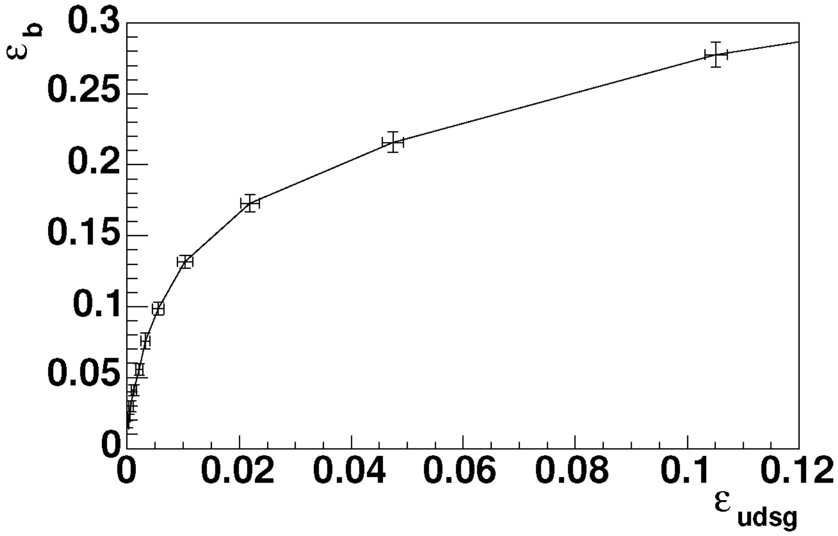

Figure 6.25: Jet lifetime probability tag performance curve. The efficiency for b jets is plotted as a function of the efficiency for light jets for jets with $E_T > 15$ GeV and $|\eta| < 1$.

	ϵ_b	$\epsilon_\mathrm{background}$
$N_\mathrm{tracks} \geq 2$	0.57 ± 0.02	0.524 ± 0.001
$\mathcal{D} > 0$	0.38 ± 0.01	0.267 ± 0.002
$\mathcal{D} > 1$	0.278 ± 0.009	0.105 ± 0.002
$\mathcal{D} > 2$	0.216 ± 0.007	0.047 ± 0.002
$\mathcal{D} > 3$	0.173 ± 0.006	0.022 ± 0.002
$\mathcal{D} > 4$	0.132 ± 0.005	0.010 ± 0.001
$\mathcal{D} > 5$	0.099 ± 0.005	0.006 ± 0.001
$\mathcal{D} > 6$	0.076 ± 0.006	0.0032 ± 0.0008
$\mathcal{D} > 7$	0.056 ± 0.004	0.0021 ± 0.0006
$\mathcal{D} > 8$	0.041 ± 0.004	0.0012 ± 0.0005
$\mathcal{D} > 9$	0.030 ± 0.004	0.0006 ± 0.0004
$\mathcal{D} > 10$	0.022 ± 0.002	0.0003 ± 0.0003

Table 6.5: Jet lifetime probability tag efficiency and background efficiency for jets with $E_T >$ 15 GeV and $|\eta| < 1$ as a function of the discriminant cut.

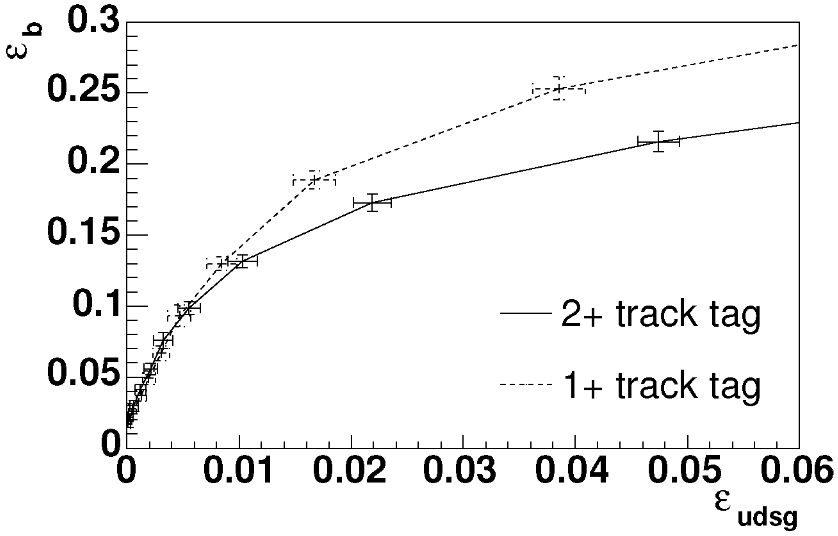

Figure 6.26: Jet lifetime probability tag performance curve requiring at least one (dashed line) or at least two (solid line) good tracks with positive b_0 to tag a jet.

Efficiency using single-track jets

One way to boost the efficiency of the tag would be to allow a positive tag based on only one track with $b_0 > 0$. This could be useful when the tag is applied to multiple jets in an event or to select a large b enriched sample. Allowing jet tags based on a single track increases the fake rate as well as the efficiency. In Fig. 6.26, the performance curve for the "single track efficiency" and the standard curve requiring two or more tracks with $b_0 > 0$ are shown. Especially for low discriminant cut values, the efficiency requiring only a single track is much higher for both background and signal samples. In fact, for low-purity applications (using a low discriminant cut), a significant gain in efficiency can be achieved requiring only a single track. At higher purity the difference decreases until the curves are about equal for discriminant cuts greater than $\mathcal{D} > 5$. The requirement that at least two tracks with $b_0 > 0$ are matched to the jet will be used throughout the rest of this thesis.

Chapter 7

Di-jet angular correlations and $\mathrm{b\overline{b}}$ production processes

As described in Chapter 2, the angular correlation between b jets in an event is directly sensitive to NLO contributions in QCD $\mathrm{b\overline{b}}$ production. The distribution of $\Delta\phi$ between b jets can therefore be used to test NLO predictions for $\mathrm{b\overline{b}}$ production, as well as Monte Carlo simulations. Because this analysis is limited to the central region, the ΔR distribution provides no significant additional information.

The best way to test the predictions would be to determine the $\mathrm{b\overline{b}}$ angular correlations corrected for background and all experimental biases. Unfortunately, the size of the data sample used in this analysis is too small to allow a model-independent background correction. Instead, the $\Delta\phi$ distributions obtained from Monte Carlo for the different production processes are folded with all experimental biases and resolutions and compared to the uncorrected data. By fitting the Monte Carlo $\Delta\phi$ distributions to the data distribution, the relative contributions of flavour creation, flavour excitation and gluon splitting processes to the total b jet production rate are extracted and compared to the prediction given by PYTHIA. The fit is performed on a sample of events with at least two reconstructed central ($|\eta| < 1$) jets, one of which has been tagged with a muon and one with the impact parameter tag. To determine the contribution of lighter flavours to the data sample, a simultaneous fit of the P_T^{Rel} distribution of the muon jet is performed.

7.1 Data selection

The data used for this analysis have been collected in the period from August 22 until October 22, 2002. The events were selected online with the MU_JT20_L2M0 trigger (see Section 4.2). Runs with bad tracking, calorimetry or muon measurement [108] were rejected. The remaining dataset corresponds to an integrated luminosity of 7.8 ± 0.6 pb^{-1}.

The $\Delta\phi$ distribution in data was obtained from events satisfying the following requirements:

- A reconstructed primary vertex with $|z| < 22$ cm;
- At least two reconstructed jets of good quality (see Section 5.1.5) with $|\eta^{\mathrm{CAL}}| < 1$ and $E_T^{\mathrm{CAL}} > 15$ GeV;

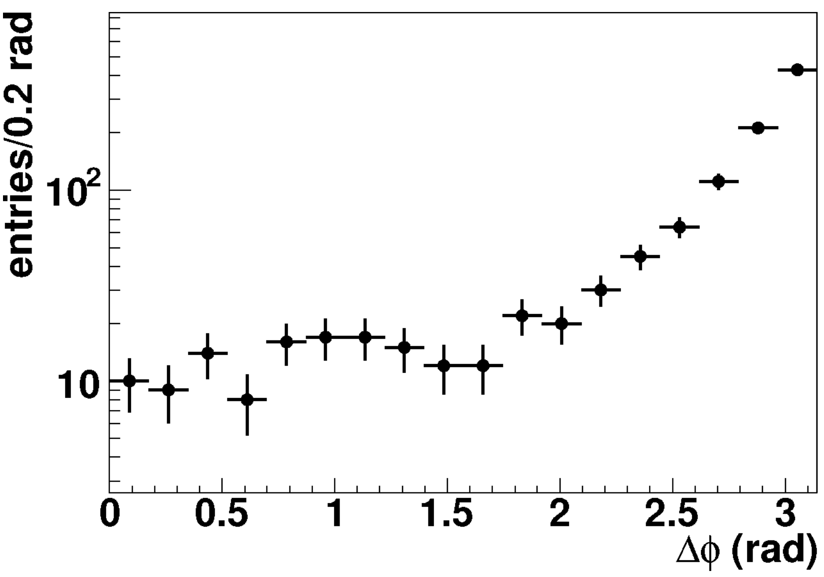

Figure 7.1: $\Delta\phi$ distributions between two tagged jets in data.

- A tight muon reconstructed in the central muon system, with $p_T > 6$ GeV$/c$ and matched to one of the jets within $\Delta R < 0.7$. Each muon was only allowed to be matched to the closest jet (see Section 6.1). The jet with the matched muon is referred to as the "muon jet". The other jet is referred to as the "away jet";
- The away jet must be tagged with a jet lifetime probability cut of $\mathcal{D} > 5$. The efficiencies for b jets and light jets are measured to be 0.099 ± 0.005 and 0.006 ± 0.001, respectively (see Section 6.2.9);
- If there are more than two good jets with $|\eta^{\rm CAL}| < 1$ and $E_T^{\rm CAL} > 15$ GeV in the event, all possible combinations are considered. Any combination including a non-b jet will later be identified as background. In the current data sample, there are no events with more than one possible combination of a muon jet and an impact parameter tagged jet;
- $\Delta\phi$ is determined as the angle between the muon jet and the away jet.

The $\Delta\phi$ distribution in data is shown in Fig. 7.1.

7.2 Angular correlations in Monte Carlo

To obtain the Monte Carlo $\Delta\phi$ distributions, five separate Monte Carlo samples were generated:

- 64,000 flavour creation (FCR) events, generated by explicitly selecting the FCR matrix element in PYTHIA;

- 153,000 gluon splitting (GSP) events, obtained by generating QCD events and selecting events with a $b\bar{b}$ quark pair in the final state, with both the b and the $\bar{b}$ quark originating from the same parent gluon;

- 136,000 flavour excitation (FEX) events, obtained by generating QCD events and selecting events with exactly one b or $\bar{b}$ quark originating from the hard scatter interaction and at least one b or $\bar{b}$ quark originating from a parent gluon;

- 236,000 $c\bar{c}$ events, obtained by generating QCD events and selecting events with at least one c quark in the final state;

- 322,000 light jet background events, obtained by generating generic QCD events.

The $b\bar{b}$ and $c\bar{c}$ samples were generated with the additional requirement that both heavy quarks had $p_T > 20$ GeV/c and $|\eta| < 2$, and that a muon was present in the final state. The PYTHIA p_T cutoff was 20 GeV/c for all samples. The CLEO QQ [56] package was used for b and c decays. In the FCR, GSP and FEX samples, all hadrons containing a b were forced to decay directly to μX or τX; the $\bar{b}$ hadrons were allowed to decay normally. Likewise, in the $c\bar{c}$ sample, all c quark hadrons were forced to decay to μX or τX but $\bar{c}$ hadrons were allowed to decay normally. The samples are the same as those used to generate the P_T^{Rel} templates (see Section 6.1).

Each selected event was run through a GEANT simulation of the DØ detector and fully reconstructed using the DØ reconstruction code. To create the templates, jets and muons were smeared to account for the different resolutions in data and Monte Carlo (see Section 6.1.4). Each event was assigned a weight equal to the trigger efficiency for the leading calorimeter jet.

After correcting the jet and muon resolutions, events were selected with at least two good reconstructed jets with $|\eta^{\rm CAL}| < 1$ and $E_T^{\rm CAL} > 15$ GeV. A primary vertex with $|z| < 22$ cm was also required. These requirements match the jet and vertex requirements for the data sample. For the three $b\bar{b}$ samples and for the $c\bar{c}$ sample, each jet was required to be matched to a B or charmed hadron within a $\Delta R < 0.5$ cone. Events containing b or c quarks were rejected from the light jet sample.

No reconstructed muon was required because of the limited size of the samples. Instead, one of the jets was required to have $E_T > 21$ GeV to account for the additional energy carried by the muon in the data. Each event was given an additional weight to account for the probability that one of the jets has a matched muon reconstructed in the central muon system, and one of the jets was tagged by the impact parameter tag. The impact parameter tag rate functions (TRFs) as a function of jet E_T, η and ϕ are given in Section 6.2.

To determine the probability that a jet has a matched reconstructed muon, reconstructed jets in the simulation were matched to Monte Carlo particle muons with $p_T > 6$ GeV/c. The probability that a matched reconstructed muon with $p_T > 6$ GeV/c was found was determined as a function of jet E_T, η and ϕ. The reconstructed muon was required to match the Monte Carlo particle muon within $\Delta R < 0.3$. The probability was determined separately for $b\bar{b}$ and light jet events. The probabilities as a function of jet E_T, η and ϕ for $b\bar{b}$ events are shown in Fig. 7.2. A parabolic parametrisation was used for the dependence on jet η. For the dependence on jet ϕ, the following

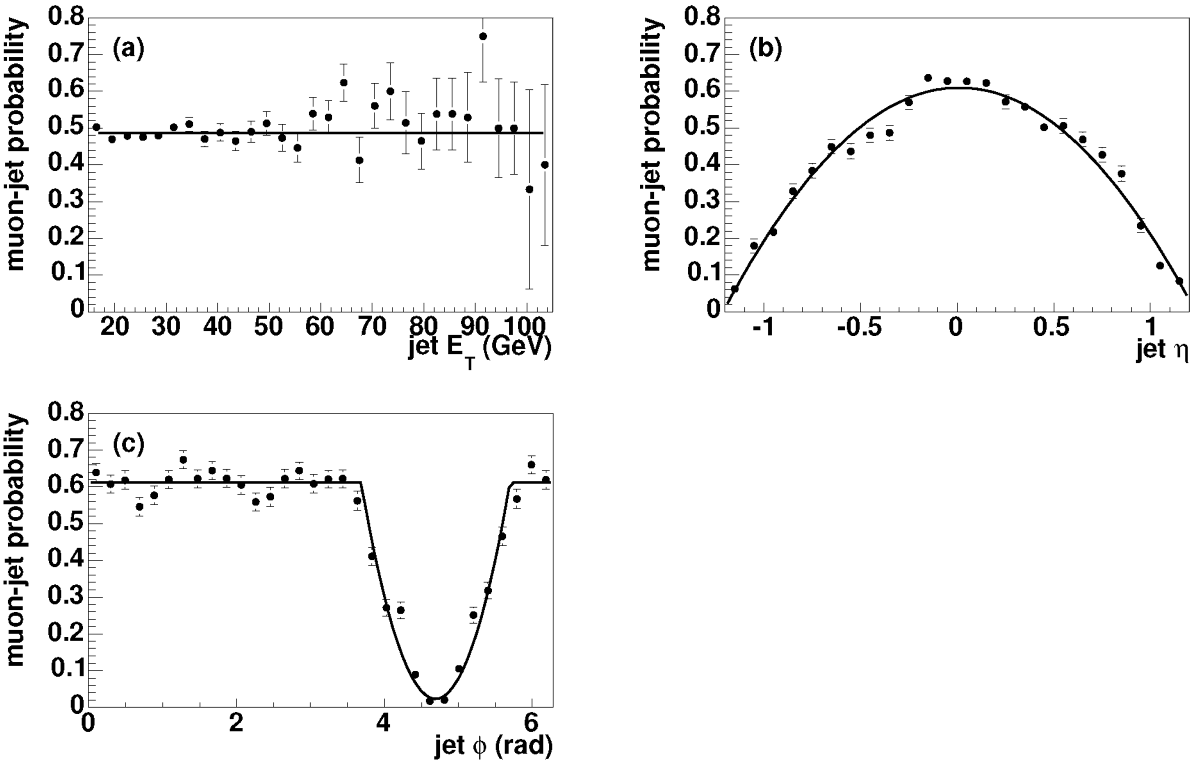

Figure 7.2: Probability to have a matched muon as a function of jet E_T, η and ϕ for $\mathrm{b\bar{b}}$ events. The fits to the probability are shown as the solid lines. The parametrisation for the fit to the probability as a function of ϕ is given in Eq. 7.1. The discontinuity at $E_T = 36$ GeV in Fig.(a) is due to the presence of different subsamples.

parametrisation was used:

$$P(\text{jet }\phi) = \begin{cases} a\phi^2 + b\phi + c & \text{if } M - p \le \phi \le M + p \\ \text{constant} & \text{otherwise.} \end{cases} \tag{7.1}$$

The free parameters in the fit are a, b, c, M and p. M is the value of ϕ for which the 2^{nd} order polynomial reaches its minimum, given by $M = -b/2a$, and the constant value for $(\phi < M - p) \vee (\phi > M + p)$ is given by the value of the polynomial at $\phi = M - p$. The constant probability for $(\phi < M - p) \vee (\phi > M + p)$ is 0.614 ± 0.005.

The $\Delta\phi$ templates for all samples are shown in Fig. 7.3.

7.2.1 Inclusive background template

Because the P_T^{Rel} and $\Delta\phi$ distributions for c and light jets are too similar to separate these two background contributions using a template fit, a single background template is used in the fits. An estimate of the fraction of $\mathrm{c\bar{c}}$ events cannot easily be given from the available Monte Carlo because of the event selection applied when the samples where generated. A 50% charm / 50% light jet

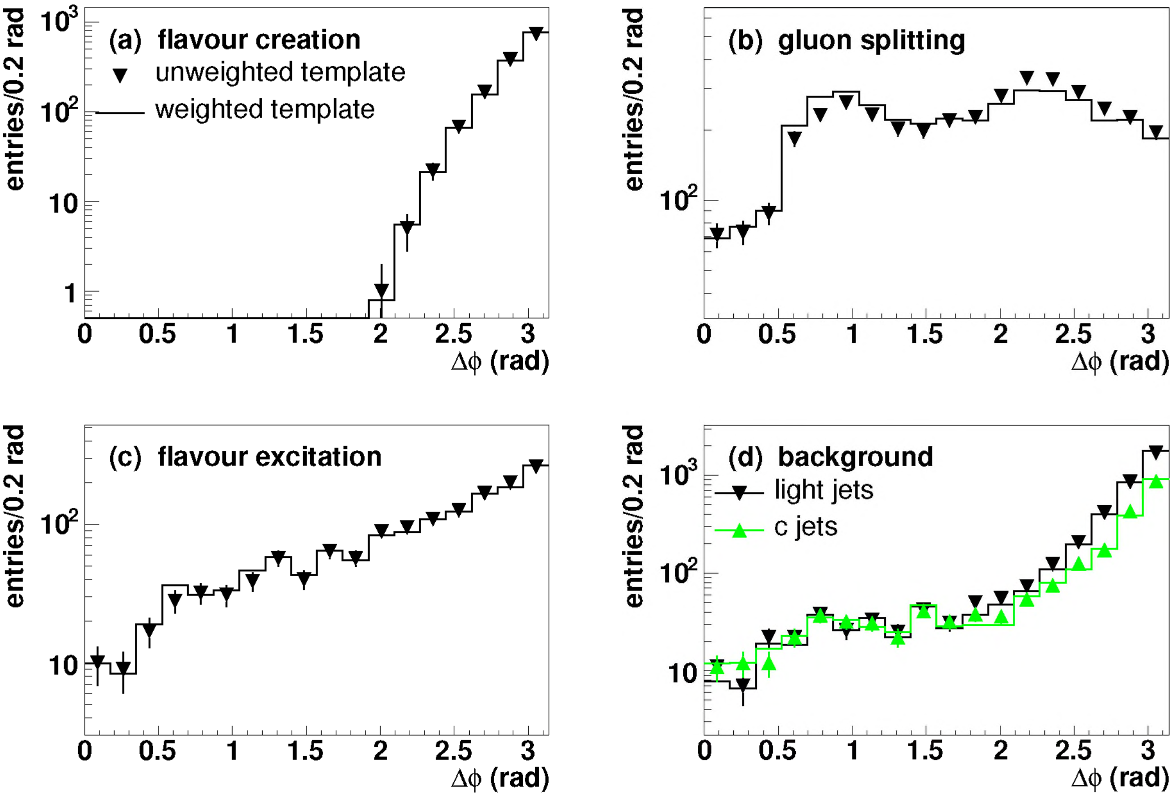

Figure 7.3: Azimuthal correlations between jets in the flavour creation (a), gluon splitting (b), flavour excitation (c) and $c\bar{c}$ and light jet background (d) Monte Carlo samples. The weighted templates (solid lines) have been scaled to the unweighted templates (triangular markers).

template is therefore used to fit the background contribution. The template was made by adding the $c\bar{c}$ and light jet templates with appropriate weights W_{udsg} and $W_{c\bar{c}}$.

To evaluate the uncertainty, the background template was also made with a charm content of $0.5 \pm 1/\sqrt{12}$, equal to one standard deviation assuming that the probability distribution of the charm fraction between zero and one is uniform.

If f_{udsg} and $f_{c\bar{c}}$ are the desired fractions of light jet and $c\bar{c}$ events in the combined template, the weights W_{udsg} and $W_{c\bar{c}}$ are chosen to be

$$\begin{cases} W_{\text{udsg}} = 1, & W_{c\bar{c}} = \frac{N_{\text{udsg}} \cdot f_{c\bar{c}}}{N_{c\bar{c}} \cdot f_{\text{udsg}}} \quad \text{if } f_{c\bar{c}} N_{c\bar{c}} > f_{\text{udsg}} N_{\text{udsg}}, \\ W_{\text{udsg}} = \frac{N_{c\bar{c}} \cdot f_{\text{udsg}}}{N_{\text{udsg}} \cdot f_{c\bar{c}}}, & W_{c\bar{c}} = 1 \quad \text{if } f_{\text{udsg}} N_{\text{udsg}} > f_{c\bar{c}} N_{c\bar{c}}, \end{cases} \tag{7.2}$$

where N_{udsg} and $N_{c\bar{c}}$ are the integrals of the light jet and c jet templates, respectively. This procedure ascertains that the Monte Carlo statistical uncertainties for the background sample are not underestimated.

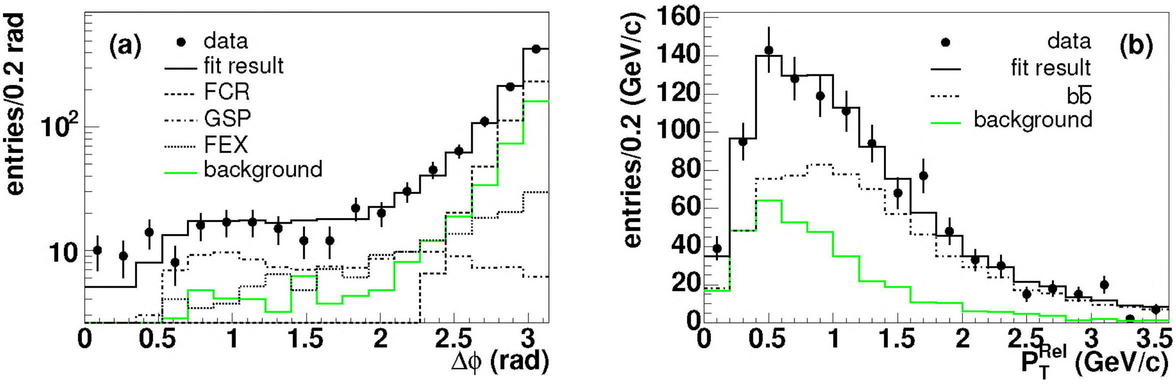

Figure 7.4: Distributions of $\Delta\phi$ (a) and P_T^{Rel} (b), and the result of the simultaneous template fit to the two distributions.

7.3 Ratio between b$\bar{\text{b}}$ production cross sections

To extract the contributions of FCR, GSP and FEX production processes to the data sample, the $\Delta\phi$ distributions for the three processes and for background events are used as templates in a fit to the data distribution. A simultaneous fit of the b$\bar{\text{b}}$ and background P_T^{Rel} templates defined in Section 6.1 is performed to determine the fraction of background events remaining in the data. The fit method is the same as that used in Section 6.1.6. The likelihood to be maximised is the product of the $\Delta\phi$ and P_T^{Rel} likelihoods, or, equivalently, the sum of the log likelihoods:

$$\begin{aligned}\ln\mathcal{L} = &\sum_{i=1}^{n} d_i \ln f_i - f_i + \sum_{i=1}^{n}\sum_{j=1}^{m} a_{ji}\ln A_{ji} - A_{ji} \\ &+ \sum_{i=1}^{k} p_i \ln g_i - g_i + \sum_{i=1}^{k}\sum_{j=1}^{l} g_{ji}\ln G_{ji} - G_{ji},\end{aligned} \tag{7.3}$$

which is an extension of Eq. 6.1. Here, d_i and p_i are the distributions of $\Delta\phi$ and P_T^{Rel} in data, respectively; f_i and g_i are the corresponding predictions of the fit, and a_{ji} and g_{ji} are the distributions of $\Delta\phi$ and P_T^{Rel} for Monte Carlo sample j. A_{ji} and G_{ji} are the assumed “true” distributions.

Because the P_T^{Rel} distributions for b jets from each process are the same, only two P_T^{Rel} templates are used (so $l = 2$): one for b jets and one for background jets. The FCR, GSP and FEX contributions are explicitly required to sum to the total b jet contribution. The same background fraction is used for both the P_T^{Rel} and the $\Delta\phi$ contributions to the likelihood.

The results of the fit and the correlation matrix are given in Tables 7.1 and 7.2. Only the statistical uncertainties, given by the fit, are shown. They include the uncertainty due to limited statistics in the Monte Carlo templates as well as to the size of the data sample. The $\Delta\phi$ and P_T^{Rel} distributions in data are shown in Fig. 7.4, together with the Monte Carlo distributions normalised to their contribution to the total fit result.

process	fraction
Flavour creation	0.40 ± 0.06
Gluon splitting	0.12 ± 0.05
Flavour excitation	0.15 ± 0.09
Background	0.33 ± 0.06
χ^2_λ/ndf	$45/32$

Table 7.1: Uncorrected results of the simultaneous fit to the data $\Delta\phi$ and P_T^{Rel} distributions.

$$\begin{array}{c|cccc} & f_{\mathrm{FCR}} & f_{\mathrm{GSP}} & f_{\mathrm{FEX}} & f_{\mathrm{BG}} \\ \hline f_{\mathrm{FCR}} & 1 & 0.5686 & -0.5174 & -0.6908 \\ f_{\mathrm{GSP}} & 0.5686 & 1 & -0.9154 & -0.1217 \\ f_{\mathrm{FEX}} & -0.5174 & -0.9154 & 1 & -0.1008 \\ f_{\mathrm{BG}} & -0.6908 & -0.1217 & -0.1008 & 1 \end{array}$$

Table 7.2: Correlation matrix for the uncorrected fit results given in Table 7.1.

7.3.1 Purity of the data sample

The distribution shown in Fig. 7.4 still contains a fraction of background events due to fake tags. The results given in Table 7.1 have to be corrected for these background events if they are interpreted as signal events by the fit. Four possible combinations have to be considered:

1. The muon jet and the away jet are both b jets;
2. The muon jet and the away jet are both non-b jets;
3. The away jet is a b jet, but the muon jet is a light jet;
4. The muon jet is a b jet, but the away jet is a falsely tagged light flavour jet.

The first two configurations are correctly identified by the P_T^{Rel} dimension of the fit as signal and background, respectively. The third configuration is identified by the fit as background, but has a $\Delta\phi$ distribution that is different from that of real light flavour production. In an inclusive QCD Monte Carlo sample, only $(1 \pm 1)\%$ of all muons in jets opposite a b jet did not originate from a b quark decay. Since these events represent only a small distortion of the $\Delta\phi$ distribution for lighter jets, their contribution is ignored in this thesis. The last configuration is seen as signal by the fit, but is considered background to the true $\Delta\phi(\mathrm{b\bar{b}})$ distribution. The contribution of this *fake IP tag* background can be determined from the data.

The total number of events remaining after applying the impact parameter tag to the away jet is given by

$$N^{\mathrm{tag}} = \epsilon_{\mathrm{signal}} \times N^{\mathrm{tot}}_{\mathrm{signal}} + \epsilon_{\mathrm{background}} \times N^{\mathrm{tot}}_{\mathrm{background}}, \tag{7.4}$$

where $\epsilon_{\mathrm{signal}}$ and $\epsilon_{\mathrm{background}}$ are the efficiency of the impact parameter tag for signal and background events and $N^{\mathrm{tot}}_{\mathrm{signal}}$ and $N^{\mathrm{tot}}_{\mathrm{background}}$ are the total number of signal events and background events in the untagged sample, respectively.

process	corrected fraction
Flavour creation	0.40 ± 0.06
Gluon splitting	0.12 ± 0.05
Flavour excitation	0.15 ± 0.09
Background	0.34 ± 0.06

Table 7.3: Results of the simultaneous fit to the data $\Delta\phi$ and P_T^{Rel} distributions corrected for the contribution of *fake IP tag* events. The uncertainties given are the fit uncertainties.

For two different operating points, Eq. 7.4 can be written down:

$$N^{(1)} = \epsilon^{(1)}_{\text{signal}} \times N^{\text{tot}}_{\text{signal}} + \epsilon^{(1)}_{\text{background}} \times N^{\text{tot}}_{\text{background}}, \tag{7.5}$$

$$N^{(2)} = \epsilon^{(2)}_{\text{signal}} \times N^{\text{tot}}_{\text{signal}} + \epsilon^{(2)}_{\text{background}} \times N^{\text{tot}}_{\text{background}}, \tag{7.6}$$

where $N^{(1)}$ and $N^{(2)}$ are the numbers of events remaining at the operating points (1) and (2) of the impact parameter tag and $\epsilon^{(1)}$ and $\epsilon^{(2)}$ are the efficiencies at these operating points. Equations 7.5 and 7.6 can be solved for $N^{\text{tot}}_{\text{background}}$, giving the total number of background events before applying the impact parameter tag:

$$N^{\text{tot}}_{\text{background}} = \frac{\epsilon^{(2)}_{\text{signal}} \times N^{(1)} - \epsilon^{(1)}_{\text{signal}} \times N^{(2)}}{\epsilon^{(2)}_{\text{signal}} \times \epsilon^{(1)}_{\text{background}} - \epsilon^{(1)}_{\text{signal}} \times \epsilon^{(2)}_{\text{background}}}. \tag{7.7}$$

The number of background events remaining in the tagged sample can then be found by multiplying $N^{\text{tot}}_{\text{background}}$ by the background jet tagging efficiency.

In this context, signal events are events where both the muon jet and the away jet are real b jets, and background events are those where the muon jet is a b jet but the away jet is not. The signal efficiency ϵ_{signal} is therefore simply the b jet efficiency. Given that the muon jet is a b jet, the probability that the away jet is a c jet is very small and $\epsilon_{\text{background}}$ is equal to the light jet efficiency. The number of tagged events N^{tag} is defined as the number of events where the muon jet is a b jet, given by the template fit at each operating point of the impact parameter tag.

The fraction of *fake IP tag* events is determined using jets with $N_{\text{tracks}} \geq 2$ and jets with $\mathcal{D} > 5$ as the two operating points of the impact parameter tag. The fractions of jets with $N_{\text{tracks}} \geq 2$ are $\epsilon^{(1)}_{\text{signal}} = 0.57 \pm 0.02$ and $\epsilon^{(1)}_{\text{background}} = 0.524 \pm 0.001$, respectively, and the efficiencies for $\mathcal{D} > 5$ are $\epsilon^{(2)}_{\text{signal}} = 0.099 \pm 0.005$ and $\epsilon^{(2)}_{\text{background}} = 0.006 \pm 0.001$ (see Section 6.2.9). The number of events with jets with $N_{\text{tracks}} \geq 2$ in the sample is 11786 and the P_T^{Rel} fit returns $f^{(1)}_{\text{b}} = 0.38 \pm 0.02$, so $N^{(1)} = 4526 \pm 289$. At $\mathcal{D} > 5$, 1062 events remain and the fraction of b jets is $f^{(2)}_{\text{b}} = 0.68 \pm 0.06$, so $N^{(2)} = 725 \pm 65$. The fraction of *fake IP tag* events remaining after applying the impact parameter tag ($\mathcal{D} > 5$) is $(0.4 \pm 0.6)\%$. The fractions of FCR, GSP, FEX and background events after correcting for this fraction are given in Table 7.3. The relative fractions of FCR, GSP and FEX events were kept constant. The corresponding correlation matrix is shown in Table 7.4. The uncertainty on the correction is treated as a systematic uncertainty in Section 7.5 and is not included in Table 7.3.

$$\begin{array}{c} & f_{\mathrm{FCR}} & f_{\mathrm{GSP}} & f_{\mathrm{FEX}} & f_{\mathrm{BG}} \\ \begin{array}{c} f_{\mathrm{FCR}} \\ f_{\mathrm{GSP}} \\ f_{\mathrm{FEX}} \\ f_{\mathrm{BG}} \end{array} & \multicolumn{4}{c}{\left(\begin{array}{cccc} 1 & 0.5686 & -0.5156 & -0.6921 \\ 0.5686 & 1 & -0.9148 & -0.123 \\ -0.5156 & -0.9148 & 1 & -0.1018 \\ -0.6921 & -0.123 & -0.1018 & 1 \end{array}\right)} \end{array}$$

Table 7.4: Correlation matrix for the corrected fit results given in Table 7.3.

process	normalised fraction
Flavour creation	0.60 ± 0.06
Gluon splitting	0.18 ± 0.07
Flavour excitation	0.22 ± 0.11

Table 7.5: Contribution of the FCR, GSP and FEX processes to the total $\mathrm{b\bar{b}}$ sample.

Ideally, the $\Delta\phi$ distribution should be corrected without using any assumption of the shape of the background distribution. This could be done by performing a P_T^{Rel} fit in bins of $\Delta\phi$ and estimating the fractions of signal and background in each bin. In the present analysis, the size of the data sample and the efficiency of the impact parameter tag are too small to do the fit in more than two bins of $\Delta\phi$ and we will rely instead on the Monte Carlo simulation to describe the shape of the background contribution.

7.3.2 Normalised distributions

To compare the measured fractions to predicted values, the measured fractions were normalised to the total $\mathrm{b\bar{b}}$ contribution:

$$\begin{aligned} f_{\mathrm{FCR}}^{\mathcal{N}} &= f_{\mathrm{FCR}}/(1 - f_{\mathrm{BG}}), \\ f_{\mathrm{GSP}}^{\mathcal{N}} &= f_{\mathrm{GSP}}/(1 - f_{\mathrm{BG}}), \\ f_{\mathrm{FEX}}^{\mathcal{N}} &= f_{\mathrm{FEX}}/(1 - f_{\mathrm{BG}}). \end{aligned}$$

The normalised fractions, along with their statistical uncertainty, are shown in Table 7.5. The statistical uncertainty was propagated using the covariance matrix of the fit.

7.4 Cross checks

7.4.1 Fit method

To check the results of the combined Monte Carlo and data likelihood fit, two additional fit methods were tried: a likelihood fit assuming infinite Monte Carlo statistics and a pseudo-2D fit to the $\Delta\phi$-P_T^{Rel} distribution.

	standard fit	infinite MC statistics	Pseudo-2D
Flavour creation	0.40 ± 0.06	0.41 ± 0.06	0.41 ± 0.04
Gluon splitting	0.12 ± 0.05	0.13 ± 0.05	0.14 ± 0.04
Flavour excitation	0.15 ± 0.09	0.13 ± 0.07	0.11 ± 0.06
Background	0.33 ± 0.06	0.33 ± 0.06	0.33 ± 0.04
χ^2_λ/ndf	$45/32$	$47/32$	$329/320$

Table 7.6: Uncorrected results of the simultaneous fit to the data $\Delta\phi$ and P_T^{Rel} distributions, using the full likelihood, assuming infinite Monte Carlo statistics and using a pseudo-2D fit.

	$0 < \Delta\phi < \pi/2$	$\pi/2 < \Delta\phi < \pi$	$0 < \Delta\phi < \pi$
b jets	1.0 ± 0.7	0.65 ± 0.07	0.68 ± 0.06
background	0.0 ± 0.6	0.35 ± 0.06	0.32 ± 0.06

Table 7.7: Results of the template fit to the P_T^{Rel} distribution in the tagged data sample, for $0 < \Delta\phi < \pi/2$, $\pi/2 < \Delta\phi < \pi$ and for the total sample.

In the template fit, the combined likelihood of the Monte Carlo distributions and the data distribution is computed with respect to the unknown "true" distribution. In the case of infinitely large Monte Carlo samples, the true distribution will be equal to the Monte Carlo distributions and the Monte Carlo likelihood does not affect the fit result. The same is true if the Monte Carlo likelihood is left out of the optimisation procedure. The result of the data likelihood only fit is given in Table 7.6 and is compatible with the previous result.

If a strong correlation between $\Delta\phi$ and P_T^{Rel} exists, the result of a true 2D $\Delta\phi$-P_T^{Rel} fit may differ from the result of the simultaneous fit to the two distributions. Because the generation of a true 2D Monte Carlo sample would take too much resources, a pseudo-2D fit was tried. Effectively, the product of the Monte Carlo $\Delta\phi$ and P_T^{Rel} distributions was fitted to the true 2D data distribution, again assuming infinite Monte Carlo statistics. Correlations between $\Delta\phi$ and P_T^{Rel} are taken into account, but correlations in the Monte Carlo are still ignored. The results are again compatible with the simultaneous fit (see Table 7.6). It should be noted that the pseudo-2D fit underestimates the statistical uncertainty.

As an additional check, a simple P_T^{Rel} fit without $\Delta\phi$ information to the tagged data sample was also tried. A single template was used to represent all $b\bar{b}$ processes. The result of the P_T^{Rel} only fit, on the whole sample and in two separate bins of $\Delta\phi$, is given in Table 7.7. The results are compatible with those of the simultaneous fit to $\Delta\phi$ and P_T^{Rel} and consistent with the presence of higher order $b\bar{b}$ production processes.

7.4.2 Kinematic distributions

As a separate check of the Monte Carlo distributions, the jet E_T^{CAL}, η^{CAL} and ϕ^{CAL} distributions of the Monte Carlo samples are compared to those of the data sample. The Monte Carlo samples, normalised to their contribution to the $\Delta\phi$ distribution as given by the fit, are shown together with

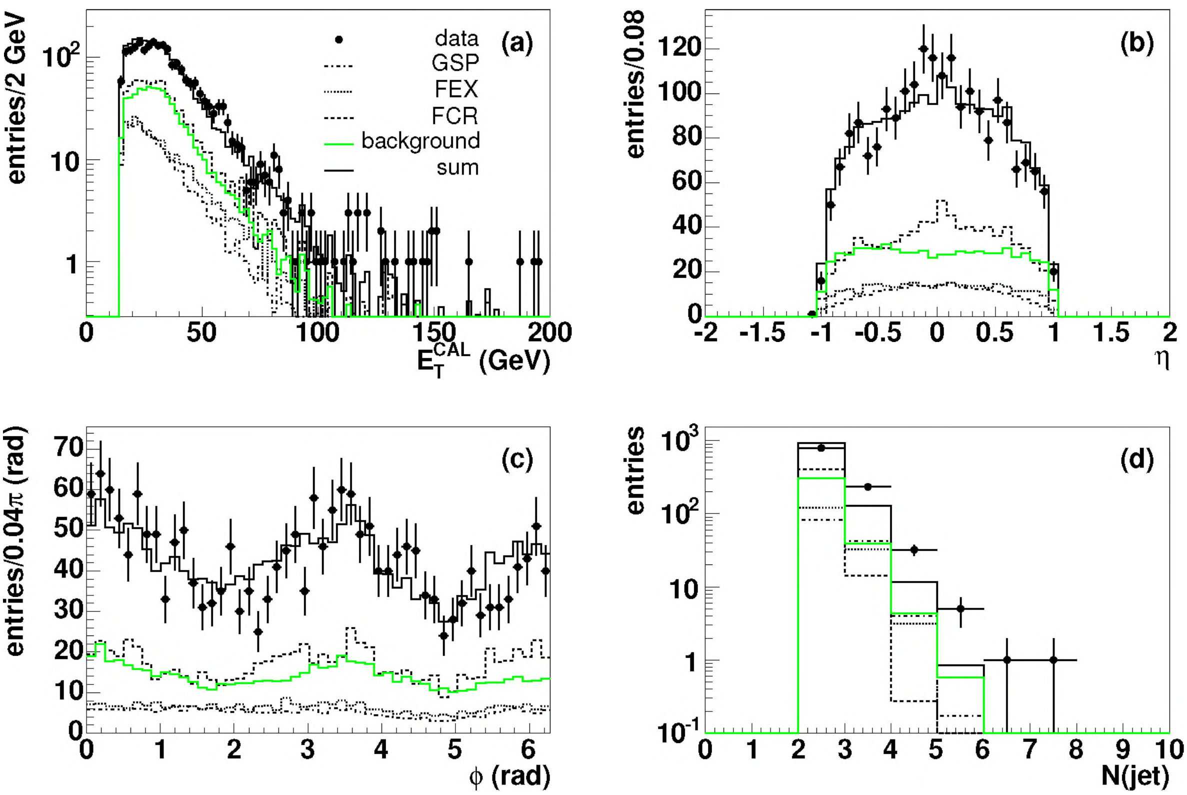

Figure 7.5: E_T (a), η (b) and ϕ (c) distributions of jets in the tagged data sample, together with the distributions of the Monte Carlo $\Delta\phi$ templates normalised to their measured contributions to the data. The distribution of the number of jets with $|\eta| < 1$ and $E_T > 15$ GeV is shown in (d).

the data distribution in Fig. 7.5. The kinematic distributions of the combined Monte Carlo samples match the data distribution well in Fig. 7.5(a)–(c).

The distribution of the number of jets per event, shown in Fig. 7.5 (d), is not very well described by the Monte Carlo samples. This may be due to the tuning of the event generator, in particular the amount of initial state radiation. The difference between the data and the Monte Carlo samples is evaluated and treated as a systematic uncertainty in Section 7.5.

The kinematic distributions of the muons in the Monte Carlo P_T^{Rel} templates, normalised to the contribution to the fit, are shown in Fig. 7.6. The distributions of the Monte Carlo templates match those in data well.

7.5 Systematic uncertainties

The systematic uncertainties can be divided in uncertainties related to the generation of the Monte Carlo templates, uncertainties related to data selection and reconstruction, and uncertainties related to corrections made to the fit result. Most of the uncertainties are determined as deviations from the central result when input parameters are fluctuated by $\pm 1\sigma$ around their central value. The

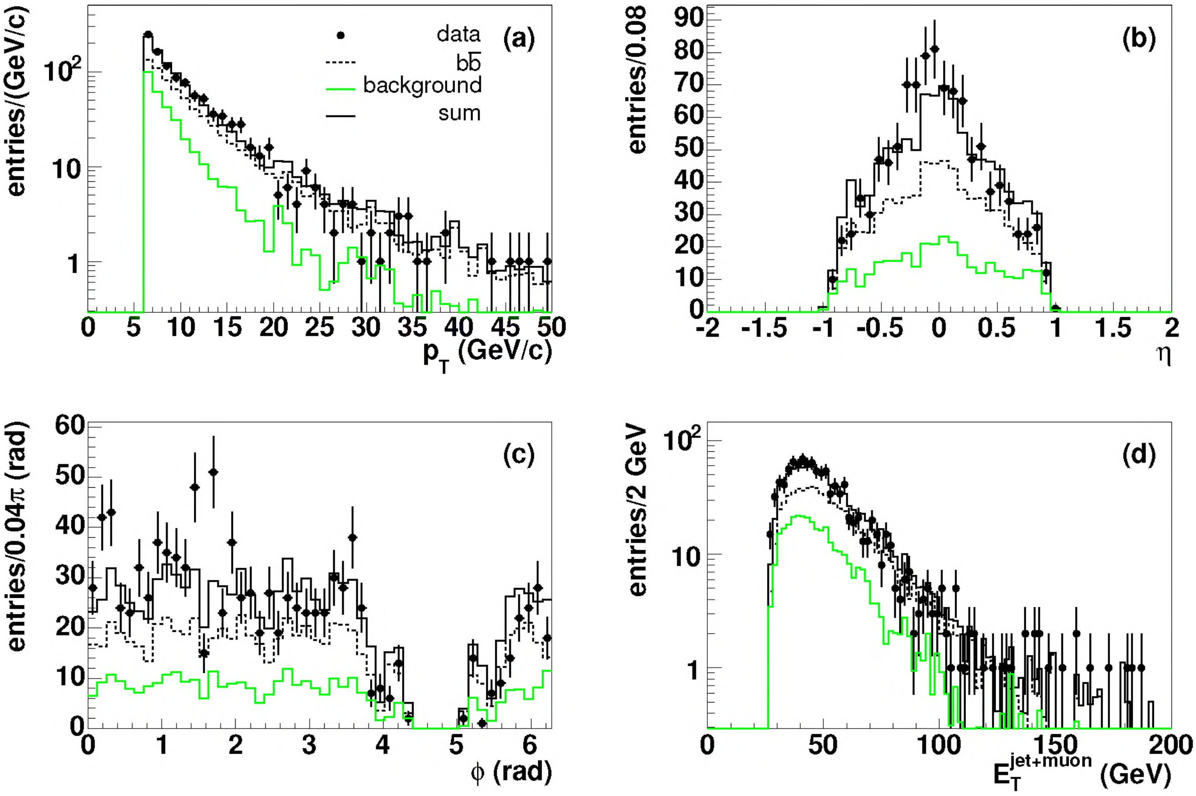

Figure 7.6: Muon distributions in the tagged data sample together with the distributions of the Monte Carlo P_T^{Rel} templates normalised to their measured contributions to the data. Figure (d) shows the combined E_T of the muon plus the associated jet.

results are summarised in Table 7.8. The normalised fractions are determined separately for each source of systematic uncertainty and are included in the table.

The systematic uncertainties on the fractions f_{FCR}, f_{GSP}, f_{FEX} and f_{BG} are summarised in Table 7.9. The systematic uncertainties on the normalised fractions are given in Table 7.10. The sources of systematic uncertainties are discussed below.

7.5.1 Background template

A large uncertainty on the result is due to the uncertainty on the fractions of $c\bar{c}$ and light events that make up the background. Assuming that the probability density of the fraction of $c\bar{c}$ events is uniformly distributed between zero and one, the best value is $0.5 \pm 1/\sqrt{12}$. The uncertainty on the result was evaluated by performing the fit with 21%/79% $c\bar{c}$/light jet and with 79%/21% $c\bar{c}$/light jet templates.

	fake IP tag corrected fit result				normalised fractions		
	f_{FCR}	f_{GSP}	f_{FEX}	f_{BG}	$f^{\mathcal{N}}_{\mathrm{FCR}}$	$f^{\mathcal{N}}_{\mathrm{GSP}}$	$f^{\mathcal{N}}_{\mathrm{FEX}}$
nominal value	0.397	0.120	0.147	0.335	0.597	0.181	0.222
background 21% $c\bar{c}$	0.434	0.146	0.137	0.283	0.605	0.203	0.192
background 79% $c\bar{c}$	0.362	0.0892	0.164	0.385	0.589	0.145	0.267
reweighted N_{jets}	0.430	0.0815	0.139	0.349	0.661	0.125	0.214
energy scale $+1\sigma$	0.431	0.176	0.102	0.291	0.608	0.248	0.145
energy scale -1σ	0.384	0.0891	0.164	0.363	0.604	0.140	0.257
trigger $+1\sigma$	0.396	0.121	0.147	0.337	0.598	0.182	0.221
trigger -1σ	0.403	0.132	0.130	0.337	0.607	0.199	0.194
IP tag $+1\sigma$	0.398	0.117	0.149	0.336	0.599	0.177	0.225
IP tag -1σ	0.397	0.124	0.145	0.335	0.596	0.186	0.219
Peterson $\epsilon_{\mathrm{b}} = 0.002$	0.391	0.119	0.147	0.343	0.595	0.181	0.225
Peterson $\epsilon_{\mathrm{b}} = 0.006$	0.387	0.118	0.147	0.349	0.594	0.181	0.225

Table 7.8: Summary of *fake IP tag* corrected fit results used to evaluate systematic uncertainties.

	f_{FCR}	f_{GSP}	f_{FEX}	f_{BG}
fake IP tag correction	-0.00395	-0.00395	-0.00395	±0.00557
background template	$+0.03683$ -0.03489	$+0.02512$ -0.03126	$+0.01618$ -0.01003	$+0.04976$ -0.05199
reweighted N_{jets}	$+0.03325$	-0.03896	-0.00836	$+0.01401$
energy scale	$+0.03367$ -0.01261	$+0.0554$ -0.03135	$+0.01624$ -0.04498	$+0.02772$ -0.04407
trigger efficiency	$+0.00566$ -0.00067	$+0.0117$ -0	$+0$ -0.01849	$+0.00142$ -0
IP tag efficiency	$+0.00043$ -0.00059	$+0.00334$ -0.00295	$+0.00187$ -0.00201	$+0.00066$ -0.00076
Peterson parameter	$+0$ -0.01056	$+0$ -0.00243	$+0$ -0.00072	$+0.0137$ -0
total	$+0.06$ -0.04	$+0.06$ -0.06	$+0.02$ -0.05	$+0.06$ -0.07

Table 7.9: Systematic uncertainties on the *fake IP tag* corrected fractions f_{FCR}, f_{GSP}, f_{FEX} and f_{BG}.

7.5.2 Fake IP tag background

The background component consisting of a real semileptonic b jet combined with a fake impact parameter tag is determined directly from data (see Section 7.3.1). The fraction of *fake IP tag* events is $(0.4 \pm 0.6)\%$. This fraction is added to the fraction f_{BG} returned by the fit and the uncertainty on the *fake IP tag* background component is added to the uncertainty on f_{BG}.

The fraction of *fake IP tag* events is subtracted from the fractions f_{FCR}, f_{GSP} and f_{FEX} preserving their relative contributions. Because it is not known whether the *fake IP tag* background events are,

	f_{FCR}	f_{GSP}	f_{FEX}
fake IP tag correction	± 0.00772	± 0.00609	± 0.00618
background template	$+0.00804$ -0.00823	$+0.0219$ -0.03612	$+0.04481$ -0.03009
reweighted N_{jets}	$+0.06395$	-0.05596	-0.00807
energy scale	$+0.01042$ -0.00627	$+0.06692$ -0.04131	$+0.03518$ -0.07724
trigger efficiency	$+0.00957$ -0	$+0.01795$ -0	$+0$ -0.02748
IP tag efficiency	$+0.00124$ -0.00157	$+0.00481$ -0.00427	$+0.00303$ -0.00328
Peterson parameter	$+0$ -0.00366	$+0.00007$ -0.00001	$+0.00357$ -0
total	$+0.07$ -0.01	$+0.07$ -0.08	$+0.06$ -0.09

Table 7.10: Summary of systematic uncertainties on normalised fit results.

in reality, FCR, GSP or FEX events, the total fraction of *fake IP tag* events is taken as an additional uncertainty of 0.4% on the fractions f_{FCR}, f_{GSP} and f_{FEX}.

7.5.3 Jet Energy Scale

The jet energy scale affects the sample composition through the jet E_T cutoff. The uncertainty due to the uncertainty on the jet energy scale was estimated by evaluating the result using the jet energy scale correction at $\pm 1\sigma$ for both Monte Carlo and data. The uncertainty due to the jet energy scale is one of the dominant contributions to the total systematic uncertainty.

7.5.4 Number of jets in Monte Carlo and data

From Fig. 7.5 (d) it is clear that the distribution of the number of jets per event N_{jets} in data is not very well described by the Monte Carlo. A possible cause of this discrepancy is the amount of initial state radiation (ISR) generated by PYTHIA. The amount of ISR directly affects the $\Delta\phi$ distribution as the number of jets in an event increases with increasing ISR. The default amount of ISR in PYTHIA 6.2 is known not to describe the data well [125].

The uncertainty due to this discrepancy was evaluated by reweighting all the templates according to the number of jets in each event to reproduce the distribution of N_{jets} in data. The difference of the result using the reweighted templates with respect to the result obtained with standard templates was taken as a systematic uncertainty on the fractions. The jet E_T^{CAL}, η and ϕ distributions of the reweighted templates show a similar agreement with the data as those of the unweighted templates, shown in Fig. 7.5.

7.5.5 Trigger efficiency

The Monte Carlo events for the templates are weighted with the trigger efficiency as a function of E_T^{CAL}. The trigger efficiency was measured on data in Section 4.2 with an uncertainty that needs to be taken into account in the final result. To evaluate the uncertainty on the final result, the templates were regenerated twice, once using the trigger efficiency fluctuated upward by 1σ and once fluctuated downward by 1σ. The maximum deviation with respect to the result obtained with the standard templates was taken as a systematic uncertainty on the fractions.

7.5.6 Fragmentation

The choice of fragmentation function directly affects the fraction of the jet momentum carried by the B meson. The use of jets as an observable rather than quarks or mesons reduces the dependence of $\Delta\phi$ on the fragmentation function, since all observable particles are included in the jet. (Only the neutrino, in the case of a semileptonic decay, escapes detection).

The P_T^{Rel} distribution is more sensitive to modelling of fragmentation. The effect of the choice of fragmentation function is evaluated by varying the Peterson fragmentation parameter ϵ_{b} between 0.002 and 0.006.

Because generating events with the full detector simulation takes a lot of time, the effect of changing the fragmentation function parameter was evaluated by generating templates at Monte Carlo particle level. The bin by bin ratios of the $\epsilon_{\mathrm{b}} = 0.002$ and $\epsilon_{\mathrm{b}} = 0.006$ templates with respect to the standard template were used to reweight the template used to perform the fit. The difference with the standard result is taken as an uncertainty on the fractions. This is a small effect.

7.5.7 Tag rate functions

The dependence of the impact parameter tag on E_T, η and ϕ of the away jet was simulated in the Monte Carlo sample by applying tag rate functions, derived from data, to the jets in the Monte Carlo sample. The TRFs are given in Section 6.2.9. The uncertainty associated with the uncertainty on the TRFs was evaluated by fluctuating the TRFs upward and downward by 1σ, just like the uncertainty due to reweighting the events with the trigger efficiency. The uncertainty due to the TRFs is so small as to be effectively negligible.

7.5.8 $\mathrm{b\bar{b}}$ jets

Jets which can be associated with more than one B hadron in the Monte Carlo are explicitly excluded from the P_T^{Rel} templates. These $\mathrm{b\bar{b}}$ jets have a different P_T^{Rel} distribution, as shown in Section 6.1.2. Their exclusion is motivated by the presence of a second tagged jet in each event. However, in the case of a fake impact parameter tag, a $\mathrm{b\bar{b}}$ jet with a matched muon may still be present.

To evaluate the impact of the presence of $\mathrm{b\bar{b}}$ jets in the data, the fraction of $\mathrm{b\bar{b}}$ jets remaining after all event selection cuts and the away side impact parameter tag is estimated from Monte Carlo. Because the generation of inclusive $\mathrm{b\bar{b}}$ events in PYTHIA is very inefficient, the MC@NLO sample (see Section 2.8) was used for this. Particle level P_T^{Rel} templates were generated from this sample by selecting muon jets with at least one other jet within the acceptance and weighting the

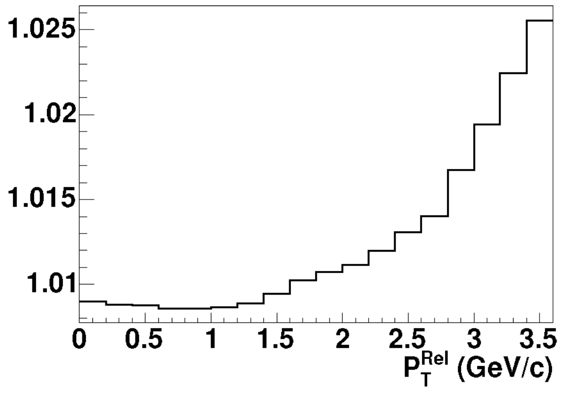

Figure 7.7: Ratio between the b jet P_T^{Rel} templates including and excluding $b\bar{b}$ jets.

events with the tagging efficiency for the away jet. The fraction of $b\bar{b}$ jets remaining after applying the impact parameter tag to the away jet is about 1%.

The Monte Carlo muons and particle jets were smeared with the full muon and jet resolutions measured in data. Two templates were generated: one with, and one without $b\bar{b}$ jets. To avoid statistical fluctuations due to the smearing method, the data set was looped over 1000 times with a different random number seed. The ratio between the two templates is shown in Fig. 7.7. This distribution was used as an additional bin by bin weight for the b jet P_T^{Rel} template. The difference with the result using standard templates was negligible, even if the fraction of $b\bar{b}$ jets was estimated to be twice as high as predicted by MC@NLO.

7.5.9 Total systematic uncertainty

The total asymmetric systematic uncertainty on f_{FCR}, f_{GSP}, f_{FEX} and f_{BG} is determined from the uncertainties given in Table 7.9 and is included in the table. For the upper uncertainty, all upward fluctuations for each fraction given in the table are added quadratically. If the fluctuations from a single source are both positive (e.g. the uncertainty on f_{GSP} due to the trigger efficiency uncertainty), the larger value is used. The lower uncertainty is determined using all downward fluctuations. The uncertainty on f_{BG} due to the uncertainty on the *fake IP tag* correction is included in both the upper and the lower systematic uncertainty.

The total systematic uncertainty on the normalised fractions is determined in the same manner from the uncertainties given in Table 7.10 and is included in the table.

7.6 Ratio of production mechanisms in Pythia

The fractions $f^{\mathcal{N}}_{\mathrm{FCR}}$, $f^{\mathcal{N}}_{\mathrm{GSP}}$ and $f^{\mathcal{N}}_{\mathrm{FEX}}$ measured in data are compared to the fractions in a sample generated with PYTHIA. To account for the reconstruction and tagging efficiencies, each event was weighted with the same weights used to create the $\Delta\phi$ templates in Section 7.2. A statistical uncertainty was derived from the unweighted events. The fractions predicted by PYTHIA are given

process	PYTHIA prediction	data
Flavour creation	0.48 ± 0.04	$0.60 \pm 0.06(\text{stat})^{+0.07}_{-0.01}(\text{syst})$
Gluon splitting	0.41 ± 0.05	$0.18 \pm 0.07(\text{stat})^{+0.07}_{-0.08}(\text{syst})$
Flavour excitation	0.11 ± 0.04	$0.22 \pm 0.11(\text{stat})^{+0.06}_{-0.09}(\text{syst})$

Table 7.11: PYTHIA predictions for the fractions f^{N}_{FCR}, f^{N}_{GSP} and f^{N}_{FEX} and the measured fractions in data normalised to the total $\text{b}\bar{\text{b}}$ fraction. The uncertainty on the predicted fractions is statistical. The first uncertainty on the measured values is the statistical uncertainty, the second the systematic uncertainty.

in Table 7.11, along with the fractions measured in data.

Despite the large uncertainties it is clear from the data that the FCR process alone cannot reproduce the total distribution. PYTHIA overestimates the GSP contribution and underestimates the FCR and FEX contributions. The discrepancy between the predicted and measured values for f^{N}_{FCR} and f^{N}_{FEX} are not very significant, however, due to the large uncertainties.

7.7 Prospects for this measurement with DØ

The total uncertainty on the present measurement is dominated by a few sources of systematic uncertainties. All these uncertainties will be reduced significantly with a larger sample size and the improved reconstruction and tagging abilities currently available at DØ.

An important improvement to the measurement can be expected from improved background rejection. With improved tagging algorithms and larger data samples allowing a tighter cut, a much higher signal purity can be obtained [126]. An improvement of more than a factor five in the rejection of charm and light jets will reduce the uncertainty due to the uncertainty on the background composition to less than 1%. The ability to use information from the central tracking systems in the muon reconstruction will also improve the P_T^{Rel} fits.

Other uncertainties are due to experimental effects which have become much better understood at DØ with increased sample sizes and improved reconstruction algorithms. The uncertainty on the jet energy scale has improved to better than 5% for central jets. Better understanding of noise and fake jets in the calorimeter (see Section 5.1.5) will also reduce the uncertainty on the trigger turnon as a function of jet E_T.

A lot of work has been done in recent years to improve the modelling of b fragmentation [11]. Applying fragmentation models which better describe Tevatron data will reduce the uncertainty due to the choice of fragmentation model and parameters.

The measurement presented in this thesis depends strongly on Monte Carlo assumptions for the shape of the background $\Delta\phi$ distribution. With a large enough sample, it is possible to determine the fraction of background remaining in the tagged sample as a function of $\Delta\phi$ by performing the P_T^{Rel} template fit in several bins of $\Delta\phi$. A background corrected $\text{b}\bar{\text{b}}$ jet $\Delta\phi$ distribution can then be obtained. After correcting this distribution for experimental biases and resolutions, the distribution can be directly compared to theory predictions, providing a powerful experimental test of NLO calculations and Monte Carlos.

With the forward muon system and the F- and H-disks fully operational, the measurement using a muon tag and a lifetime tag can easily be extended to pseudorapidities larger than one. With a larger acceptance in η, the ΔR distribution can also be used to separate the various $\mathrm{b\overline{b}}$ production processes.

Finally, with the larger data sample, an E_T dependent measurement of the fractions f_{FCR}, f_{GSP} and f_{FEX} can be done.

7.8 Conclusions

In this thesis the production mechanisms in QCD for $\mathrm{b\overline{b}}$ production are studied, using the angular correlation between the b quark and the $\mathrm{\overline{b}}$ quark in the event. The azimuthal correlation $\Delta\phi$ is measured between a b jet tagged with a muon and a b jet tagged with an impact parameter based lifetime tag and compared to PYTHIA predictions for flavour creation, gluon splitting and flavour excitation $\mathrm{b\overline{b}}$ production processes. The measured fractions for flavour creation (f_{FCR}), gluon splitting (f_{GSP}) and flavour excitation (f_{FEX}) are

$$\begin{aligned} f_{\mathrm{FCR}} &= 0.60 \pm 0.06(\mathrm{stat})^{+0.07}_{-0.01}(\mathrm{syst}), \\ f_{\mathrm{GSP}} &= 0.18 \pm 0.07(\mathrm{stat})^{+0.07}_{-0.08}(\mathrm{syst}), \\ f_{\mathrm{FEX}} &= 0.22 \pm 0.11(\mathrm{stat})^{+0.06}_{-0.09}(\mathrm{syst}). \end{aligned}$$

These fractions cannot be compared directly to theory predictions. They must first be unfolded for detector and fragmentation effects. Instead of unfolding the measured fractions, in this thesis the values are compared to the fractions in a PYTHIA simulation, folded with the detector behaviour. The measurement does not agree very well with the PYTHIA prediction, but the large uncertainties make a definite statement impossible. In addition, the default settings of PYTHIA may not yield the most accurate representation of real data. Alternative values for the amount of initial state radiation and other parameters are studied in e.g. [51].

With the large data samples now recorded by DØ and the improved understanding of the detector and the data reconstruction, the measurement of the fractions f_{FCR}, f_{GSP} and f_{FEX} can be used to test event generators to high accuracy. Parameters in PYTHIA that affect the $\Delta\phi$ distribution, especially the amount of initial state radiaton, and the relative contributions of flavour creation, flavour excitation and gluon splitting events can be tuned to reproduce the data more accurately. A pure $\mathrm{b\overline{b}}$ $\Delta\phi$ distribution can be compared directly to $\mathrm{b\overline{b}}$ calculations and event generators, and will provide a precise test of NLO $\mathrm{b\overline{b}}$ production in hadron collisions.

Appendix A

Goodness of fit for likelihood fits

Unlike χ^2 fits, likelihood fits do not automatically yield a "goodness of fit" parameter. Once the solution of the fit has been found, however, the likelihood ratio can be used to estimate the quality of the fit [127].

For a fit to a histogram, $L(\vec{y};\vec{n})$ is the likelihood of the distribution $\vec{y}$ to yield the data histogram bin contents $\vec{n}$. The predicted bin contents $\vec{y}$ are given by the maximisation of $L(\vec{y};\vec{n})$ as a function of the fit parametrisation.

In truth, the data $\vec{n}$ are generated from the true - unknown - distribution $\vec{m}$. The likelihood ratio is then defined as the ratio of the likelihood that the fitted distribution $\vec{y}$ generated the data $\vec{n}$ over the likelihood that the data are generated from the true distribution $\vec{m}$:

$$\lambda = \frac{L(\vec{y};\vec{n})}{L(\vec{m};\vec{n})}. \tag{A.1}$$

In practise, the true distribution $\vec{m}$ is replaced by the data distribution $\vec{n}$, and the likelihood $L(\vec{m};\vec{n})$ becomes the likelihood that the data distribution is generated by the data distribution itself.

The goodness of fit parameter χ^2_λ (also called the likelihood χ^2) is defined as

$$\chi^2_\lambda = -2\ln\left(\frac{L(\vec{y};\vec{n})}{L(\vec{m};\vec{n})}\right) = -2\ln(L(\vec{y};\vec{n})) + 2\ln(L(\vec{m};\vec{n})). \tag{A.2}$$

The value of χ^2_λ is smallest when $L(\vec{y};\vec{n})$ is at its maximal value, so maximising the likelihood is equivalent to minimising χ^2_λ. The distribution of χ^2_λ asymptotically approaches a true χ^2 distribution.The number of degrees of freedom ndf is given by the number of data points minus the number of free parameters, as for a χ^2 minimisation fit.

A.1 Goodness of fit for template fits

When fitting Monte Carlo templates to a data distribution with n bins, the Poisson likelihood is maximised (adopting the terminology of [121]):

$$\ln L(\vec{f};\vec{d}) = \sum_{i=1}^{m}\left(d_i \ln f_i - f_i - \ln d_i!\right), \tag{A.3}$$

where d_i are the contents of bin i and f_i is the prediction for that bin, given by

$$f_i = \sum_{j=1}^{m} p_j a_{ji}. \tag{A.4}$$

Here, a_{ji} are the contents of bin i in Monte Carlo sample j and p_j is the fraction of that sample contributing to the total prediction. The likelihood χ^2 after maximisation is then given by

$$\chi^2_\lambda = -2 \ln L(\vec{f}; \vec{d}) + 2 \ln L(\vec{d}; \vec{d}) \tag{A.5}$$

and the number of degrees of freedom is $ndf = n - m$.

When taking the limited statistics in the Monte Carlo samples into account, the likelihood to be maximised changes to

$$\ln L(f, d; A, a) = \sum_{i=1}^{n} \big(d_i \ln f_i - f_i - \ln d_i!\big) + \sum_{i=1}^{n} \sum_{j=1}^{m} \big(a_{ji} \ln A_{ji} - A_{ji} - \ln a_{ji}!\big), \tag{A.6}$$

where $\{A_{ji}\}$ is the (unknown) *true* distribution from which the Monte Carlo distribution $\{a_{ji}\}$ is generated. The f_i are now given by

$$f_i = \sum_{j=1}^{m} p_j A_{ji}. \tag{A.7}$$

After the maximum has been found (see [121]), all parameters in Eq. A.6 are known and the likelihood can be computed. The likelihood ratio is then given by

$$\lambda = \frac{L(f, d; A, a)}{L(d, d; a, a)} \tag{A.8}$$

and χ^2_λ is given by Eq. A.5.

For the maximisation of the likelihood given in Eq. A.6, the number of fit points considered is $(m+1) \times n$; n bins in the data distribution and $m \times n$ bins in the Monte Carlo samples. However, the A_{ji} must then be considered free parameters of the fit and the total number of degrees of freedom is given by

$$ndf = (m + 1) \times n - m - m \times n = n - m, \tag{A.9}$$

which is expected since no new independent information is added.

References

[1] S. Eidelman et al. Review of particle physics. *Phys. Lett.* B592 (2004) 1.

[2] T. Kinoshita and W. B. Lindquist. Eighth-order magnetic moment of the electron. V. Diagrams containing no vacuum-polarization loop. *Phys. Rev.* D42 (1990) 636.

[3] M. Gell-Mann. A schematic model of baryons and mesons. *Phys. Lett.* 8 (1964) 214.

[4] S. W. Herb et al. Observation of a dimuon resonance at 9.5 GeV in 400 GeV proton-nucleus collisions. *Phys. Rev. Lett.* 39 (1977) 252.

[5] W. R. Innes et al. Observation of structure in the Upsilon region. *Phys. Rev. Lett.* 39 (1977) 1240.

[6] C. Albajar et al. Beauty production at the CERN proton-antiproton collider. *Phys. Lett.* B186 (1987) 237.

[7] C. Albajar et al. Beauty production at the CERN $\mathrm{p\bar{p}}$ collider. *Phys. Lett.* B256 (1991) 121.

[8] P. Nason, S. Dawson and R. K. Ellis. The total cross section for the production of heavy quarks in hadronic collisions. *Nucl. Phys.* B303 (1988) 607.

[9] P. Nason, S. Dawson and R. K. Ellis. The one particle inclusive differential cross section for heavy quark production in hadronic collisions. *Nucl. Phys.* B327 (1989) 49.

[10] W. Beenakker, W. L. van Neerven, R. Meng, G. A. Schuler and J. Smith. QCD corrections to heavy quark production in hadron hadron collisions. *Nucl. Phys.* B351 (1991) 507.

[11] M. Cacciari and P. Nason. Is there a significant excess in bottom hadroproduction at the Tevatron? *Phys. Rev. Lett.* 89 (2002) 122003.

[12] M. Narain and U. Heintz. Observability of the decay $\mathrm{Z}^0 \rightarrow \mathrm{b\bar{b}}$ in Run II. DØ internal note 3604 (1999).

[13] F. Halzen and A. D. Martin. Quarks and Leptons: An Introductory Course in Modern Particle Physics. Wiley, New York, USA (1984).

[14] R. Brock et al. Handbook of perturbative QCD. *Rev. Mod. Phys.* 67 (1995) 157.

[15] B. Abbott et al. Improved precision on the top quark mass. *Nature* 429 (2004) 638.

[16] D. J. Gross and F. Wilczek. Ultraviolet behaviour of non-abelian gauge theories. *Phys. Rev. Lett.* 30 (1973) 1343.

[17] H. D. Politzer. Asymptotic freedom: an approach to strong interactions. *Phys. Rep.* 14 (1974) 129.

[18] The CTEQ collaboration.
URL `http://cteq.org/`

[19] Durham University online Parton Distribution Plotting and Calculation.
URL `http://durpdg.dur.ac.uk/HEPDATA/PDF`

[20] B. Andersen, G. Gustafson, G. Ingelman and T. Sjöstrand. Parton fragmentation and string dynamics. *Phys. Rep.* C97 (1983) 31.

[21] T. Sjöstrand, P. Edén, C. Friberg, L. Lönnblad, G. Miu, S. Mrenna and E. Norrbin. High-energy physics event generation with PYTHIA 6.1. *Comp. Phys. Comm.* 135 (2001) 238.

[22] C. Albajar et al. Measurement of the bottom quark production cross section in proton-antiproton collisions at $\sqrt{s} = 0.63$ TeV. *Phys. Lett.* B213 (1988) 405.

[23] C. Albajar et al. Measurement of $\mathrm{b\overline{b}}$ correlations at the CERN $\mathrm{p\overline{p}}$ collider. *Z. Phys.* C61 (1994) 41.

[24] F. Abe et al. Measurement of the B-meson and b-quark cross sections at $\sqrt{s} = 1.8$ TeV using the exclusive decay $\mathrm{B}^{\pm} \rightarrow \mathrm{J}/\psi\mathrm{K}^{\pm}$. *Phys. Rev. Lett.* 68 (1992) 3403.

[25] F. Abe et al. Inclusive J/ψ, $\psi(2\mathrm{S})$, and b-quark production in $\mathrm{p\overline{p}}$ collisions at $\sqrt{s} = 1.8$ TeV. *Phys. Rev. Lett.* 69 (1992) 3704.

[26] F. Abe et al. Measurement of bottom quark production in 1.8 TeV $\mathrm{p\overline{p}}$ collisions using muons from b-quark decays. *Phys. Rev. Lett.* 71 (1993) 2396.

[27] F. Abe et al. Measurement of the bottom-quark production cross section using semileptonic decay electrons in $\mathrm{p\overline{p}}$ collisions at $\sqrt{s} = 1.8$ TeV. *Phys. Rev. Lett.* 71 (1993) 500.

[28] F. Abe et al. Inclusive χ_c and b-quark production in $\mathrm{p\overline{p}}$ collisions at $\sqrt{s} = 1.8$ TeV. *Phys. Rev. Lett.* 71 (1993) 2537.

[29] F. Abe et al. Measurement of the B meson and b quark cross-sections at $\sqrt{s} = 1.8$ TeV using the exclusive decay $\mathrm{B}^0 \rightarrow \mathrm{J}/\psi\mathrm{K}^*(892)$. *Phys. Rev.* D50 (1994) 4252.

[30] F. Abe et al. Measurement of correlated $\mu - \overline{\mathrm{b}}$ jet cross sections in pp-bar collisions at $\sqrt{s} = 1.8$ TeV. *Phys. Rev.* D53 (1996) 1051.

[31] F. Abe et al. Measurement of $\mathrm{b\overline{b}}$ production correlations, $\mathrm{B}^0\overline{\mathrm{B}}^0$ mixing, and a limit on epsilon(B) in $\mathrm{p\overline{p}}$ collisions at $\sqrt{s} = 1.8$ TeV. *Phys. Rev.* D55 (1997).

[32] D. Acosta et al. Heavy flavor properties of jets produced in $\mathrm{p\overline{p}}$ interactions at $\sqrt{s} = 1.8$ TeV. *Phys. Rev.* D69 (2004) 072004.

[33] S. Abachi et al. Inclusive μ and b-quark production cross sections in $\mathrm{p\overline{p}}$ collisions at $\sqrt{s} = 1.8$ TeV. *Phys. Rev. Lett.* 74 (1995) 3548.

[34] S. Abachi et al. J/ψ production in $\mathrm{p\overline{p}}$ collisions at $\sqrt{s} = 1.8$ TeV. *Phys. Lett.* B370 (1996) 239.

[35] B. Abbott et al. Small-angle muon and bottom-quark production in $\mathrm{p\overline{p}}$ collisions at $\sqrt{s} = 1.8$ TeV. *Phys. Rev. Lett.* 84 (2000) 5478.

[36] B. Abbott et al. The $\mathrm{b\overline{b}}$ production cross section and angular correlations in $\mathrm{p\overline{p}}$ collisions at $\sqrt{s} = 1.8$ TeV. *Phys. Lett.* B487 (2000) 264.

[37] F. Stichelbaut. Properties of $\mathrm{b\overline{b}}$ production at the Tevatron. In: Proceedings of the XXXII Rencontres de Moriond (QCD) (J. Tran Thanh Van, editor), page 126. Editions Frontieres, Gif-sur-Yvette, France. FERMILAB-CONF-97-159-E (1997).

[38] D. Acosta et al. Measurement of the ratio of b quark production cross sections in $\mathrm{p\overline{p}}$ collisions at $\sqrt{s} = 1800$ GeV. *Phys. Rev.* D66 (2002) 032002.

[39] F. Abe et al. Measurement of the B meson differential cross section $\mathrm{d}\sigma/\mathrm{d}p_T$ in $\mathrm{p\overline{p}}$ collisions at $\sqrt{s} = 1.8$ TeV. *Phys. Rev. Lett.* 75 (1995) 1451.

[40] D. Acosta et al. Measurement of the B^+ total cross section and B^+ differential cross section $\mathrm{d}\sigma/\mathrm{d}p_T$ in $\mathrm{p\overline{p}}$ collisions at $\sqrt{s} = 1.8$ TeV. *Phys. Rev.* D65 (2002) 052005.

[41] M. Cacciari. Bottom hadroproduction vs. QCD. Presented at XXXIX Rencontres de Moriond, La Thuile, March 2004 (2004).

[42] M. Cacciari, S. Frixione, M. L. Mangano, P. Nason and G. Ridolfi. QCD analysis of first b cross section data at 1.96 TeV. hep-ph/0312132 (2003).

[43] R. D. Field. The sources of b quarks at the Tevatron and their correlations. *Phys. Rev.* D65 (2002) 094006.

[44] S. Frixione, P. Nason and B. R. Webber. Matching NLO QCD and parton showers in heavy flavour production. *JHEP* 08 (2003) 007.

[45] C. Peterson, D. Schlatter, I. Schmitt and P. M. Zerwas. Scaling violations in inclusive $\mathrm{e}^+\mathrm{e}^-$ annihilation spectra. *Phys. Rev.* D27 (1983) 105.

[46] J. Chrin. Upon the determination of heavy quark fragmentation functions in $\mathrm{e}^+\mathrm{e}^-$ annihilation. *Z. Phys.* C36 (1987) 163.

[47] B. Abbott et al. Cross section for b-jet production in $\mathrm{p\overline{p}}$ collisions at $\sqrt{s} = 1.8$ TeV. *Phys. Rev. Lett.* 85 (2000) 5068.

[48] S. Frixione and M. L. Mangano. Heavy-quark jets in hadronic collisions. *Nucl. Phys.* B483 (1997) 321.

[49] C. Albajar et al. Study of heavy flavour production in events with a muon accompanied by jet(s) at the CERN proton-antiproton collider. *Z. Phys.* C37 (1988) 489.

[50] F. Abe et al. Measurement of $\mathrm{b\bar{b}}$ rapidity correlations in $\mathrm{p\bar{p}}$ collisions at $\sqrt{s} = 1.8$ TeV. *Phys. Rev.* D61 (2000) 32001.

[51] D. Acosta et al. Measurements of bottom anti-bottom azimuthal production correlations in proton antiproton collisions at $\sqrt{s} = 1.8$ TeV. hep-ex/0412006 (2004).

[52] M. L. Mangano and P. Nason. Heavy quark multiplicities in gluon jets. *Phys. Lett.* B285 (1992) 160.

[53] R. Akers et al. Studies of charged particle multiplicity in b quark events. *Z. Phys.* C61 (1994) 209.

[54] P. Abreu et al. Measurement of the charged particle multiplicity of weakly decaying B hadrons. *Phys. Lett.* B425 (1998) 399.

[55] D. Coffman et al. Measurement of the inclusive decay properties of charmed mesons. *Phys. Lett.* B263 (1991) 135.

[56] The CLEO collaboration. QQ - The CLEO Event Generator.
URL `http://www.lns.cornell.edu/public/CLEO/soft/QQ`

[57] S. Frixione and B. R. Webber. Matching NLO QCD computations and parton shower simulations. *JHEP* 06 (2002) 029.

[58] F. Abe et al. Observation of top quark production in $\mathrm{p\bar{p}}$ collisions with the Collider Detector at Fermilab. *Phys. Rev. Lett.* 74 (1995) 2626.

[59] S. Abachi et al. Observation of the top quark. *Phys. Rev. Lett.* 74 (1995) 2632.

[60] D. A. Crane et al. Status report: Technical design of neutrino beams for the Main Injector (NuMI). FERMILAB-TM-1946 (1995).

[61] S. van der Meer. Stochastic cooling and the accumulation of antiprotons. In: Nobel Lectures, Physics 1981-1990 (G. Ekspång, editor). World Scientific Publishing Co., Singapore (1993).

[62] S. Abachi et al. The DØ detector. *Nucl. Inst. Meth.* A338 (1994) 187.

[63] S. Kesisoglou*for the DØ Collaboration*. Production and testing of the DØ silicon microstrip tracker. *Int. J. Mod. Phys.* A16-1C (2001) 1087.

[64] M. Narain. A silicon track trigger for the DØ experiment. *Nucl. Inst. Meth.* A447 (2000) 223.

[65] B. Quinn. The DØ silicon microstrip tracker. *Nucl. Inst. Meth.* A501 (2003) 7.

[66] A. Bean *for the DØ Collaboration*. Status of the DØ silicon microstrip tracker. *Nucl. Inst. Meth.* A466 (2001) 262.

[67] D. Mihalcea *for the DØ Collaboration*. The assembly and testing of the DØ silicon detector. *Nucl. Inst. Meth.* A473 (2001) 49.

[68] F. Filthaut *for the DØ Collaboration*. Production and testing of the DØ silicon microstrip tracker. *IEEE Trans. Nucl. Sci.* 48 (2001) 1002.

[69] F. Lehner. The phenomenology of the micro discharge effects on DØ silicon modules. DØ internal note 3804 (2000).

[70] R. J. Yarema et al. A beginners guide to the SVX II chip. FERMILAB-TM-1892 (1994).

[71] T. Zimmerman et al. The SVX II readout chip. *IEEE Trans. Nucl. Sci.* NS-42 (4) (1995).

[72] R. Lipton *for the DØ Collaboration*. The DØ silicon tracker. *Nucl. Inst. Meth.* A418 (1998) 85.

[73] A. Juste *for the DØ Collaboration*. The readout system for the silicon microstrip tracker of the upgraded DØ detector. *Nucl. Inst. Meth.* A461 (2001) 155.

[74] P. Azzi et al. Radiation damage experience at CDF with SVX'. *Nucl. Inst. Meth.* A383 (1996) 155.

[75] F. Lehner and S. Choi. What do we know about radiation damage in silicon detectors? DØ internal note 3803 (2000).

[76] R. Lipton. Lifetime of the DØ silicon tracker. DØ internal note 4077 (2002).

[77] DØ Layer Ø silicon group. DØ Layer Ø conceptual design report. DØ internal note 4415 (2004).

[78] S. J. de Jong. Status of the OPAL microvertex detector and new radiation monitoring and beam dump system. *Nucl. Inst. Meth.* A418 (1998) 22.

[79] P. F. Derwent. Radiation monitoring for vertex detectors at the Tevatron. *Nucl. Inst. Meth.* A447 (2000) 110.

[80] S. N. Ahmed, R. Lipton, D. A. Wijngaarden, S. Duensing, A. Naumann and S. J. de Jong. DØ SMT radiation protection system. DØ internal note 3915 (2001).

[81] S. N. Ahmed, R. Lipton, D. A. Wijngaarden, S. Duensing, A. Naumann and S. J. de Jong. DØ SMT radiation monitoring system. DØ internal note 4022 (2002).

[82] S. J. de Jong, C. Galea and C.-M. Anăstăsoaie. Radiation dose history in the SMT. DØ internal note 4653 (2004).

[83] Crocker Nuclear Laboratory, Davis, California, USA. The proton radiation test beam at the UC Davis Crocker Nuclear Laboratory (CNL) was set up and instrumented through a joint effort of CNL and the US Naval Research Laboratory.

[84] A. Juste, M. Tripathi and D. A. Wijngaarden. Measurement of the single event upset cross-section in the SVX IIe chip. *Nucl. Inst. Meth.* A500 (2003) 371.

[85] M. Adams et al. Design report of the central preshower detector for the DØ upgrade. DØ internal note 3014 (1996).

[86] M. Bhattacharjee et al. Technical design report of the forward preshower detector for the DØ upgrade. DØ internal note 3445 (1998).

[87] A. M. Patwa. The forward preshower system and a study of the J/ψ trigger with the DØ detector. Ph.D. thesis, SUNY at Stony Brook (2002).

[88] R. Brun et al. GEANT: Simulation program for particle physics experiments. User guide and reference manual. CERN-DD/78/2 (1978).

[89] N. V. Mokhov. The MARS code system user's guide version 13(95). FERMILAB-FN-0628 (1995).

[90] V. Sirotenko. Choice of better shielding materials for DØ detector upgrade. DØ internal note 3530 (1998).

[91] A. Brandt et al. A forward proton detector at DØ. FERMILAB-PUB-97-377 (1997).

[92] G. A. Alves. The forward proton detector at DØ. hep-ex/9804005 (1998).

[93] J. Bantley, A. Brandt, R. Partridge, J. Perkins and D. Puseljic. Improvement to the DØ luminosity monitor constant. FERMILAB-TM-1930 (1996).

[94] The updated DØ luminosity determination. DØ internal note 4328 (2004).

[95] C.-C. Miao *for the DØ Collaboration*. The DØ Run II luminosity monitor. DØ internal note 3573 (1998).

[96] S. H. Ahn, O. Atramentov, M. Begel, G. Geurkov, J. Hauptman, A. Kupco, S. W. Lee, P. Mal, C.-C. Miao, J. W. Park, R. Partridge, H. Schellman and M. Verzocchi. Luminosity and performance of DØ during the first year of Run II. DØ internal note 3973 (2002).

[97] A. Haas. DØ Level 1 and Level 2 calorimeter trigger performance in multi-jet events. DØ internal note 4073 (2003).

[98] T. Christiansen. The DØ L2-muon trigger performance in p11. DØ internal note 4053 (2002).

[99] Private communication with V. Buescher.

[100] O. Peters. Measurement of the b-jet cross section at $\sqrt{s} = 1.96$ TeV. Ph.D. thesis, University of Amsterdam (2003).

[101] G. C. Blazey et al. Run II jet physics. hep-ex/0005012 (2000).

[102] DØ JetMet group. Hot cells and missing transverse energy in Run II. DØ internal note 3986 (2002).

[103] B. Oliver et al. NADA - a new event by event hot cell killer. DØ internal note 3687 (2000).

[104] G. Bernardi and S. Trincaz-Duvoid. Improvement of the NADA algorithm: Hot cell killing in DØ Run II data. DØ internal note 4057 (2002).

[105] F. Canelli et al. First jet energy scale at DØ in Run II. DØ internal note 4110 (2002).

[106] J. Coss et al. Jet energy scale for p11 data. DØ internal note 4112 (2002).

[107] J. Zhu. Determination of electron energy scale and energy resolution using p14 $Z^0 \to e^+e^-$ data. DØ internal note 4323 (2003).

[108] E. Barberis et al. Top group ROOT tuples selection and data quality monitoring. DØ internal note 3942 (2002).

[109] F. Fleuret, F. Beaudette and S. Protopopescu. The DØ soft electron reconstruction package SEMReco. DØ internal note 3872 (2001).

[110] F. Fleuret. The DØ electron/photon analysis package EMAnalyze. DØ internal note 3888 (2001).

[111] D. Adams. Finding tracks. DØ internal note 2958, CMS TN/96-062 (1996).

[112] G. Hesketh. A measurement of the Z^0 boson production cross section times muon branching fraction in $p\bar{p}$ collisions at 1.96 TeV. Ph.D. thesis, University of Manchester (2003).

[113] T. LeCompte and H. T. Diehl. The CDF and DØ upgrades for Run II. *Ann. Rev. Nucl. Part. Sci.* 50 (2000) 71.

[114] G. R. Lynch and O. I. Dahl. Approximations to multiple coulomb scattering. *Nucl. Inst. Meth.* B58 (1991) 6.

[115] A. Schwartzman and M. Narain. Secondary vertex reconstruction using the Kalman filter. DØ internal note 3908 (2001).

[116] A. Schwartzman and M. Narain. Primary vertex selection. DØ internal note 3906 (2001).

[117] A. Cerri, S. Donati and L. Ristori. Measuring beam width and SVX impact parameter resolution. CDF internal note 4189 (1997 (rev. 2001)).

[118] O. Peters. Muon segment reconstruction - linked list algorithm. DØ internal note 3901 (2001).

[119] Muon ID Group. Muon ID version 1.0 (2002).

[120] J. M. Butler. Local muon momentum resolution. DØ internal note 4002 (2002).

[121] R. Barlow and C. Beeston. Fitting using finite Monte Carlo samples. *Comp. Phys. Comm.* 77 (1993) 219.

[122] T. Sjöstrand, L. Lönnblad and S. Mrenna. PYTHIA 6.2: Physics and manual. hep-ph/0108264 (2001).

[123] D. Bloch, B. Clément, D. Gelé, S. Greder and I. Ripp-Baudot. Performance of the jet lifetime probability method for b-tagging in DØ data. DØ internal note 4158 (2003).

[124] Private communication with M. Hildreth.

[125] V. M. Abazov et al. Measurement of dijet azimuthal decorrelations at central rapidities in $p\bar{p}$ collisions at $\sqrt{s} = 1.96$ TeV. hep-ex/0409040 (2004).

[126] D. Bloch, B. Clément, D. Gelé, S. Greder and I. Ripp-Baudot. Performance of the JLIP btagger in p14. DØ internal note 4348 (2004).

[127] S. Baker and R. D. Cousins. Clarification of the use of chi square and likelihood functions in fits to histograms. *Nucl. Inst. Meth.* A221 (1984) 437.

Summary

Measurements of the b quark production cross section at the Tevatron and at Hera in the final decades of the 20th century have consistently yielded higher values than predicted by Next-to-Leading Order (NLO) QCD. This discrepancy has led to a large efforts by theorists to improve theoretical calculations of the cross sections and simulations of b quark production. As a result, the difference between theory and experiment has been much reduced. New measurements are needed to test the developments in the calculations and in event simulation.

In this thesis, a measurement of angular correlations between b jets produced in the same event is presented. The angular separation between two b jets is directly sensitive to higher order contributions. In addition, the measurement does not depend strongly on fragmentation models or on the experimental luminosity and efficiency, which lead to a large uncertainty in measurements of the inclusive cross section.

At the Tevatron, $b\overline{b}$ quark pairs are predominantly produced through the strong interaction. In leading order QCD, the b quarks are produced back to back in phase space. Next-to-leading order contributions involving a third particle in the final state allow production of b pairs that are very close together in phase space. The Leading Order and NLO contributions can be separated into three different processes: flavour creation, gluon splitting and flavour excitation. While the separation based on Feynman diagrams is ambiguous and the three processes are not each separately gauge invariant in NLO QCD, the distinction can be made explicitly in terms of event generators using LO matrix elements.

Direct production of a $b\overline{b}$ quark pair in the hard scatter interaction is known as flavour creation. The quarks emerge nearly back to back in azimuth. In gluon splitting processes, a gluon is produced in the hard scatter interaction. The gluon subsequently splits into a $b\overline{b}$ quark pair. The quarks are very close in phase space. The flavour excitation process can be interpreted as production of a $b\overline{b}$ quark pair before the hard scatter interaction. One of the b quarks interacts with a particle from the other beam hadron and emerges with high p_T. The other quark stays close to the beam axis but may still be recorded by the detector. The azimuthal correlation between the b quarks is weak. In leading order event generators, the gluon splitting and flavour excitation processes are simulated by final- and initial state showering.

The b quarks produced in the proton-antiproton collisions at the Tevatron are detected through the signature of their decay products in the DØ detector. The particles associated with the production and decay of a b hadron are reconstructed as a jet in the calorimeter. These b jets are distinguished from light flavour background using two methods.

The first method is based on the association of a muon with the jet. In about 20% of b hadron decays, a muon is created. Due to the large mass of the b hadron, this muon will have large transverse momentum with respect to the flight axis of the b hadron. This relative transverse momentum or P_T^{Rel} is approximated by the P_T^{Rel} of the muon with respect to the jet axis. The fraction of b jets in a muon plus jet sample can be determined by fitting the P_T^{Rel} distributions for b jets and background jets determined from Monte Carlo to the data distribution.

The second method uses the relatively long lifetime of b hadrons. The tracks of the decay products of the b hadron do not point back to the production point but to the decay point of the hadron, which is displaced from the primary vertex by an average of $c\tau\gamma \approx 0.5\gamma$ mm. Combined with the large mass of the hadron, this means the tracks are also displaced from the production point. By comparing the distance of shortest approach of each track to the distribution for background tracks, the probability that each track comes from a background process is determined. The probabilities of all tracks associated with a jet are combined to compute the lifetime probability for the jet to come from a background process.

In this thesis, the angle between a pair of b jets is determined as the angle $\Delta\phi$ between a jet with an associated muon and a jet with a very low background lifetime probability. After selection, 1062 events remain. About 67% of all selected jet pairs are b jet pairs.

The relative contributions of the flavour creation, gluon splitting and flavour excitation processes and of the remaining light flavour background are determined by simultaneously fitting the P_T^{Rel} distribution of the muon jet and the angle $\Delta\phi$ between the two jets with the distributions obtained from Monte Carlo samples generated for each process using PYTHIA. The fit method takes into account the limited sample size of both the data and the Monte Carlo samples.

The measured fractions of flavour creation, flavour excitation and gluon splitting, after background subtraction, are

$$\begin{array}{ll} \text{flavour creation} & 0.60 \pm 0.06(\text{stat})^{+0.07}_{-0.01}(\text{syst}), \\ \text{gluon splitting} & 0.18 \pm 0.07(\text{stat})^{+0.07}_{-0.08}(\text{syst}), \\ \text{flavour excitation} & 0.22 \pm 0.11(\text{stat})^{+0.06}_{-0.09}(\text{syst}). \end{array}$$

As expected, the contributions of the higher order gluon splitting and flavour excitations are important. The measured fractions are not the same as those predicted by PYTHIA but the uncertainties are too large to allow a precise test of the simulation. The DØ experiment now has access to a more than one hundred times larger dataset and to improved reconstruction and tagging algorithms. With the larger dataset now available, theoretical calculations and simulations can be tested to high accuracy. The methods and results presented in this thesis show the way for these new measurements.

Samenvatting

Hoekcorrelaties bij beauty quark productie bij het Tevatron bij $\sqrt{s}$ = 1.96 TeV

In dit proefschrift wordt een meting beschreven van de hoekcorrelatie tussen een beauty quark en een anti-beauty quark die samen worden geproduceerd. De beauty quarks worden geproduceerd in de proton-antiproton botsingen in de Tevatron deeltjesversneller van Fermilab, vlakbij Chicago in de Verenigde Staten, en geregistreerd met de DØ detector.

Het beauty- of bottom quark of eenvoudig b-quark is het op één na zwaarste van de zes quarks die worden beschreven in het Standaard Model van de elementaire deeltjesfysica. De twee lichtste quarks, up en down, zijn de bouwstenen van protonen en neutronen en wegen niet veel meer dan een paar duizendste maal de massa van een waterstofatoom. Het beauty quark is iets zwaarder dan een heliumatoom. Beauty quarks kunnen in de huidige deeltjesversnellers gemakkelijk worden gecreëerd. Dat, samen met hun grote massa, maakt ze zeer geschikt om bepaalde theoretische voorspellingen te toetsen.

Bij proton-antiproton botsingen ontstaan beauty quarks vooral door de sterke kernkracht. In het Standaard Model wordt deze kracht beschreven door de Quantum ChromoDynamica (QCD). De voorspellingen van QCD kunnen niet exact worden uitgerekend. In plaats daarvan worden experimenteel meetbare grootheden meestal uitgedrukt in storingsreeksen in de interactiesterkte van de sterke kracht α_s. De storingsreeks is een machtreeks waarbij steeds hogere machten van α_s een steeds kleinere bijdrage leveren aan de berekende grootheid. In de eenvoudigste benadering worden alleen de laagste orde termen meegenomen, in dit geval $\mathcal{O}(\alpha_s^2)$. In tegenwoordig gangbare hogere orde berekeningen worden ook de $\mathcal{O}(\alpha_s^3)$ termen meegenomen.

De koppelingssterkte α_s is niet constant maar hangt af van de energieschaal van het proces: hoe hoger de energieschaal, hoe zwakker de sterke kracht en hoe kleiner α_s. Als α_s klein genoeg is kunnen de hogere orde termen worden verwaarloosd. Als de energieschaal te laag is wordt α_s te groot om de storingstheorie nog te kunnen toepassen. Bij de productie van beauty quarks wordt de energieschaal bepaald door de massa en de impuls van de quarks. De grote massa van de quarks zorgt ervoor dat de storingsrekening kan worden toegepast.

Beauty quarks worden bij de sterke wisselwerking altijd gecreëerd in een quark-antiquark paar. Al in de jaren tachtig van de vorige eeuw is gebleken dat hogere orde termen een significante bijdrage leveren aan de totale productie van beauty quarks bij proton-antiproton botsingen. In de jaren negentig leken ook hogere orde berekeningen voor de productiewaarschijnlijkheid niet overeen te komen met de waarden die door experimenten op Fermilab werden gemeten. Sindsdien hebben theoretici veel werk verzet om het verschil te verklaren, en laten nieuwe berekeningen en simulaties een veel minder significant verschil zien. Om deze nieuwe berekeningen en simulaties te testen zijn nieuwe metingen nodig. Door te kijken naar de correlaties tussen beauty quarks geproduceerd in dezelfde botsing kan de bijdrage van de hogere orde termen direct worden bestudeerd. Bovendien vallen bij een dergelijke meting grote onzekerheden weg die anders zouden worden geïntroduceerd door de normering van de productiewaarschijnlijkheid.

De laagste orde term en de verschillende hogere orde termen kunnen worden geclassificeerd in drie groepen: flavour creation, gluon splitting en flavour excitation.

Bij het flavour creation proces worden het b-quark en het anti-b quark direct gecreëerd uit de botsing van de deeltjes in het proton en het antiproton. Door behoud van impuls verlaten de quarks het botsingspunt onder een hoek van bijna 180° ten opzichte van elkaar in het vlak loodrecht op de bundel.

Bij het gluon splitting proces wordt eerst een gluon gecreëerd. Het gluon is het deeltje dat wordt uitgewisseld in de sterke kracht en de quarks in bijvoorbeeld protonen bij elkaar houdt. Het speelt dezelfde rol in de sterke kernkracht als het foton in de elektromagnetische kracht. Het gecreëerde gluon kan opsplitsen in een beauty quark-antiquark paar. De quarks krijgen allebei een deel van de impuls van het gluon en de hoek tussen de quarks is gemiddeld veel kleiner dan 180°.

Het flavour excitation proces kan worden geïnterpreteerd als de creatie van een beauty quark paar in een van de bundels vóór de botsing. Bij de botsing verlaat één van de twee beauty quarks het botsingspunt onder een grote hoek met de bundel. Het andere quark komt minder ver van de bundel maar kan vaak nog steeds door de detector worden geregistreerd. In het vlak loodrecht op de bundel is de correlatie tussen het quark en het antiquark zeer zwak.

Door de gemeten hoekverdeling in het vlak loodrecht op de bundel te vergelijken met de verdelingen voor flavour creation, gluon splitting en flavour excitation die zijn verkregen met een simulatie kan de relatieve bijdrage van elk proces aan de totale productie worden bepaald.

De beauty quarks die bij een botsing worden gecreëerd gaan onder de invloed van de sterke kracht verbindingen aan met andere quarks en vormen zo gebonden toestanden die hadronen worden genoemd. Deze b-hadronen vervallen te snel om direct te kunnen worden waargenomen. In plaats daarvan wordt hun aanwezigheid na een botsing afgeleid uit hun stabielere vervalsproducten. Die vervalsproducten worden waargenomen in de DØ detector die rond het botsingspunt is gebouwd.

De elektrisch geladen deeltjes die ontstaan bij het verval van een b-hadron laten eerst elektrische signalen achter in het binnenste deel van de detector (de “sporenkamers”), waardoor hun vluchtpad kan worden gereconstrueerd. In het volgende deel van de detector (de calorimeter) veroorzaken zowel elektrisch geladen als neutrale deeltjes een lawine van secundaire deeltjes die geheel door de detector wordt geabsorbeerd. Deeltjes die dicht bij elkaar liggen worden samen een jet genoemd. Een jet die het gevolg is van een vervallend b-hadron wordt een b-jet genoemd.

De b-jets worden op twee manieren onderscheiden van andere jets. In ongeveer 20% van de vervallen van b-hadronen ontstaat ook een muon, een deeltje met veel dezelfde eigenschappen als een electron maar met een veel grotere massa. Het muon veroorzaakt geen deeltjeslawine en kan ook achter de calorimeter nog een spoor veroorzaken, waardoor het makkelijk kan worden geïdentificeerd. Dankzij de relatief grote massa van b-hadronen krijgen hun vervalsdeeltjes een grote impuls in het vlak loodrecht op de bewegingsrichting van het b-hadron. Deze relatieve impuls, of P_T^{Rel}, kan gemeten worden als de relatieve impuls van het muon ten opzichte van de jet. Muonen afkomstig van een b-quark verval hebben gemiddeld een grotere waarde van P_T^{Rel} dan muonen die in andere processen zijn ontstaan. Door de verdeling van P_T^{Rel} te vergelijken met simulaties van b-jets en van jets in achtergrondprocessen kan het aantal b-jets bepaald worden.

De tweede manier om b-jets te herkennen berust op het feit dat b-hadronen gemiddeld iets langer leven dan belangrijke, onstabiele achtergronddeeltjes. Hierdoor vliegen ze gemiddeld bijna een halve millimeter van het botsingspunt voordat ze vervallen. De sporen van de vervalsproducten van een deeltje dat direct vervalt wijzen terug naar het punt waar de botsing heeft plaatsgevonden. Bij het verval van een b-hadron wijzen de sporen echter terug naar het vervalspunt, dat iets is verplaatst ten opzichte van het productiepunt. Gecombineerd met de grote massa van het b-hadron leidt dit ertoe dat ook de sporen verplaatst zijn ten opzichte van het botsingspunt. De kortste afstand tussen de sporen en het botsingspunt in het vlak loodrecht op de richting van de bundels bedraagt bij b-vervallen gemiddeld ongeveer 80 micrometer. Dankzij de hoge precisie siliciumdetector in het binnenste deel van de DØ detector kan deze afstand met een resolutie van ongeveer 20 micrometer bepaald worden. De sporen binnen de jet worden gebruikt om de "levensduurwaarschijnlijkheid" dat de jet het gevolg is van een vervallend b-hadron te bepalen.

In dit proefschrift wordt de hoek tussen twee b-jets bepaald als de hoek tussen een jet met een geassocieerd muon en een jet met een hoge levensduurwaarschijnlijkheid. Na selectie van botsingen die aan deze criteria en een aantal andere kwaliteitscriteria voldoen blijven 1062 botsingen over. Ongeveer tweederde van de jet-paren in deze gevallen bestaat uit twee b-jets.

De fracties jets in deze botsingen als gevolg van flavour creation, flavour excitation en gluon splitting processen en achtergrondprocessen worden bepaald door tegelijkertijd de P_T^{Rel} verdeling van de muon-jets en de hoekverdeling tussen de muon-jet en de levensduur-geselecteerde jet te vergelijken met de verdelingen die voor alle processen met de PYTHIA simulator zijn gegenereerd. De P_T^{Rel} variabele zorgt hier voor het onderscheid tussen b-jets en niet-b-jets. De hoekverdeling bepaalt het onderscheid tussen de drie processen voor de productie van beauty quarks.

De vergelijking gebeurt met een likelihood fit. De fit procedure bepaalt de verhoudingen waarin de verdelingen voor de afzonderlijke processen bij elkaar opgeteld moeten worden om zo goed mogelijk met de experimenteel bepaalde verdeling overeen te komen. De methode houdt hierbij rekening met de statistische onzekerheid als gevolg van het aantal botsingen in zowel het experiment als de simulatie.

De gemeten fracties voor flavour creation, flavour excitation en gluon splitting, na aftrekken van de niet-b achtergrond, zijn

flavour creation	$0.60 \pm 0.06(\text{stat})^{+0.07}_{-0.01}(\text{syst})$,
gluon splitting	$0.18 \pm 0.07(\text{stat})^{+0.07}_{-0.08}(\text{syst})$,
flavour excitation	$0.22 \pm 0.11(\text{stat})^{+0.06}_{-0.09}(\text{syst})$.

Zoals verwacht zijn de bijdragen van de hogere orde gluon splitting en flavour excitation processen belangrijk. De gemeten waarden komen niet goed overeen met de voorspellingen van de simulatie maar de onzekerheden zijn te groot om harde uitspraken te doen. Inmiddels heeft het DØ experiment de beschikking over een bijna honderd maal grotere en met hogere precisie gemeten gegevensset. Met de nieuwe gegevens kan deze meting herhaald worden en kunnen simulaties met hoge nauwkeurigheid worden getoetst. De methoden en resultaten die in dit proefschrift zijn beschreven vormen hiervoor de basis.

Dankwoord

Ten eerste wil ik mijn promotor Sijbrand de Jong en co-promotor Frank Filthaut bedanken. Zonder hun kennis en hun inzicht in problemen waar ik de oplossing niet voor zag was dit proefschrift niet tot stand gekomen. Sijbrand sprak al over correlaties voordat ik naar Fermilab vertrok, en zijn optimisme was altijd aanstekelijk. Frank zette mij op het spoor van de lifetime probability tag en zijn dagelijkse, kritische feedback was zeer belangrijk voor de analyse en het schrijven van het proefschrift.

Tijdens de eerste twee jaar van mijn promotieonderzoek heb ik meegewerkt aan het testen van de stralingsmonitors. Cees, Jan en Ed wil ik bedanken voor alles wat ik in die tijd van hen heb geleerd. At Fermilab, I continued working on testing and installing the radiation monitors. Special thanks go out to Naeem Ahmed and Ron Lipton, who shared and coordinated a lot of the work. I also want to thank my colleagues in the DØ SMT group, especially those with whom I worked on debugging the readout electronics. One of the highlights of this period was working on the Single Event Upset test with Aurelio Juste and Mani Tripathi. Ik wil Marcel Demarteau bedanken voor de frequente gesprekken over het werk en over het leven in Amerika.

Toen ik in Amerika aankwam had ik niets behalve twee goede vrienden en collega's: Onne en Silke. Het was soms moeilijk en een huis, en een cubicle , en een auto met zijn drieën te moeten delen maar zonder hen was het nog veel moeilijker geweest, en ik ben ze zeer dankbaar. Onne was ook in het tweede jaar een fantastische huisgenoot en aan zijn proefschrift heb ik bovendien heel veel gehad.

Later kwamen er steeds meer studenten naar Fermilab. De "Nederlanders" Axel, Freya, Paul, Lukas en Johanna wil ik bedanken voor de discussies en de gezelligheid, zowel op als buiten Fermilab. I also want to thank the other students who attended the Friday night barbecues and the poker nights, especially the usual hosts, Daniel (the basement that time forgot) and Kirby.

Terug in Nederland stortte ik mij eerst op b-tagging en daarna op mijn analyse. I want to thank Rick van Kooten and Ariel Schwartzman for the motivating discussions in the BID meetings during the time the lifetime tag was first shown to work. Ik ben veel dank verschuldigd aan Axel (die tevens voor korte tijd mijn derde DØ-huisgenoot was) voor zijn ROOT expertise en voor het SEED pakket, waar ook Onne, Paul en Lukas een belangrijke bijdrage aan hebben geleverd. De analyse was onmogelijk geweest zonder de hulp van Willem van Leeuwen bij het genereren van de enorme hoeveelheden Monte Carlo op de farm in Amsterdam. Eric Laenen wil ik bedanken voor het doorlezen en corrigeren van het theorie-hoofdstuk.

In Nijmegen heb ik veel steun en gezelligheid genoten van Annelies, Gemma, Marjo, Peter, Charles en alle andere mensen van de afdeling. Nijmegen would have been a lonely place without the dinners and drinks with other students and I want to thank Achileas, Angelica, Cristina, Marcela and Jason, Miran, Pieter, Qin and Zhiming, Tamas, and Zahara for their company. De meeste oudere promovendi waren al weg toen ik terugkwam, maar Wim (nog een keer naar Duitsland steppen?), Henric (ijsje?) en Michiel (vorbeşti româneşte?) mag ik hier niet vergeten te noemen.

Een constant gegeven gedurende de zes jaar was de dagelijkse stortvloed aan mail. Het is prettig om elke ochtend tussen alle spam ook onzin te vinden die leuk is om te lezen. Alec, Freya, Len, Miente, Peter, Torsten en Vince wens ik een heel goede moge.

Martijn Rengelink ben ik zeer dankbaar voor zijn vriendschap en voor de de tijd die hij altijd bereid was vrij te maken voor een goed gesprek en een goed glas drank.

Het belangrijkst zijn de mensen die je het meest na staan. Mijn ouders en mijn zusje wil ik bedanken voor hun onvoorwaardelijke steun. Zij hebben mij nooit laten vergeten dat de mens altijd voor gaat. Finally, I want to thank Miruna for her love and for her support during the times I needed it most. I am looking forward to our future together. Te iubesc.

Curriculum Vitae

Daniel Abraham Wijngaarden [redacted]. Daar behaalde hij in 1993 zijn VWO diploma aan het Barlaeus Gymnasium. Na zijn eindexamen begon hij aan de studie experimentele natuurkunde aan de Universiteit van Amsterdam. In de zomer van 1997 was hij zomerstudent bij CERN in Genève en werkte aan een benchmark voor het vertex-trigger algoritme voor het LHCb experiment. Daarna deed hij zijn afstudeeronderzoek aan het Nikhef onder begeleiding van Gras van Apeldoorn. Met het doctoraalexamen in september 1998 sloot hij zijn studie af. De titel van zijn afstudeerscriptie was “Electron drift velocities in fast argon and CF_4-based drift gases”. Tijdens zijn studietijd was hij actief in de studentenvereniging NSA en in de faculteitsraad en de facultaire studentenraad.

In october 1998 begon hij met zijn promotieonderzoek in de experimentele hoge energie fysica aan (toen nog) de Katholieke Universiteit Nijmegen onder professor Sijbrand de Jong. Van april 1999 tot en met december 2000 was hij gedetacheerd aan het Fermi National Accelerator Laboratory (Fermilab) nabij Chicago, waar hij een bijdrage heeft geleverd aan de constructie van de DØ Silicon Microstrip Tracker. Tijdens zijn verblijf in de Verenigde Staten nam hij deel aan het outreach programma van Fermilab en bezocht een aantal lagere scholen. Na zijn terugkomst in Nijmegen was hij betrokken bij het geven van onderwijs aan 2^e, 3^e en 4^e jaars studenten. Het proefschrift “Angular correlations in beauty production at the Tevatron at $\sqrt{s} = 1.96$ TeV” werd in 2005 voltooid. Voorlopige resultaten uit het onderzoek werden gepresenteerd in 2002 op de April meeting van de American Physical Society in Albuquerque, New Mexico, en in augustus 2004 op de jaarvergadering van de Division of Particles and Fields van de American Physical Society in Riverside, Californie. De resultaten werden ook gepresenteerd op de jaarvergaderingen van de Nederlandse Natuurkundigen Vereniging in Lunteren in het najaar van 2002 en 2004. Hij bezocht in 1999 en in 2000 de Joint Belgian-Dutch-German Summer School on Particle Physics en in 2001 het SLAC Summer Institute in Stanford, Californie.